Wolfson School of Mechanical Electrical and Manufacturing Engineering

Dynamic Deformation, Damage and Failure of Carbon Fibre Composites under Ballistic and Blast Loading

Laurence Alexander Coles
CEng, MEng (Hons)

A Doctoral Thesis
Submitted in fulfilment of the requirements for the award of
Doctor of Philosophy at Loughborough University

September 2018

Dedication

To my mother, Margerat Anne Coles, who's belief
and confidence in me has never failed.

Abstract

Carbon Fibre Reinforced Polymers (CFRPs) have proven to be a popular choice in many applications given their higher desired and advantageous high strength to weight ratio, which makes them ideal for extreme loading conditions such as; low velocity impacts through airborne debris (1-100 m/s), high velocity impacts with fragmenting hailstone clouds, or even close-proximity air blast shock waves. In a real environment, these dynamic loading conditions are very rarely mutually exclusive, and so it is necessary to analyse the combined loading of both an impact and air blast shockwave which then creates the following question. Which is the most destructive, an impact closely followed by an air blast or visa-versa?

With this in mind, the presented research is first focused on the experiment testing of a consistent CFRP specimen material to ballistic rigid steel and fragmenting ice projectiles, as well as air blast shock wave loading with in-situ deformation analysis via digital image correlation from high speed photography alongside the post loading damage analysis via x-ray tomography. The second part of the research then focuses on the development of a meso-scale modelling strategy for carbon fibre reinforce polymer (CFRP) via a phenomenological continuum damage approach, which delivers accurate through-thickness stress responses, strain-rate sensitive behaviour, and full damage-initiation and evolution tracking of various damage modes with stiffness degradation. The modelling approach was incorporated into Abaqus Explicit 6.14-4 as a user defined subroutine (VUMAT), with inter-ply delamination modelled via cohesive zone surfaces (CZSs).

Following a new approach to obtaining and extrapolating material parameters for CFRPs utilising a comparative literature search to obtain an array of common ratios, the CFRP model was validated against the ballistic and air blast experiments, the results of which demonstrate the model delivering accurate correlation of both the specimens

deformation behaviour and observed resultant damage to the various experimental loading conditions without modification of the modelling parameters. Finally, the modelling approach was then employed to predict and analyse the hypothetical scenarios of the impact closely followed by an air blast and visa-versa, subjecting the CFRP to set combined loading conditions within the limits of those set out within the scope of the experiment studies.

Keywords – Carbon fibre-reinforced polymer; Finite-element model; Ballistic impact; Air-blast; VUMAT; Damage; Failure; X-ray tomography.

Acknowledgements

Firstly I'd like to express my utmost appreciation and thanks to my supervisors. To Dr Anish Roy who has been my greatest mentor over the past 6 years, I thank you for pushing me to make the most of every opportunity presented. Then to Professor Vadim Silberschmidt for his guidance throughout the past 4 years, along with two fantastic opportunities for international collaboration which have helped me grow both professionally and personally. Their endless support, understanding and drive through both academic and personal challenges has been invaluable throughout my research.

Secondly I must give thanks to Professor Mikhail Nikhamkin, Leonid Voronov, Boris Bolotov and Sergey Semyonov from the Perm National Research Polytechnical University, and to Prof. Arun Shukla and Craig Tilton from the University of Rhode Island for inviting me into their research groups and supporting me through the various experimental test regimes detailed throughout my research.

Then to all the members of the Mechanics of Advanced Materials (MoAM) research group, it has been a real pleasure to have been part of this group and to have engaged with so many people on our journeys to advance various topics of scientific knowledge.

I'd like to give a special thanks to my girlfriend Sarah Frawley, and then all my family and friends, who's support and encouragement has been one of the great driving forces behind the completion of my research and this thesis.

Finally to all the supporting staff in the Wolfson School and The Doctoral College, I thank you for your support and guidance throughout my various roles as a representative of the postgraduate community at Loughborough University. I'm proud to have helped shape the positive changes seen at the University over the past few years, and I thank you again for the experiences gained alongside my research.

Publications

Journal Papers

Coles, L. A., Roy, R., Sazhenkov, N., Voronov, L., Nikhamkin, M., Silberschmidt, V. V. (2018) Ice vs. Steel: Ballistic Impact of Woven carbon/epoxy composites Part I - Deformation & Damage Behaviour. *Engineering Fracture Mechanics*. Accepted.

Coles, L. A., Roy, R., Silberschmidt, V. V. (2019) Ice vs. Steel: Ballistic Impact of Woven carbon/epoxy composites Part II – Numerical Modelling. *Engineering Fracture Mechanics*. Accepted.

Coles, L. A., Tilton, C., Roy, R., Shukla, A., Silberschmidt, V. V. (2017) Dynamic damage in woven carbon/epoxy composites due to air blast. *Procedia Structural Integrity*. 6, pp 5-10.

Coles, L. A., Roy, R., Voronov, L., Semenov, S., Nikhamkin, M., Sazhenkov, N., Silberschmidt, V. V. (2017) Impact damage in woven carbon fibre/epoxy laminates: analysis of damage and dynamic strain fields. *Procedia Engineering*. 199. pp 2500-2505.

Coles, L. A., Roy, R., Silberschmidt, V. V. (2017) Micro CT Analysis of Dynamic Damage in Laminates: Impact vs. blast loading. *Journal of Physics: Conference Series*. 842 (1). pp 012077.

Coles, L. A., Tilton, C., Roy, R., Shukla, A., Silberschmidt, V. V. (2016) Dynamic fracture in carbon-fibre composites: Air-blast loading. *Procedia Structural Integrity.* 2. pp 417-421.

Coles, L. A., Roy, R., Voronov, L., Semenov, S., Nikhamkin, M., Silberschmidt, V. V. (2016) Dynamic Fracture in Carbon-fibre Composites: Effect of Steel and Ice Projectiles. *Procedia Structural Integrity.* 2. pp 366-372.

Conference Contributions

Coles, L. A., Roy, R., Voronov, L., Bolotov, B., Tilton, C., Nikhamkin, M., Shukla, A., Silberschmidt, V. V. (2017) Dynamic Damage in Carbon Fibre/Epoxy Laminates: Air Blast and Impact. *21st International Conference on Composite Materials, ICCM'21.* Xi'an, China.

Coles, L. A., Tilton, C., Roy, R., Shukla, A., Silberschmidt, V. V. (2017) Dynamic damage in woven carbon/epoxy composites due to air blast. *XXVII International Conference "Mathematical and Computer Simulations in Mechanics of Solids and Structures". Fundamentals of Static and Dynamic Fracture, MCM 2017.* Petersburg, Russia.

Semenov, S., Nikhamkin, M., Voronov, L., Sazhenkov, N., Silberschmidt, V. V. Roy, R., Coles, L. A., (2017) Impact damage in carbon plastics: analysis of damage and dynamic strain fields. *International Conference on Structural Dynamics, EURODYN 2017.* Rome, Italy.

Coles, L. A., Roy, R., Silberschmidt, V. V. (2017) Micro CT Analysis of Dynamic Damage in Laminates: Impact vs. blast loading. *12th International conference on damage assessment of structures, DAMAS.* Kitakyushu, Japan.

Coles, L. A., Roy, R., Voronov, L., Semenov, S., Nikhamkin, M., Silberschmidt, V. V. (2016) Impact Damage in Woven Carbon Fibre/Epoxy Laminates: Effect of Steel and Ice Projectiles. *17th European Conference on Composite Materials, ECCM'17.* Munich,

Germany.

Coles, L. A., Roy, R., Voronov, L., Semenov, S., Nikhamkin, M., Silberschmidt, V. V. (2016) Impact Damage in Woven Carbon Fibre/Epoxy Laminates: Analysis of Damage and Dynamic Strain Fields. *International Conference on Carbon Materials and Material Sciences, ICCMM 2016.* Istanbul, Turkey.

Coles, L. A., Roy, R., Voronov, L., Semenov, S., Nikhamkin, M., Silberschmidt, V. V. (2016) Dynamic Fracture in Carbon-fibre Composites: Effect of Steel and Ice Projectiles. *21st European Conference on Fracture, ECF'21.* Catania, Italy.

Coles, L. A., Tilton, C., Roy, R., Shukla, A., Silberschmidt, V. V. (2016) Dynamic fracture in carbon-fibre composites: Air-blast loading. *21st European Conference on Fracture, ECF'21.* Catania, Italy.

Coles, L. A., Roy, R., Silberschmidt, V. V. (2015) Finite-Element Modelling of 3D Oblique Ultrasonically Assisted Turning of TI-6AL-4V. *Advanced Problems in Mechanics.* St. Petersburg, Russia.

Contents

List of Figures

List of Tables

List of Symbols

Symbols related to elasticity and strength of laminates

E_c	Elastic modulus of a composite
E_r	Elastic modulus of fibre
E_m	Elastic modulus of matrix
V_r	Volume fraction of fibre
V_m	Volume fraction of matrix
ρ	Density
E_{11}, E_{22}, E_{33}	Elastic moduli in each of the orthogonal directions
$\nu_{12}, \nu_{13}, \nu_{23}$	Poisson's ratio in each of the shear directions
G_{12}, G_{13}, G_{23}	Shear moduli in each of the shear directions
$X_{11t}, X_{22t}, X_{33t}$	Tensile strengths in each of the orthogonal directions
$X_{11c}, X_{22c}, X_{33c}$	Compressive strengths in each of the orthogonal directions
S_{12}, S_{13}, S_{23}	Shear strengths in each of the shear directions
X_{ii}^{Quasi}	Quasi-static strength in each of the orthogonal directions
X_{ii}^{Dyn}	Dynamic strength in each of the orthogonal directions
G_{ft}	Tensile damage evolution energy release rate (ERR)
G_{fc}	Compressive damage evolution energy release rate (ERR)
G_{mt}	Tensile damage evolution energy release rate (ERR)
G_{mc}	Compressive damage evolution energy release rate (ERR)
G_{sh}	Shear damage evolution energy release rate (ERR)

Symbols related to delamination

k_n, k_t, k_s	Interlaminar stiffness (mode I, II and III)
t_n, t_t, t_s	Instantaneous interlaminar stress (mode I, II and III)
t_n^0, t_t^0, t_s^0	Maximum interlaminar strength (mode I, II and III)
G_n, G_t, G_s	Interlaminar energy release rate (ERR) (mode I, II and III)
β	Mixed mode parameter

Symbols related to finite-element analysis

P	External forces applied to a node
I	Internal forces applied to a node

m	Mass of a structure
$\ddot{a}$	Acceleration of a structure
L_e	Characteristic length of a mesh element
C_o	Speed of sound within the material
$\dot{\varepsilon}$	Strain rate
Symbols related to continuum damage mechanics (CDM)	
σ_{ij}	Second order stress tensor
ε_{ij}	Second order strain tensor
τ_{ij}	Second order shear stress tensor
γ_{ij}	Second order shear strain tensor
C_{ijkl}	Fourth order stiffness tensor
$\mathbf{d}$	Damage tensor
di_{ij}	Damage initiation parameters
de_{ij}	Damage evolution parameters
ε_{ii}^{0}	Equivalent strain at damage initiation
ε_{ii}^{f}	Strain at complete damage evolution
γ_{ij}^{e}	Elastic component of shear strain
γ_{ij}^{in}	In-elastic component of shear strain
$\gamma_{ij,0}^{in}$	In-elastic shear strain at damage initiation
γ_{ij}^{f}	Shear strain at complete damage evolution
$lDelFlag$	Element deletion flag

List of Acronyms

2D	Two-dimensional
3D	Three-dimensional
ALE	Adaptive lagrangian eulerian
CDM	Continuum damage mechanics
CEL	Coupled eulerian lagrangian
CFRP	Carbon fibre–reinforced polymer
CT	Computed Tomography
CZE	Cohesive zone element
CZS	Cohesive zone surface
DIC	Digital image correlation
FEM	Finite-element method
FPS	Frames per second
FRC	Fibre-reinforced composite
FSI	Fluid structure interaction
ILSS	Interlaminar shear strength
ILTS	Interlaminar tensile strength
MLT	Matzenmiller-Lubliner-Taylor
RVE	Representative volume element
SHPB	Split Hopkinson pressure bar
SHTB	Split Hopkinson tensile bar
SPH	Smooth particle hydrodynamics
UMAT	User defined material subroutine
VUMAT	Vectorised user defined material subroutine
WWFE	World-wide failure exercise

Chapter 1

Introduction

Over the last few decades the use of fibre-reinforced composites (FRCs) has risen considerably across many areas of application, including automotive, aerospace, naval, defence, energy and sport thanks to their increasing specific stiffness and strength as well as other benefits. In all these applications, dynamic loading of FRCs caused by various objects and environmental conditions is extremely likely; hence there is a need to understand their deformation and damage behaviour under transient loading conditions. Some typical examples of dynamic loading conditions are low velocity impacts with airborne debris on runways, railway lines and automotive race tracks (1-100 m/s), high-velocity flight at Mach 1-2 (300-600 m/s) of fast jets or intercontinental ballistic missiles (ICBM) through a hailstone cloud, and close-proximity explosions or sudden pressure increases resulting in air-blast shockwaves. As well as this, the combined loading of both an impact and air-blast shockwave, which is fairly typical in some dynamic load cases, also becomes of great interest. So the following questions can be asked:

- Which is the most destructive case, an impact closely followed by an air-blast or visa-versa?
- Does the local penetration of the impact enhance the air-blast damage, or does the air-blast aid in the mitigation of localised loading during an impact?
- Does the global acceleration of the blast help to minimise the local impact damage of the projectile, but then does the local impact damage lead to initiation zones in the FRP? Does this result in any significant difference?

Before any of these questions can be answered, there is a fundamental need to fully

understand the dynamic events for separate loading conditions in detail for both deformation behaviour as well as initiation and propagation of damage for the same specimens and analysis methods. Only after this is achieved individually, can combined loading be studied accurately.

There is a vast amount of studies aimed towards characterising the response of FRCs to various dynamic loading conditions, but direct quantitative analytical comparisons of these studies is challenging and often impossible due to major differences linked to geometry, experimental conditions and methodology. Many studies reviewing the previous research (Abrate 1991, Abrate 1994, Cantwell and Morton 1991) confirmed this for the impact behaviour of composites, drawing only general, qualitative conclusions about the fundamental behaviour and impact resistance of continuous fibre-reinforced composites. Typically, a high volume of experimental studies involving carbon-fibre composites focused on the resulting deformation and damage caused by rigid spherical (typically steel) projectiles. Obviously, similar conclusions can be expected following the typical analysis of visible and sometimes hidden damage through to comparisons of a link between impact energy and typical diamond shaped damaged area aligned to the weave directions, decreasing in size as the velocity increases.

The important aspect of the dynamic loading conditions is the interaction of the projectile objects with the target over the impact duration. Typically, spherical steel projectiles are considered to remain rigid (with only small elastic deformation) upon impact with the target material but interaction behaviour of a similarly sized projectile made of ice is more complex. In recent years efforts were focused on understanding the impact process of ice projectiles and its effect on carbon-fibre composite specimens considering its fragmentation on impact and then the subsequent distribution of load and dispersion of kinetic energy during the impact duration (Asp and Juntikka 2009; Tippmann et al. 2013). Similarly, air-blast and shock-wave loading creates a purely distributed loading condition. Many studies analysed the effect of such loading on various materials (Langdon et al. 2014; LeBlanc et al. 2007; Tekalur et al. 2008b; Kumar et al. 2013) but drawing comparisons between them is again challenging.

To date there are no direct comparisons of impacts with fragmenting (ice) and rigid (steel) projectiles or even air-blast loading, especially focused on deformation behaviour during the event and resulting damage. One study by Appleby-Thomas et al. (2011) does reference to comparisons with the literature stating that rigid projectiles lead to more

localised damage and easier penetration thanks to the higher energy density upon impact, whereas the brittle nature fragmenting (ice) projectiles result in the distribution of impact energy over a greater area as well as an increased amount of surface and internal damage. Therefore developing a full understanding of these types of dynamic loading conditions separately and their effect on the response of FRCs is extremely important, in terms of both local and global deformation as well as visible and hidden damage. Only then can we answer the three questions posed previously, regarding the combined dynamic loading scenarios of ballistic impacts and blast.

1.1 Research Aim and Objectives

The aim of this research project was to study in-depth the deformation and, specifically, damage of the same CFRP subjected to both ballistic impact and air-blast dynamic loading conditions. This has enabled a direct comparison caused by deformation and damage of ice projectiles and their effect with those by more typical steel projectiles, employing consistent analysis methodologies. This has aided in drawing solid conclusions from the results obtained, and allow accurate comparisons on the basis of using the same specimen material.

The results from the experimental case studies has provide validation for a newly developed modelling strategy for carbon fibre reinforced polymers (CFRPs), employing a meso-scale phenomenological continuum-damage approach to implement accurate expicit simulations of various dynamic loading conditions without parameter modification. In order to achieve the aim of this research project, the following objectives have been defined:

1. Characterisation of the assumed consistent CFRP composite, under quasi-static and dynamic loading conditions for numerical finite-element modelling (defining parameters).

2. Conducting experimental dynamic case studies on the CFRP composite including ballistic and air-blast loading conditions, with detailed deformation and damage analysis using digital image correlation and X-ray tomography.

3. Development and validation of a full 3D finite-element model accounting for initiation and evolution of damage within the CFRP under the case study dynamic loading.

1.2 Research Methodology

A systematic layout of the conducted research is shown in Figure 1.1, and this structure also relates each chapter of this thesis to the work presented. This thesis covers eight main areas - (i) introduction; (ii) literature review; (iii) experimental methodologies; (iv) deformation analysis; (v) damage analysis; (vi) development of user defined material model; (vii) numerical simulations, and (viii) conclusions and future work. Each of the ten chapters presented is linked to previous chapters, forming also the basis for the subsequent ones and creates a succinct and yet detailed description of the research and analysis undertaken.

It should be noted that, although both the ballistic impact and air-blast experimental studies were conducted using facilities at the Perm National Research Polytechnical University in Russia and the University of Rhode Island in the USA respectfully, I was directly responsible for the design of the experiments and in control of their implementation and analysis. Full acknowledgement is given to the relevant members of the institutions, for allowing me to use their equipment and for the collaborative research opportunity.

Detailed analysis of the experimental results to the development of the phenomenological continuum-damage approach, which was based upon a modified and combined version of the existing work of Hashin (1980) and Puck and Schürmann (1998). All numerical model case studies presented in this thesis were performed using the commercial FE software Abaqus Explicit (Version 6.14-4). Intra-ply behaviour of the CFRP was modelled using the presented vectorised user defined material model (VUMAT) and inter-ply damage was modelled using cohesive zone surfaces (CZS). The numerical model results were validated against experimental data, using digital imagine correlation (DIC) for deformation analysis and X-ray tomography for damage analysis. The validated model has then used to predict behaviour in the two hypothetical scenarios of combined dynamic effects mentioned previously. Finally, conclusions were drawn, and further topics for future work are discussed.

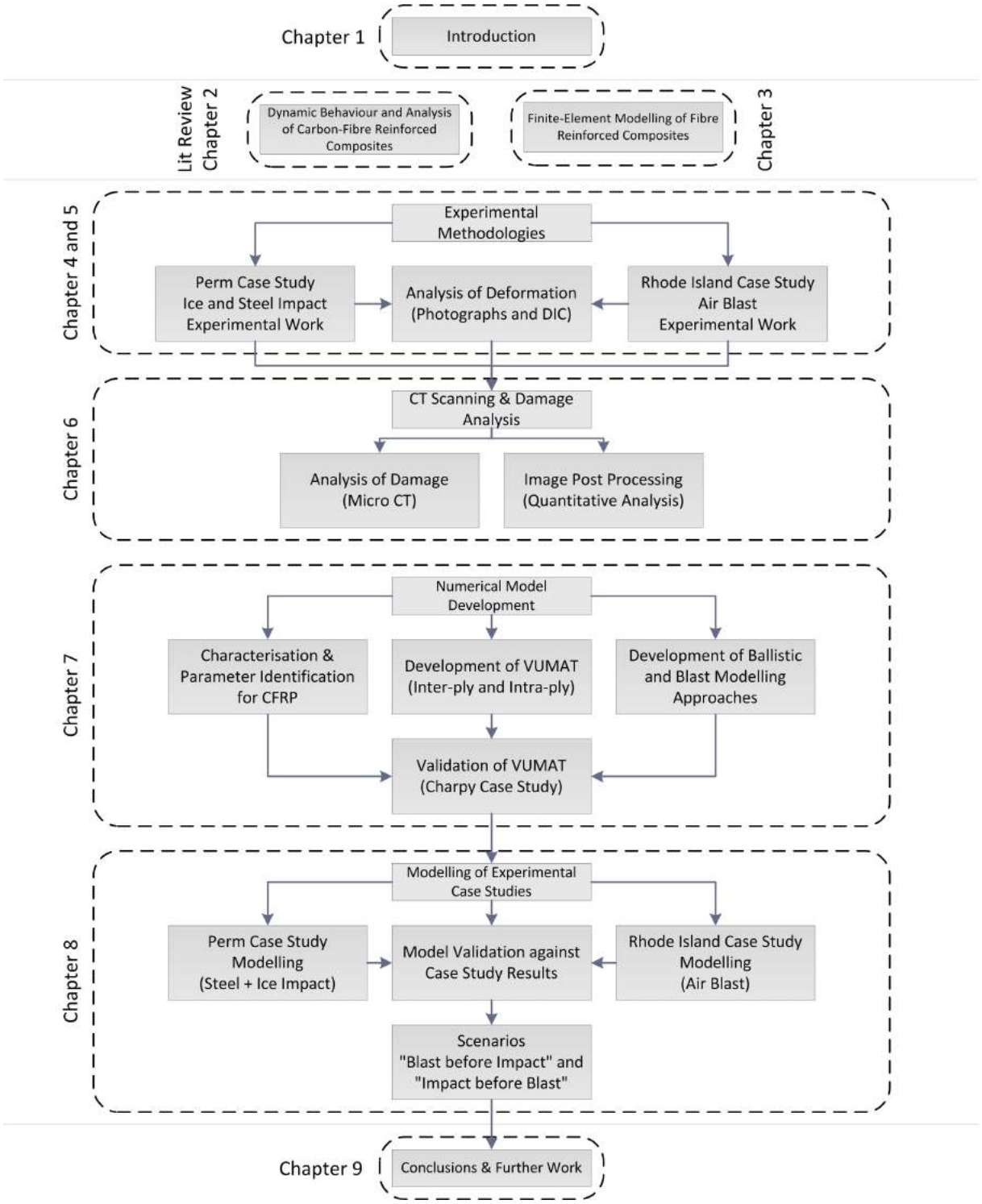

Figure 1.1: Research project breakdown and thesis structure

Chapter 2

Dynamic Behaviour and Analysis of Carbon Fibre Reinforced Composites

---

The utilisation of the new engineered composites we see today actually started back in the early 1960's (Agarwal et al. 2006), and since then the utilisation of composite materials across a vast number of application including: automotive, aerospace, naval, defence, sports and many others have increased. The primary benefit of using composite materials is to take advantage of the high strength to weight ratio that can be achieved, Figure 2.1 shows how composites compare with other materials. This can be engineered even further in that the reinforcing elements can be distributed and aligned so that directional strength can be achieved within a component, this can allow further weight reduction and enable for intelligent design (Herakovich 1998).

Secondary benefits of using Fibre Reinforced Composites (FRCs) over traditional metallic materials include: greater dimensional stability under thermal loading, increased fatigue life, low thermal conductivity, better corrosion resistance, and non-conductive or non-magnetic properties if required (Herakovich 1998). All of these benefits make FRCs incredibly versatile, and over many centuries has lend to advancements in technology. Boeing (2006), for example, utilised more composite materials within it's 787 airframe than any of it's previous commercial aeroplanes, this demonstrated in figure 2.2 below. With the resulting airframe comprising of nearly half carbon fibre reinforced plastic and

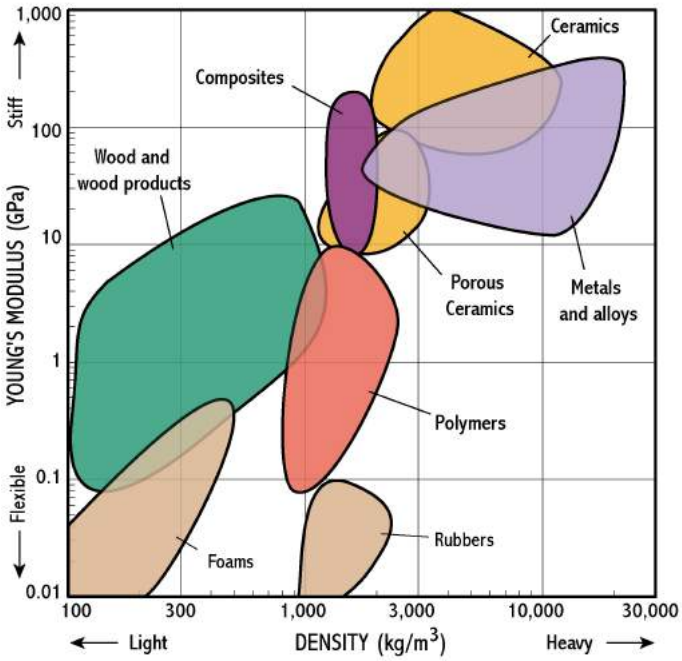

Figure 2.1: Elastic modulus vs. density (Cambridge University 2002)

other composites, they achieved a weight saving average of 20 % compared to more conventional aluminium designs.

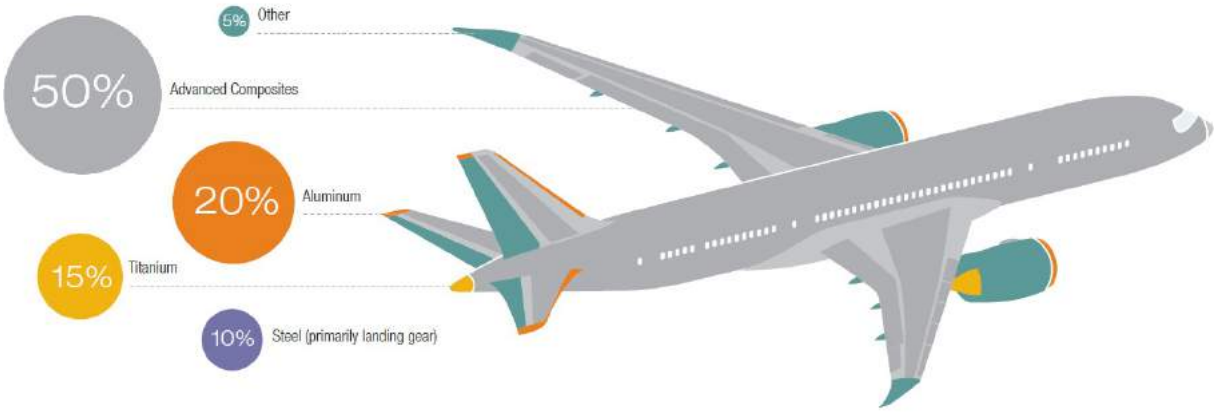

Figure 2.2: Composite utilisation within Boeing's 787 (Boeing 2006)

Due to these advantages many FRCs are widely used in aerospace and defence applications, in which they're subjected to extreme environments like ballistic and blast loading. Therefore it is critical to understand the response and behaviour of these composite materials when subjected to dynamic loading.

This chapter first reviews the effects of strain rate, followed by the effects of time

dependent loading on a materials behaviour. Then a brief summary of the continuous fibre reinforced composite (FRC) behaviour including deformation and failure mechanics, followed by the effect of time dependence on loading a fibre reinforced composite (FRC) shall be discussed in more details with reference to strain rate. Finally it shall then move onto the analysis of composites subjected to dynamic ballistic and blast loading conditions, while also covering the common non-invasive analysis techniques used to access deformation and damage of a specimen.

2.1 Strain Rate Effects

The effect of time dependency on the loading of a material determines the rate at which a material is deformed, this is known as the strain rate. If the strain is measured with reference to time as shown in Equation 2.1, the strain rate within the material can then be defined using Equation 2.2:

$$\epsilon(t) = \frac{L(t) - L_0}{L_0}\,, \tag{2.1}$$

$$\dot{\epsilon}(t) = \frac{d\epsilon}{dt} = \frac{d}{dt}\left(\frac{L(t) - L_0}{L_0}\right) = \frac{1}{L_0}\frac{dL}{dt}(t) = \frac{v(t)}{L_0}\,, \tag{2.2}$$

where $\epsilon(t)$ is strain, $L(t)$ is instantaneous length, $L(0)$ is original length, $\dot{\epsilon}(t)$ is strain rate and $v(t)$ is the speed of deformation. Quasi-static loading where the strain rate is considered to be low is usually between the range of 10^{-4} to 10^{-2} s^{-1}, then dynamic loading where the strain rate is considered to be high and inertial and wave-propagation effect become prominent the value is in excess of 10^2 s^{-1}. A full breakdown of the strain rate ranges can be seen in Table 2.1 as defined by Meyers (1994).

Table 2.1: Typical ranges of strain rate (Meyers 1994)

Deformation Speed	Strain Rate
Creep	10^{-8} to 10^{-4} s^{-1}
Quasi-Static	10^{-4} to 10^{-2} s^{-1}
Intermediate	10^{-2} to 10^{2} s^{-1}
Dynamic	10^{2} to 10^{4} s^{-1}
Hyper Dynamic	$> 10^{4}$ s^{-1}

Past experimental studies have shown that the strength of a material can increase with increasing strain rate, this is known as strain rate sensitivity and is an important phenomenon when considering dynamic loading. This strain rate sensitivity has been very widely studied and methods have even been developed to study the tensile vs compressive strain rate sensitivity of materials including composites (Naik and Kavala 2008; Naik et al. 2010). The typical procedure for accessing a materials strain rate sensitivity is to use a Split Hopkinson Pressure Bar experimental setup which was first developed by Hopkinson (1914) and then later refined by Kolsky (1949). The typical increase in strength and the effect on the materials stress strain relationship can be seen in Figure 2.3.

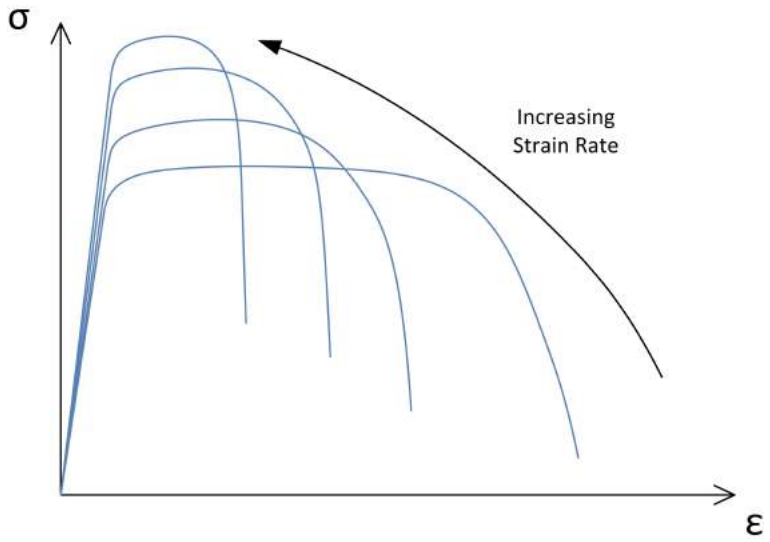

Figure 2.3: Effect of strain rate on a material's stress strain behaviour (Meyers 1994)

2.2 Time Dependent Loading

For static loading in components with uniform cross-section and material, the strain rate within it is most likely uniform due to uniform deformation, but in the case of dynamic loading the strain rate within the component can vary immensely. This is due to the introduction of wave propagation at higher velocity (dynamic) loading conditions, where localised deformation usually occurs first before the wave propagation allows the deformation to advance through the material at a specific velocity and strain rate. This wave propagation velocity is limited to the speed of sound in the material undergoing the deformation and is defined as follows in Equation 2.3 (Bourne 2013):

$$C_o = \sqrt{\frac{E}{\rho}}, \tag{2.3}$$

where E is the material elastic modulus and ρ is the materials density. This behaviour can be demonstrated by considering a beam that is subjected to 3 point static bending, this will show deformation across the whole component and therefore a more uniform strain rate distribution. For dynamic impact loading, the beam will show localised deformation and wave propagation and as a result varying strain rate. It should be noted that propagating waves can and will reflect off material interfaces and boundaries, and can increase in magnitude due to superposition of reflected waves.

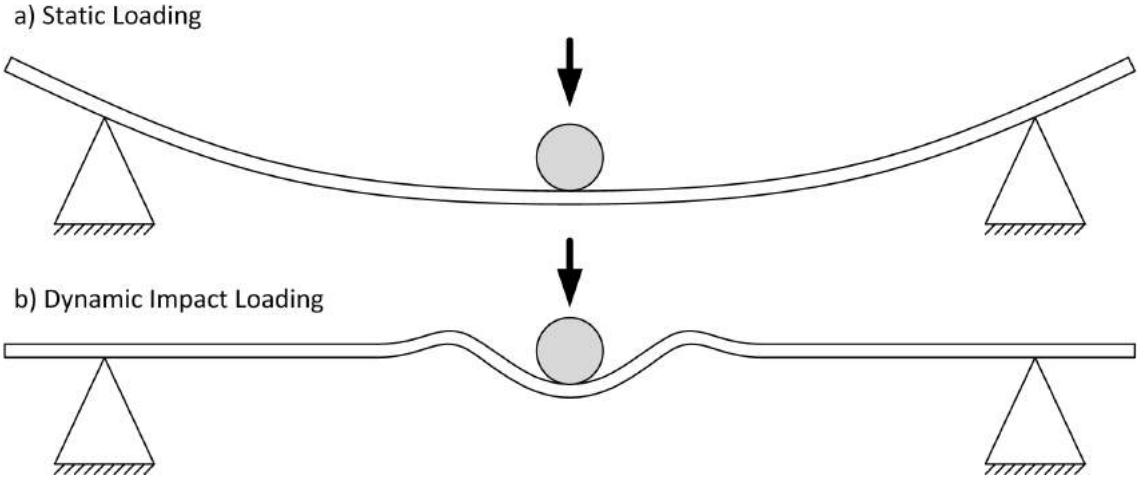

Figure 2.4: An example of static (a) vs. dynamic (b) loading and the resultant deformation

Dynamic Impact Loading

Figure 2.4 has been generalised to "dynamic" loading to demonstrate the fundamentals of this behaviour, but dynamic loading can be divided into the following ranges as shown in Figure 2.5. Leading towards hyper-velocity impacts, where this localised behaviour will become more and more refined as the localised strain rates increase until projectiles have been seen to perforate targets without causing large amounts of wide scale deformation (Schneider and Schäfer 2001; Katayama et al. 1997; Piekutowski 1987; Ohtani et al. 2006).

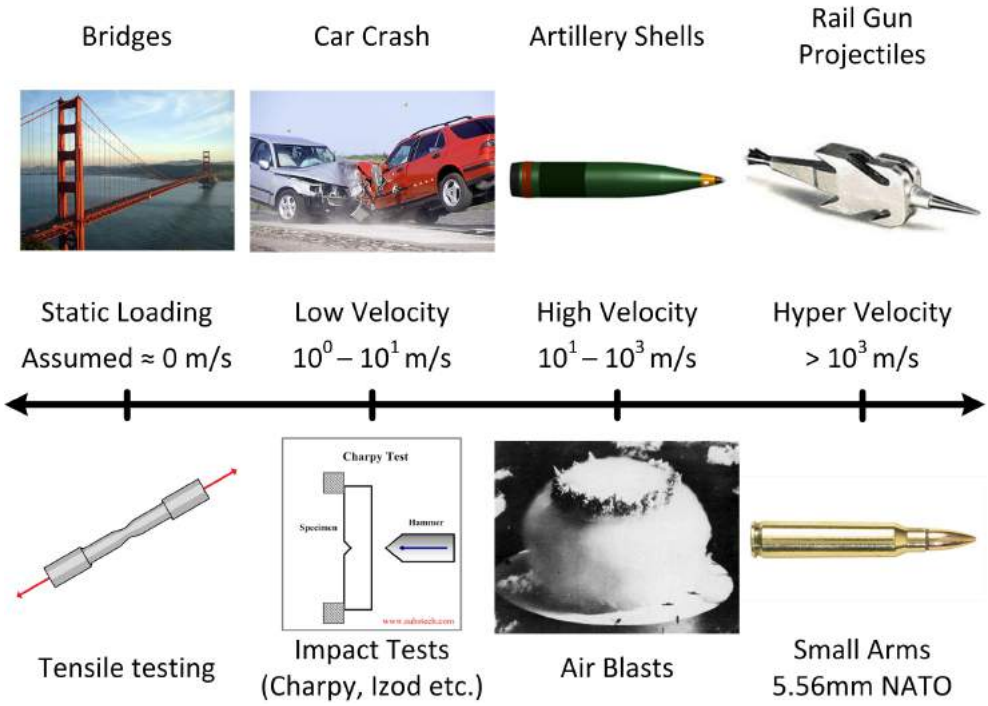

Figure 2.5: Approximate dynamic loading velocity ranges

2.3 Mechanical Behaviour of Fibre Reinforced Composites (FRCs)

Following a brief discussion on the general fundamentals of deformation, fracture and failure behaviour of materials, this section of the chapter shall discuss the mechanical behaviour of FRCs. A method of estimating composite strength shall then be discussed, before covering the damage mechanics commonly observed within FRCs.

2.3.1 Estimating a Composites Volume Fraction

One of the most important properties to characterise first is the proportion of reinforcing elements to the matrix within the FRC, this can be given as either weight or volume fractions. The weight fraction of a composite is easier to determine through experimental methods, but the volume fraction is more useful for theoretical analysis. So it is important to derive an expression to convert between the two fractions. First the volume and weight of a composite can be defined as Equation 2.4 and 2.5 respectively, where (v_*), (w_*), (x_c), (x_r) and (x_m) represent the individual volume and weight, composite, reinforcement

and matrix respectively. Then the volume (V_*) and weight (W_*) fractions can be defined with respect to either the reinforcement or matrix element of the composite, as shown in Equations 2.6 and 2.7 respectively:

$$v_c = v_r + v_m \,, \tag{2.4}$$

$$w_c = w_r + w_m \,, \tag{2.5}$$

$$V_r = \frac{v_r}{v_c} \,, \quad V_m = \frac{v_m}{v_c} \,, \tag{2.6}$$

$$W_r = \frac{w_r}{w_c} \,, \quad W_m = \frac{w_m}{w_c} \,. \tag{2.7}$$

The volume and weight fractions are then related via the ratio of the respective densities of the individual materials, this is shown in equation 2.8 (Agarwal et al. 2006).

$$V_r = \frac{\rho_c}{\rho_r} W_r \,, \quad V_m = \frac{\rho_c}{\rho_m} W_m \,. \tag{2.8}$$

2.3.2 Continuous Fibre Reinforced Composites

Continuous fibre-reinforced composites then fall into 3 categories: unidirectional, woven or non-woven as shown in the Figure 2.6, with each one showing differing levels of anisotropic behaviour.

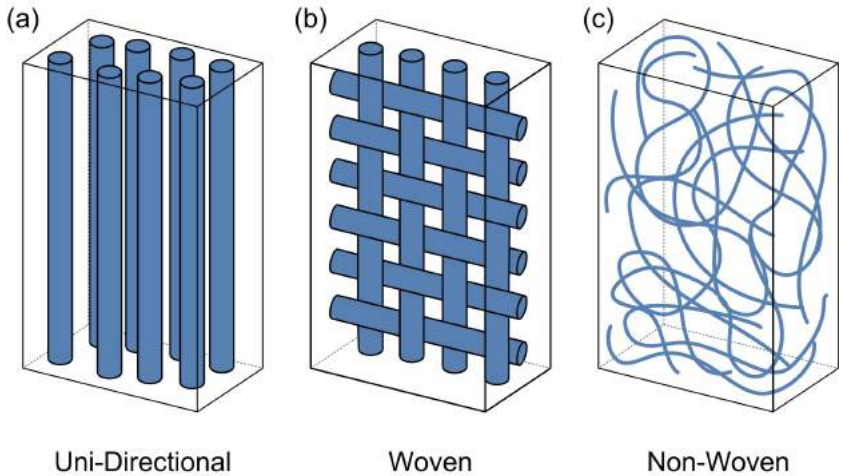

Figure 2.6: Types of continuous fibre reinforced composite

As can be seen from Figure 2.6 there can be a vast difference in the fibre orientation and distribution through a continuous fibre-reinforced composite, which as to be expected will have a significant effect on its global stiffness. For single uni-directional and woven ply FRC it is obvious that the in-plane macro-scale elastic modulus of the composite will change depending on the angle between the applied stress and the fibre alignment, where uni-directional shows greater strength in only one direction compared to the biaxial woven which shows a more even distributional of strength but at a reduced level due to the addition of the cross woven fibres. This has been studied by many researchers (Wang et al. 2014), and is shown in Figure 2.7.

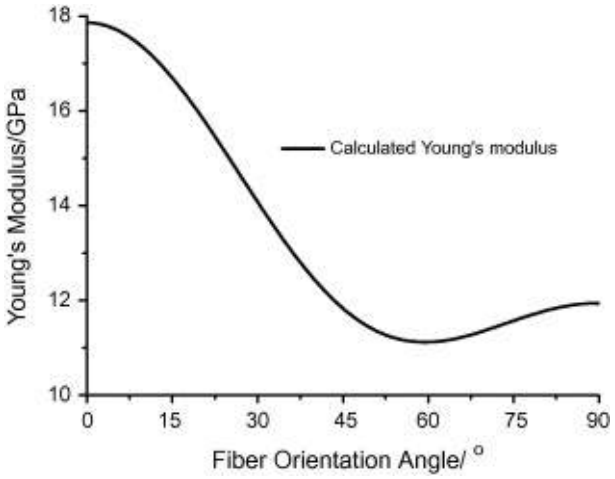

Figure 2.7: Relationship between the Young's modulus and fibre orientation angle with 0 ° being parallel to fibre direction and 90 ° being perpendicular to fibre direction (Wang et al. 2014)

With this orientation based behaviour in mind the type of weave pattern used can also have a major effect on a composites behaviour, including the effect on the composites stiffness, damage and failure during deformation making it an important factor when selecting the composite for an application (Kotaki and Hamada 1997; Alif et al. 1998). Each woven layer of the continuous fibre fabric is usually then laminated together to form plies in the finished composite, this then helps achieve more uniform strength or better directional strength in a local area within a component (Soden et al. 1998).

2.3.3 Estimating Composite Stiffness

It is typically assumed that a composite shares the applied load between the reinforcing elements (fibres) and the matrix materials. A unidirectional continuous fibre reinforced

composites displayed orientation based changes in stiffness, and this can be estimated using the rule of mixtures using the volume fraction discussed previously. This assumption takes the individual properties of the micro-scale sized elements of the composite to then estimate a macro-scale stiffness (assuming no plasticity or damage), this can be used to estimate both axial and transverse stiffness as shown in Figure 2.8.

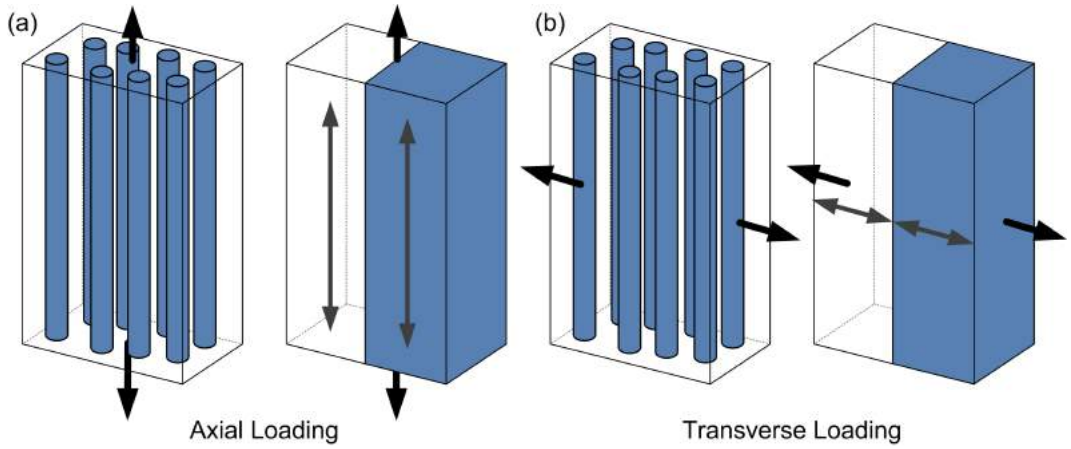

Figure 2.8: Rule of mixtures assumption for continuous fibre-reinforced composites (a) axial Loading and (b) transverse loading

For the axial loading case the stiffness of the composite can be estimated using the Voigt Model which assumed equal strain applied to both the matrix and reinforcing elements, and is defined as Equation 2.9 where E_* is the elastic modulus of each element and V_* is the volume fraction with respect to the reinforcing elements. Then for the transverse loading case the stiffness of the composite can be estimated using the Reuss Model which assumed equal stress applied to both the matrix and reinforcing elements, and is defined as Equation 2.10:

$$E_c = V_r E_r + (1 - V_r) E_m \,, \tag{2.9}$$

$$E_c = \left(\frac{V_r}{E_r} + \frac{1 - V_r}{E_m} \right)^{-1} . \tag{2.10}$$

For the case of an off-axis ply (not at $0\,^\circ$ or $90\,^\circ$) a transformation matrix can be used to find the resultant stiffness. However the Reuss model is actually a poor approximation for the transverse stiffness since regions of the matrix within the composite, in between and along the loading direction, will be subjected to a higher stress similar to that carried by the reinforcing element. Whereas other regions of the matrix adjacent laterally to

then have the same strain as the fibres carrying a lower stress. This leads to a non-uniform distribution of stress during transverse loading, a more successful estimate uses the semi-empirical Halpin-Tsai model as shown in Equation 2.11. The Voigt and Reuss (or semi-empirical Halpin-Tsai) models then form the upper and lower bounds of the composite strength respectively Agarwal et al. 2006. Further models used to describe composite behaviour will be discuss in Chapter 4.

$$\begin{aligned} E_c &= \frac{E_m(1+\xi\eta V_r)}{(1-\eta V_r)}\,, \\ \eta &= \frac{\left(\frac{E_r}{E_m}-1\right)}{\left(\frac{E_r}{E_m}-\xi\right)}\,, \quad \xi \approx 1\,. \end{aligned} \tag{2.11}$$

An example of a fibre reinforced composites elastic behaviour with regards to the individual fibre and matrix elastic behaviour can be seen in Figure 2.9, this demonstrates that the composites resultant stiffness will fall between the stiffness's of the individual materials depending on the volume fraction of the fibre reinforcement. Tables 2.2 and 2.3 show approximate values for the individual materials within the carbon fibre-reinforced composite, then by using these models to estimate the stiffness of fibre-reinforced composites it can easily be seen that carbon fibre reinforced would have a higher stiffness than glass fibre-reinforced composites, this can be seen in Figure 2.10.

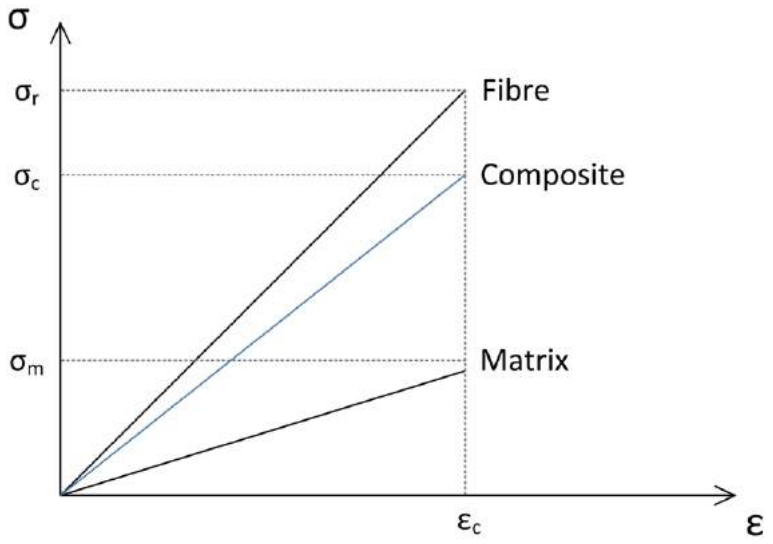

Figure 2.9: Resultant approximated composite elastic stress strain behaviour vs. the fibre and matrix behaviour

Table 2.2: Mechanical properties of typical fibre materials (Agarwal et al. 2006; Wallenberger and Bingham 2010)

Property (Units)	Carbon
Density (kg/m^3)	1700 to 2200
Elastic Modulus (GPa)	170 to 980
Tensile Strength (MPa)	1925 to 6200
Range of Diameter (μm)	5 to 11
CTE (μ/°C)	-0.4 to -1.6

Table 2.3: Approximate mechanical properties of typical polymer matrix materials (Agarwal et al. 2006)

Property (Units)	Epoxy
Density (kg/m^3)	1200 - 1300
Elastic Modulus (GPa)	2.75 - 4.10
Tensile Strength (MPa)	55 - 130
CTE (μ/°C)	45 - 65
Water Absorption in 24 h (%)	0.08 - 0.15

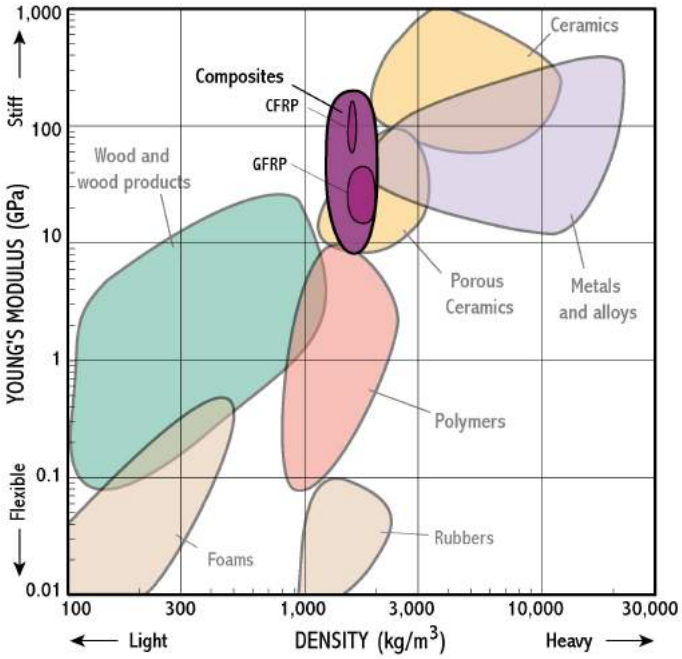

Figure 2.10: Elastic modulus vs. density - fibre-reinforced composites (Cambridge University 2002)

2.3.4 What Determines a Fibre Reinforced Composites Strength?

The previously mentioned rule of mixture models (section 2.3.3) accurately predicts the macro-scale stress strain behaviour of a composite when subjected to a load, but only while all the elements within the composite deform elastically with no initiation of damage to the materials or the interfaces between them. After this initial linear elastic region of deformation fibre reinforced composites will generally progress onto one of the following stages with reference to the associated length scale.

(a) Damage and delamination of individual plies within the composite (meso-scale).

(b) Both the fibres and matrix continue to deform elastically, but the interface begins to show signs of damage (micro-scale).

(c) The fibres continue to deform elastically, but the more ductile matrix material begins to yield and deform plastically in between the fibres (micro-scale).

(d) The stiffer and usually brittle fibres begin to fracture before the matrix material begins to yield and deform plastically (micro-scale).

All of the above affect the composites structural integrity at a meso- and micro-scale, which then causes and shows non-linearity and failure in the composites macro-scale response and stress strain behaviour. So the meso- and micro-scale behaviour and interaction of the individual elements within the composite determine the overall macro-scale response of the material.

2.3.5 Failure Mechanisms in Fibre Reinforced Composites

The static and dynamic energy absorption capabilities of a material is directly influenced by its failure and fracture behaviour, for fibre-reinforced composites this is no exception as there are many ways in which they can absorb energy either by deformation or the creation of new fracture surfaces. Following the previous section it can be seen that most of these mechanisms are initiated at a meso- or micro-scale in the fracture process zone, then propagate onto the fracture of the composite at a macro-scale. These failure mechanisms can be grouped into the following corresponding length scales and are shown in Figure 2.11 then defined as follows (Agarwal et al. 2006), physical evidence of the effect of these failure mechanisms will be discussed in the next chapter.

(a) Inter-ply Delamination

A process in which the interface between two adjacent plies (unidirectional or woven) within a composite lay up begin to crack and separate, this mechanism absorbs a significant amount of fracture energy. Delamination typically occurs during the flexural bending of composite containing individual plies, this is due to different types of ply having different tensile and compressive stiffness leading to varying strains between plies.

(b) Intra-ply Fibre Breakage

Given the usually vast difference in stiffness between the matrix and fibre materials, the matrix tends to be more ductile than the fibres, and so the fibres will fracture at a much lower failure strain. Once this strain has been reached the fibres can fracture before the matrix has even yielded, this means that given the fibres low failure strain there energy absorption capability is comparatively low.

(c) Intra-ply Matrix Cracking

Eventually the matrix material will need to fracture before the composite has completely failed. For polymer matrix materials that can undergo large amounts of deformation before failure, the energy absorption capability will come mainly from the elastic and plastic deformation rather than the fracture energy required to create the new fracture surface.

(d) Intra-ply Fibre Interface Debonding

Similar to inter-ply delamination where there is a separation of two elements, this process is defined as the separation of the fibres from the matrix. This mechanism occurs when the fibres are stronger than the interface between them and the matrix material, then the more ductile deformation of the matrix causes large strain differences between the elements causing the debonding. Depending on the extent of this debonding and the creation of multiple new fracture surfaces, this mechanism can absorb significant amounts of fracture energy during the failure of the composite.

(e) Intra-ply Fibre Pullout

The pullout of fibres from the matrix occurs when the fibres are considered to be brittle and fracture at locations with smaller cross sections, as a result the matrix deforms further in the localised stress concentration region of the fibre breakage. Often the fibre breakage points are not located at the matrix fracture plane and so as the matrix yields the fibre matrix interface fails leading to the pullout of the fractured fibres.

(f) Intra-ply Fibre Kinking

Most of the failure mechanisms discussed cover mainly tensile loading (some can occur under compression), but fibre kinking occurs only under compressive loading and is described as the micro-buckling of fibres in localised regions cause instability. This is usually the result of matrix cracking that is perpendicular to the fibre direction, therefore creating buckling regions due to the lack of support.

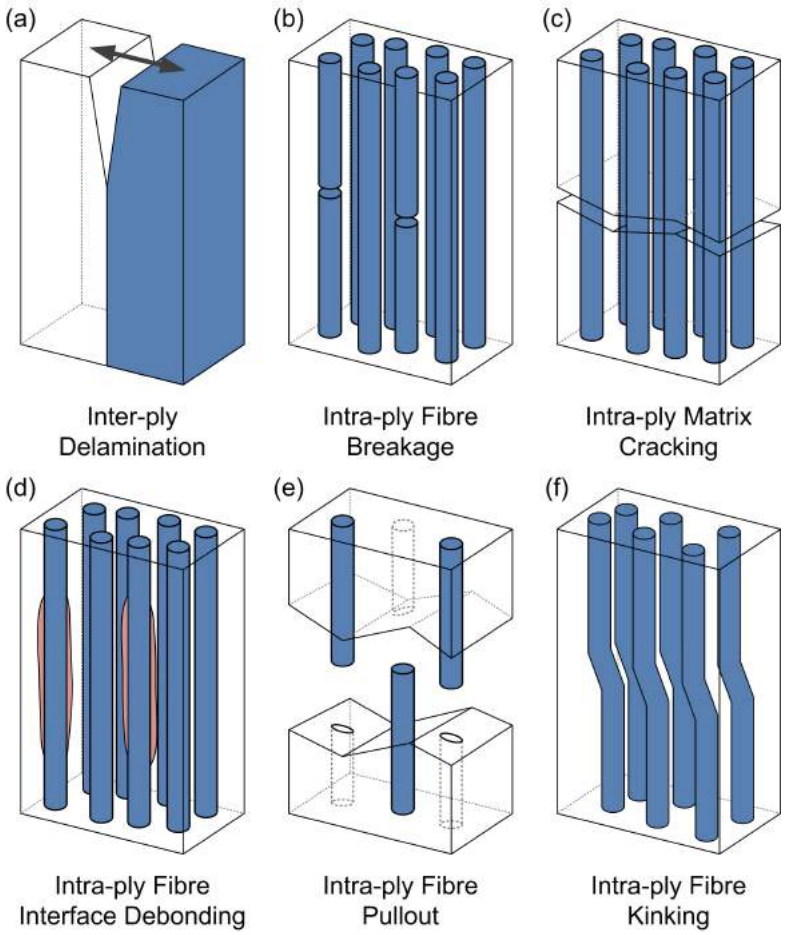

Figure 2.11: Fibre-reinforced failure mechanisms

2.4 Material Characterisation Techniques

2.4.1 Tensile and Compressive Testing

Tensile testing is the industry standard method for basic quasi-static characterisation of many materials, where by using a "dog bone" shaped sample of a known orientation loaded in uni-axial tension until failure while set at a constant rate of deformation (directly linked to strain rate). By recording the load - displacement data during the loading of the sample the materials stress strain response can be deduced, and from it the materials elastic modulus, yield strength, plastic behaviour, ultimate strength and fracture energy. Compressive testing is then preformed using the same method as described above but with a compressive load and resultant negative strains, this then provides a method of determining any asymmetric material behaviour under tensile and compressive loading. It is important to note that true stress and true strain (as discussed in Chapter 2) should be calculated from the stress strain relationship determined from the load displacement data for any tests where the strain value exceed 5 - 10 %, this is to ensure that the instantaneous cross sections are used in cases of large deformation.

Although this characterisation technique is most commonly used for the uni-axial loading of isotropic materials (including individual materials used within a composite), anisotropic materials (composites for example) can also be characterised providing that the testing orientation of the sample is recorded and referenced for all tests conducted and when referencing the results. As well as determining the standard anisotropic macro-scale response of FRPs researchers like Dai et al. (2015) went on to use this characterisation technique to show the micro-scale failure mechanisms and damage including matrix cracking and delamination as discussed in Section 2.3.5. The study also went on to contrast and compare the differences due to compressive loading, and also accessed the micro-scale failure mechanisms and damage after testing. Many researchers have used this characterisation technique to not only access a composites macro-scale anisotropic response, but also study the micro-scale failure mechanisms and resultant damage (Callus et al. 1999; Gu 2007; Yazici 2009; Bogdanovich et al. 2013).

The tensile testing technique can also be adapted and used to determine both the meso-scale interlaminar tensile (mode I failure) and shear (mode II failure) strength and fracture toughness between the plies of a composite, which can then be used to describe

the delamination failure mechanism. Although many researchers have conducted this experiment in the past, Manshadi et al. (2014) demonstrate this technique for determining the interlaminar tensile behaviour while studying a GFRP consisting of several plies of uni-direction E-Glass fibre.

Another example of using the modified tensile testing technique to determine the meso-scale interlaminar shear behaviour is shown by Ünal and Bansal (2002), where an accurately notched tensile "dog bone" shaped sample is placed under uni-axial tension so that the inter-ply region of interest lies parallel to the loading direction.

2.4.2 Dynamic Kolsky Pressure Bar

The regime of dynamic loading is assumed to have a loading velocity of between 10 - 1000 m/s, and would have an approximate strain rate range of between 10^2 to 10^4 s^{-1} s^{-1}. In order to characterise a material at high strain rates, the most commonly used test and experimental setup is a Kolsky or Split Hopkinson Pressure Bar (SHPB) which can be used to test materials in compression at strain rates between 10^1 to 10^4 s^{-1}. This experimental technique was first developed by Hopkinson (1914), then later developed by Kolsky (1949).

Newer more modern SHPB equipment (Figure 2.12) conduct each experiment by firing a striker bar from a high pressure gas gun or vacuum cannon at a incident bar to generate a compressive stress wave (measured with a strain gauge, replacing the condenser microphone used by Kolsky) which propagates down the bar towards the material sample which is then placed between the incident bar and a transmitter bar. Once the compressive stress wave reaches the sample part of the wave and its energy propagates through the sample and into the transmitter bar (which is then measured with another strain gauge), then the remaining energy is reflected back up the incident bar.

This results in the sample deforming at a high strain rate and by using the recorded incident, transmitted and reflected stress waves, the resultant dynamic stress strain curve and approximated strain rate for the sample can be indirectly determined using Equations 2.12, 2.13 and 2.14:

$$\sigma(t) = \frac{A_b E \varepsilon_t(t)}{A_s}\,, \tag{2.12}$$

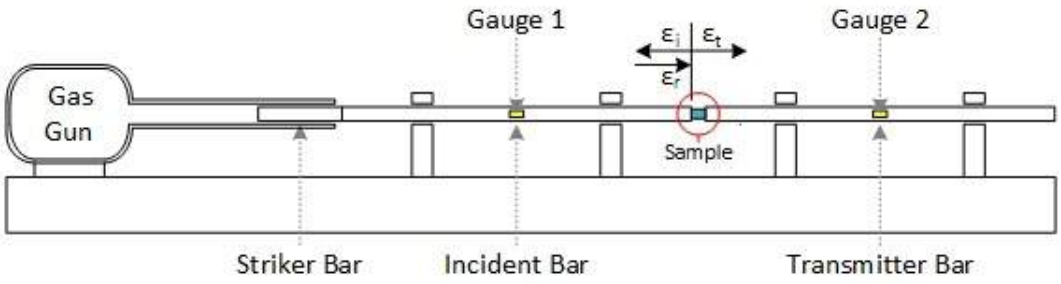

Figure 2.12: Modern split hopkinson pressure bar equipment

$$\varepsilon(t) = \frac{2C_0}{L_s} \int_0^t \varepsilon_r(t)dt\,, \tag{2.13}$$

$$\dot{\varepsilon}(t) = \frac{2C_0\varepsilon_r(t)}{L_s}\,, \tag{2.14}$$

where A_b, E, and C_0 are the cross sectional area, Youngs modulus, and the speed of sound of the bar material respectively, L_s and A_s are the length and cross sectional area of the specimen, and ε_r, and ε_t are the reflected and transmitted stress pulses. Over the years this technique has been developed to correct for things like wave dispersion (Gorham 1983), and even pulse shaping techniques (Naghdabadi et al. 2012). Care should be taken to ensure that the pressure bar and sample interfaces are lubricated to avoid any bulging of the sample during deformation that arises as a result of friction at the interface.

One problem that arises when performing this test is that at the early stages of compression, when the incident bar first strikes the sample, there is an inhomogeneous field of deformation which causes a problem when deriving the resultant stress strain relation for the sample material, as one of the assumptions made is that the sample is subjected to a homogeneous stress state throughout the test Demiral et al. 2011. As a result, each experiment conducted should be critically assessed to ensure accurate data is obtained.

Although this experiment is most commonly conducted in compression at room temperature, this characterisation technique has been developed to study the effect of high temperature and tensile dynamic loading. To achieve high temperature testing Kajberg and Sundin (2013) simply uses an induction coil to heat the sample in-situ. For a tensile SHPB there are many problems that arise and these include: determining a method to subject the sample to a dynamic tensile load, securing the sample so it received the tensile load and to ensure any problematic stress concentrations are minimised. Because

of this the Split Hopkinson Tensile Bar (SHTB) tests are very difficult to conduct. Most recently Sasso et al. (2008) and Gerlach et al. (2012) managed to conduct this experiment with Gerlach et al. even designing a new SHTB experimental setup, both of which were successful with the new design enabling the experimental characterisation of a wide range of materials ranging from ductile metals to brittle and high strength composites.

It is well known that this split hopkinson pressure bar technique is the most popular way of characterising materials at high strain rates, given that it is the simplest way of creating dynamic loading conditions that can be accurately measured. For most cases this technique can be used to determine the macro-scale dynamic response of a homogeneous and often isotropic material, but for composites this is often not the case as like with the quasi-static technique discussed earlier in the chapter the orientation of the inhomogeneous composite samples should be recorded carefully. Given that this high strain-rate dynamic technique has been in use for many decades, it has become a well defined process and has been used by many researchers to characterise the macro-scale response of many fibre-reinforced composites. Some of which include: studies on the effect of orientation of a satin weave carbon/epoxy composite when subjected to high strain-rate compressive loading (Hosur et al. 2004b), studies on the temperature effect on a woven graphite/epoxy composite when subjected to high strain-rate compressive loading (Hosur et al. 2004a) and studies of a woven E-Glass/epoxy (Ravikumar et al. 2013).

Given this technique is dynamic and is often seen to shatter more brittle samples, accessing the damage and modes of failure within the sample material is often very difficult. As a result, most studies have accessed the damage post-test, using techniques like light microscopy or scanning electron microscopy. A recent study conducted by Pankow et al. (2011) used digital image correlation (DIC) to try to access the out of plane deformation and damage of a 3D woven composite in-situ, and found that the composite demonstrated a transition in failure mode at higher rates along with architecture dependent strains showing that there were distinct shear bands where the fibres and matrix were in different strain states.

Pankow et al. also subjected the 3D woven composite to in plane loading and observed delamination between the plies in the centre of the sample with kink bands forming in the outer plies, although DIC was used during this loading condition as well the best observation of the damage was made post test.

From this study it can be seen that DIC may not be the most ideal method of accessing

deformation and damage during the SHPB technique, as later images show material failure and severe out of plane deformation causing severally blurred images. This image blurring can lead to image non-correlation in the DIC analysis, other possible methods of accessing in-situ damage could be through the use of high-speed video. Therefore it is clear that only an estimate of meso- and macro-scale damage can be access during the dynamic loading, and that any assessment of micro- scale damage must be conducted post test.

2.5 Analysing Composites Subjected to Dynamic Loading Conditions

The dynamic loading regimes covered in this section shall include both ballistic and blast interactions, which are commonly used to test complete components rather than specific material properties. This section of the chapter shall also discuss common non-invasive analysis techniques used to access deformation and damage of the specimen, as collecting data from dynamic experiments can often be a difficult task as mentioned previously.

2.5.1 Ballistic Response

"Rigid" Projectile Interactions

Dynamic ballistic loading can come in many forms, the most common of which is from a small bullet sized projectile. There are however many more forms of projectile and can range from: ballistic sand particles on solar panels, hail stone (ice) impacting fast jet aircraft (Mach $>$ 1), large artillery / missile sized projectiles, and even organic projectiles in the form of bird strikes on aircraft. Then the size, speed and resultant kinetic energy of the projectile will determine the extent of the localised deformation and failure region as mentioned in Section 2.2.

The failure of a target subjected to dynamic impact loading can then be initiated in many ways, Backman and Goldsmith (1978) studied mechanics of the penetration of projectile into a target in great detail and a summary of the perforation mechanisms is shown in Figure 2.13. These initiation of these perforation mechanisms are dependent on the dynamic response of the target material (ductile, brittle, toughness and fracture energies), and although these mechanisms were identified for homogeneous materials many of them

can also be seen during the impact of fibre-reinforced composites (these mechanisms shall be referenced throughout this section of the chapter).

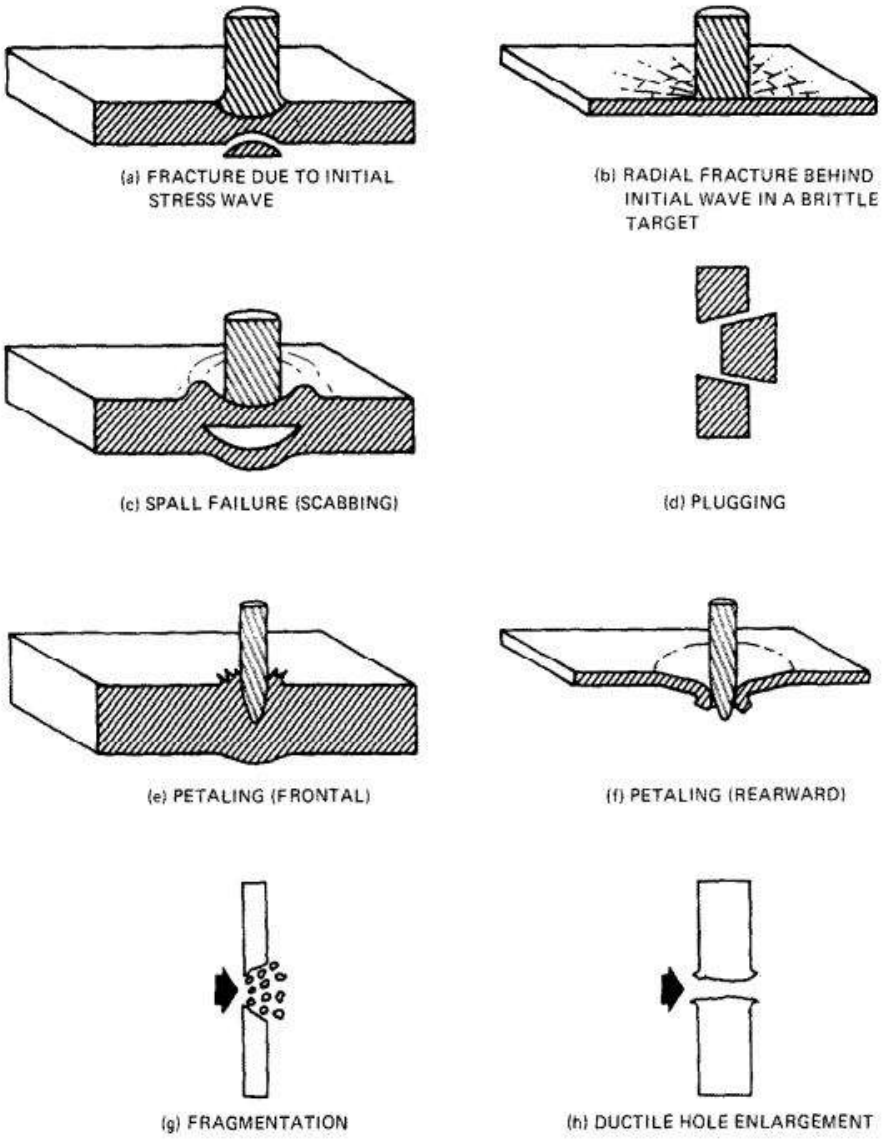

Figure 2.13: Perforation mechanisms as a result of a dynamic impact of a projectile (Backman and Goldsmith 1978)

Spallation is a failure mechanism worth noting and can occur as a result of high velocity impact loading in which a shock wave propagates through the target material to the free surface on the opposite side and then reflects back as a rarefaction wave with an extremely short rise time and high amplitude, this wave can cause hydrostatic tension at the back surface of the target of sufficient amplitude to instantaneously cause tensile failure of the material (Hiermaier 2008). For the case of composites this causes delamination of the

plies furthest from the initial impact surface, this was observed by Le-tian et al. (1984).

When it comes to assessing a materials response to ballistic impact, the most common factor that is determined is the ballistic limit of the target under test. This limit is defined as the velocity limit in which a project will perforate a target if exceeded. In reality given the probable variation in manufactured targets and components it is usual to take a probabilistic approach, in which the performance of a target is recorded to gather a large database of the projectiles exact striker velocity, residual velocity and any comments on perforation. From this a critical velocity value can be determined and defined as: the impact velocity for which there is a 50% probability of perforation of the target as defined by Zukas (1976). It is important to note that ballistic limit value is unique for the target under test and the projectile used, this includes the material(s) and geometry used for both.

There have been many other studies that access only the visual damage (Nunes et al. 2004; Sevkat 2012; Shaktivesh et al. 2013a; Pandya et al. 2013a; Mohan and Velu 2014; Yahaya et al. 2014a; Yashiro et al. 2013), but this approach only offers an assessment of the approximate damage within the target (inter-ply delamination is clear) with no assessment on the actual failure mechanisms present in the around the region of failure which may reveal further damage below the surface. Many studies have shown the advances of using X-ray tomography for assessing hidden damage in composites (Sket et al. 2012; Sket et al. 2014; Ullah et al. 2013), proving that it is well suited to provide critical information about damage mechanics without having to disturb the specimens by destructively examining them. A more recent study conducted by Karthikeyan et al. (2013) used moiré interferometry to measure the surface deformation of the target up until perforation, then used X-ray tomography to visualise the damage in the targets both in-situ and post impact. With these methods of analysis the delamination of the plies is clearly present leading to partial rearward petaling and fragmentation, but although the assessment techniques are more detailed the micro scale failure mechanisms can not be seen.

Other studies have also investigated the effect of the projectiles nose shape on the ballistic limit and perforation of targets. A study conducted by Ulven et al. (2003) investigated the perforation performance of projectiles with flat, conical, hemispherical and fragment simulating nose shapes on a carbon-fibre/epoxy satin weave composite, they showed that a conical nosed projectile resulted in the greatest amount of energy absorbed

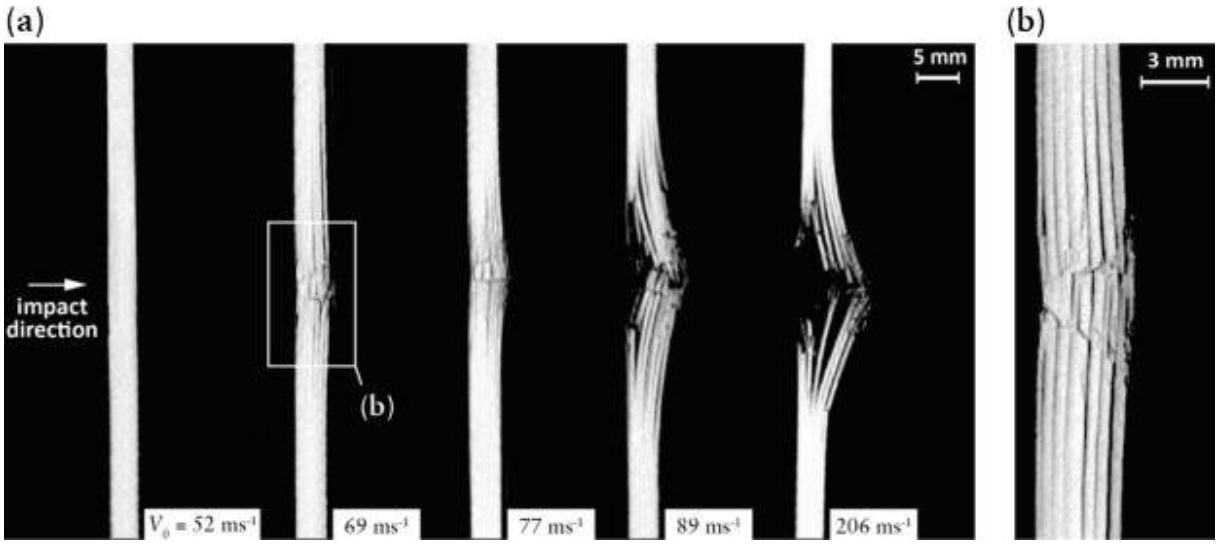

Figure 2.14: (a) X-ray tomography images of the targets impacted by a 8.3g steel ball at selected impact velocities below and above the ballistic limit (b) A high resolution image of the target show in (a) as seen by Karthikeyan et al. (2013)

at the ballistic limit followed by flat, hemispherical, and fragment simulating nose shapes. At a macro-scale perforation mechanisms including plugging, separation of fibres and a combination of both were observed during impact of the different projectiles, and the study also showed that panels of different thickness's demonstrated different failure mechanisms which resulted in different ballistic limits.

Another study conducted by Appleby-Thomas et al. (2015) aimed to investigate the effect of 2D flat and various peaked-nosed projectiles on a carbon fibre-reinforced polymer (CFRP). Their study used ultrasonic c-scans to show that the more oblique projectiles were found to more efficiently penetrate the targets, leading to less sub-surface delamination seen post-impact due to a change in perforation mode. Although the ultrasonic c-scans were of limited resolution, making any observation about the exact perforation mode or micro-scale damage only an approximation, this can also be seen in a study by Kim and Sham (2000). The study also used high speed video footage to record the impact of the projectiles, this is shown in Figure 2.15.

X-ray tomography has been proven to provide the missing assessment of internal damage, but it should be noted that there are also drawbacks to this methodology. There is often a trade off between image resolution and fidelity vs. the total scan area based upon the fundamentals of the system, therefore scan date should be interpreted carefully with a full understanding between voxel resolution and recognisable observable features (Bull

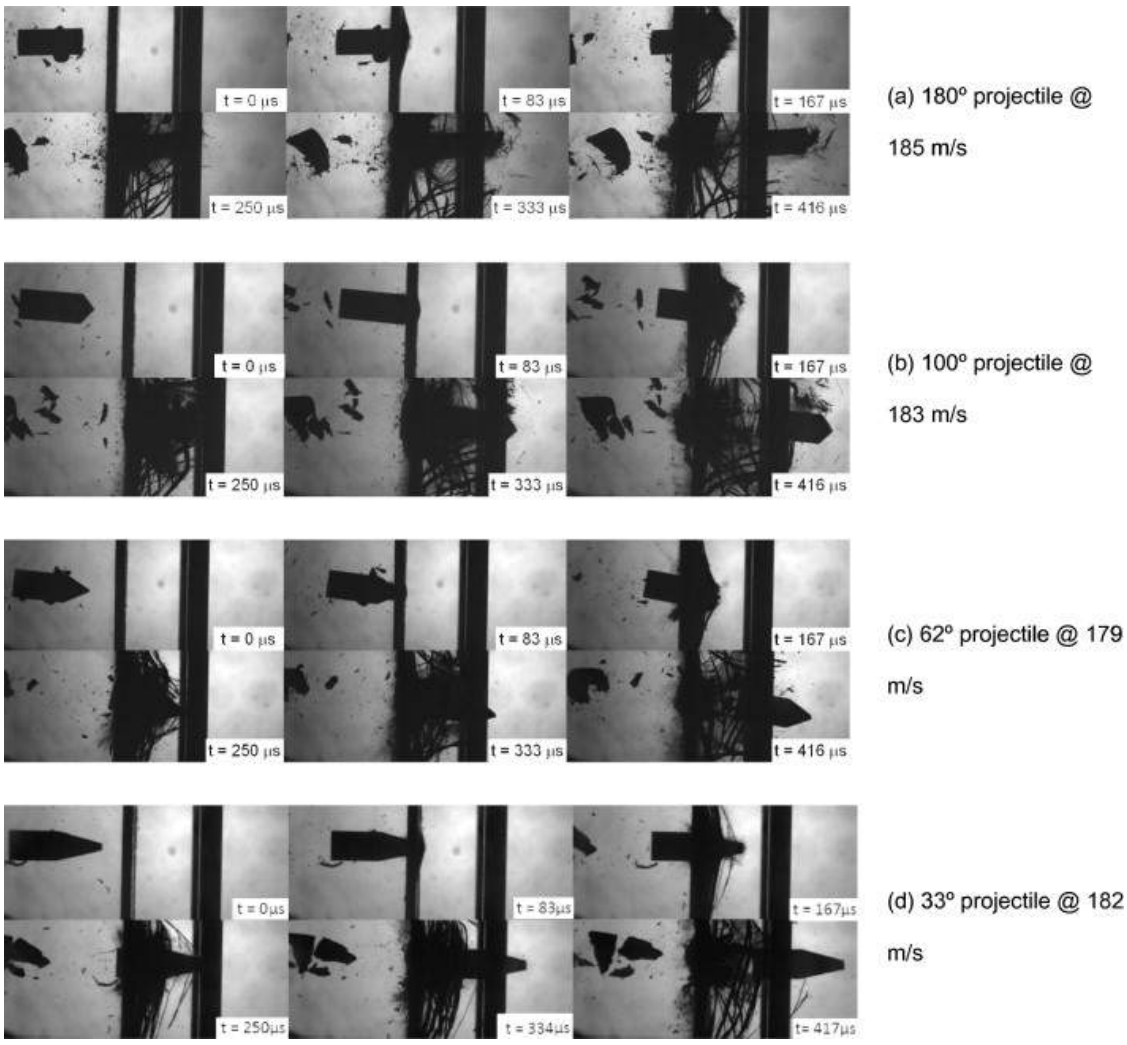

Figure 2.15: High-speed video footage showing the impact of the projectiles of varying geometry into the CFRP targets as seen by Appleby-Thomas et al. (2015)

et al. 2013). A recent study conducted by Muñoz et al. (2015) demonstrates the use of micro scale X-ray tomography for study post impact damage in CFRPs. The study was conducted to assess the dynamic ballistic impact response of a hybrid 3D woven mixed carbon/glass fibre orthogonal composite in an epoxy-vinylester resin. An example of their micro-scale X-ray micro-tomography images is shown in Figure 2.16, and shows a whole range of micro-scale failure mechanisms common in fibre-reinforced composites which are clearly shown.

All of the studies mentioned previously in this section lead to suggesting that inter-ply delamination is the main failure mechanisms responsible for fibre-reinforced composite failure when subject to ballistic loading and is also confirmed by Shi et al. (2012), but the result of the experiments conducted by Muñoz et al. show that the inter-ply stitching

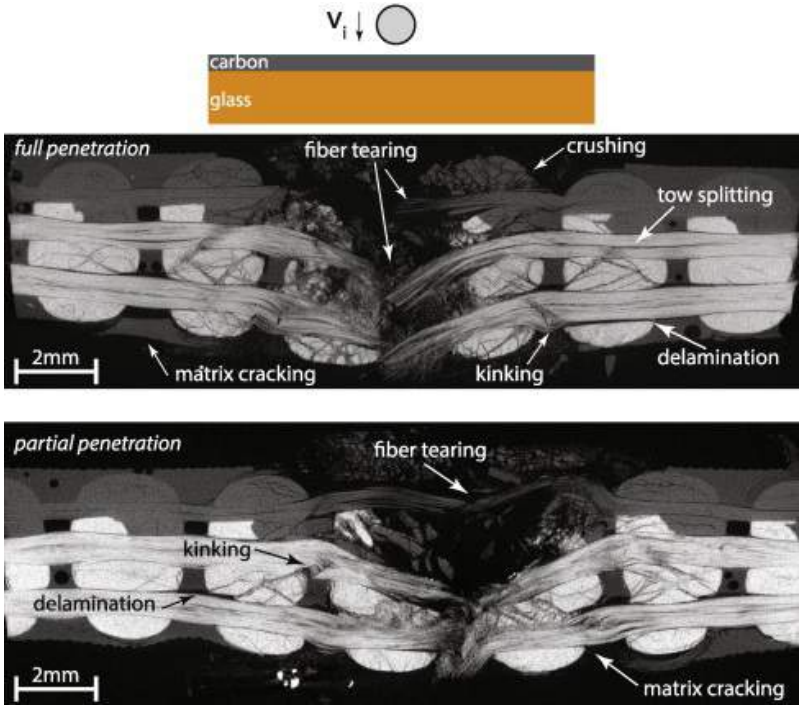

Figure 2.16: X-ray micro-tomography of the damaged seen in two of the hybrid 3D composites impacted (top) impact velocity 360 m/s and resultant velocity 12 m/s causing full perforation (bottom) impact velocity 341.5 m/s and resultant velocity 0 m/s causing partial perforation as seen by Muñoz et al. (2015)

yarns help hold the plies together. This significantly reducing the extent of delamination and spallation seen in the target, and as a result the energy dissipated was enhanced before final perforation.

"Fragmenting" Projectile Interactions

An important aspect of a ballistic dynamic loading condition is understanding the specific behaviour of the loading condition, and how it interacts with the specimen over time. For example typically a high volume of both experimental and numerical studies like the ones mentioned in the previous section of this chapter have been focused on the resulting deformation and damage from rigid (typically steel) projectiles, but in recent years efforts have been made towards understanding the impact process of fragmenting ice projectiles.

Early studies investigated the ductile to brittle failure of ice under compression, stating that cracks in both ductile and brittle regimes form but only individual cracks only propagation when brittle (Mellor and Cole 1982; Schulson 1990; Batto and Schulson 1993). Another study then goes onto say that the compressive strength of the ice is related

to the friction observed during the cracking (Schulson 1997), and that the compressive strength increased with increasing strain rate (Jones 1997). It is also worth noting that during the impact process it has also been found that under impact conditions, the exact micro-structure formed has no effect on the impact interaction when high strain-rates are present in the deformation process (Combescure et al. 2011). A study by Tippmann et al. (2013) shows the propagation of the crack through the projectile upon impact, this is shown in Figure 2.17.

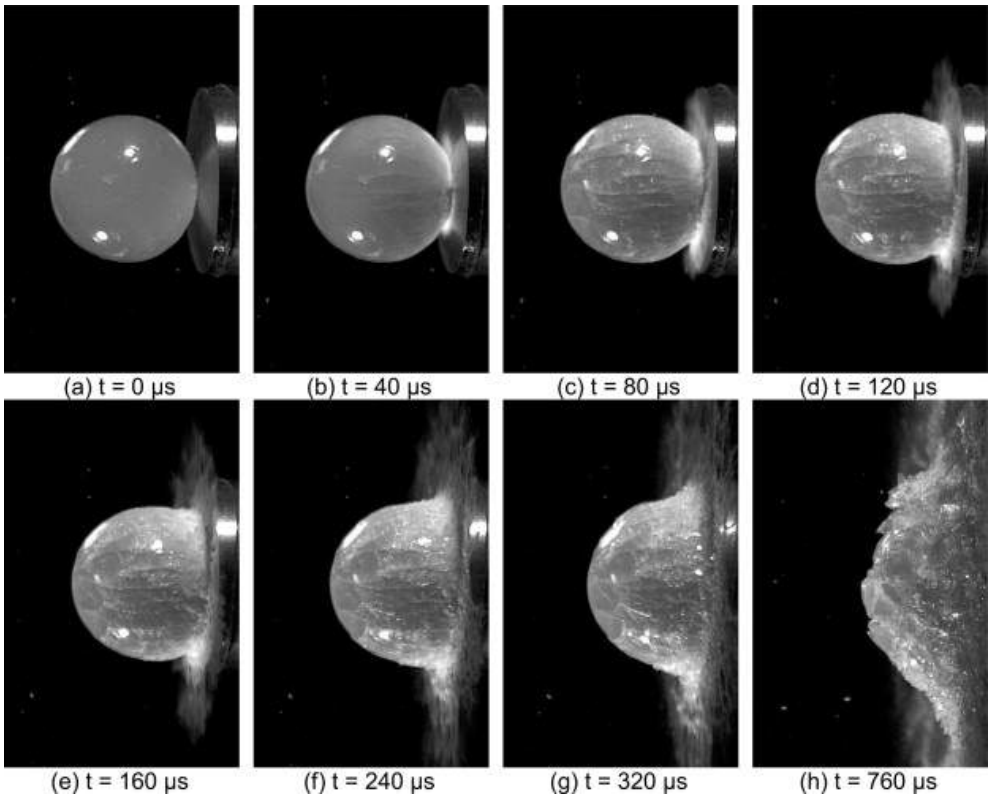

Figure 2.17: High speed video of ice impact on FMB; test DS2-191: 61.0 mm diameter SHI at 61.8 m/s (201 J) as seen by Tippmann et al. (2013)

A more recent study conducted by Pernas-Sánchez et al. (2015) has investigated the impact process and confirms these theories and show that the fragmentation occurs at very early stages of the impact (shown in Figure 2.18), and hence becomes an agglomeration of particles rather than a rigid projectile like steel to deliver a distributed dynamic loading condition as the impact process transitions. They also confirm that the maximum peak forces tends to be a function of the kinetic energy only regardless of the size of the projectile, given the distortion energy density to fragment the project is negligible when compared to the kinetic energy just before impact.

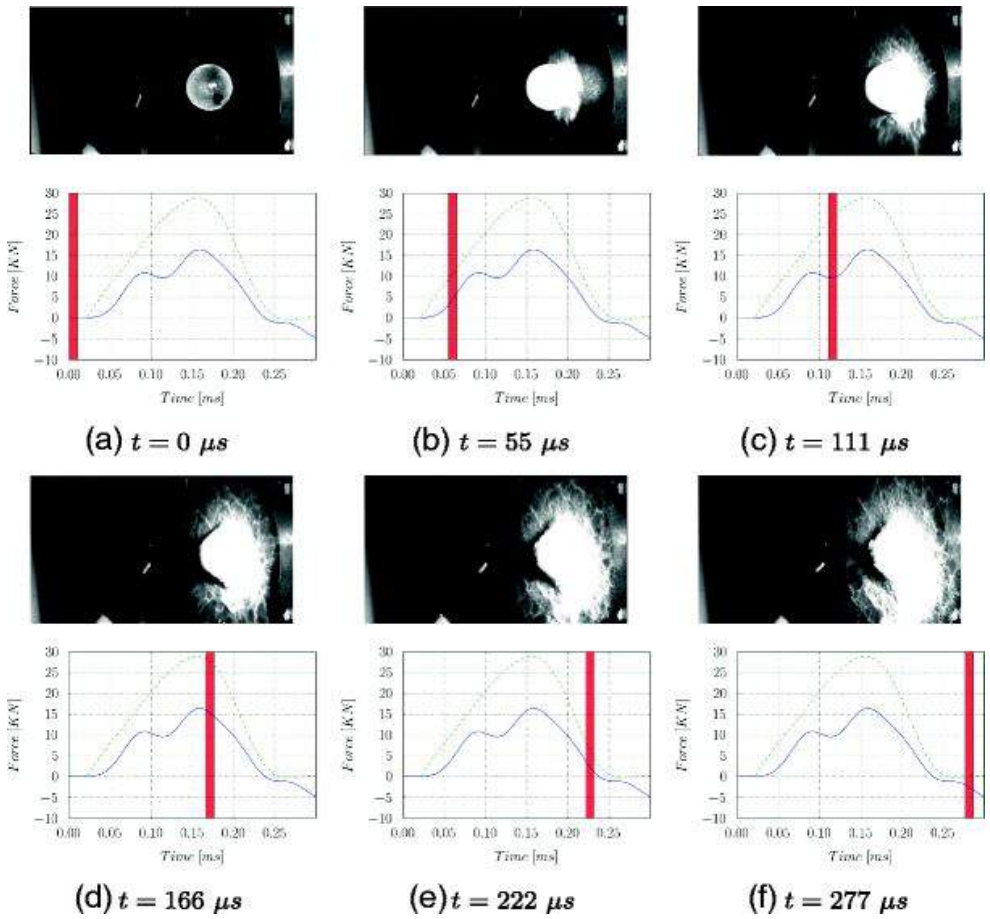

Figure 2.18: Impact sequence frames and force histories synchronized for an impact of 40 mm diameter ice projectile at 109 m/s as seen by Pernas-Sánchez et al. (2015)

When considering how these type of fragmenting loading condition effect composite specimens there have been a number of studies conducted over the past few decades, many of the studies again confirm the characteristics of the impact process as mentioned previously (Asp and Juntikka 2009). A further study conducted by Pernas-Sánchez et al. (2016) then went onto state that the ice projectiles are very unlikely to penetrate the specimen due to the fragmentation during the early stages of the impact, and instead the resulting particle deflect along the front surface reducing the chances of localised impact. They also stated that inter-ply delamination was the most prominent form of damage observed in the FRC specimens, and appeared well before any other signs of damage.

A study conducted by Kim et al. (2003) stated that the energy threshold for observable damage scales linearly with specimen thickness as to be expected, and that small projectile diameters lead to a more localised impact before fragmentation which then in turn results in more significant damage.

To date there are no comprehensive studies of the difference in the damage mechanisms witness in CFRP specimens when subjected to fragmenting project impacts when compared to that of rigid (steel) projectile impacts, especially when studying and comparing the deformation behaviour during the impact event.

2.5.2 Blast Response

At the other end of the scale air blast and shock wave loading creates a purely distributed loading condition over the subjected area, and again many studies have studied the effect of the shock wave loading on many specimen materials but drawing comparisons is again challenging due to the differing materials, methodologies, and analysis techniques (Langdon et al. 2014; LeBlanc et al. 2007; Tekalur et al. 2008b; Kumar et al. 2013).

Dynamic blast loading can be the result of many external events most commonly explosives and even the bow shock-wave travelling in front of a projectile travel at hyper velocities, but unlike ballistic loading a blast loading condition will always result in a pressure wave travelling through the surrounding medium. This pressure wave can vary in amplitude and velocity, but will usually always form a 3D uniform curved wave front if left to propagate. The extent of the localised deformation and failure region as mentioned in Section 2.2, will depend on the area subjected to the blast along with the amplitude and velocity of the wave. Many of the common non-invasive analysis techniques used to access the deformation and damage of a sample subjected to dynamic ballistic loading, can be utilised to analysis the behaviour as a result of blast loading.

A blast pressure wave is characterisation as follows: firstly the velocity of the wave is limited to the speed of sound within the medium the wave is travelling. Then the wave duration or impulse width is defined, this determines the time in which the energy from the pressure wave is transferred into or reflected off the target. Finally the maximum amplitude and pulse shape of the wave is defined in terms of pressure, the pulse shape will consist of a rise (shock-wave front) and fall region (trailing expansion wave) which will also vast effect the characteristic of the pressure wave (Meyers 1994). An example of a blast pressure wave is shown in Figure 2.19.

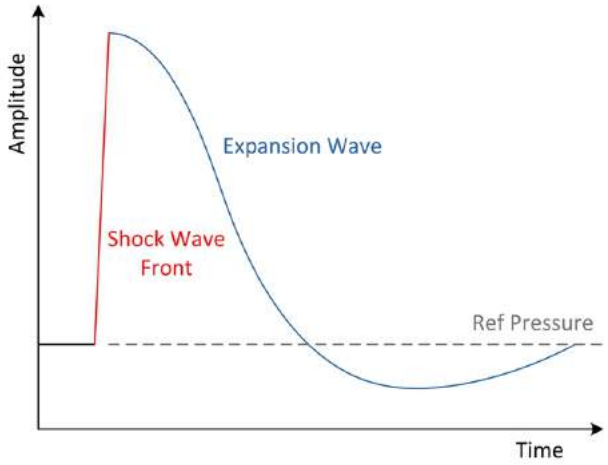

Figure 2.19: Example blast pressure wave

There are two experimental methodologies used to create shock loading conditions, this can either be small explosive charges or shock tubes (LeBlanc and Shukla 2011a; Tekalur et al. 2008b). Typically shock tubes are seen as the more desirable method given they create plane wave fronts and wave parameters that are easily repeatable, as small explosive charges have associated issues such as spherical wave fronts and pressure signatures which are often spatially complex and difficult to capture to than quantify.

Given the larger distribution of the dynamic load (dependent on blast area) during the blast loading of a target compared to a ballistic load, the target is likely to show more globalised deformation rather than localised. A study conducted by Langdon et al. (2015) investigated the influence of material type (including glass fibre reinforced polypropylene) on the response of plates to air-blast loading, their experimental setup saw the air-blast loading being generated by detonating circular disks of PE4 plastic explosive at the centre of the plates with stand-off distances of 25 mm and 38 mm. For lower volumes of explosive resulting in a lower blast magnitude, the GFPP plates showed minimal damage and very low permanent deformation because of their high stiffness. Then for larger volumes of explosive, the plates showed fibre fracture in the central region and longitudinal cracking along the fibre directions. An example of the GFRP plate failure observed in this study is shown in Figure 2.20, in this case the air-blast resulted in more localised deformation and failure similar to that of a ballistic impact given the proximity and loading area of the blast. As a result it is worth noting that localised blast loading can produce similar damage to that of ballistic loading. Other failure mechanisms observed included inter-ply delamination, matrix cracking and burn damage on the front face due to the close

proximity of the blast load as a result of the low melting temperature of the polypropylene matrix. As to be expected, closer stand-off distances resulted in increased damage.

Figure 2.20: Photographs of selected blast tested GFPP plates, showing that closer proximity loading causes more extreme failures (both tested at 20 g PE4, 50 mm charge diameter) (a) 25 mm stand-off (b) 38 mm stand-off as seen by Langdon et al. (2015)

This study concluded that the displacement-thickness ratio was found to increase linearly with the increasing non-dimensional impulse, confirming the earlier work of Nurick and Martin (1989a & 1989b) could be applied and extended to aluminium alloys, fibre-reinforced polymers and armoured steels up to the point of plate rupture. Nurick and Martin provided a useful method of predicting the maximum central deflection of circular and rectangular plates under impulsive (blast) loading. But again, like many of the ballistic studies, this study was limited to a visual level of damage providing only a approximate assessment of the micro-scale failure mechanisms.

Most commonly the typical type of composite tested under blast loading consist of sandwich (laminate) panels with, for example, a 3-D woven E-glass fibre reinforced composite skins and stitched foam core utilized in the naval and aerospace industry for their weight saving and high specific strength advantages to protect against such blast loading scenarios. Many researchers have studied these sandwiched composite laminates, and used high speed video footage to analyse the failure mechanics resulting from the blast loading in-situ (Tekalur et al. 2009; Langdon et al. 2012; Langdon et al. 2013). Jackson and Shukla (2011) even conducted a study to assess the blast response of these sandwiched composite laminates following multiple low velocity impacts.

Although some observations of the failure mechanisms could be observed from the high speed video footage, again like with ballistic loading it is very difficult to make a

detailed in-situ assessment of the damage at the micro-scale. As a result the previously mentioned studies only made assessments about the meso-scale damage including obvious fibre breakage and delamination, an example of this visual damage is shown in Figure 2.21.

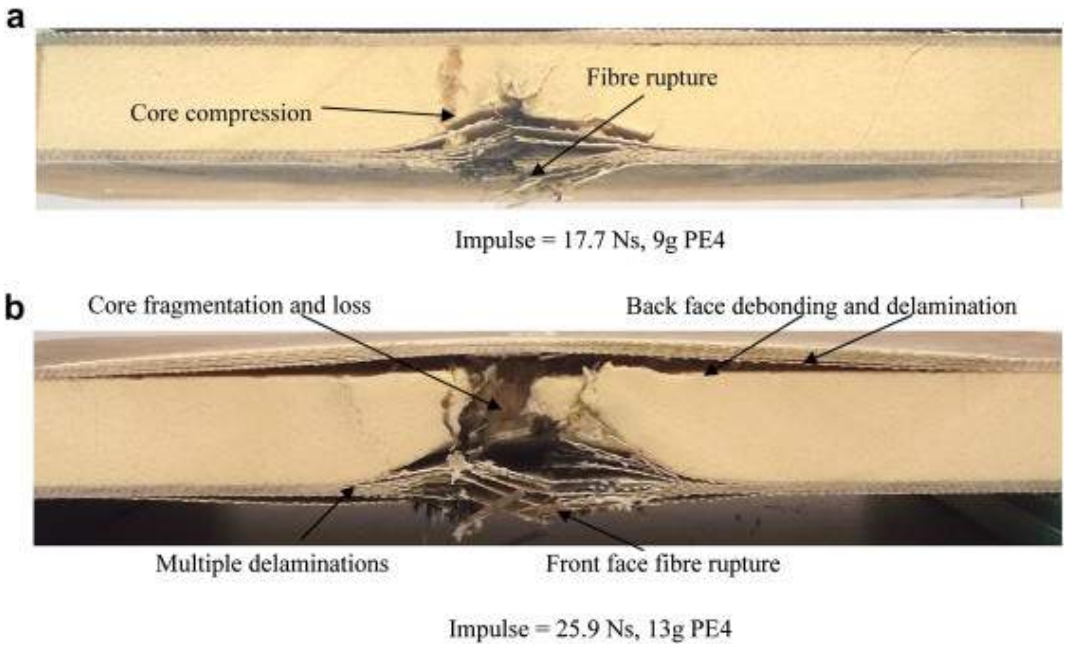

Figure 2.21: Cross-section photographs of various blast-loaded sandwich composite panels as seen by Langdon et al. (2013)

As well as the vast amount of research into the blast response of sandwiched composite laminates, single flat sheets of fibre reinforced composites have also be studied (LeBlanc et al. 2007; Tekalur et al. 2008b; Tekalur et al. 2008a). LeBlanc et al. (2007) claimed that their research was the first of its kind, in which a relatively new type of composite had been studied under blast loading. The aim of the investigation was to study the effects of blast loading on the response of four 3D woven fibre reinforced composites with different weave architectures (including inter-ply stitching) and thicknesses.

Like many of the previous studies their research utilised visual post blast analysis to observe the failure and damage mechanisms, as well as measuring the permanent deflection as a result of the blast loading. From these studies it is clear that as a result of blast loading it is common to observe daamage located t the edges of the clamped boundaries, this is due to the 'rigid' support creating localised stress concentrations is the target deforms globally under the distributed pressure wave load. From visual observations the areas showing the most surface damage, also showed the most internal delamination cracks

and breakage of the inter-ply stitching. This indicates that high through thickness tensile wave propagation (also known as spallation), is capable of causing delamination within the composite.

A study conducted by Kumar et al. (2013) also investigated the effect of panel curvature (A - flat, B - 305mm radius and C - 112mm radius) on the blast response of a 32 ply carbon fibre reinforced composite panels, their investigation utilised a 3D Digital Image Correlation (DIC) technique along with high-speed video to observe and obtain the out-of-plane deformation as well as the in-plane strain on the back faces of each panel. An example of the DIC technique is shown for the flat panel in Figure 2.22.

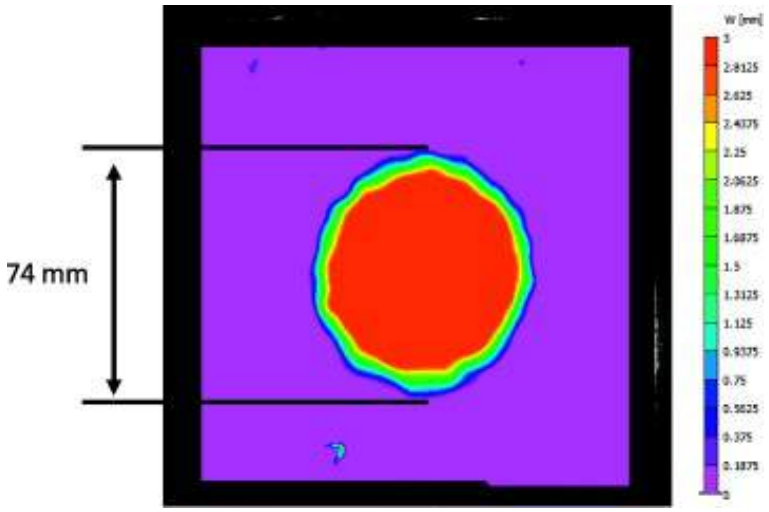

Figure 2.22: DIC analysis showing the loading area during shock impingement on the flat panel (A) at t = 50 μs as seen by Kumar et al. (2013)

A schematic diagram shown in Figure 2.23 demonstrates the deformation behaviour observed in the three different panels, where panel A and B show more 'indentation' behaviour with panel B showing flexural fixed at the edges. This diagram demonstrates how the panels in the study show flexural deformation decreasing and indentation deformation increasing as the curvature of the panels increase. The study also suggested that as the curvature increasing, the effect of the blast loading on the panel will decrease due to pressure wave deflection as a result of larger incident angles.

This study again observed two dominant failure mechanisms in the three panels including: fibre breakage and inter-ply delamination. As demonstrated by panel C the study showed that increased panel curvature allows increased energy absorption and dissipation, as a result panels with increased curvature can withstand more severe blast waves without

initiation of catastrophic damage.

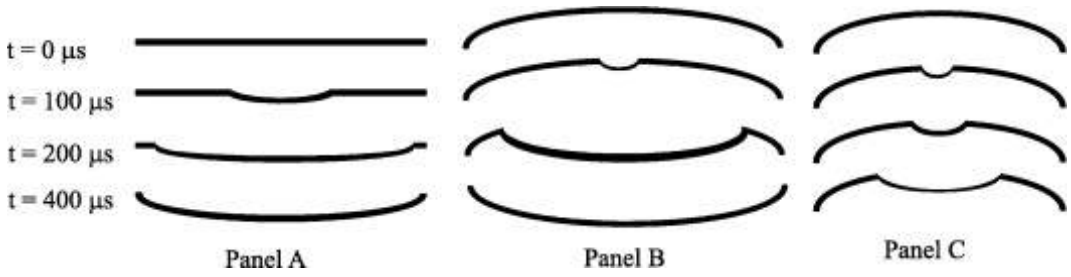

Figure 2.23: Schematic showing the deformation modes in three different panels as seen by Kumar et al. (2013)

The post blast assessment of the damage observed in panel B is shown in Figure 2.24, and clearly demonstrates vast amounts of inter-ply delamination and fibre breakage. It also demonstrates the effect of a rigid clamping system around the edges of the panel, which again results in vast fibre breakage and composite failure along clamping edge due to large global deflections. It is therefore often more favourable to simply support the panel, instead of rigidly fixing it.

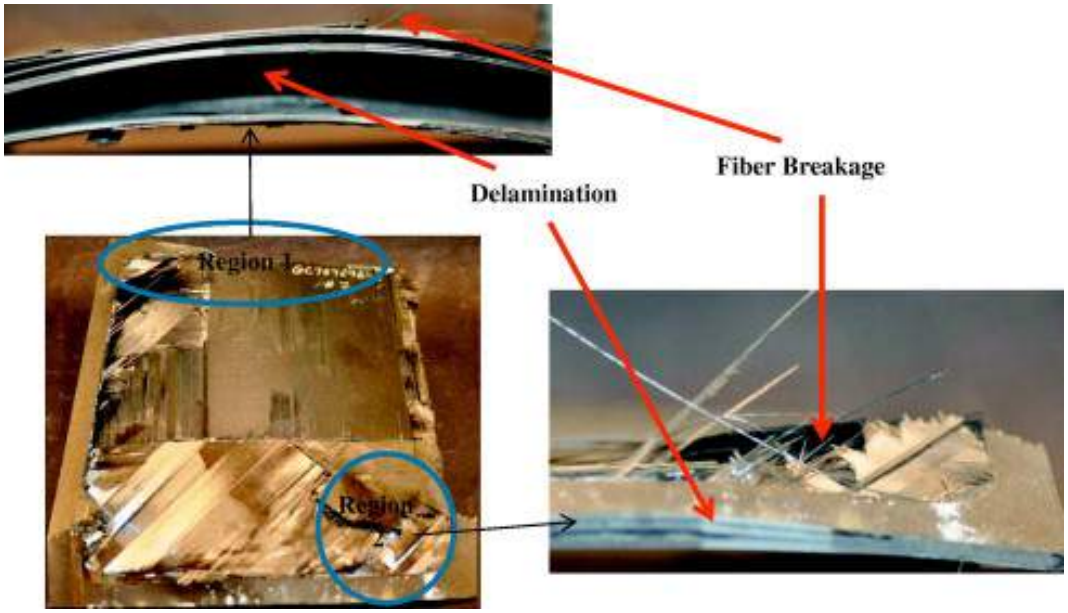

Figure 2.24: Post blast assessment of the damage observed in panel B as seen by Kumar et al. (2013)

There have also been many studies to investigate the dynamic response of flat and curved fibre reinforced composite panels to underwater explosive loading, including those conducted by LeBlanc and Shukla 2011a; LeBlanc and Shukla 2011b; Gauch et al. 2012.

These studies showed very similar dynamic responses to that of air-blast loading, demonstrating vast fibre breakage, matrix delamination and inevitable localised damage and failure at rigid supports.

Typically, the analysis of the resultant damage is limited to a visual inspection of external surfaces, or a using invasive techniques to study internal damage which could add additional unwanted damage making the analysis difficult (Nunes et al. 2004; Sevkat 2012; Shaktivesh et al. 2013b; Pandya et al. 2013b; Yahaya et al. 2014b). Although some studies have begun to investigate damage using X-ray tomography (Karthikeyan et al. 2013).

2.6 Chapter Summary

This chapter introduces fibre-reinforced composites (FRCs) along with several examples of their applications, and also covered a brief comparison against other common materials as well as their many advantages. The importances of strain rate was discussed, before introducing the importance of considering the factor of time dependants on a loading condition which is of major importance for this research project.

Following this the fundamental behaviour of FRCs was discussed, starting with an brief overview of the many different types and how the content of the reinforcing elements is defined before focusing on continuous fibre-reinforced composites. An introduction to estimating composite strength was discussed with a comparison before different composites and over materials, before covering what determines a composites strength and the many failure mechanisms which lead to the initiation of damage. The overview of fundamental fibre reinforced composites was covered with respect to the scale in which the different physical behaviour is observed, showing that the majority of macro-scale observable composite behaviour and damage occurs at the micro length scale. Next the chapter looked at the current methods of macro-scale material characterisation, which include tensile and compressive for quasi-static behaviour, then the split hopkinson pressure bar techniques for the tensile and compressive dynamic behaviour. It has also investigated the limitations of each technique, along with key observation on fibre reinforced composite behaviour. All of this observed behaviour has been considered when progressing onto the development of the meso-scale modelling strategy for carbon fibre reinforce polymer (CFRP).

Finally the analysis of composites subjected to dynamic ballistic and blast loading conditions was reviewed, while investigating the common non-invasive analysis techniques used to access deformation and damage of a sample. During ballistic and blast loading there are usually two main failure mechanisms observed, fibre breakage/matrix cracking and vast inter-ply delamination. Common methods of surface deformation measurement include moiré interferometry and digital image correlation (DIC), where DIC is shown to be the best technique for observing the deformation up until sample failure or perforation and has been taken forward for use in the presented research. Many methods were used for assessing the damage and failure as a result of the dynamic loading, including macro-scale visual techniques (desktop scanner and photos), high-speed video, optical microscopy, scanning electron microscopy and X-ray tomography. With high-speed video showing the best in-situ results of observing deformation and larger scale damage initiation and propagation, then scanning electron microscopy and X-ray tomography showed the best results for post test assessment of damage and failure mechanisms from the macro to micro scales. For the research presented in this thesis, X-ray tomography was taken forward to give insight into the internal damage.

Following a review of the literature, to date there are no comprehensive studies into the differences in the damage mechanisms witness when a CFRP specimen is subjected to rigid and fragmenting projects impacts and air-blast shock-waves. With this gap in the literature identified, the research presented in this thesis shall directly compare these loading conditions with a consistent CFRP specimen material, experiment methodology and analysis techniques to compare both deformation and damage behaviour during the loading events.

The next chapter shall discuss finite-element modelling of fibre reinforced composites, with respect to their deformation, damage and failure under dynamic loading conditions as discussed in this chapter.

Chapter 3

Finite-Element Modelling of Carbon Fibre Reinforced Composites

---

Numerical methods have been vastly employed for component design, and over the last few decades have been increasingly utilised for the analysis of composite materials including the prediction damage. The finite-element method (FEM) was employed to model damage mechanisms at various length scales to assess the macro-scale response of a composite component, in which homogenisation techniques can be utilised to capture the effect of the structure and to improve computational efficiency. Although this approach can provide good predictions against experimental validation, the homogenisation reduces the accuracy of the micro-scale mechanisms leading to the damage initiation and propagation. Another category of models deals with responses of either a smaller single reinforcing element unit cell, or a representative volume that describes the behaviour of an average periodic volume. This approach does not employ any homogenisation of the micro-structure and can, therefore, be used to model the micro-scale damage mechanisms. Thus, accurately modelling composite behaviour at various length scales while studying their effect on the macro-scale behaviour has become the main focus of this research field.

This chapter first covers some important areas of FE modelling related to this research, before reviewing the current progress of multi-scale modelling with the FE method for fibre-reinforced composites (FRCs). The review includes techniques used at macro-scale

as well as micro-scale modelling, and covers examples of dynamic ballistic and blast modelling accounting for the failure criteria used and the damage mechanisms observed. Finally some conclusions have been drawn on gaps currently within the research area of multi-scale FRC modelling.

3.1 Finite-Element Method

The finite-element method is a numerical technique used to solve problems of continuum mechanics. The continuum or internal volume of a component is discretised to form a finite number of smaller local volumes known as elements connected at common points known as nodes. These combined individual elements represent the larger continuum globally, across a finite-element mesh. As a result, this finite-element discretisation process breaks down a continuous boundary-value problem into a system of partial differential equations, with discrete nodal variables, which can then be solved with the use of variational principles. There are many types of elements available in the FEM; choosing the correct one is dependent on the problem to be solved. The approximate numerical FEM-based solution can be improved by refining the finite-element mesh (element size) globally, or at localised regions with a high resultant continuum field gradient. This global and localised mesh refinement is known as h refinement. Another method of increasing solution accuracy can be to use elements with higher-order shape functions; this method is known as p refinement. A suitable combination of these two methods of mesh refinement can be found with a mesh convergence study, in which a parametric analysis is conducted on the mesh parameters. This can then provide the most accurate solution for the given complex geometry and boundary conditions; care should be taken at this stage as discretisation errors can vastly affect solution accuracy (Cook et al. 2010).

Within the framework of the finite-element method, two approaches are to describe the kinematics of a continuum. The Lagrangian scheme describes the deformation behaviour and motion of a continuum, where the material is associated with an element throughout the entire analysis. In contrast, the Eulerian scheme describes a continuum with elements fixed in space and the material flowing through them. As a result, the mass of an element in a Lagrangian mesh remains constant while its volume can vary, whereas in a Eulerian mesh the mass can vary but the volume remains the same.

The Lagrangian approach is preferable for the FE analysis of solid components with

fixed boundaries, which may include contact defined between multiple components where the history of the continuum can be tracked. It leads itself perfectly to the focus of this research project, modelling micro-scale dynamic deformation and damage of FRCs. It should be noted that this approach does begin to break down under severe deformation, where the mesh can become highly distorted, still mesh distortion control and re-meshing techniques can resolve these issues if properly implemented. The Eulerian approach is most commonly used for computation of fluid mechanics problems, which within the bounds of this research could be used to model the blast pressure-wave propagation towards the target described by employing a Lagrangian scheme via a Fluid-Structure Interaction (FSI) modelling technique. These domain considerations are discussed below in the chapter.

The finite-element method is one of the most popular methods for obtaining an approximate solution to many complex engineering problems. This is thanks to its versatility and resultant ability to model a vast range of scenarios, which may include varying geometry, various loading conditions and changes in material properties, without investing in expensive physical prototyping and experimental trials. The application of this FE method to the static or dynamic modelling of composite materials requires specific discretisation and element formulation, as well as material models to accurately represent their typically anisotropic behaviour. Then as introduced previously, both macro-scale and micro-scale modelling approaches with different complexities can be solved; it is discussed in more detail in Sections 3.3 & 3.4 of this chapter.

3.2 Implicit vs. Explicit Solution Methods

Within the framework of FEM, two techniques implicit and explicit can be used to solve linear and non-linear systems of equations. The implicit solution method is based on static equilibrium for a continuum problem; its basic requirement is that the internal forces (I) within the meshed continuum (as a result of element stresses) and external forces (P) acting on the meshed continuum are balanced using: $P - I = 0$ (Cook et al. 2010). For static continuum problems, the implicit solver iterates successively, most commonly the Newton-Raphson method, until convergence of the result is found.

This is achieved by dividing the loading condition into a series of smaller increment stages in order to preform the iteration process for each. Then, by continuously updating a

global stiffness matrix for the meshed continuum, the solutions can be found incrementally. This solution method is unconditionally stable, with no limitation of the increment size and no time-dependent factors. But one of the most challenging issues that arises when using this implicit solution method is the convergence towards a solution for more complex FE simulations; this is discussed in more detail below.

The explicit solution method extends the discussed static equilibrium to a dynamic equilibrium state, in which the sum of the internal and external forces must match the inertial forces: $P - I = m\ddot{a}$, where m is the mass and $\ddot{a}$ is the acceleration of the structure (Cook et al. 2010). The explicit method uses the integration of the equations of motion, with respect to time, along with the kinematic boundary conditions at one increment to calculate the force at the next increment.

Unlike the implicit solution method, the explicit solver is conditionally stable due to the fact that it uses information from a past increment to calculate the current increment. So, in order to achieve stability of the solution, the time step for each increment has to be small enough so that the wave-propagation effect mentioned in Chapter 2 does not travel across more than one element per time step. This time step limit is known as the stable time increment, and can be calculated using: $\Delta t = \frac{L_e}{C_o}$, where L_e is the element length and C_o is the speed of sound in the material as calculated in Section 2.2 of Chapter 2 (Cook et al. 2010).

For this explicit solution method convergence of the solution is more likely to be achieved in comparison in the implicit method, but the stable time increment restriction makes the explicit method unsuitable for physical continuum problems with longer durations. Sometimes this method can be used to simulate quasi-static continuum problems by artificially increasing the load rate or the materials density via mass scaling. This increases the stable time increment, but care should be taken to ensure that the energy and deformation mechanisms in the simulation are still representative of the original problem. Still, the explicit solver is ideal for continuum problems that can cause severe changes to the stiffness matrix, resulting in the degradation and possible failure of a material. As a result, explicit dynamic analysis is typically employed to model cases with large deformations, material non-linearities and complex contact behaviours. It can also effectively model severe discontinuities that may occur in the continuum as a result of material failure, element deletion or crack propagation.

Comparing the two solution methods, the implicit scheme requires more computational

resources and a higher computation time per increment than the explicit scheme, as the large matrices need to be stored and a large system of equations should be solved for each iteration. The explicit method has a lower computation time per stable time increment, but usually requires more increments to achieve the final solution. As a result, the implicit method is most commonly used for static and comparatively low velocity dynamic problems, in which the loading conditions can be assumed to be quasi-static. The explicit method is ideally suited to non-linear dynamic problems such as higher velocity ballistic impact or blast and even large deformation resulting from quasi-static loading.

3.3 Modelling Considerations at Varying Length Scales

As discussed previously, the mechanical behaviour of a composite at a global macro-scale can be tailored by changing the structure and distribution of the reinforcing element at a micro-scale. It would be very expensive to test experimentally the infinite variations of micro-structured composite, and so the FE method provides a means to predict its response and, as a result, optimise a composite before production. Given that the physical observable behaviour varies at different length scales as discussed in Chapter 2, it is important to carefully consider the length scale used in the FEM study.

When considering different length scales with the aim of predicting the macro-scale response of a material, it becomes important to have a method to link the observed mechanical behaviour between the varying length scales. Micro-mechanics is a method of estimating the combined effect of local deformations of the heterogeneous micro-scale, into a representative volume using suitable homogenisation techniques. But in order to do this, a method of decomposition or sub-structuring must be employed to first identify suitable smaller sub-domains which can represent the behaviour of the micro structure accurately (Zohdi et al. 2001; Talreja 2006). Figure 3.1 shows a typical breakdown of this continuum decomposition method used for fibre-reinforced composite materials, with reference to length scale.

As shown in Figure 3.1 and with reference to the damage mechanisms discussed in Chapter 2, the macro-, meso- and micro-scale modelling approaches can be typically introduced (Talreja and Singh 2008). This is discussed in general terms, with specific material behaviour models and techniques for fibre-reinforced composites at each length

scale considered later in the chapter.

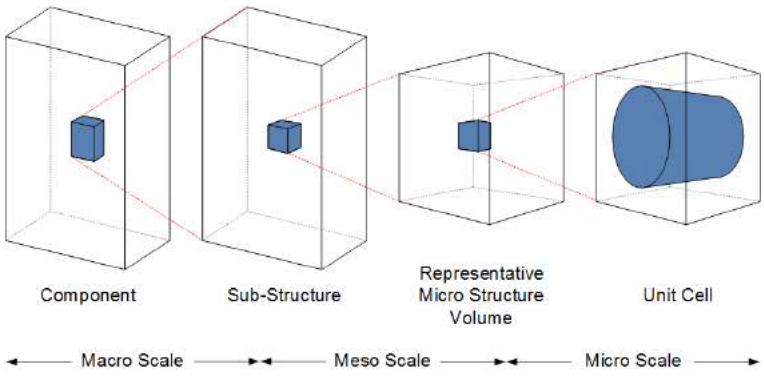

Figure 3.1: Typical breakdown of the continuum decomposition method used for fibre-reinforced composites

3.3.1 Macro-scale

As mentioned above, the macro-scale is defined at the level, at which the continuum of the component or sub-structure under analysis is completely homogeneous, either isotropic or anisotropic. Typically, the global structural response of a smaller component made from a homogeneous material can be modelled using FEM, including damage initiation, propagation and failure. At this scale, a fibre-reinforced uni-directional or woven composite made up from multiple plies can usually be homogenised to an anisotropic continuum, meshed with solid elements. This is only useful for purely linear elastic analysis but any predictions with regard to non-linear deformation, delamination or other damage mechanisms may not be accurate due to the geometric limitations of the model.

3.3.2 Meso-scale

The meso-scale typically takes any plies or layers within the component or sub-structure into consideration. For the case of uni-directional FRCs, each of the plies is modelled as an anisotropic homogeneous continuum (depending of fibre orientation), in which non-linear deformation or other damage mechanisms can be estimated with more accuracy. This length scale is suitable for modelling inter-ply delamination (Abisset et al. 2011), which, as mentioned in Chapter 2, is the only damage mechanism associated with FRCs that is clearly measurable at this scale. For woven FRCs, damage mechanisms such as intra-weave cracking can also be modelled and predicted at a meso-scale along side inter-ply

delamination (Carvalho et al. 2012a; Fagiano et al. 2014; Obert et al. 2014).

To use this meso-scale approach in order to analyse the macro-scale response of a composite component, the laminate structure of FRCs is constructed by stacking the anisotropic homogeneous plies at different orientation, depending on the fibre orientation and stacking sequence. FE meshes could then consist of either a single layer of shell or solid elements, in which full continuum based 3D elasticity could be modelled. Typically cohesive zone elements or surfaces with a traction separation law between the plies are employed to model the delamination mechanisms including initiation and propagation. This allows for the intra-ply and inter-ply damage mechanisms to be modelled separately at the macro-scale, enabling the complex analysis of interactions between them. This is suitable for modelling larger components, with the results showing good accuracy for predicting the failure behaviour when compared with experimental data (Higuchi et al. 2017; Lópes et al. 2009; Mendes and Donadon 2014; Phadnis et al. 2013; Phadnis et al. 2014; Shi et al. 2012; Ullah et al. 2012b; Zhang et al. 2017).

As discussed later is this chapter, this meso-macro scale approach can lead to an increase in computational efforts due to the necessary reduction of the element size. On top of this, the introduction of multiple plies makes modelling of more complex geometries more difficult.

3.3.3 Micro-scale

The micro scale approach is employed at the length scale, at which, for fibre-reinforced composites, the fibres are introduced directly into the model. So, the fibre and matrix elements within a uni-directional or woven ply are modelled separately, including the interface between them, allowing for all of the intra-ply and inter-ply damage mechanisms associated with FRCs to be modelled.

Given the presence of individual fibres at this micro-scale modelling approach, the fibre/matrix interface is of great interest, with many models developed over the years to study interaction and debonding of this interface. Early modelling attempts saw the development of mono-dimensional shear lag models to study the fibre 'push-out' test (Zidi et al. 2000; Zidi et al. 2001). In recent years, both cohesive zone elements (CZEs), with a traction separation law and finite fracture mechanics have become popular choices for modelling the interface (Greco et al. 2013; Carraro and Quaresimin 2014; Garcia

et al. 2015). There is a need for more research to be conducted within the area of modelling micro-scale behaviour of FRCs, in order to understand, develop and improve FRC performance but this approach is not suitable for larger component modelling given the computational challenges. The extent of this limitation is introduced and discussed in more detail in the next section of this chapter.

3.3.4 Stable Time Increment (Explicit Solver)

When reducing the length scale chosen for modelling, the inevitable reduction in the element size needed to represent the FRCs structure has a negative effect on the computation time required for both the implicit and explicit solvers. As this research project is focused on dynamic behaviour of composites under ballistic and blast loading, the development of the models will be based on the explicit solution technique, in which this effect is most noticeable. This effect can be demonstrated as follows by considering the effect on the stable time increment, which directly affects the computational efficiency.

With reference to Equation 2.3 in Section 2.2 of Chapter 2 and the material properties for a fibre and matrix (taken the average from the properties in Tables 2.2 and 2.3 in Chapter 2, the approximate stable time increment can be calculated using: $\Delta t = \frac{L_e}{C_o}$, where L_e is defined as the average unit length associated with each scale. For the case of the micro-scale assumption, this is equivalent to 10 elements across the diameter of a $10\mu m$). A breakdown of the average material properties and speed of sound in an average fibre and matrix element, along with the resulting stable time increments calculated are shown in Table 3.1.

Table 3.1: Approximate stable time increments for different length scales for explicit modelling

Material Considered		Fibre	Matrix
Average Density (kg/m^3)		2000	1200
Average Elastic Modulus (GPa)		100	3.5
Average Speed of Sound in Material (m/s)		7071	1708
Stable Time Inc. Δt (s)	Macro (L_e = 1x10^0 m)	1.414 × 10^{-4} s	5.855 × 10^{-4} s
	Meso (L_e = 1x10^{-3} m)	1.414 × 10^{-7} s	5.855 × 10^{-7} s
	Micro (L_e = 1x10^{-6} m)	1.414 × 10^{-10} s	5.855 × 10^{-10} s

As can be seen from the results in Table 3.1, this approximation demonstrates the

importance of considering and controlling the minimum element size within the model due to its strong effect on the stable time increment. With the Abaqus 6.14 explicit solver implementing a lower time increment limit value of $1x10^{-15}$ s is which the micro-scale is approaching (ABAQUS 2014), it is clear that modelling FRCs at the micro-scale involves a careful balance between the accuracy of micro structure modelling and the resulting computation efficiency as well as minimising the total element count. With this in mind, a more commonly used meso-scale approach with a larger minimum element size provides a much more computationally efficient analysis of larger structures, but, as mentioned previously, cannot model accurately all of the damage mechanisms observed in FRCs.

3.3.5 Homogenisation

When considering the mechanical response of any material it is clear that modelling its exact atomic structure for the entire macro-scale component would lead to the most accurate results. But, in reality, modelling large components using this approach would require phenomenal computation power to even solve the simplest problems. In order to over come this challenge, the materials structural behaviour can be homogenised at a larger scale to improve the overall computational efficiency. As seen in Figure 3.1, there is a defined procedure for the decomposition or sub-structuring of a continuum to smaller sub domains to model the behaviour of heterogeneous materials such as FRCs at varying length scales.

The homogenisation technique is defined as the process of characterising the behaviour of a material that is heterogeneous at a smaller scale by representing it as a single homogenised continuum at a larger scale. For FRCs this technique can approximate the mechanical response to volume-averaged field model using FEM at two scales: (i) the fibre/matrix micro structure (micro-scale) can be represented as a homogeneous continuum in each ply at the meso-scale, or (ii) the interaction of plies in the stacking sequence with different orientations (meso-scale) can represent the overall global response of the FRC at the macro-scale.

It is very important that this volume averaging approach considers the statistical distribution of the constituents at each length scale; this could be the distribution of individual fibres in the matrix, the type of weave pattern or the orientation of the plies in the

stacking sequence. When modelling the representative volume it has to be large enough to reproduce the average response, while also considering computational efficiency and not modelling an unnecessary amount of the substructure. This approximated subdomain is known as a representative volume element (RVE). Determining the size of the RVE is highly dependent on the composite structure and the level of detail required to capture the smaller scale behaviour (Bunsell and Renard 2005), but a suggested procedure for accounting for random microstructure homogenisation of fibre distribution was defined by Silberschmidt (2008) stating that the RVE size should be approximately 5 times larger then the average fibre diameter for less than 1% error or large enough to include approximately 30 fibres. This is becoming common practice when modelling FRCs; an example of a RVE used by Okereke and Akpoyomare (2013) is shown in Figure 3.2. There are also many techniques that can be used to generate the fibre distribution geometry needed for FEM modelling, examples include using a Monte Carlo style algorithm for geometry generation or using images of an actual composites micro-structure.

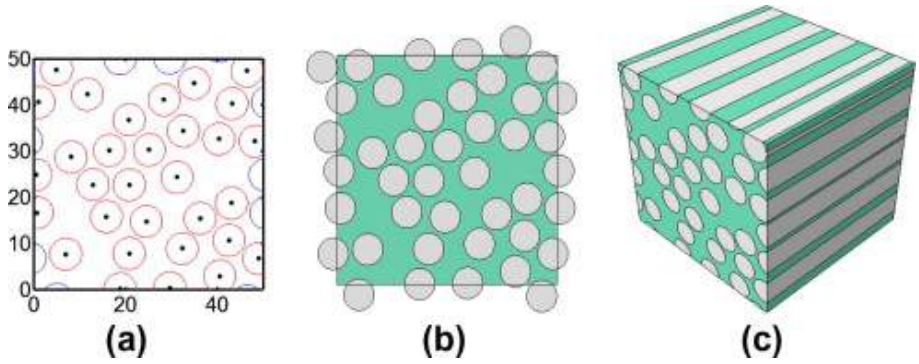

Figure 3.2: Determination and construction of a RVE used by Okereke and Akpoyomare (2013).

Okereke and Akpoyomare (2013) also investigated the effect of the boundary conditions on the RVE and concluded that, given the nature of the physical deformation shown by the RVE in the larger scale continuum, it is very important that the RVE is constrained with periodic boundary conditions. An important consideration for the implementation of periodic boundary conditions is that any fibre that lies on the RVE boundary must re-appear on the opposite side of the RVE.

It is clear that this method of using RVEs to homogenise, for example, the micro-structure of a FRC to a meso-scale within each ply, would provide a great computational benefit when modelling larger macro-scale components under various loading conditions

to analyse their response. But as mentioned previously, it must be understood that as a result there will be limitation regarding the assessment of micro-scale damage mechanisms. Methods of describing these mechanisms are discussed below.

3.4 Meso-scale Modelling of Fibre Reinforced Composite Behaviour

As mentioned previously, when considering computational efficiency, the process of homogenisation at each length scale provides great benefits in terms of the component size that can be modelled. But by approximating the composites meso- and macro-scale response at each level, the observable micro-structure behaviour and damage mechanisms are increasingly lost. By undertaking and limiting the homogenisation to the meso-scale through the use of representative volume elements, the average anisotropic response of an FRC can be found for a single ply.

3.4.1 Continuum Based 3D Elasticity Theory

In some cases composite plies are modelled using 2D shell elements representing each ply; these elements are limited in there degrees of freedom and do not capture through thickness out-of-plane shear behaviour. As discussed in the previous chapter, the FRCs through thickness behaviour does have a significant effect on the response of each ply especially under dynamic loading. The component formed of multiple plies can be subjected to non-linear behaviour in various ways, including; large deformations, buckling instabilities, failure via brittle fracture and even softening during delamination. All of these conditions show links to the degrees of freedom missing from the 2D shell element theory.

For this meso-scale modelling approach it is therefore very important to include all six degrees of freedom via solid elements formulated with the 3D continuum elasticity theory. Only then can delamination and interlaminar shear behaviour be captured along with the through thickness normal stress components, which can then be used to more accurately determine the failure of the FRC as discussed in the next section.

3.4.2 Models for Predicting Damage and Failure in FRC Plies

Many models in this area of numerical modelling, with different strength based criteria, were developed to mathematically describe and predict the degradation and failure with the 3D continuum elasticity theory. For uni-directional FRCs, the World Wide Failure Exercises (WWFE 1 & 2) held between 1998 and 2013 are the greatest advancement in this research field. During these exercises authors of the models were invited to evaluate them against standardised tests and extensive experimental results, with the aim of clarifying and exposing the strengths and weaknesses of each model in order to drive further development. As expected, the results predicted by each theory differed significantly, providing strong evidence that there is still a need for further research in this field (Soden et al. 2004; Kaddour and Hinton 2013). A third WWFE was proposed but is yet to yield the results (Kaddour et al. 2013).

The first WWFE suggested that from the original 14 theoretical approaches presented initially, the models by Tsai (1971), Puck (1992) and Zinoviev (1998) were more suitable and showed the best agreement to the experimental results, and from additional approaches, models by Cuntze (2004) and Bogetti (2004) can be added. From the second WWFE, models by Pinho (2005) and Carrere (2012) were also recommended. To date is it said that based upon the validation against the WWFE data, the Puck criterion is said to the standard German aviation industry, and has been used by many researchers as a basis for failure prediction improvement including Nasa's Langley Research Centre (Paris et al. 2001). Based on this, a few of the noteworthy criteria are discussed here, highlighting their strengths and weaknesses.

Maximum Stress or Strain Criterion

This criterion is based on the maximum allowable stress or strain in either tension, compression or shear in any direction and forms the most basic failure criterion. This criterion is fully decoupled, i.e. the behaviour in each direction is independent of the others; as a result, the stress or strain in one direction can not influence the failure in another. Even though this criterion does not reflect actual failure behaviour, it is still commonly used to predict the onset of damage given its simplicity.

Tsai-Wu Criterion

This criterion was suggested to predict the failure of an anisotropic material by assessment of its stress invariants (Tsai and Wu 1971). Although this criterion is among the most commonly used for composite materials it is a structurally phenomenological criteria, that is based on macro-scale observations and, therefore, can not predict the mechanisms of failure. The Tsai-Wu Failure criterion has the following form:

$$F_1\sigma_1 + F_2\sigma_2 + F_{11}\sigma_1^2 + F_{22}\sigma_2^2 + F_{66}\tau_{12}^2 + 2F_{12}\sigma_1\sigma_2 = 1\,, \tag{3.1}$$

where:

$$\begin{aligned} F_1 &= \frac{1}{S_1^t} + \frac{1}{S_1^c}\,, \quad F_2 = \frac{1}{S_2^t} + \frac{1}{S_2^c}\,, \quad F_{11} = -\frac{1}{S_1^t S_1^c}\,, \\ F_{22} &= -\frac{1}{S_2^t S_2^c}\,, \quad F_{12} = f\sqrt{F_{11}F_{22}}\,, \quad F_{66} = -\frac{1}{S_{12}^2}\,. \end{aligned} \tag{3.2}$$

The constant f can either be found through experiment, or an additional assumption can be made setting $f = -0.5$ for plane stress and the von Mises criterion. Then S_*^t and S_*^c denote the tensile and compressive strength respectively.

Hashin Criterion

The Hashin criterion is developed from the Hashin-Rotem criterion, which is a partially coupled development of the Maximum Stress or Strain criterion, meaning that failure can be the result of mixed normal and shear stress or strain state. The Hashin criterion includes the beneficial influence of the compressive stresses on the matrix strength (Hashin 1980). The criterion is defined as follows: Equation 3.3 - tensile fibre failure, Equation 3.4 - compressive fibre failure, Equation 3.5 - tensile matrix failure and Equation 3.6 - compressive matrix failure:

$$\left(\frac{\sigma_{11}}{S_{11}^t}\right)^2 + \left(\frac{\tau_{12}}{S_{12}}\right)^2 \geq 1\,, \tag{3.3}$$

$$\left(\frac{\sigma_{11}}{S_{11}^c}\right)^2 \geq 1\,, \tag{3.4}$$

$$\left(\frac{\sigma_{22}}{S_{22}^t}\right)^2 + \left(\frac{\tau_{12}}{S_{12}}\right)^2 \geq 1\,, \tag{3.5}$$

$$\left(\frac{\sigma_{22}}{2S_{23}}\right)^2 + \left[\left(\frac{S_{22}^c}{2S_{23}}\right)^2 - 1\right]\left(\frac{\sigma_{22}}{S_{22}^c}\right) + \left(\frac{\tau_{12}}{S_{12}}\right)^2 \geq 1\,. \tag{3.6}$$

Puck Criterion

There has been many iterations of Puck criteria, the first of which was proposed by Puck and Schneider in 1969, with modifications later to incorporate elements of Hashins criteria (Puck 1992; Puck and Schürmann 1998; Puck and Schürmann 2002). The criterion covered five failure mechanisms including and defined in their simplest form as: Equation 3.7 - fibre tensile failure, Equation 3.8 - fibre compressive failure, Equation 3.9 - matrix combined shear and tensile failure, Equation 3.10 - matrix pure shear failure and Equation 3.11 - matrix combined shear and compression:

$$\left(\frac{\sigma_{11}}{S_{11}^t}\right) \geq 1\,, \tag{3.7}$$

$$\left(\frac{\sigma_{11}}{S_{11}^c}\right) \geq 1\,, \tag{3.8}$$

$$\sqrt{\left(\frac{\tau_{12}}{S_{12}}\right)^2 + \left(1 - p_{12}^+\frac{S_{22}^t}{S_{12}}\right)^2\left(\frac{\sigma_{22}}{S_{22}^t}\right)^2} + p_{12}^+\frac{\sigma_{22}}{S_{12}} \geq 1\,, \tag{3.9}$$

$$\frac{1}{S_{12}}\sqrt{\tau_{12}^2 + \left(p_{12}^-\sigma_{22}\right)^2} + p_{12}^-\sigma_{22} \geq 1\,, \tag{3.10}$$

$$\left[\left(\frac{\tau_{12}}{2(1+p_{22}^-)S_{12}}\right)^2 + \left(\frac{\sigma_{22}}{S_{22}^c}\right)^2\right]\frac{S_{12}}{-\sigma_{22}} \geq 1\,, \tag{3.11}$$

where p_{12}^+, p_{12}^- and p_{22}^- are inclination parameters, with the method for obtaining them was also defined by Puck and Schürmann (2002). The puck criteria are three dimensional and will be presented as such in the next chapter in a generalised form.

Although the concluding remarks from the WWFE suggest that these failure criteria (including those mentioned at the beginning of the section) are the most recommended models for predicting composite behaviour within a single ply at the meso-scale with some

suggesting an indication of failure mechanisms (purely fibre or matrix dominated failure), they still do not describe any observable micro-scale damage.

3.4.3 Continuum Damage Mechanics Approach

With the strength based failure criteria mentioned above predicting the initiation of the various failure mechanisms within a FRCs ply, an approach must be chosen to track the accumulation of damage until the FRC ply reaches ultimate failure. The simplest and most commonly used way of doing this is via continuum damage mechanics (CDM), and was first proposed by Kachanov in 1958. This approach is used to predict the degradation of stiffness and evolution the damage seen over time as it accumulates. The application of this approach introduces a damage variable D into the constitutive model and represents the initiation and progression of damage, and can be formed from the summation of multiple separate damage mechanisms. The general approach to this is shown in Equation 3.12:

$$\{\sigma\} = (1 - D)E\{\varepsilon\} \ , \tag{3.12}$$

where the variable D degrades from 0 (undamaged) up to 1 (completely damaged) resulting in a total loss of stiffness.

This approach became popular following the work by Talreja (1985 & 1992), and describes the damage as the appearance of cracks, diminishing the associated area supporting the applied load. This is equivalent to directly defining the effective strain or stress to the associated damage, and is popular with many researchers.

Early variations of this approach, like the Matzenmiller-Lubliner-Taylor (MLT) model (Matzenmiller et al. 1995), were developed to include strain softening and account for damage in warp, weft and shear directions as shown is Equation 3.13:

$$\begin{bmatrix} \varepsilon_{11} \\ \varepsilon_{22} \\ \varepsilon_{12} \end{bmatrix} = \begin{bmatrix} \frac{\sigma_{11}}{E_{11}(1-d_{11})} & \frac{\nu_{12}\sigma_{11}}{E_{11}} & 0 \\ \frac{\nu_{21}\sigma_{22}}{E_{22}} & \frac{\sigma_{22}}{E_{22}(1-d_{22})} & 0 \\ 0 & 0 & \frac{\sigma_{12}}{G_{12}(1-d_{12})} \end{bmatrix} . \tag{3.13}$$

These approaches were developed further to align with a continuum based 3D elasticity theory for woven composites, and can take the form shown in Equation 3.14 presented by Muñoz et al. (2015):

$$\begin{bmatrix} \varepsilon_{11} \\ \varepsilon_{22} \\ \varepsilon_{33} \\ \gamma_{12} \\ \gamma_{23} \\ \gamma_{13} \end{bmatrix} = \begin{bmatrix} \frac{1}{(1-d_{11})E_{11}} & -\frac{\nu_{12}}{E_{11}} & -\frac{\nu_{13}}{E_{11}} & 0 & 0 & 0 \\ -\frac{\nu_{12}}{E_{11}} & \frac{1}{(1-d_{22})E_{22}} & -\frac{\nu_{23}}{E_{22}} & 0 & 0 & 0 \\ -\frac{\nu_{13}}{E_{11}} & -\frac{\nu_{23}}{E_{22}} & \frac{1}{(1-d_{33})E_{33}} & 0 & 0 & 0 \\ 0 & 0 & 0 & \frac{1}{(1-d_{12})G_{12}} & 0 & 0 \\ 0 & 0 & 0 & 0 & \frac{1}{G_{23}} & 0 \\ 0 & 0 & 0 & 0 & 0 & \frac{1}{G_{13}} \end{bmatrix} \begin{bmatrix} \sigma_{11} \\ \sigma_{22} \\ \sigma_{33} \\ \tau_{12} \\ \tau_{23} \\ \tau_{13} \end{bmatrix}. \tag{3.14}$$

This MLT model is developed further for the model proposed in Chapter 7.

3.5 Modelling Ballistic Impact and Blast

As previously discussed in Section 3.3 of this chapter, inter-ply delamination is the first associated FRC damage mechanism to be visually observable at the meso-scale between homogenised plies. Apparently, the cohesive zone technique with a traction separation law is the most commonly used approach for modelling the inter-ply delamination. It gives the modelling regime the ability to provide results, which prove to be an accurate match when compared to experimental data (Lópes et al. 2009; Mendes and Donadon 2014; Phadnis et al. 2013; Phadnis et al. 2014; Zhang et al. 2017).

For ballistic impact modelling, using this approach for modelling delamination is equally valid (Johnson et al. 2009; Varas et al. 2013; Muñoz et al. 2015; Riccio et al. 2014). A study conducted by Deka et al. (2009) investigated the response of a GFRP subjected to multiple localised impacts with this modelling approach, and concluded that the multiple sequential impacts resulted in a 23.0% and 14.2% increase in delamination damage between plies for two and three impacts respectively. And as expected, the residual velocity of the projectile post impact was influenced by the introduced amount of delamination damage; this was due to the decrease in local stiffness because of the delamination, lowering the ability to absorb energy and increasing the exit velocity of the projectile after perforation. An example of the delamination prediction vs the experiment results from this study can be seen in Figure 3.3.

Sastry et al. (2014) did not implement any model for delamination, but instead rigidly ties the plies and studied the effect of the stacking sequence on a Carbon/Epoxy, E-

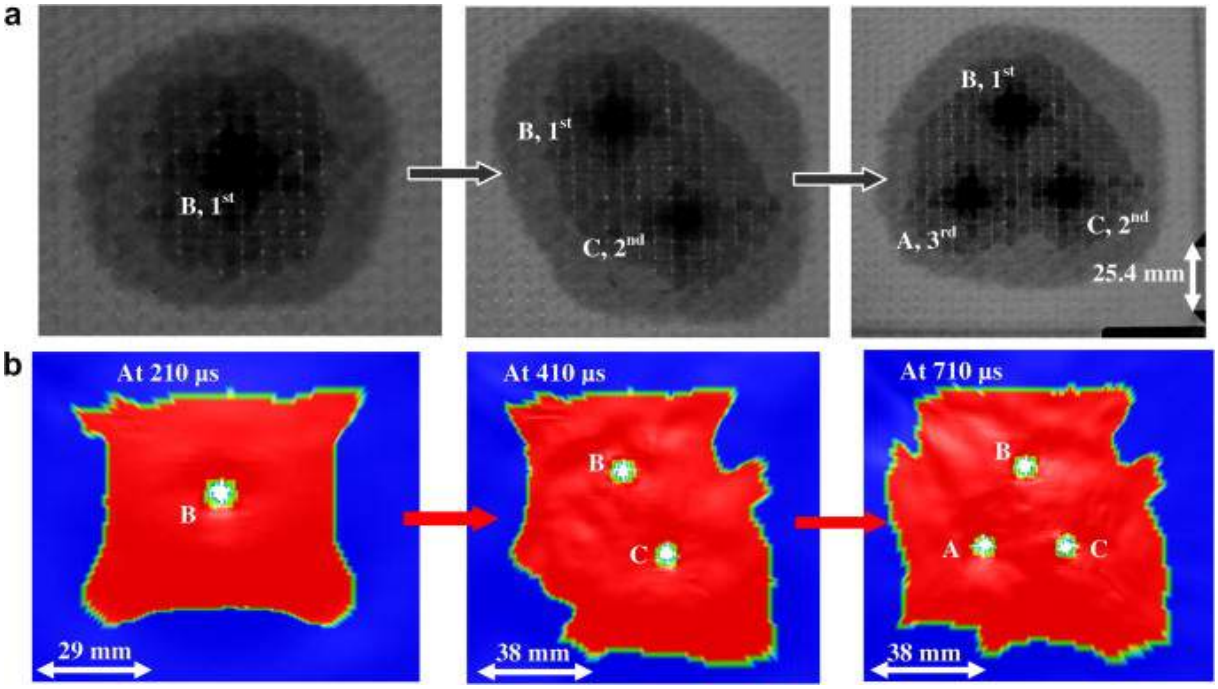

Figure 3.3: Delamination progression for sequential impact with three projectiles (a) experiments (b) simulation (Deka et al. 2009)

Glass/Epoxy and Kevlar/Epoxy FRCs. Their study evaluated the absorption of kinetic energy on impact before perforation, and also made comments on the most common element deletion method for modelling failure and its effect on the loss of mass, and the effect of the model energies. The results from this study are likely to be valid, but the absence of a delamination mechanisms between the plies in the model raises the question of whether the quantitative results from the study are accurate given that it was proven that delamination accounts for a large amount of energy absorption as discussed in Chapter 2.

When approaching the complex behaviour of a fragmenting ice projectile, a method needs to be implemented for its failure. Pernas-Sánchez et al. (2012) utilised the Drucker–Prager criteria, which allows tensile / compressive asymmetric behaviour, then used a failure criteria based on tensile pressure cut-off in order to describe the ice fragmentation. They then examined three numerical approaches to model the complex large deformation behaviour, resulting in the complex loading condition. These approaches included Lagrangian meshing, Adaptive Lagrangian Eulerian (ALE) and Smooth Particle Hydrodynamics (SPH), the results of which are shown in Figure 3.4. The study concluded that all the methods adequately reproduced the behaviour of ice in terms of the force induced during the impact, one of the results from the study is shown in Figure 3.5.

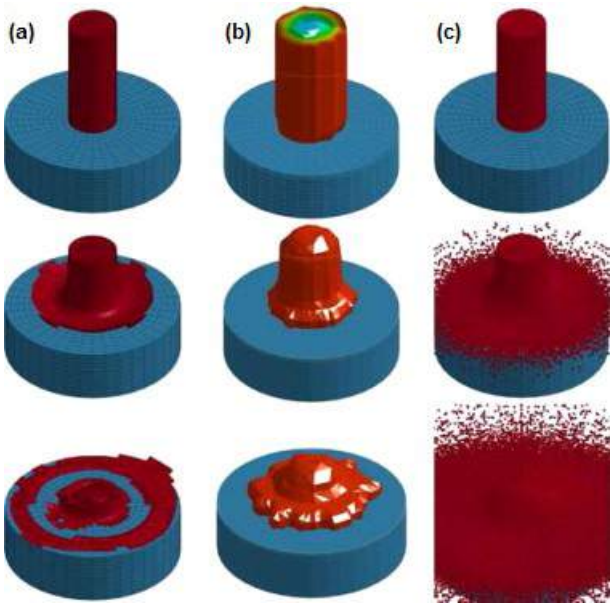

Figure 3.4: Impact sequence for three integration procedures (a) Lagrangian, (b) ALE and (c) SPH (Pernas-Sánchez et al. 2012)

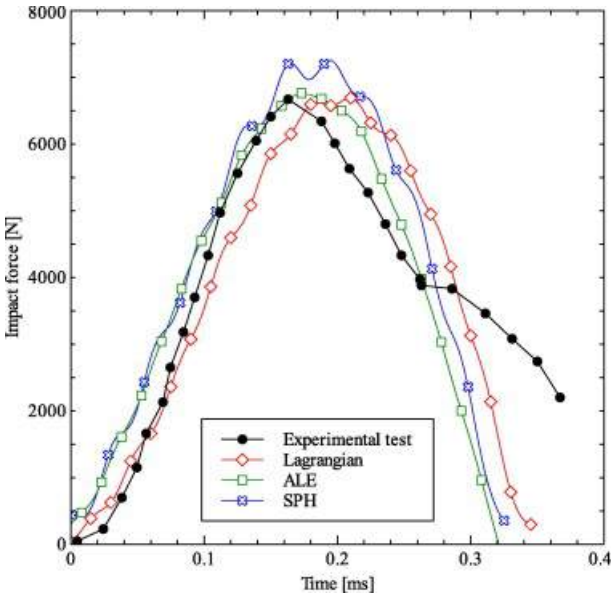

Figure 3.5: Impact force vs. time curves; experimental and numerical results for three numerical solvers. Impact velocity: 152 m/s (Pernas-Sánchez et al. 2012)

Another approach for modelling the behaviour of ice was presented by Tippmann et al. (2013). In their study they employed a strain rate dependant compressive strength based model with a failure criterion based on a tensile pressure cut-off to describe the ice fragmentation. Results from their study are shown in Figure 3.6, and show a good correlation for the effect on peak impact force on the projectiles kinetic energy.

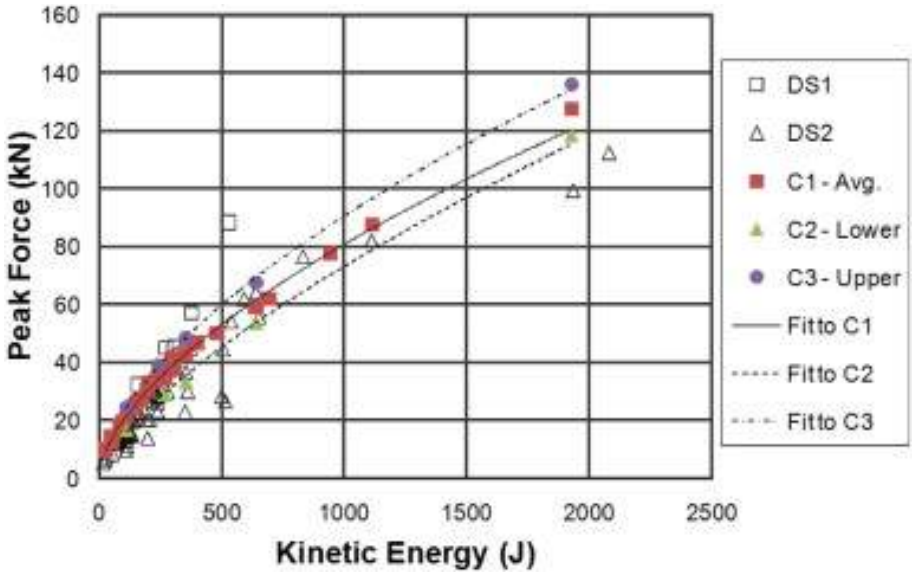

Figure 3.6: Effect of peak force on the kinetic energy showing all simulation and experimental results (Tippmann et al. 2013)

A study conducted by Phadnis et al. (2014) of the effect of an air-blast on curved CFRP plates which was mentioned in Chapter 2, used the same model developed to predict the damage caused by drilling of a CFRP laminate. The model was developed for the meso-scale using the Abaqus Explicit FE solver, and contained 3D continuum elements within each ply of the laminate, joined by cohesive zone elements (CZEs). A combination of both Hashin's and Puck and Schürmann's failure criteria was employed to estimate the damage of the fibres and matrix in the plies, respectively, while also introducing a strain rate dependency for the matrix material and a bilinear traction separation law with a quadratic nominal-stress failure criterion for the CZEs. The air-blast loading was modelled using the incident-wave interaction approach available in Abaqus Explicit.

Given the method in which the inter-ply failure criteria was defined, fibre breakage was determined to be the dominant mode of damage observed under the blast loading. It was captured reasonably accurately with the developed FE model (Figure 3.7). Even though this modelling technique presents a good method to predict the macro-scale response of a laminated FRC using the meso-scale, it only provides an indication of the dominant mode of damage, since the failure criteria used in the model did not account for intra-ply debonding of the fibre/matrix interface. There were many other modelling studies modelling air-blast loading on composites, all of which follow nearly the same approach (Wei et al. 2013a; Wei et al. 2013b).

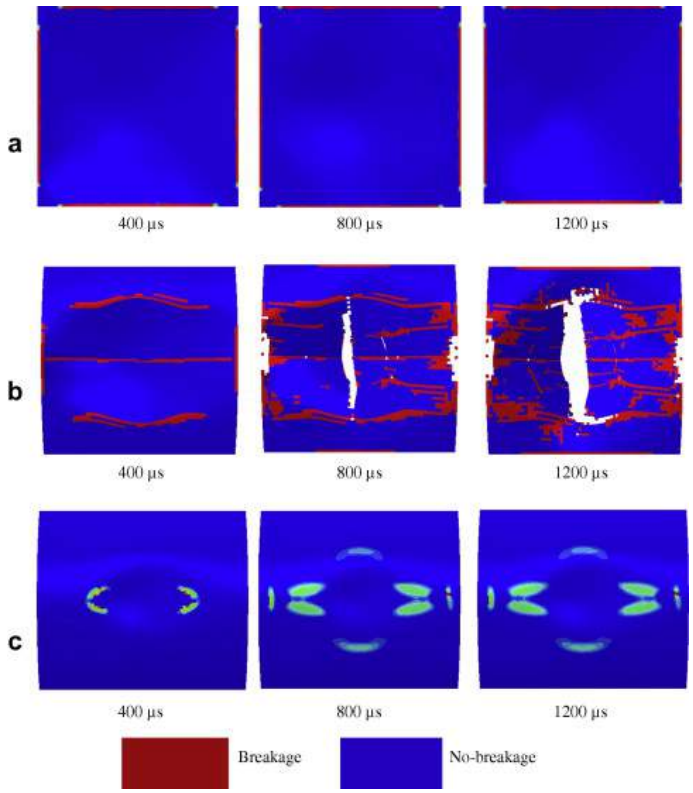

Figure 3.7: Damage evolution in plates under blast loading: (a) fibre breakage in front face of panel A at failure load; (b) panel B at failure load; (c) panel C at threshold load – no global fracture is observed. (**Phadnis2014719**)

3.6 Chapter Summary

In this chapter, the idea of and reasoning behind, the use of the finite-element method for composite materials was introduced, before providing a brief discussion of some key areas that are important for the aim of this research project. Subsequently, considerations about modelling at different length scales were discussed covering typical observations at each length scale (with reference to Chapter 2) and providing many examples of the effect of the chosen length scale on the computational efficiency of a model using the explicit solution method. An initial review of the micro-scale modelling approaches was presented for completeness. Although these methods can accurately predict the micro-scale failure mechanisms, only small component volumes can be modelled given the computational limitations and, therefore, it is not practical to use such approaches for larger scale specimen modelling.

A summary of current meso-scale modelling approaches were considered making ref-

erence to noteworthy failure criteria and their limitations used to model structural degradation in FRCs given there is no definitive criteria, before providing an overview on meso-scale analysis of dynamic ballistic and blast regimes via finite-element method. It is clear from this overview that although the meso-scale modelling regime can accurately predict the macro-scale response of a FRC under dynamic loading, the approach can only provide approximation as to the dominant failure mode, which can either be fibre or matrix failure, or delamination of the plies given the homogenised approach to the material definition. Currently, this approach can not provide any prediction on the actual micro-scale failure mechanisms.

Following a review of the literature and similar to the experimental side covered in the previous chapter, to date there are no comprehensive modelling efforts in which a single meso-scale modelling strategy is used to study CFRP specimens subjected to rigid and fragmenting projects impacts and air-blast shock-waves. With this gap in the literature identified, the research presented in this thesis shall directly model these loading conditions with a consistent meso-scale CFRP material model to compare both deformation and damage behaviour during the loading events.

Thus, from this literature review, the chosen approach to the finite-element modelling shall be a meso-scale model of fibre-reinforced composites, following the intra-ply continuum damage approaches proposed by Hashin (1980) and by Puck and Schürmann (1998) given the success during the WWFE and continuing usage by many researchers. For the inter-ply delamination, the cohesive zone method shall be utilised given the combined strength and toughness-based failure criteria available via a bilinear traction separation law which has be proven to demonstrate accurate damage predictions. This behaviour shall be included via cohesive zone surfaces in order to avoid the computational challenges surround the insertion of thin elements within the explicit model. The development of the chosen modelling approach is discussed in great detail in Chapter 7. With the literature review concluded, the following chapters shall begin to discuss experimental methodologies and experimental results.

Chapter 4

Ballistic and Air-blast Case Studies: Experimental Methodologies

---

Following the review of literature and the identification of the gaps in the research field with regards to dynamic behaviour and analysis of carbon fibre-reinforced composites in Chapter 2 and finite-element modelling of fibre-reinforced composites in Chapter 3, this chapter describes the composite specimens subject to the various loading conditions in this research followed by outlining the loading conditions which are the focus of the two experimental case studies. These studies include both ballistic impact loading with steel (rigid) and ice (fragmenting) projectiles, and also air-blast loading. The results from the case studies are investigated and discussed in detail, including non-invasive in situ analysis of digital image correlation (DIC) data gathered in Chapter 5 followed by detailed visible and hidden damage analysis via X-ray tomography in Chapter 6.

4.1 Material and Specimens

The CFRP used in the case studies in the presented research was pre-fabricated from 10 plies of fabric, pre-impregnated with a toughened epoxy matrix (IMP530R - major constituents being polyepoxide and phenol). The 10 plies are formed into a laminate of 2 surface plies and 8 central bulking plies; full details of the plies are given in Table 4.1.

The layup of the composite is shown in Figure 4.1; all plies were aligned to a $0/90°$ layup configuration and had nominally orthotropic behaviour.

Table 4.1: Properties of plies within the composite

Ply	Description	Weave	Fabric Density	Distribution	
				Warp	Weft
Surface	T300 3K	2×2 Twill	220 g/m^2	50%	50%
Mid (Bulking)	T300 12K	2×2 Twill	630 g/m^2	49%	51%

All specimens were manufactured using the autoclave process, cured at 120 °C with a 1.5 °C per minute ramp rate and a soak time of 160 minutes at a pressure of 90 PSI whilst under full vacuum. The resulting composite specimens had a nominal total thickness of approximately 5.6 mm, with a theoretical density of 1600 $kg/m,^3$. The average tow dimensions and fibre diameter are of approximately 2.7 mm × 0.3 mm and 7 μm respectfully, were measured from microscopy images seen in Figures 4.3 and 4.2. The overall fibre volume fraction in the composite was approximately 47% as confirmed by image processing. Each specimen measured approximate 200 mm × 200 mm; the exact dimensions are specified for each experimental setup below.

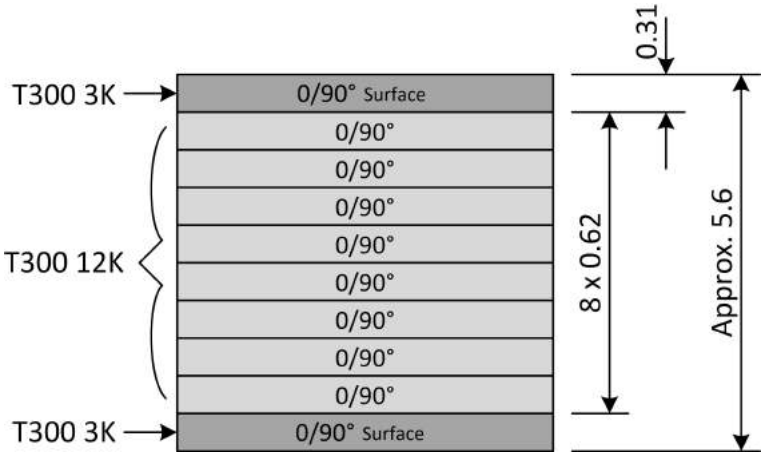

Figure 4.1: Composite panel configuration (all dimensions in mm)

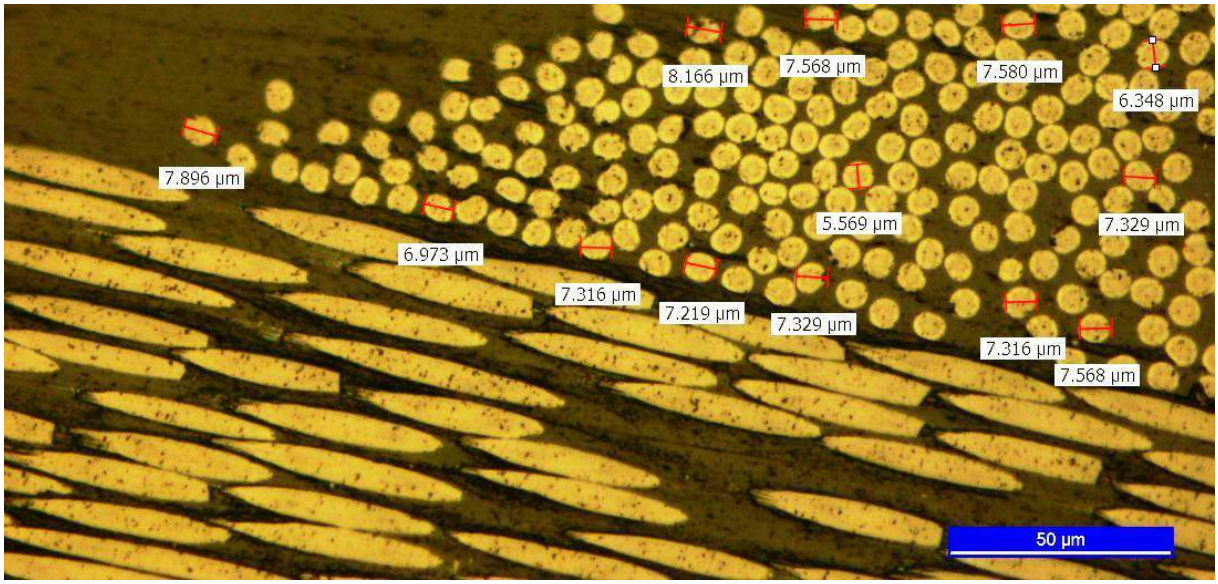

Figure 4.2: Microscopy image: average fibre size

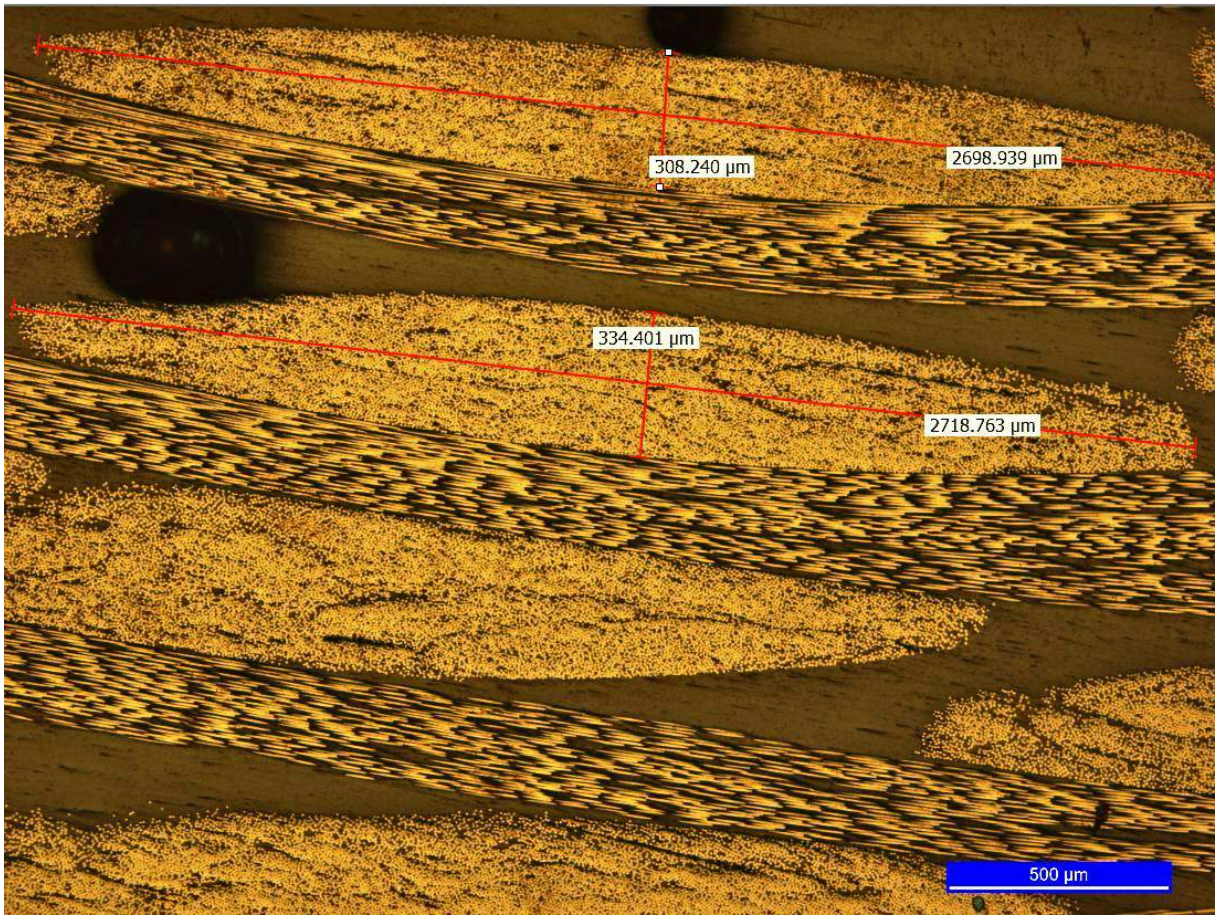

Figure 4.3: Microscopy image: average tow size

4.1.1 Preparation for Digital Image Correlation

In both the ballistic and blast loading case studies Digital Image Correlation (DIC) was used to record the displacement of each specimen during the experiments by tracking changes seen in a regular speckle pattern applied to each specimen. The process of capturing the DIC data is described in detail for each case study in respective sections, but the process of applying the speckle pattern was the same for all the specimens.

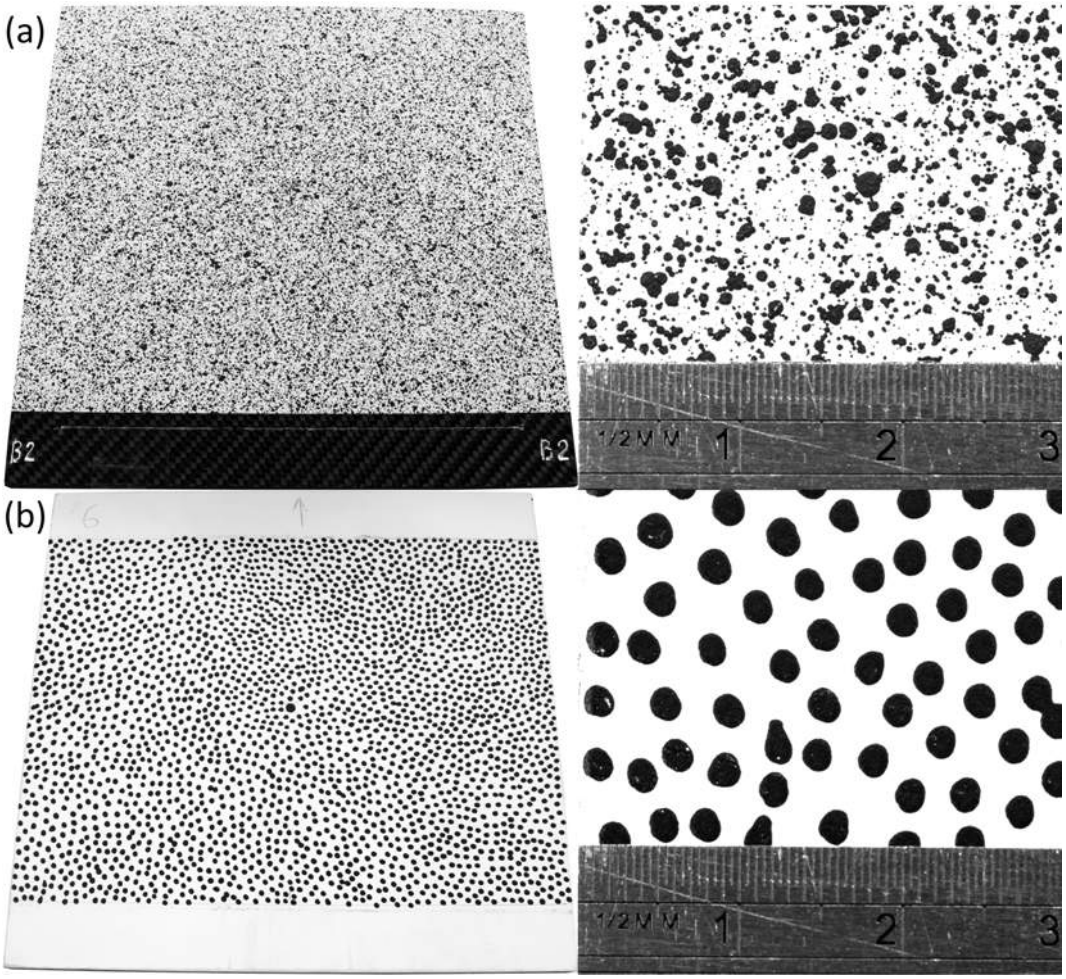

Figure 4.4: Speckle patterns applied to specimens: (a) ballistic experiments; (b) blast experiments.

Given that DIC relies on tracking the changes in grey scale images of the speckle pattern, it is important that these patterns on each specimen are clear and consistent across all specimens. A study conducted by Lecompte et al. (2007) suggested that using a pattern, yielding speckles of approximately 2-6 pixels in size when captured by the chosen cameras would be the most accurate solution when compared to patterns with larger or

smaller average speckles or wider ranges of their size. As a result, two speckle patterns where chosen and applied to all the specimens. Figure 4.4 shows the patterns used for the ballistic (Figure 4.4a) and blast experiments (Figure 4.4b) respectfully. It should be noted that different application methods were used for each set of specimens to achieve the correct sizes for the pixel size, a spray paint technique for the ballistic experiments and a hand dotting technique for the air-blast experiments. Even though these methods were different, since the majority of the speckles had sizes within the 3-6 pixel size range, any effect on the obtained results were not deemed to be significant.

4.2 Description of Ballistic Experiments

The following section of this chapter outlines the full experimental procedure used during the ballistic experiments performed at the Perm National Research Polytechnic University in Perm, Russia. These experiments were conducted to investigate and compare the effect of an ice projectile impact on the carbon fibre composite specimens, when compared to a more typically studied steel projectile.

4.2.1 Pneumatic Gun and Test Setup

The investigation was performed on specially developed ballistic experimental apparatus utilising a pneumatic gun as shown in Figure 4.5.

The CFRP specimens were installed and aligned with the barrel as shown in Figure 4.6, resulting in a cantilever clamping regime, with all specimens being subjected to a perpendicular impact. The projectile was accelerated to the required speed in the barrel using compressed air, and muzzle velocity measurements were collected using a light gate device installed between the specimen and the end of the barrel. Projectile velocities were determined using the time difference between the signal peaks from the light gates. The experiment was controlled with a PC via a PXI system (National Instruments). The impact process was captured using two high-speed cameras (Photron Fastcam SA5) configured in two arrangements, the first of which captured the front and top views (as shown in Figure 4.5) and the second captured the rear surface for digital image correlation (DIC) as described later in the chapter.

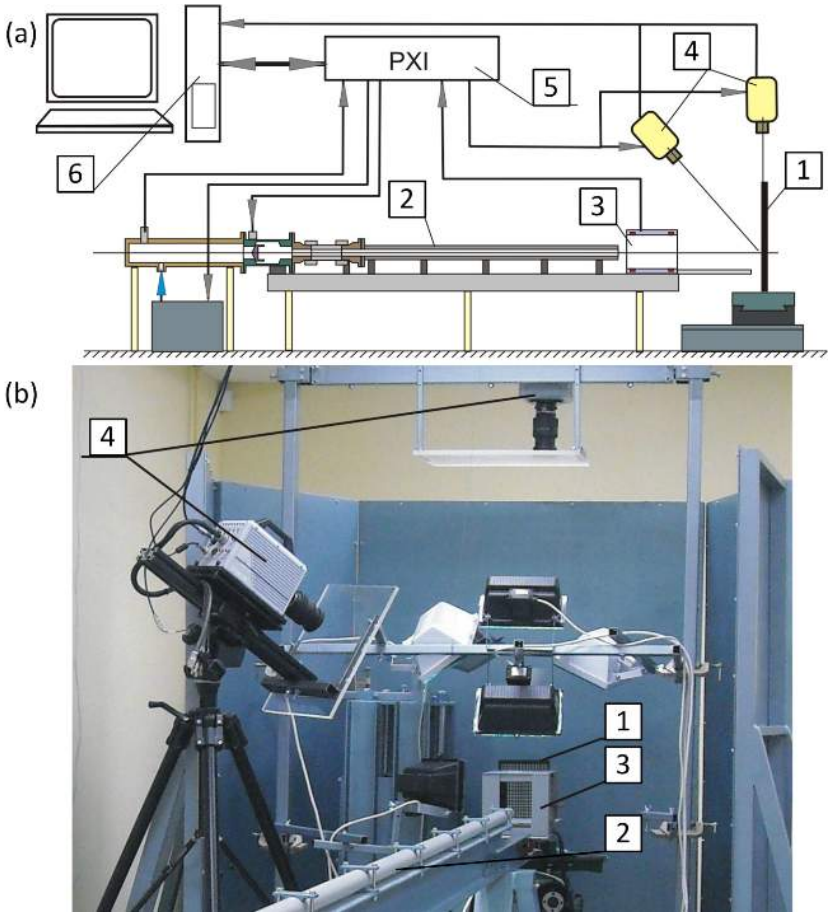

Figure 4.5: Schematic (a) and photograph (b) of ballistic experimental apparatus: 1 - specimen; 2 – pneumatic gun; 3 – velocity measurement device; 4 – high-speed cameras; 5 – PXI system (National Instruments); 6 – PC.

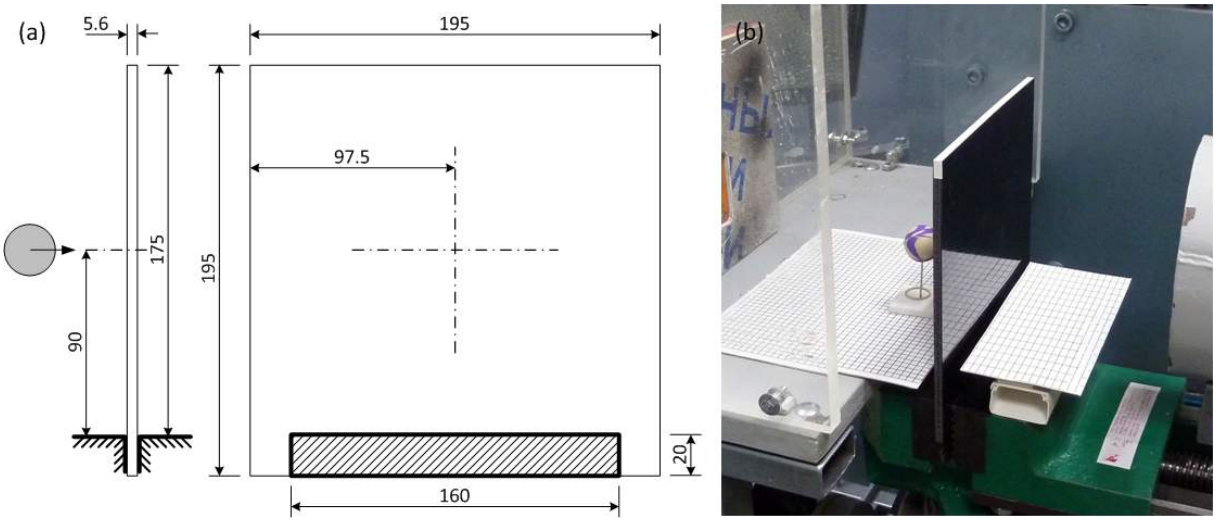

Figure 4.6: Ballistic experimental cantilever fixture: (a) schematic diagram (all dimensions in mm); (b) photograph

4.2.2 Projectile and Experiment Parameters

Two types of projectile were used in the ballistic tests, rigid steel and fragmenting ice. All the rigid (steel) projectiles had a diameter of 23.8 mm with a weight of 54.7 g, and the ice (hail-stone imitation) projectiles had a diameter 25 mm with a weight of 7.5 g at a temperature of $-20\,^{\circ}\mathrm{C}$. The ice projectiles were manufactured with a two layer freezing method to form the final sphere, and were quickly moved into the firing position before impact to keep the projectile frozen while firing. A loading area ratio can be defined for the projectiles and specimens as the ratio between their minor dimensions, which for this case of ballistic loading is approximately equal to $25 \div 175 = 0.143$ (with reference to Figure 4.6).

The impact velocities were chosen in the primary tests to produce 3 levels of damage within the specimens: minor, medium and major (with penetration), and were determined during calibration experiments. It should be noted that for the ice impacts the projectile fragmented upon contact with the specimen; therefore, full penetration of the specimen was not achieved for the highest velocity and hence no resultant velocity could be measured. Instead of penetration, other major damage was observed for the increased velocity of the ice projectile, which is discussed in more detail in Chapter 7. Thus, for the experimental study velocities of 59.5 m/s, 78.5 m/s, 91.5 m/s were chosen for rigid (steel) projectiles and velocities of 304 m/s, 403 m/s, 480 m/s for the ice projectile which fragments on impact. A full breakdown of the test parameters and high-speed camera configurations are shown in Table 4.2. Digital image correlation was not conducted for the major damage case because of the risk of penetration and damage to the cameras. As a result, the deformation analysis discussed in Chapter 6 does not cover the major damage cases, still, full damage analysis is given in Chapter 7 for all the cases. Also, since the DIC camera configuration the cameras where viewing the rear surface of the specimen, the resultant velocity of the steel projectiles could not be measured for the minor and medium damage cases, as the top view was used to determine the resultant speeds at the highest velocity. As can be seen from the table, each of the velocities used for the 3 different damage levels remained consistent and, as a result, the can be considered repeatable for comparison purposes.

Table 4.2: Velocities and energies of the ballistic steel and ice projectiles

	Damage Level	Sample	Initial Velocity (m/s)	Incident Energy (J)	Resultant Velocity (m/s)	Resultant Energy (J)	Absorbed Energy (J)	Camera Configuration
Steel	Major	D4	91.40	228.48	-14.30	5.59	222.89	Front and Top View
		E3	91.20	227.48	12.30	4.14	223.34	
		E5	91.80	230.49	12.00	3.94	226.55	
	Medium	C3	78.40	168.11	-	-	-	Digital Image Correlation
		D2	78.60	168.97	-	-	-	
		D5	78.40	168.11	-	-	-	
	Minor	B2	59.40	96.50	-	-	-	
		B4	60.00	98.46	-	-	-	
		B5	59.00	95.21	-	-	-	
Ice	Major	E1	481.00	867.60	Fragmented	-	-	Front and Top View
		E2	480.00	864.00	Fragmented	-	-	
		E4	479.00	860.40	Fragmented	-	-	
	Medium	C2	402.00	606.02	Fragmented	-	-	Digital Image Correlation
		D1	403.00	609.03	Fragmented	-	-	
		D3	402.00	606.02	Fragmented	-	-	
	Minor	A4	304.00	346.56	Fragmented	-	-	
		B1	304.00	346.56	Fragmented	-	-	
		B3	303.00	344.28	Fragmented	-	-	

4.2.3 High-speed Video and Digital Image Correlation

In both cases of ballistic tests, a high-speed photography system consisting of two cameras (Photron SA5 Photron USA, Inc., CA, USA) were used to capture the ballistic impact events and dynamic response of the specimens through a clear protective window at the rear of the ballistic experimental apparatus. For the front and top view configuration of the cameras, the impact event was recorded at acquisition rates of between 25,000 - 50,000 fps. For the DIC configuration viewing the rear surface of the specimen where the speckle pattern was applied (as shown in Figure 4.7), the event was recorded at 60,000 frames per second. The captured images were then used for Digital Image Correlation (DIC) using the VIC-3D (Correlated Solutions) system, the results of which are discussed in Chapter 6. To obtain the 3D displacement and deformation information through DIC, the relative position of the cameras was determined during calibration of the system using a high-contrast grid with known dot sizes and positions. Additional flood lighting was used to illuminate the specimen during the experiment, and the system was configured to ensure synchronised time across the recorded frames so the resultant DIC would be accurate throughout the impact event.

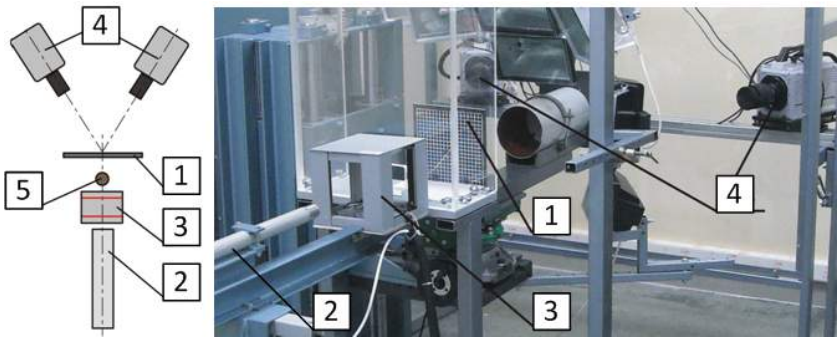

Figure 4.7: Ballistic apparatus and digital image correlation configuration (rear surface view): 1 – specimen; 2 – pneumatic gun; 3 – velocity measurement device; 4 – high-speed cameras; 5 – projectile.

4.3 Description of Air-blast Experiments

The following section of this chapter outlines a full experimental procedure used in the air-blast experiments conducted at The University of Rhode Island in the USA. These experiments were conducted to investigate and compare the effect of different air-blast pressures on the CFRP specimens.

4.3.1 Shock Tube Setup

The shock tube apparatus employed in the air-blast tests was 8 m in length, consisting of a driver, diaphragm and driven section (as shown in Figure 4.8). It was used to subject the centre of the specimens to a dynamic air- blast load in the form of a shock wave. The driver and driven sections were separated by a disposable diaphragm, which controlled the magnitude of the air-blast load. The driver section was pressurised with helium gas until a critical pressure is reached, after which the diaphragm has ruptured creating a dynamic air-blast pressure wave profile that travels through into the driven section. The driven portion of the shock tube consists of a converging section that transitions the rapid release of gas into a shock-wave front which travels through the driven gases. The interface between the driver (helium) and driven (air) gases is known as the contact surface, and it follows the shock-wave at a lower velocity. The diaphragms are made up of 10 mil (0.254 mm) Mylar sheets, with the number of layers controlling the initial pressure in the driving section of the shock tube.

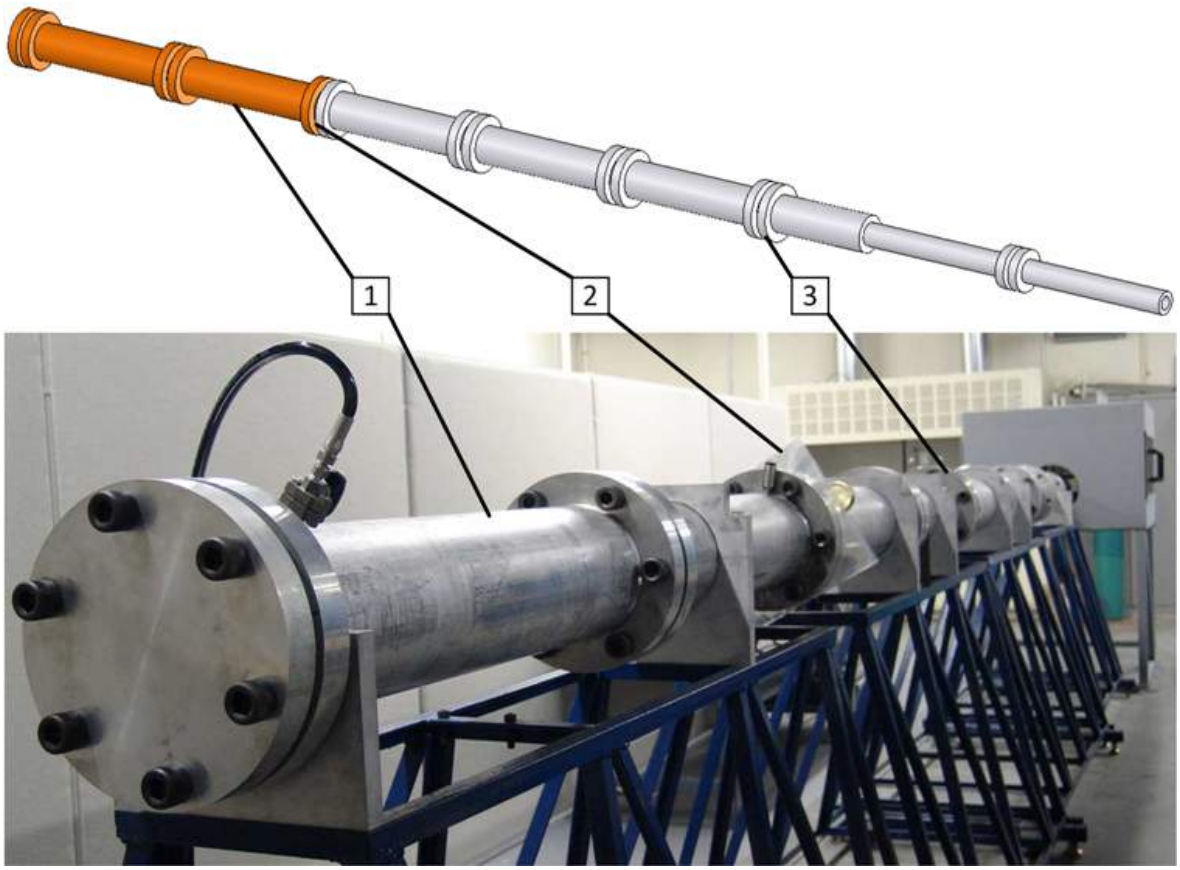

Figure 4.8: Air-blast experimental apparatus and shock tube arrangement: 1 - driving section; 2 – mylar diaphragms; 3 – driven section.

The muzzle of the shock tube ends in a final section with an inner and outer diameter of 76.2 mm and 152.4 mm respectfully, where two PCB102A dynamic pressure sensors are located at 20 mm and 180 mm from the end of the muzzle. The pressure sensors were connected to an oscilloscope where the pressure-wave profiles were recorded at a sampling rate of 100 MHz.

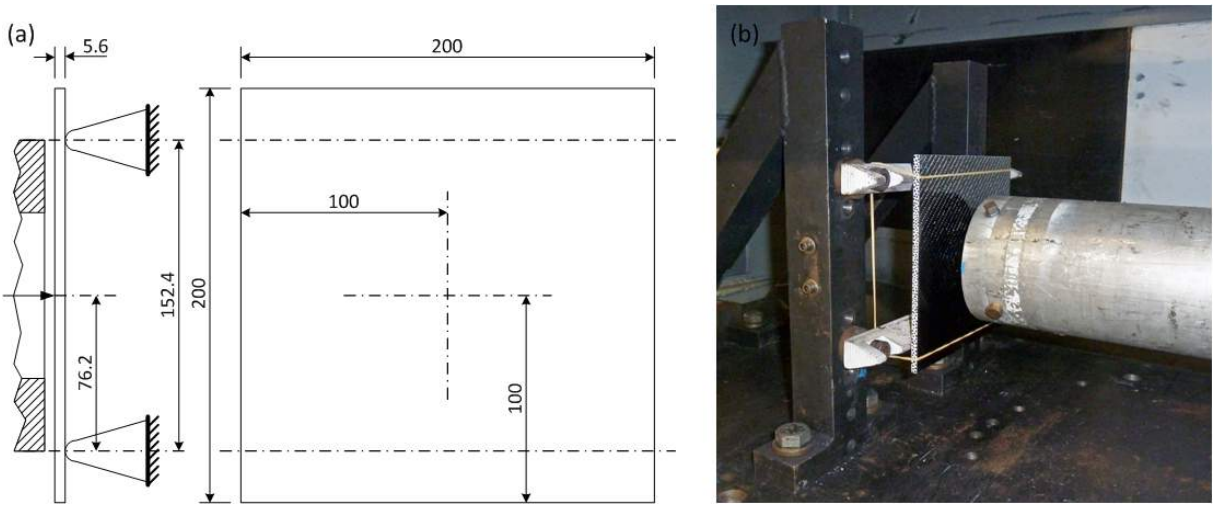

Figure 4.9: Air-blast experimental three-point bending fixture; (a) schematic diagram (all dimensions in mm); (b) photograph

The specimens were positioned vertically on the three-point bending type fixture which consisted of two slightly rounded knife edges located 152.4 mm apart, the remainder of the specimen was unsupported (as shown in Figure 4.9). A rubber band was used to keep the specimen firmly against the knife edges. The muzzle of the shock tube was then moved towards the specimen until there was only a paper thin gap between the specimen and the muzzle (approximately 0.1-0.2 mm). A loading area ratio can be defined between the shock tube and specimens as the ratio between the minor dimensions, which for this case of air-blast loading was approximately equal to $76.2 \div 152.4 = 0.5$ (see Figure 4.9).

4.3.2 Air-blast Pressures Profiles and Shock Waves

The air-blast and resultant pressure magnitudes were then chosen to produce 3 levels of damage in the specimens: minor, medium and major (with the specimens still intact), which were determined during calibration experiments. Thus, for the experimental study levels of 0.4 MPa, 0.6 MPa and 0.8 MPa were chosen as the incident pressures that first pass the pressure sensor located at the end of the shock tube. The resultant pressure-wave

profiles, including the incident and reflected pressures of the air blast, are shown in Figure 4.10. Initially, the area of loading started as a circle with a diameter of 76.2 mm, but as the specimens deformed the circular loading area changed to an elliptical loading area as the specimens became curved. For the major damage cases, it should be noted that two of the specimens (8 and 16, see Table 4.3) failed completely for the highest incident pressure (0.8 MPa), while another two specimens (2 and 10) did not. As a result, the major damage case shall be divided into two cases, major and failure, at approximately equal pressures for the deformation and damage analysis that follows in Chapters 6 and 7. A full breakdown of the test parameters and high speed camera configurations are shown in Table 4.3. As can be seen from the graphs and table, each of the pressure profiles used for the 4 different damage levels remained consistent and, as a result, they can be considered repeatable for comparison purposes.

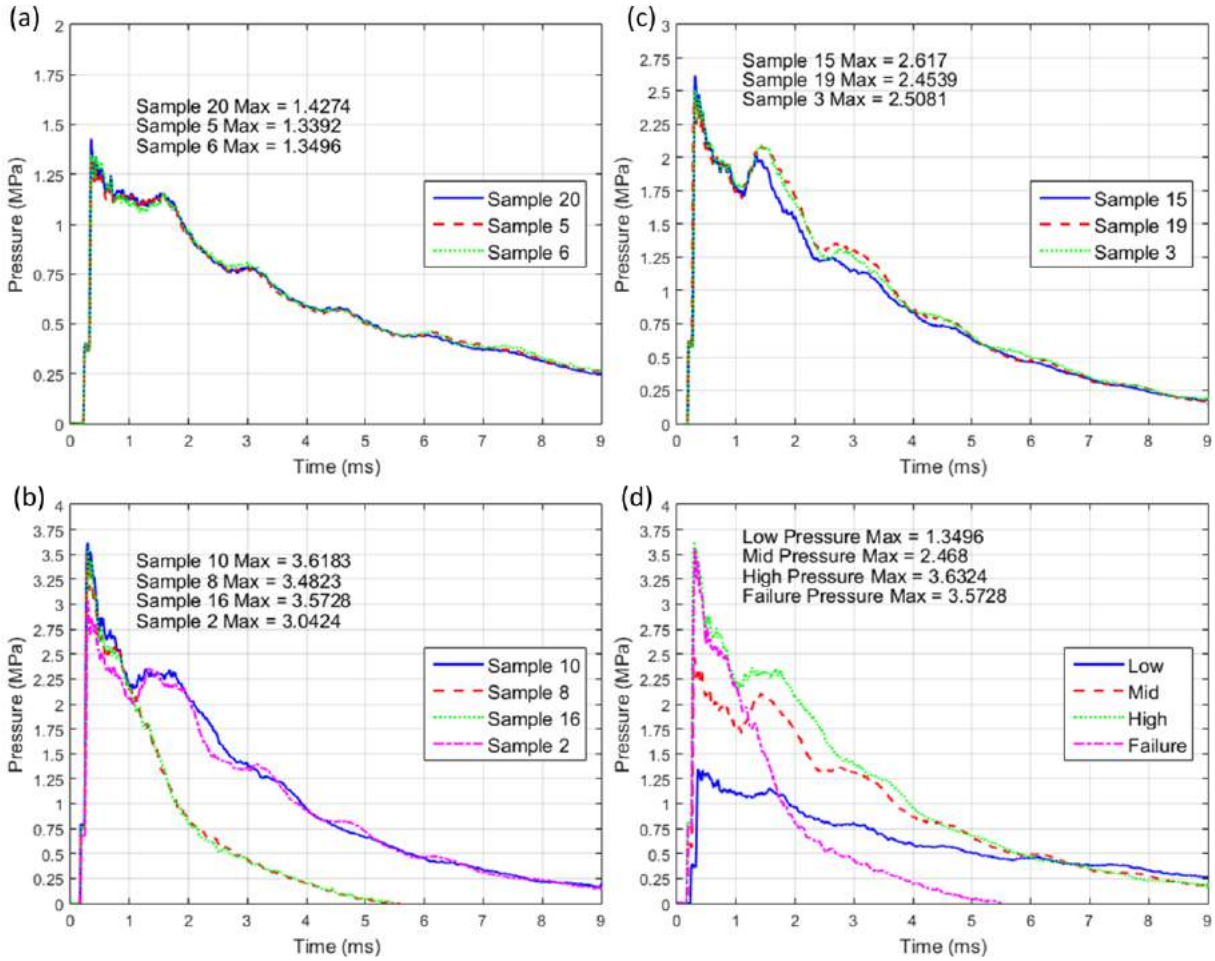

Figure 4.10: Air-blast pressure profiles at sensor 1: (a) minor damage; (b) medium damage; (c) major damage; (d) comparison of pressure profiles

Table 4.3: Air-blast pressure parameters and shock-wave velocities

	Damage Level	Sample	Initial Incident Pressure (MPa)	Resultant Reflected Pressure (MPa)	Reflected / Incident Ratio	Shock-wave Velocity (m/s)	Camera Configuration
Air Blast	Failure	16	0.7765	3.597	4.63	921.7	Digital Image Correlation + Side View
		8	0.7699	3.484	4.53	954.7	
	Major	2	0.6955	3.035	4.36	908.7	
		10	0.8009	3.597	4.49	955.9	
	Medium	3	0.6202	2.501	4.03	851.0	
		19	0.6072	2.473	4.07	889.6	
		15	0.6255	2.613	4.18	859.8	
	Minor	5	0.3973	1.332	3.35	682.7	
		6	0.3973	1.351	3.40	683.2	
		20	0.4038	1.354	3.35	692.9	

4.3.3 High-speed Video and Digital Image Correlation

A high-speed photography system consisting of three cameras (Photron SA1 Photron USA, Inc., CA, USA) was used to capture the air-blast events and dynamic response of the specimens through the clear windows of the fixture enclosure. Two cameras, recording at 28,800 fps, viewed the rear surface of the specimen, where the speckle pattern was applied, and were used to obtain images for DIC using the VIC-3D (Correlated Solutions) system, the results of which are discussed in Chapter 6. To obtain the 3D displacement and deformation information through DIC, the relative position of the cameras was determined during calibration of the system employing a high-contrast grid with known dot sizes and positions. The third camera, also recording at 28,800 fps, was placed perpendicular to the edge of the specimen to acquire side-view images and observe the mechanisms of failure for each specimen. Three 400 W flood lights, one parallel with each camera, were used to illuminate the specimen during the experiment. The arrangement of the high-speed cameras is shown in Figure 4.11.

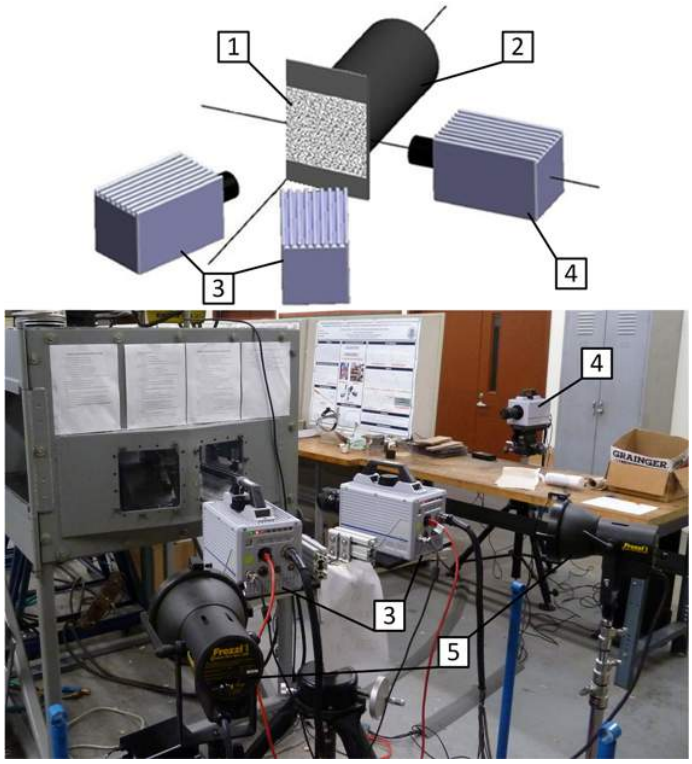

Figure 4.11: Air-blast experimental apparatus and digital image correlation configuration (rear surface view): 1 – specimen; 2 – shock tube; 3 – high-speed cameras (rear view); 4 – high speed cameras (side view); 5 – flood lights.

Once the pressure at the sensor at the end of the stock tube reached a pre-set value, the oscilloscope sent out a trigger pulse to the three cameras, which began recording ensuring synchronised time across the system. The cameras were then synced together so that the recorded frames and resultant DIC could be compared throughout the loading event.

4.4 Chapter Summary

In summary methods for both the ballistic and air-blast experiment case study were described in detail along with their individual experimental parameters and data to be obtained. From the initial results obtained, each loading condition was proven to be repeatable, therefore confirming that from the perspective of the loading conditions, the full results obtained should demonstrate the typical deformation and damage patterns seen for each specimen at the chosen parameters. It should be noted that, in order to obtain the varying levels of damage across all specimens and loading conditions, velocities and energy levels were in fact very different and are not directly comparable. And so it should be made clear that the deformation and damage analysis presented in Chapters 6 and 7, is used to compare the cases against each other with respect to the resultant damage seen and not the energy level of the loading condition.

Studying the effect of these different loading conditions on the same specimen material should allow the comparison of the loading conditions, as all analysis techniques used after the experiments have also consistent. It should be noted that the experimental parameters were chosen to create varying levels of damage, which is the focus of the research analysis and allow for loading conditions to be compared to understand the dynamic response required to achieve similar damage. The new contribution to this field of research is in the form of the direct comparison of impacts with ice projectiles and their effect on deformation and damage with those of the more typical steel projectiles, as well as the comparison to air-blast / shock-wave loading. Chapters 6 and 7 discuss and analyse the deformation events under each dynamic loading condition using digital image correlation and the resultant visible and hidden damage studied with X-ray tomography respectively.

Chapter 5

Deformation Analysis with Digital Image Correlation

With the experimental methodology outlined in Chapter 5, this chapter presents and discusses the analysis of the CFRP specimens that were subjected to both the ballistic impact and air-blast loading conditions. The deformation behaviour was gathered from in-situ high-speed photography of the specimens during the dynamic loading event, and analysed using Digital Image Correlation (DIC).

5.0.1 Observed Behaviour During Each Loading Condition

Following the experimental case studies, some preliminary observation may be made from each loading condition. Examples of the general behaviour during each of the different highest damage loading conditions can been seen in Figures 5.1 - 5.3, it should be noted that these specific images were used to record the impact / blast behaviour of calibration tests and not used for Digital Image Correlation (DIC).

First, the ballistic impact behaviour of the ice (as shown in Figure 5.1), showed that the ice projectile initially indents into the specimen before fragmenting within it causing major wide spread delamination of the first few plies as show from t = 0.381ms onwards. The steel projectile results in major indentation before full penetration, leaving more

localised damage when compared to that of the ice projectiles (as shown if Figure 5.2). The damage caused as a result of the air-blast loading (Figure 5.3) show some similarities with that of a static three-point bending loading case, where global flexural bending of the specimen causes initial tensile failure at the rear surface of the specimen.

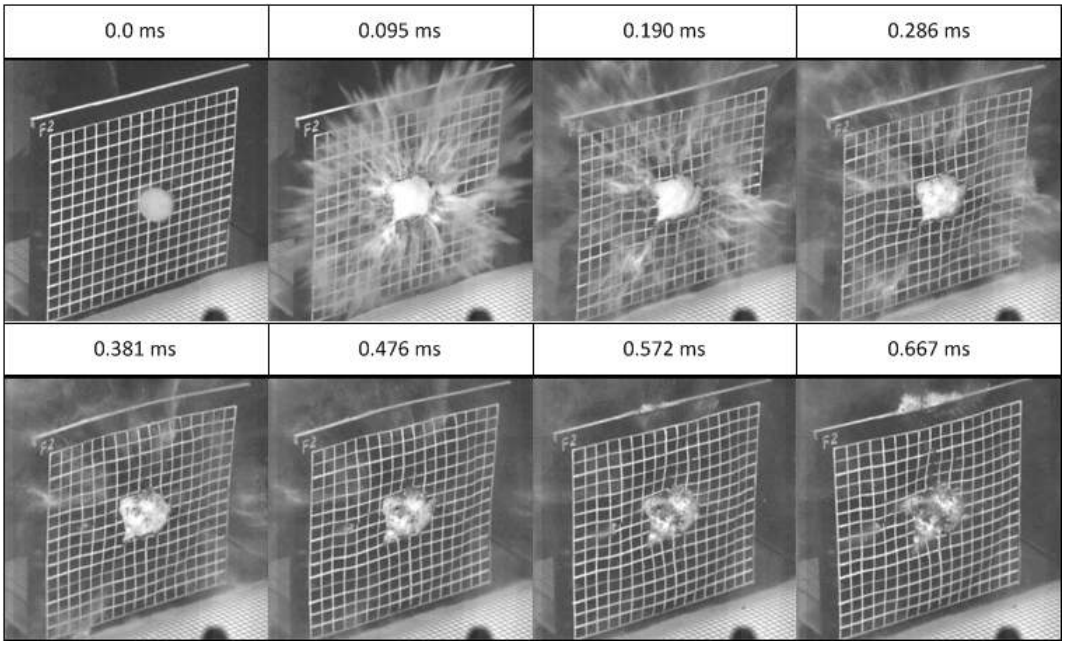

Figure 5.1: Resultant visual behaviour of specimen - ice impact at 480.0 m/s (front view high-speed video)

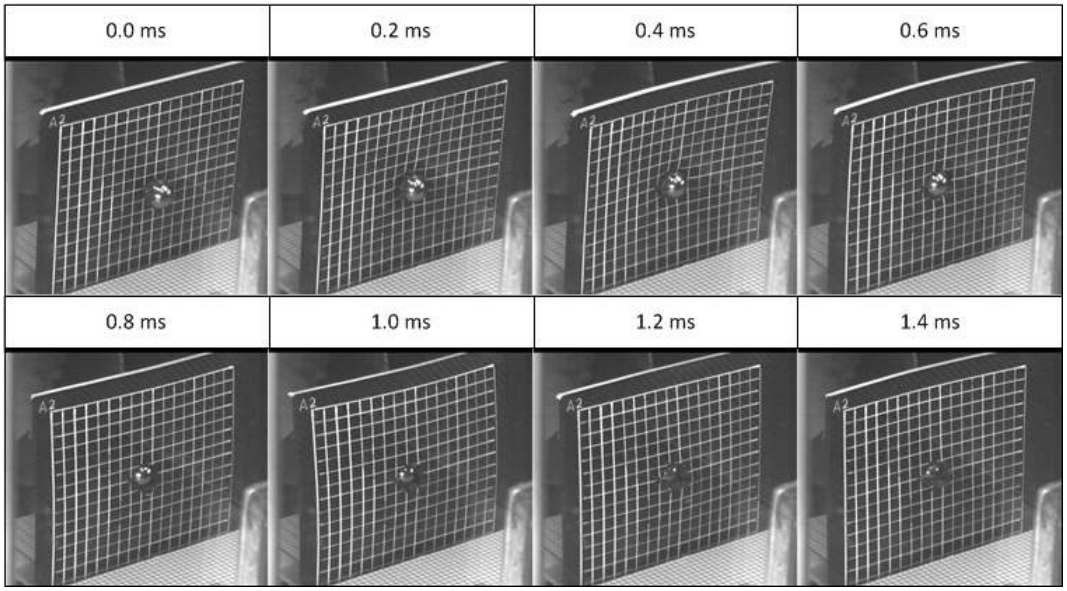

Figure 5.2: Resultant visual behaviour of specimen - steal impact at 91.5 m/s (front view high-speed video)

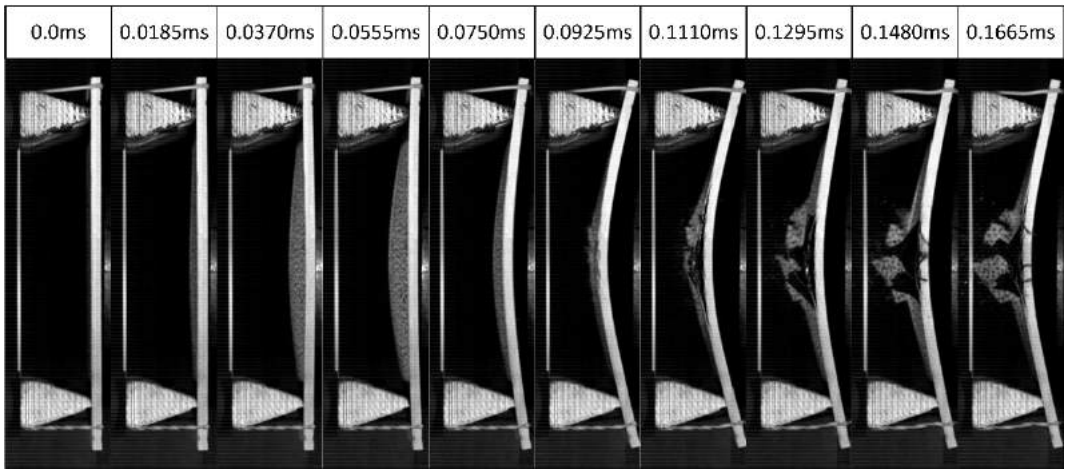

Figure 5.3: Resultant visual behaviour of specimen - air-blast at 0.80 MPa (side view high-speed video)

The initial differences between these all 3 loading conditions can be classified as a localised process zone in the case of the rigid steel projectile, a local to global deformation process for the ice projectile during fragmentation, and finally a global process zone for the case of the air-blast loading.

5.1 Analysis Methodology

As discussed in the previous chapter, a similar experimental setup was used to record the specimen's response to different dynamics loading cases. The recorded high-speed video frames were then used as input for the DIC. This enabled the assessment of the out-of-plane displacement and therefore deformation of the specimens through the ballistic and air-blast loading events.

Even though the loading conditions are different in terms of energy and surface area, the justification behind this analysis is that the resultant damage seen as a result of the loading conditions produces visually the same levels of damage that would have a similar global effect to the structural integrity of the specimen. Here, we define minor damage as minimal front and/or rear surface damage, through to major damage which was defined as significant damage to the front and/or rear surfaces, in some cases full penetration / perforation maybe be observed. This approach provides for a qualitative estimate of damage within each composite specimen.

It should be noted that due to the risk of damage to the experimental equipment

that may have resulted from the highest speed ballistic impacts, no DIC was conducted on the specimens subjected to major damaged for both ice and steel projectiles. A full breakdown of the DIC data collected is presented in Table 5.1.

Table 5.1: The use of DIC during each case study

Case Study	Damage Level	DIC via High Speed Video?
Ballistic Ice Impact	Major	No
	Medium Minor	Yes
Ballistic Steel Impact	Major	No
	Medium Minor	Yes
Air Blast	Failure Major Medium Minor	Yes

In order to analyse the recorded data, vertical and horizontal line slices at the centre of the specimen were extracted for every time increment starting at t = 0, which corresponds to just before the application of the load. Centre point displacement data was also extracted for the air-blast load case specimens given that the rear surface remained mostly intact throughout the loading event. Figure 5.4 shows the location of each line slice with reference to the original fixture locations shown in Chapter 5. Global displacement of each specimen was then represented by these horizontal (AB) and vertical (CD) line sections for each increment in time, with reference to its original starting position.

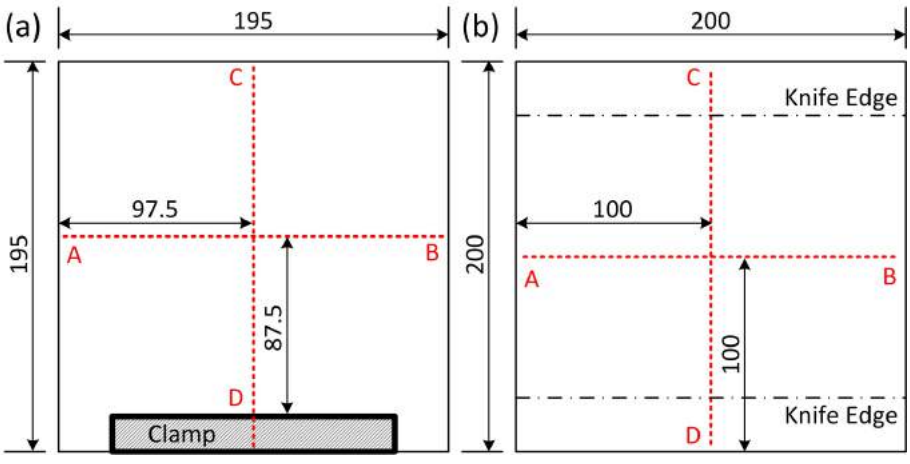

Figure 5.4: Location of horizontal and vertical slices takens from DIC: (a) ballistic impact; (b) air-blast (all dimensions in mm)

The analysis of each specimen's dynamic response caused by the different loading conditions were then broken down into several stage, firstly the horizontal line sections (AB) were analysed as this show the centre of loading to the free edge. The global displacement was then removed from the specimen's response by setting the free edges of each line section to zero displacement, thereby recovering the local deformation with reference to the free edge. This then clearly shows the dynamic response of each specimen, and any oscillation that may be present. The localised behaviour was then normalised against the maximum displacement of each individual specimen, finally the normalised displacements were compared for each time step till maximum displacement. It should be noted that the maximum displacement was reported, in case of damage the closest available point along the horizontal line slice was chosen.

5.2 Global to Localised Deformation

This section of the chapter covers the analysis of the global displacement seen in each specimen, and how the localised deformation then deduced from this. First the results have been discussed for the ballistic case study, followed by the air-blast case study.

5.2.1 Ballistic Ice and Solid (steel) Projectile Impacts

First the out-of-plane dynamic response of the specimens at the horizontal (AB) and vertical (CD) locations were analysed. Figures 5.5 and 5.6, then Figures 5.7 and 5.8 show the steel then ice, minor then medium out-of-plane displacement plots respectively. For each figure plot (a) demonstrates the global displacement over 5 ms capturing the first full oscillation of the plate, then plot (b) shows the first 0.5 ms of displacement during the initial stages of the impact. Each plot then has the right half of the horizontal line section displacements localised to only the specimen's deformation moving the free edges of the line sections to zero displacement. All additional plots can be found in Appendix A for all other repeated tests.

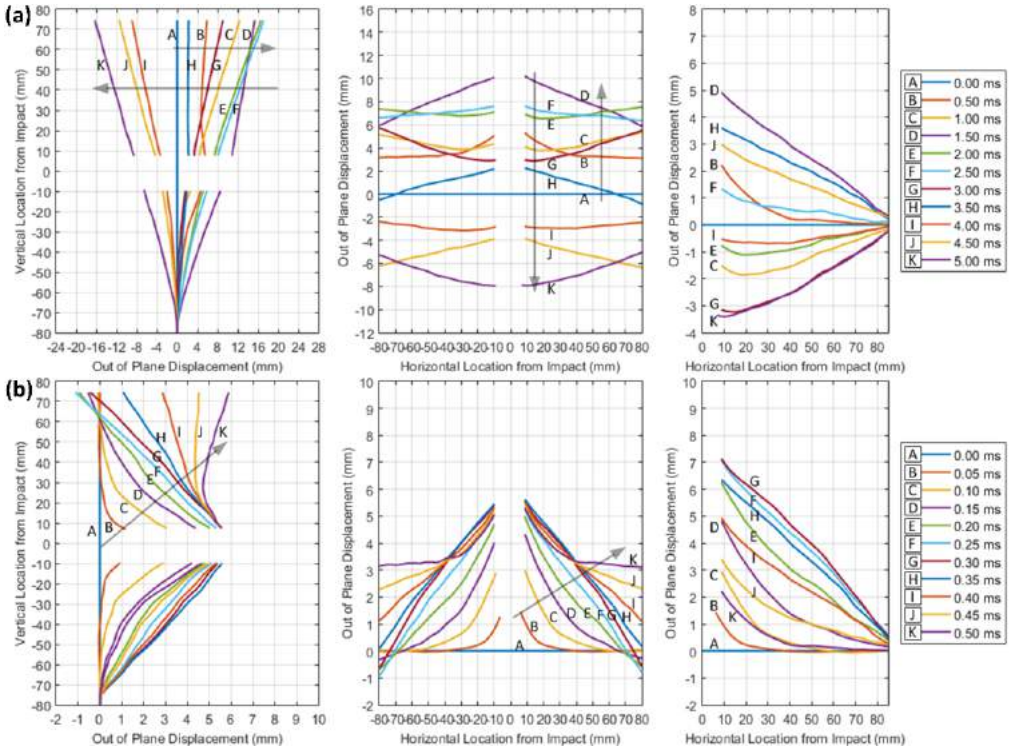

Figure 5.5: Displacement - steel impact low velocity at 59.5 m/s: (a) 0-5ms; (b) 0-0.5ms (sample B2)

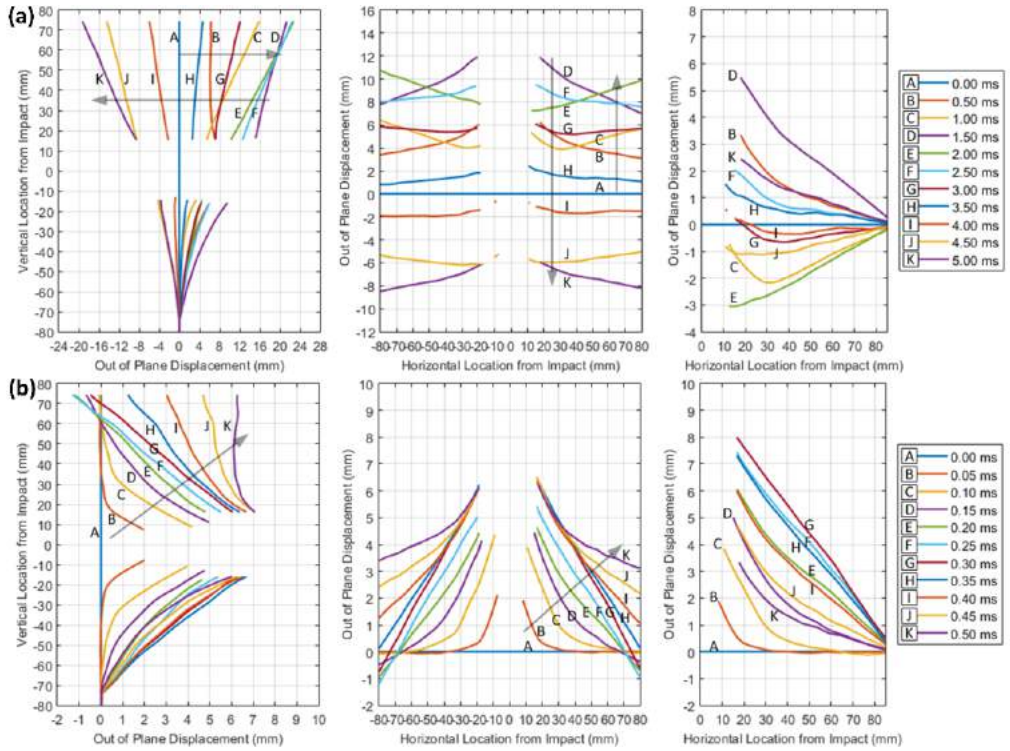

Figure 5.6: Displacement - steel impact mid velocity at 78.5 m/s: (a) 0-5ms; (b) 0-0.5ms (sample C3)

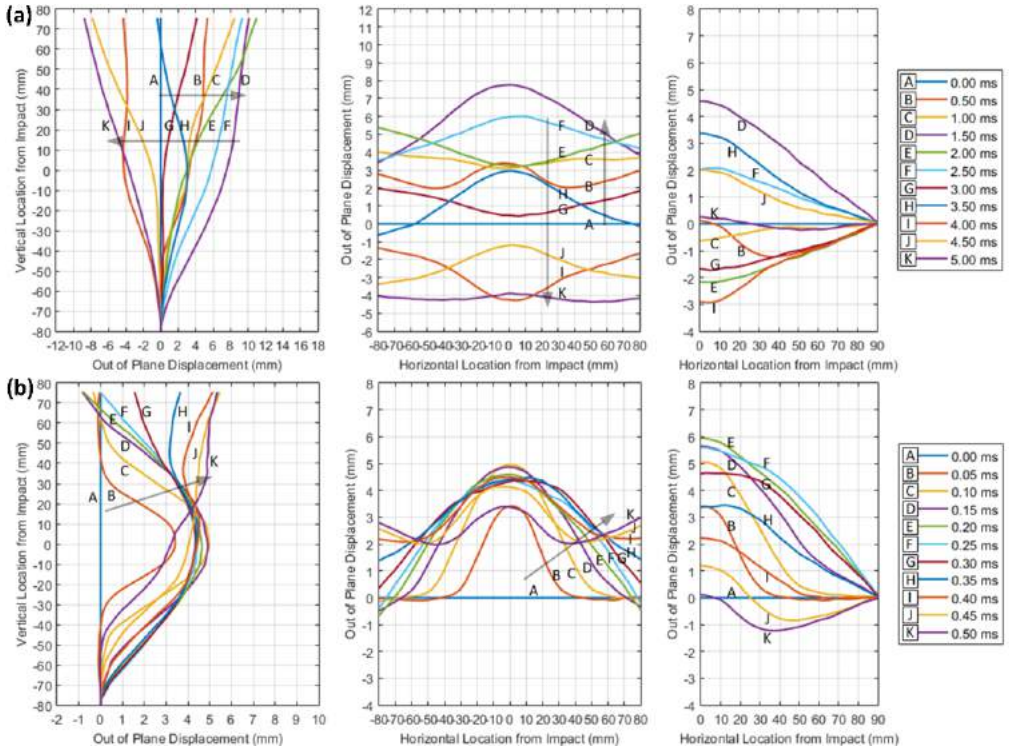

Figure 5.7: Displacement - ice impact low velocity at 304.0 m/s: (a) 0-5ms; (b) 0-0.5ms (sample B1)

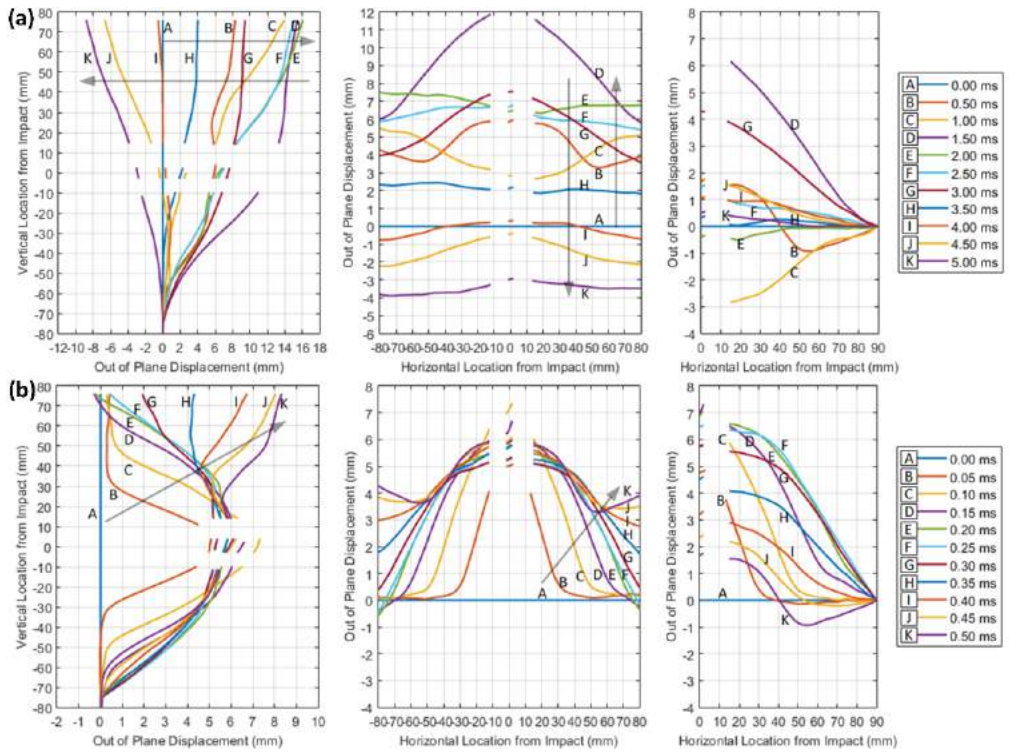

Figure 5.8: Displacement - ice impact mid velocity at 403.0 m/s: (a) 0-5ms; (b) 0-0.5ms (sample D1)

From the observed deformation, it was clear that due to the more rigid nature of the steel projectile when compared to fragmenting ice, the line plots (Figures 5.5 - 5.8) demonstrate more indentation deformation of the specimens before the transition into global flexural bending as supported by the loading area ratio of 0.143 as calculated in the previous chapter. When analysing the deformation caused by the ice projectiles this initial indentation was still present, however upon fragmentation of the projectile the local indentation transitions to a distributed loading state leading to global flexural bending. For the fragmenting (ice) projectiles we observe that with an increase in energy (and therefore velocity), the composite specimens demonstrate greater modes of bending once the deformation transition to global flexural bending mode.

Comparing the two different impact regimes of the ice and steel projectiles for similar levels of damage, it can be seen that the out-of-plane displacements for the minor and medium damage were similar but the deformation and shape of the specimens during the loading were different. For the rigid (steel) projectile impact the specimen's deflection mode was local indentation leading to damage at the rear surface (no correlation with gap in data, speckle pattern damaged), then transitions to simple mode 1 global flexural bending of the specimens horizontally and cantilever bending vertically.

However, the ice projectiles fragment on impact resulting in any local indentation of the specimen to become more widespread, transitioning to distributed loading with reduced failure at the rear surface (still correlation with no gap in data, speckle pattern undamaged) and more complex modes of bending as time progresses. Aside from the obvious central deformation of the specimens, observations can be made about the general curvature of the specimens around the impact location. For rigid (steel) impacts (Figures 5.5 and 5.6) the curvature was minimal with transitions between concave and convex curvature happening gradually, whereas for the ice projectile (Figures 5.7 and 5.8) the transition in curvature was more rapid and include multiple modes as discussed previously.

5.2.2 Air-blast

In the case of the air-blast loading, the rear surface of the specimens mostly remained intact at the centre and so the centre point displacement can be analysed comprehensively. Figure 5.9 shows the centre point displacement plots for all of the specimens, starting with (a) minor, (b) medium, (c) major damage cases with (d) containing a comparison

between the reference specimens to be analysed. It can be seen from these plots that the lower pressure air-blast test cases shows excellent repeatability in terms of displacement magnitude and oscillation frequency, with the higher pressure blasts showing some variability.

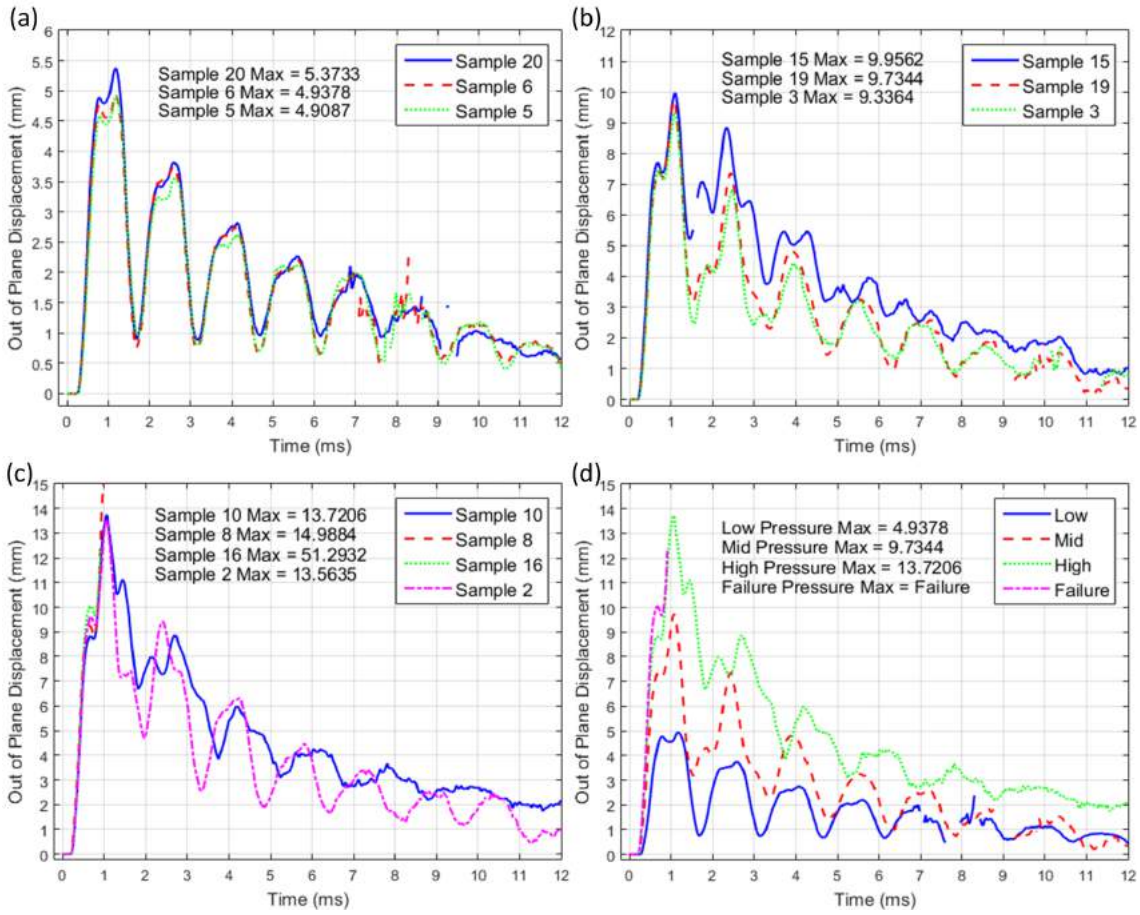

Figure 5.9: Displacement - air-blast centre point comparisons at (a) 0.4 MPa, (b) 0.6 MPa, (c) 0.8 MPa and (d) Comparison of Reference Specimens

All specimens show an initial oscillation achieving maximum displacement, followed by damped oscillations. Upon visual inspection of the specimen post experiment, the minor damage due to loading condition results in no visual damage whereas the medium and major cases result in clear rear surface failure and signs of delamination (see Chapter 7). For the experimental case sustaining minor damage (Figure 5.9a) we observe with each oscillation consists of double peaks, where as it can be seen for the case with greater damage triple peaks as well as double peaks occurs (Figure 5.9b). The double peaks were due to the oscillation of the specimens from the central displacement laterally to the free edges and back again, leading to a mode 1 bending across the specimen at its maximum

out-of-plane displacement. It was thought that the resultant damage and delamination seen causes the triple peaks in a similar manner to the double peaks, but the damaged and delaminated rear plies were free to move and displace further as a result of a reduced local stiffness. Notice that for the median damage case the first triple peak occurs during the second oscillation, whereas for the major damage cases this occurs immediately during the first oscillation suggesting that in the medium damage case the damage was progressively degrading the specimen. After the appearance of these triple peaks thought to be caused by delamination, both the amplitude and frequency of the following oscillations changes due to the expected reduction in specimen stiffness. This was also supported in the minor damage case where no visible damage or delamination that would affect the stiffness can be seen (including no triple peaks in the centre point displacement plots), and so the amplitude and frequency remains consistent throughout. The changes in the oscillation period before and after the appearance of delamination is shown in Table 5.2, proving that the reduced stiffness resulting from the damage does affect the specimen's response by a 25% increase in the oscillation period where it can be measured before and after damage.

Table 5.2: Air-blast oscillation frequency before and after Damage

	Damage Level	Sample	Period Before Damage (ms)	Period After Damage (ms)	Percentage Change
Air Blast	Failure	16	-	-	-
	Major	10	-	1.63	-
	Medium	19	1.32	1.77	25%
	Minor	6	1.42	-	0%

Plots of both the horizontal (AB) and vertical (CD) out-of-plane displacement line sections shows the deformation resulting from the different air-blasts appears to be similar, Figures 5.10 to 5.13 show the minor through to failure damage out-of-plane displacement plots respectively. For each figure plot (a) demonstrates the global displacement over 2.10 ms capturing a full oscillation of the plate (expect for the failure case which covers 0.73 ms), then plot (b) shows only the first 0.35 ms to show the displacement during the initial stages of the air-blast more clearly.

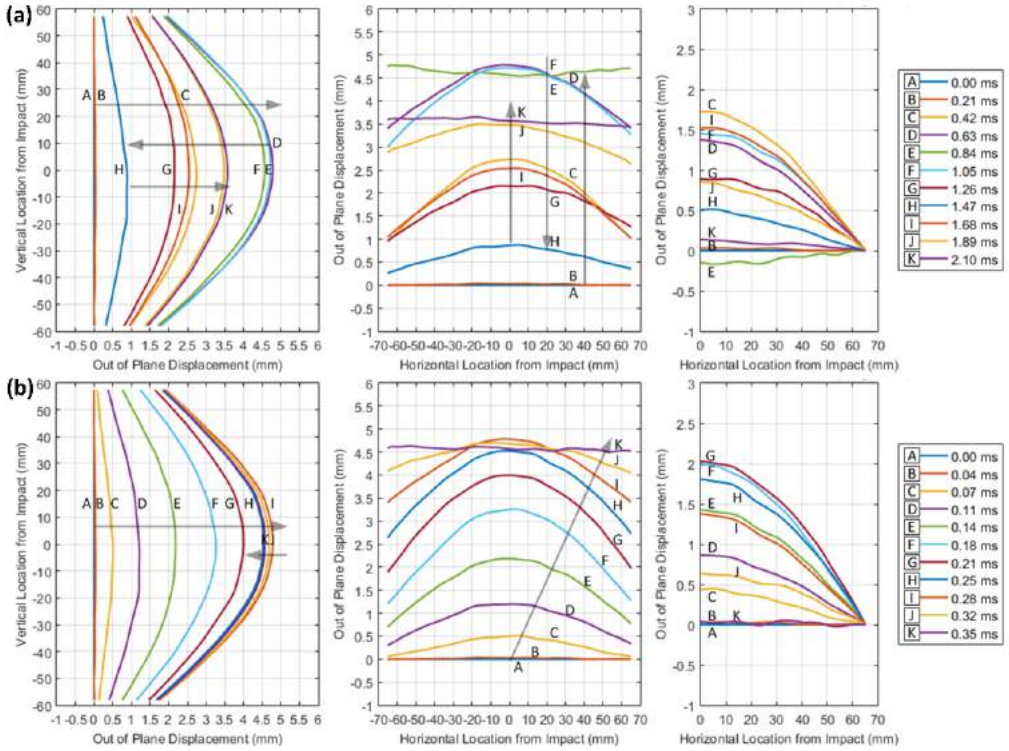

Figure 5.10: Displacement - air-blast at 0.40 MPa (low), (a) 0-2.10ms and (b) 0-0.35ms (sample 6)

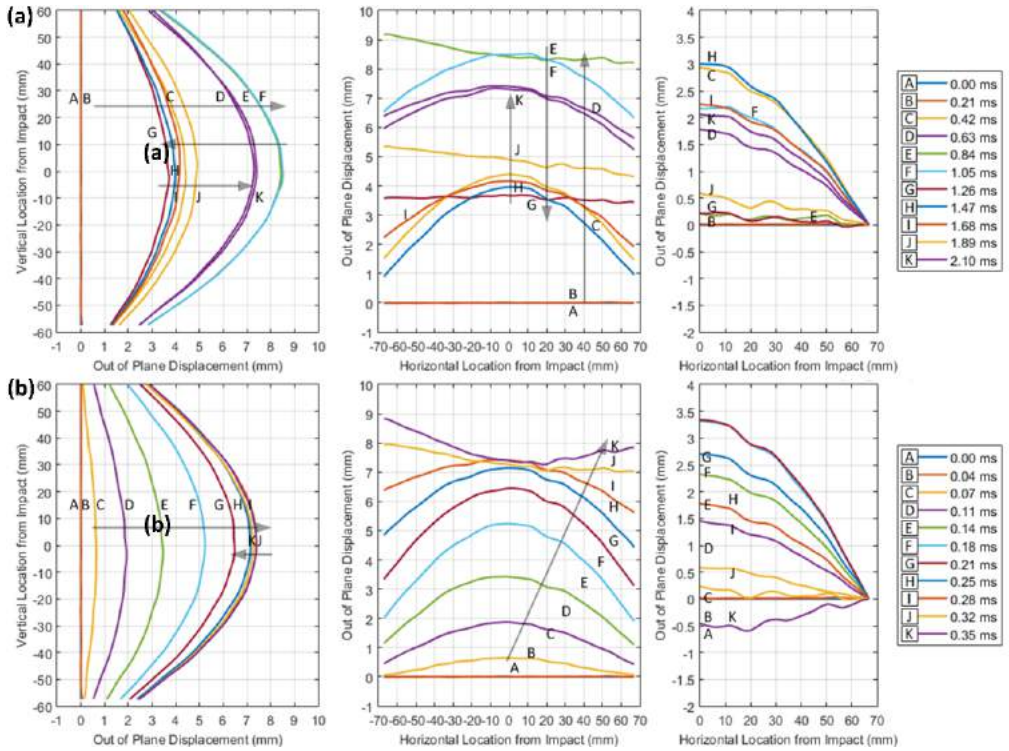

Figure 5.11: Displacement - air-blast at 0.62 MPa (mid), (a) 0-2.10ms and (b) 0-0.35ms (sample 19)

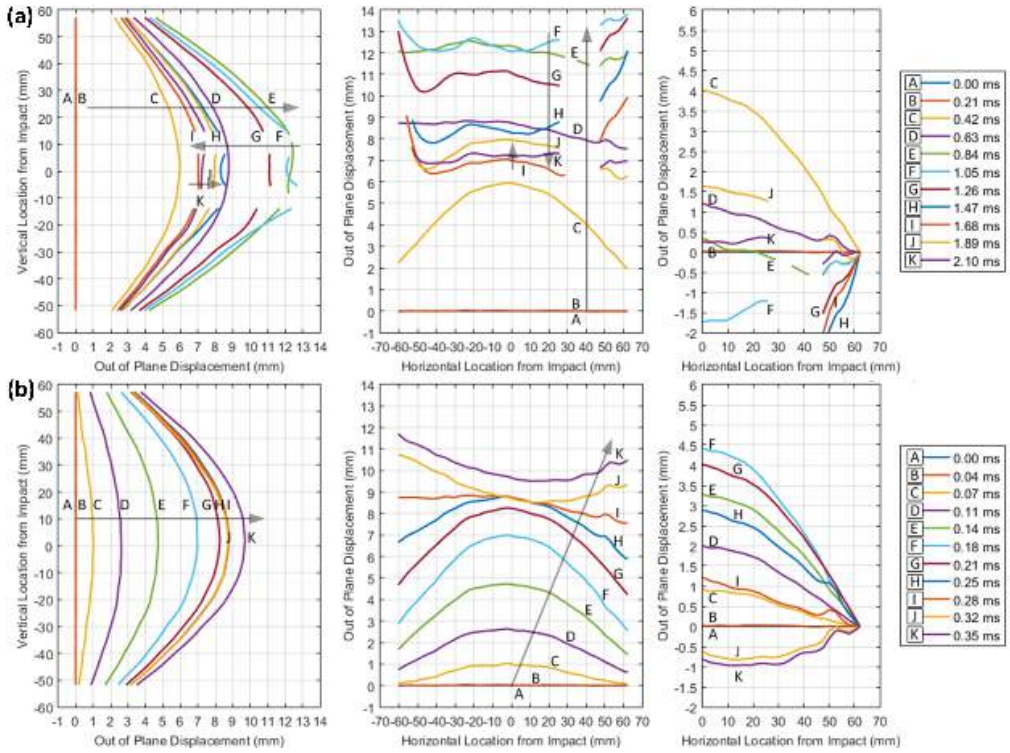

Figure 5.12: Displacement - air-blast at 0.80 MPa (high), (a) 0-2.10ms and (b) 0-0.35ms (sample 10)

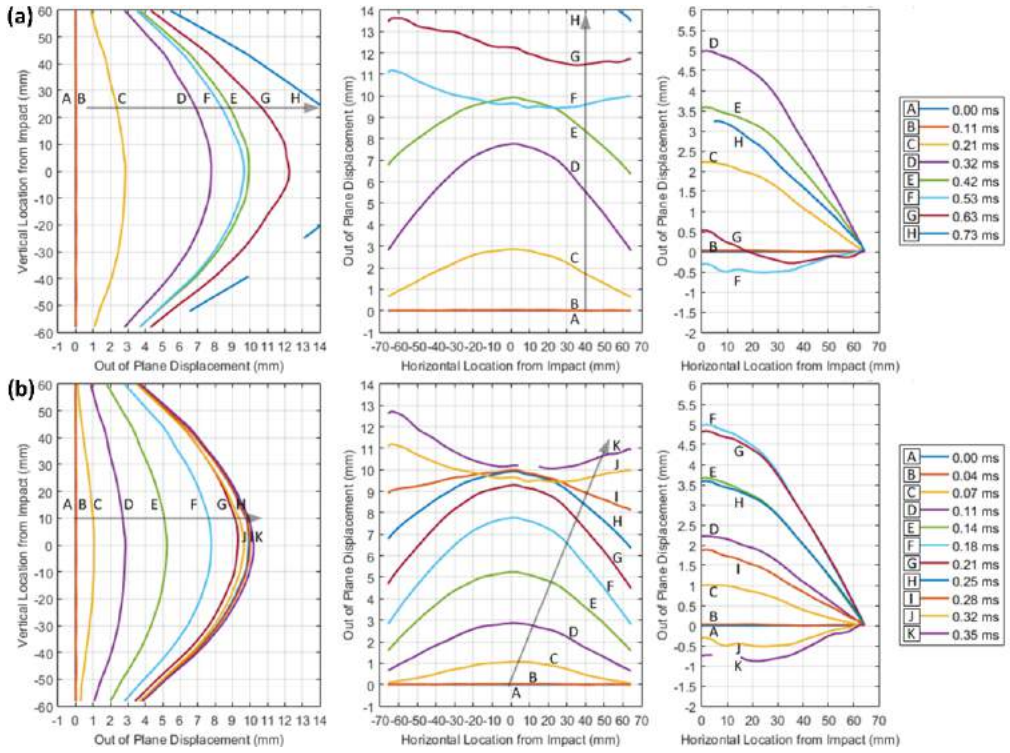

Figure 5.13: Displacement - air-blast at 0.78 MPa (failure), (a) 0-0.73ms and (b) 0-0.35ms (sample 16)

Each plot then has the right half of the horizontal line section displacements (AB), which can be seen to be symmetrical, localised to only the specimen's deformation by moving the free edges of the line sections to zero displacement. Initial observations support the typical deformation seen with this type of specimen fixture, demonstrating a spherically distributed loading area that propagates into an elliptical shape as the free edges deform away from the shock tube muzzle. All additional plots can be found in Appendix A for all other repeated specimens.

At this stage, analysing each of the plots for the varying damage levels yields no obvious differences except from increasing out-of-plane displacement as expected, but it was clear that each specimen was subjected to distributed loading leading to early global flexural bending, therefore avoiding any obvious localised indentation at the start which was supported by the loading area ratio of 0.5. One major difference seen from the specimen which failed under the high pressure blast (0.8 MPa incident) (Figure 5.13), shows higher displacement values before the DIC failed to track the speckle pattern due to specimen failure. For each of the damage case which remained intact, the localised deformation behaviour also appears to be similar in terms of the general concave curvature of the specimens during loading, and the modes of global flexural bending were shown to gradually transition between concave and convex curvature due to the changes in the distributed loading area. The only real exception to this was for the major damage case which demonstrates greater deformation at the free edges as shown in Figure 5.12, which may be due to the increased bending stress and resultant tensile failure and delamination of the first few plies. Although this was more obvious for the major damage case, the progression of deformation at the free edge can be seen at each damage level before resulting in a clear failure at the major and failure cases (to be discussed further in Chapter 7). For both the major and failure damage loading cases, any failure or damage of the speckle pattern seen at the rear surface is shown as gaps in data.

5.2.3 Initial Summary of Observations

Following this initial analysis of the global displacement and localised deformation behaviour, we observe distinct differences for ballistic loaded specimens whereas for the air-blast specimen's the differences were minimal and further analysis was required. The ballistic impact cases caused localised indentation and greater localised damage, while the

air-blast cases cause global flexural bending. Between these two extremes is the ballistic ice impact case, which starts out as a localised indentation loading regime but upon fragmentation transitions to a wider distributed loading (showing similarities to the air-blast loading). In the next section, the analysis of the normalised data and out-of-plane displacement plots was performed so that more accurate comparisons can be drawn before making any final conclusions.

5.3 Analysis of Normalised Deformation Responses

Here, we analyse the normalised deformation seen in each specimen under different loading conditions. As before, first the results were discussed for the ballistic case study, followed by the air-blast case study. Studying the normalised deformation behaviours against both maximum displacement and the time at maximum displacement of each specimen for all available time increments, this has allowed for comparison to be made across all of the loading conditions and comparative analysis.

5.3.1 Ballistic Ice and Rigid (steel) Projectile Impacts

For the ballistic impact loading condition, Figures 5.14 and 5.15 demonstrate the response for the steel projectile and Figures 5.16 and 5.17 at low and medium velocities resulting in minor to medium damage respectively. In each figure plots (a) contain the original out-of-plane deformation (localised - free edge set to zero) with only normalised time, then plots (b) contain the normalised out-of-plane deformation.

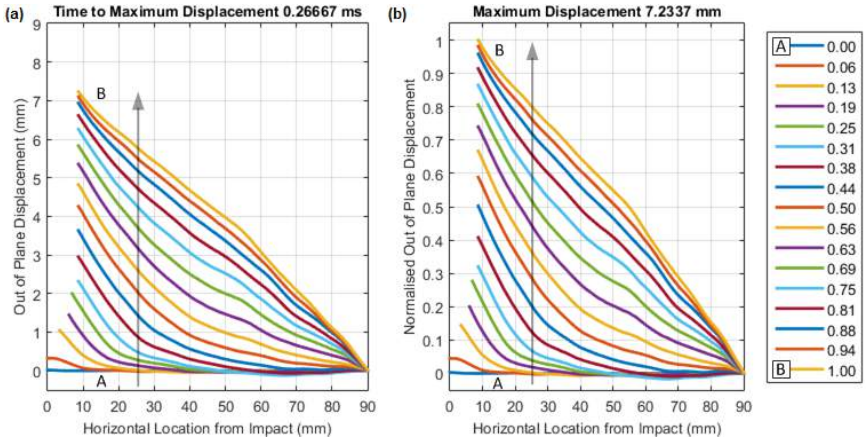

Figure 5.14: Steel low velocity at 59.5 m/s - normalised: (a) time; (b) displacement (sample B2)

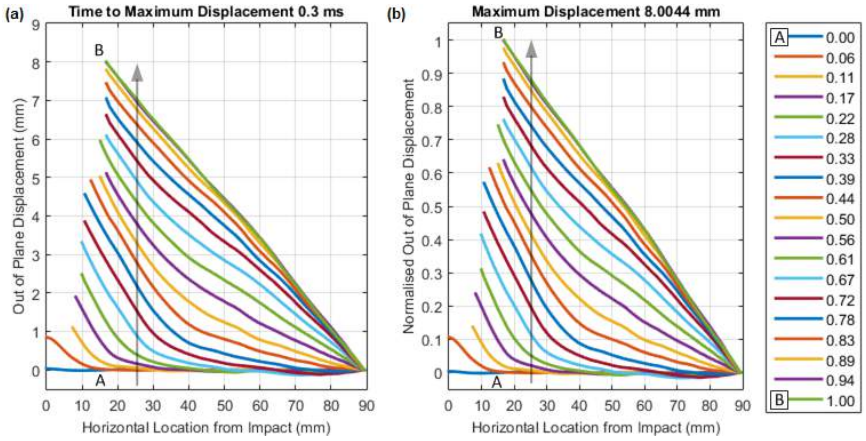

Figure 5.15: Steel mid velocity at 78.5 m/s - normalised: (a) time; (b) displacement (sample C3)

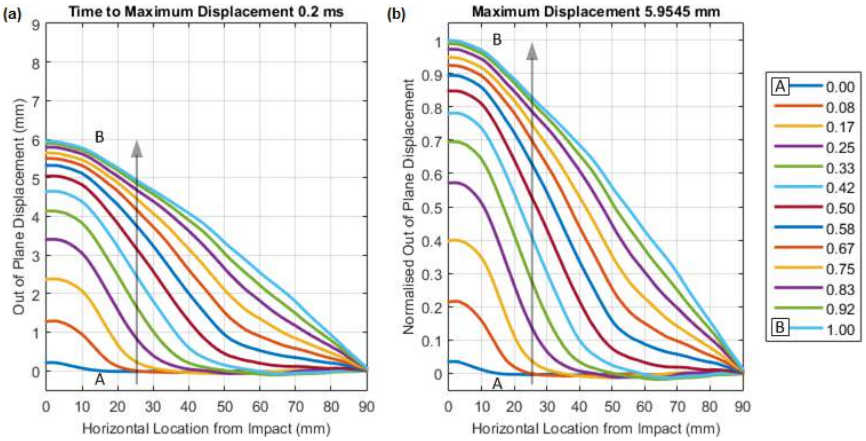

Figure 5.16: Ice low velocity at 304.0 m/s - normalised: (a) time; (b) displacement (sample B1)

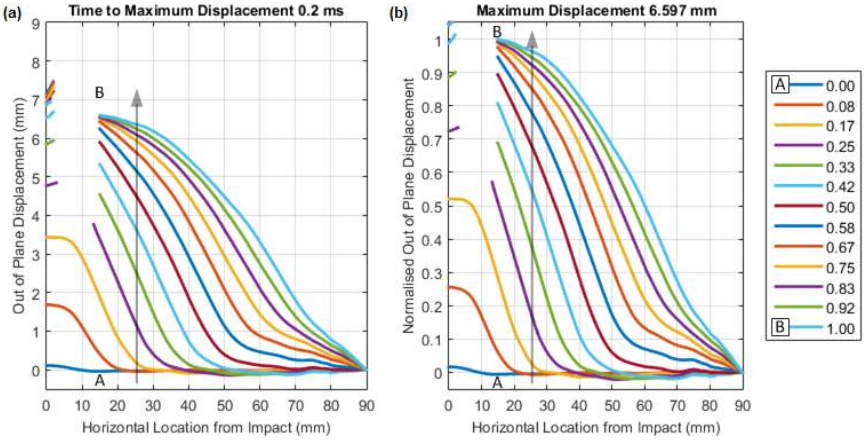

Figure 5.17: Ice mid velocity at 403.0 m/s - normalised: (a) time; (b) displacement (sample D1)

Damage at the rear surface of the specimens (enough to affect the speckle pattern and DIC) occurs much sooner when the projectile was rigid (steel) than that of the ice projectile, this was likely due to the almost instantaneous fragmentation of the ice projectile on impact causing more widely distributed loading and therefore a longer impact duration even at higher impact energies. The increased impact duration together with the physical destruction of the ice projectile has helped with the transfer and dissipation of kinetic energy within the specimens, which results in differences in the specimens out-of-plane displacement and the appearance of damage at the rear surface.

When studying the maximum out-of-plane displacement observed from each specimen it was clear that an increase in projectile velocity (energy), leads to greater deformation of the specimens for both projectiles. Although the trend was not as clear due to the limit of time resolution (directly linked to frame rate of camera) the same can be said about the time taken until maximum displacement, with the increased velocities (energies) resulting in a reduced time till max displacement. A full breakdown of the maximum out-of-plane displacements and times can be seen in Table 5.3.

Table 5.3: Ballistic steel and ice maximum and normalised out-of-plane displacement

	Damage Level	Sample	Max Out of Plane Displacement (mm)	Time till Max Displacement (ms)
Steel	Major	D4	-	-
		E3	-	-
		E5	-	-
	Medium	C3	8.0044	0.3000
		E3	8.8848	0.2667
		E5	7.5900	0.3000
	Minor	B2	7.2337	0.2667
		B4	7.3570	0.2667
		B5	7.2650	0.2667
Ice	Major	E1	-	-
		E2	-	-
		E4	-	-
	Medium	C2	6.6298	0.1833
		D1	6.5970	0.2000
		D3	6.4210	0.1500
	Minor	A4	5.3490	0.2167
		B1	5.9545	0.2000
		B3	5.8823	0.2000

As discussed previously the effect of the loading resulting from the rigid (steel) or fragmenting (ice) projectiles does lead to a difference in the response of the specimens, a simplified form of this is shown in Figure 5.18. This figure shows a comparison of the normalised out-of-plane behaviour of the reference specimens at 0.25, 0.50, 0.75 and 1.00 normalised time, taken from the figure shown previously. Each specimen undergoes a level of localised indentation before entering a transitional state, before finally reaching a global flexural bending at its maximum out-of-plane displacement at t = 1.0.

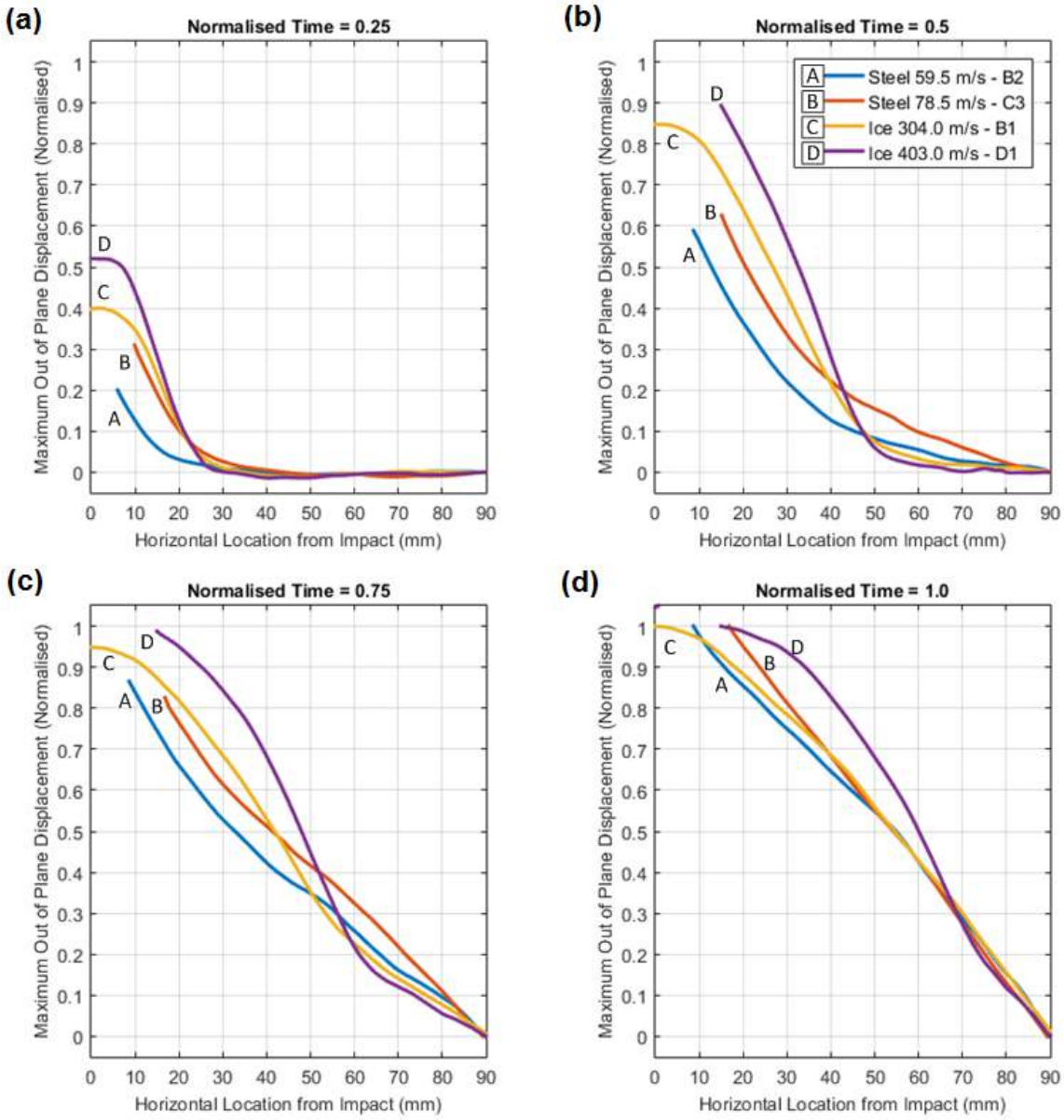

Figure 5.18: Comparison of ballistic impacts at (a) 0.25, (b) 0.50, (c) 0.75 and (d) 1.00 normalised time.

Comparing each of the specimens responses directly at the given normalised times demonstrates that impacts with the same projectile materials show similar responses as expected, but the comparison between the two different projectile materials yield different results as expected. Firstly, as mentioned previously, the indentation stage was shown at t = 0.25 to be more localised for that of the rigid projectile, even at significantly lower impact energies proving the fragmentation leads to more widely distributed loading even at high energy levels. After indentation the specimens enter a transitional stage of behaviour, where again, the two different projectile materials show different responses. Due to the damage appearing at the rear surface the rigid (steel) projectiles cause a convex deformation profile throughout the transitional stage, whereas the fragmenting (ice) projectiles causes a more prominent concave deformation profile towards the centre before a sudden change to a convex profile.

By considering each available time increment, these stages of deformation can be defined for each projectile type and velocity in order to begin to understand typical impact behaviour. Figure 5.19 aims to define these stages of deformation, where stage 1 through to 3 were defined as local indentation, transitional (when the whole surface has left its initial zero displacement position) and global flexural bending respectively.

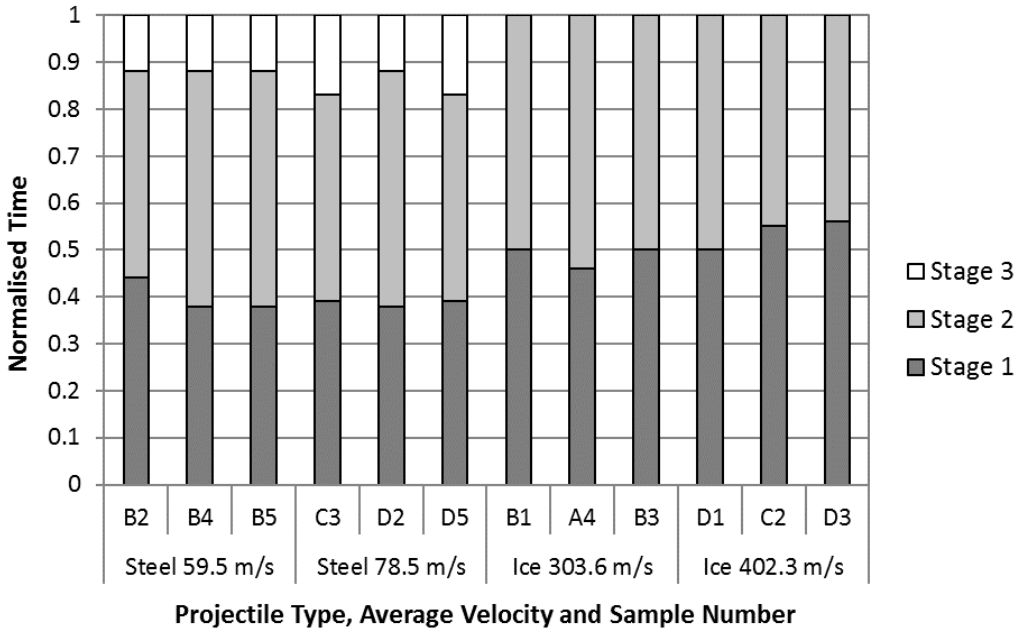

Figure 5.19: Comparison of projectile types and velocities against the normalised stages of deformation

As can be seen from Figure 5.19 it is clear that for the rigid (steel) projectiles the global flexural bending (stage 3) was clearly present when approaching t = 1.0, but for the fragmenting (ice) projectiles there was no clearly distinguishable stage 3 for most cases until t = 1.0. This could be the result of two factors, either the higher impact energy leading to an increased period of indentation (increased stage 1) or the fragmentation and interact of the projectile lead to a more complex state of transition (stage 2). The resulting specimen behaviour for both the rigid (steel) and fragmenting (ice) projectiles does show that each of the impacts can be generalised to the 3 stages of deformation, Table 5.4 contains the final averaged proportions for each stage with respect to normalised time.

Table 5.4: Impact stages of deformation with respect to normalised time

	Projectile	
	Steel	Ice
Stage 1	0.39	0.51
Stage 2	0.47	0.49
Stage 3	0.14	0

From this table we conclude that the indentation stage for the fragmenting (ice) projectiles was marginally longer than that of the rigid (steel) projectile, which is a result of the higher impact energy of the ice projectiles. The transitional stage then appears to be almost identical for both cases, with any variation or increase when considering the fragmenting projectile resulting from the more complex interaction of the distributed loading. Finally, with the rigid projectiles causing greater localised deformation, the specimens reach global flexural bending (stage 3) sooner than that of the fragmenting projectiles.

5.3.2 Air-blast

For the air-blast case study, unlike the ballistic impacts, the difference between the specimen's dynamic responses at each loading condition was somewhat less obvious. Figures 5.20 to 5.23 show each reference specimen's response from minor through to failure damage respectively. As before within each figure plots (a) contain the original out-of-plane deformation (localised - free edge set to zero) with only normalised time, and plots (b) contain the normalised out-of-plane deformation.

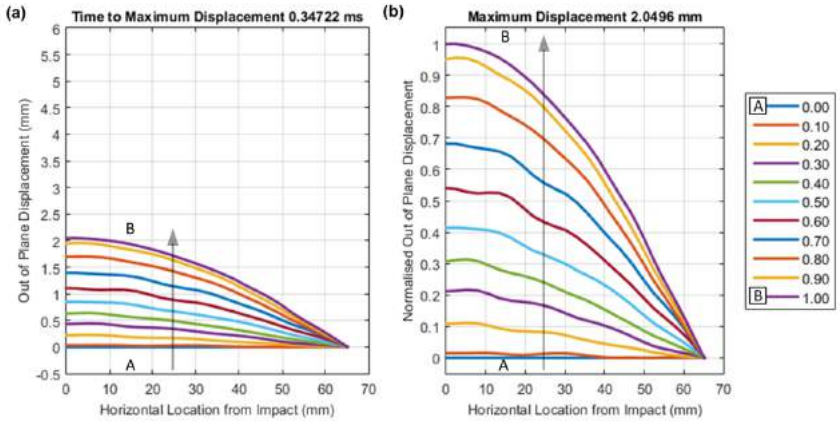

Figure 5.20: Air-blast low pressure – 0.40 MPa - normalised: (a) time; (b) displacement (sample 6)

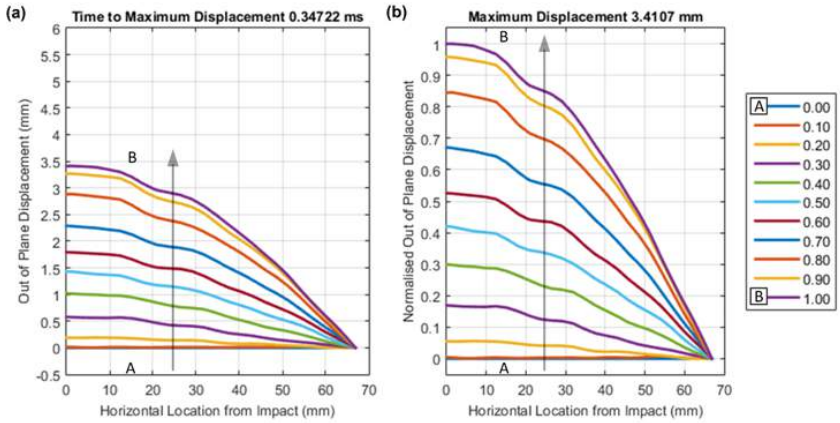

Figure 5.21: Air-blast mid pressure – 0.62 MPa - normalised: (a) time; (b) displacement (sample 19)

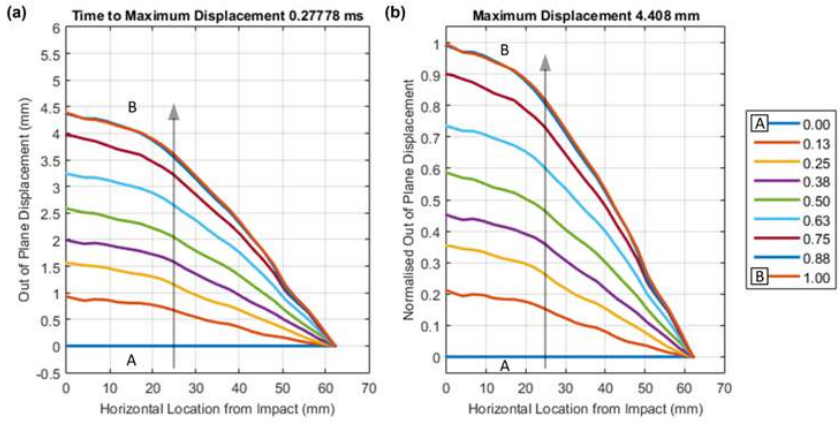

Figure 5.22: Air-blast high pressure – 0.80 MPa - normalised: (a) time; (b) displacement (sample 10)

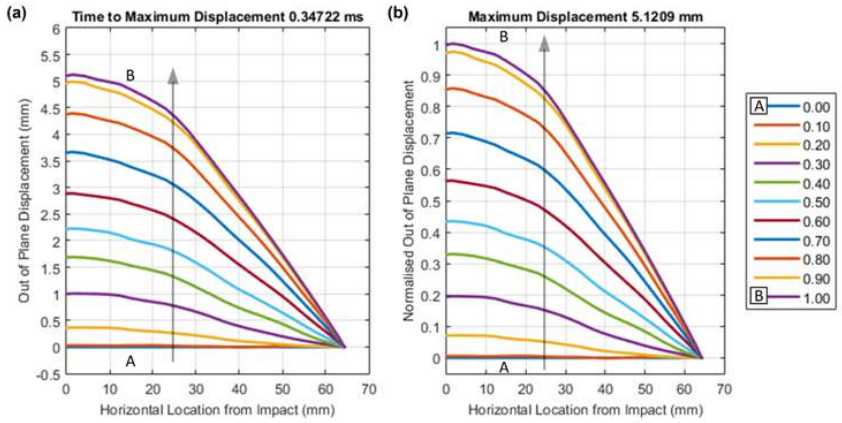

Figure 5.23: Air-blast failure pressure – 0.78 MPa - normalised: (a) time; (b) displacement (sample 16)

We observe that for the first oscillation of the specimens localised behaviour, there was no visible damage at the rear surface of the specimens (i.e. the speckle pattern was unaffected and DIC can be performed). Unlike the ballistic impact cases, the dynamic response of each specimen due to the varying air-blast loading was very similar in specimen curvature and shape, demonstrating minimal to no signs of initial indentation or any transitional stages of deformation. As a result, the only difference expected was an increasing maximum out-of-plane displacement with increasing air-blast incident pressure, along with a decrease in the time taken until maximum displacement. A full breakdown of the maximum out-of-plane displacements and times can be seen in Table 5.5, the observed decreasing trend in time till max out-of-plane displacement was not as clear due to the limit of time resolution (directly linked to frame rate of camera).

Table 5.5: Air-blast maximum and normalised out-of-plane displacement

	Damage Level	Sample	Max Out of Plane Displacement (mm)	Time till Max Displacement (ms)
Air Blast	Failure	16	5.1209	0.3472
		8	4.7031	0.3125
	Major	2	4.6574	0.3472
		10	4.3730	0.3472
	Medium	3	3.3604	0.3472
		19	3.4107	0.3472
		15	3.7350	0.3472
	Minor	5	1.9913	0.3819
		6	2.0496	0.3472
		20	2.2588	0.3472

To compare the dynamic responses of each specimen subjected to the varying loading conditions, the horizontal line slices can be compared at given internals and a simplified form of this is shown in Figure 5.24. This figure shows a comparison of the normalised out-of-plane behaviour of the reference specimens at 0.25, 0.50, 0.75 and 1.00 normalised time, taken from the figures shown previously. First we notice an almost identical normalised specimen behaviour at each increment of normalised time, proving that the incident air-blast pressure magnitude has no effect on the specimen's response up until maximum displacement for similar boundary conditions. Some level of localised indentation can be witnessed at very early stages ($t \leqslant 0.25$), before all specimens enter full global flexural bending ($t \geqslant 0.25$) up until maximum out-of-plane displacement at $t = 1.0$.

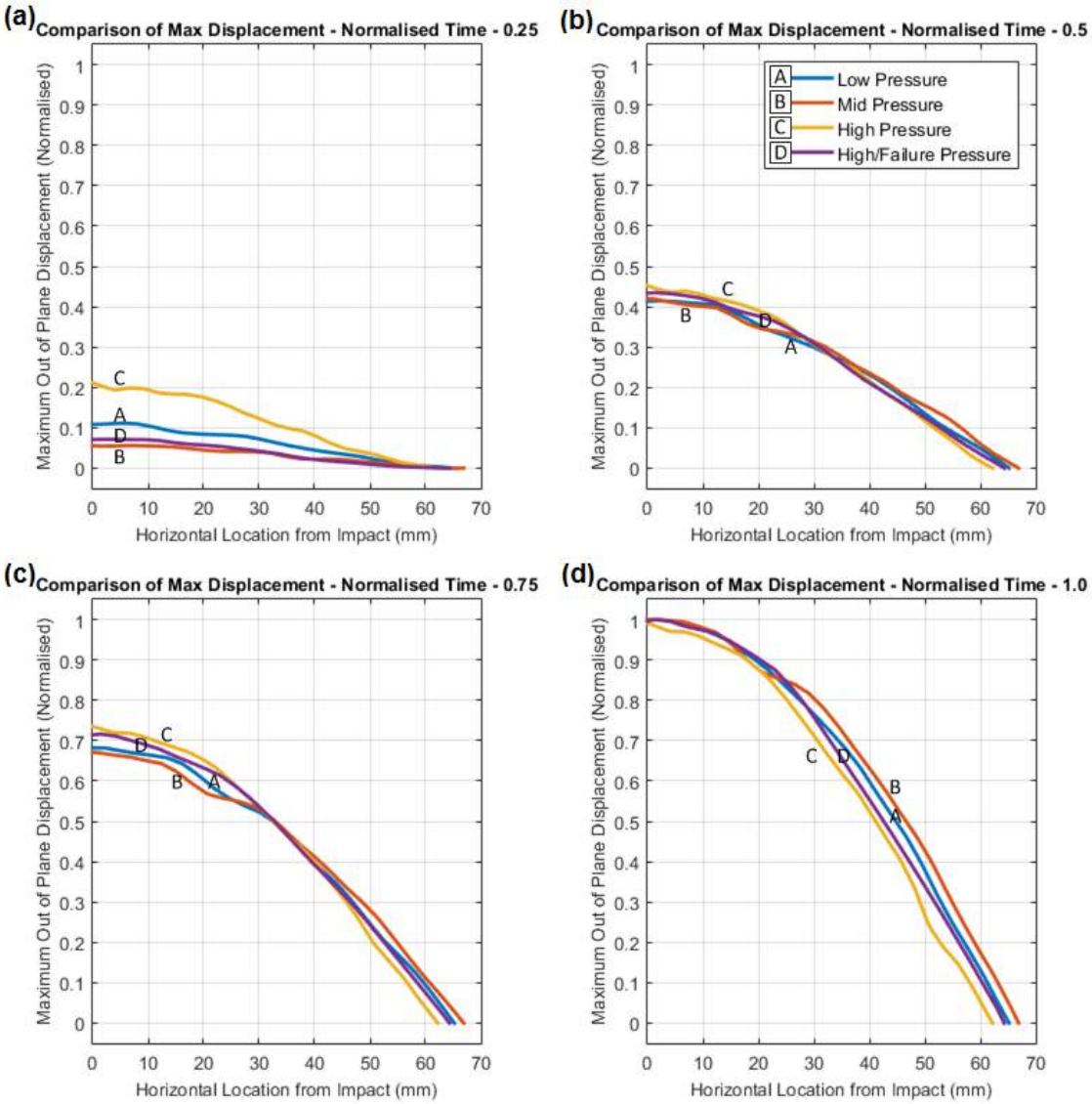

Figure 5.24: Comparison of air-blasts at 0.25, 0.50, 0.75 and 1.00 normalised time.

By considering each available time increment, stages of deformation can be defined for each air-blast incident pressure to begin to understand the typical air-blast behaviour. Figure 5.25 aims to define these stages of deformation, where stage 1 through to 3 were defined as local indentation, transitional (when the whole surface has left its initial zero displacement position) and global flexural bending respectively.

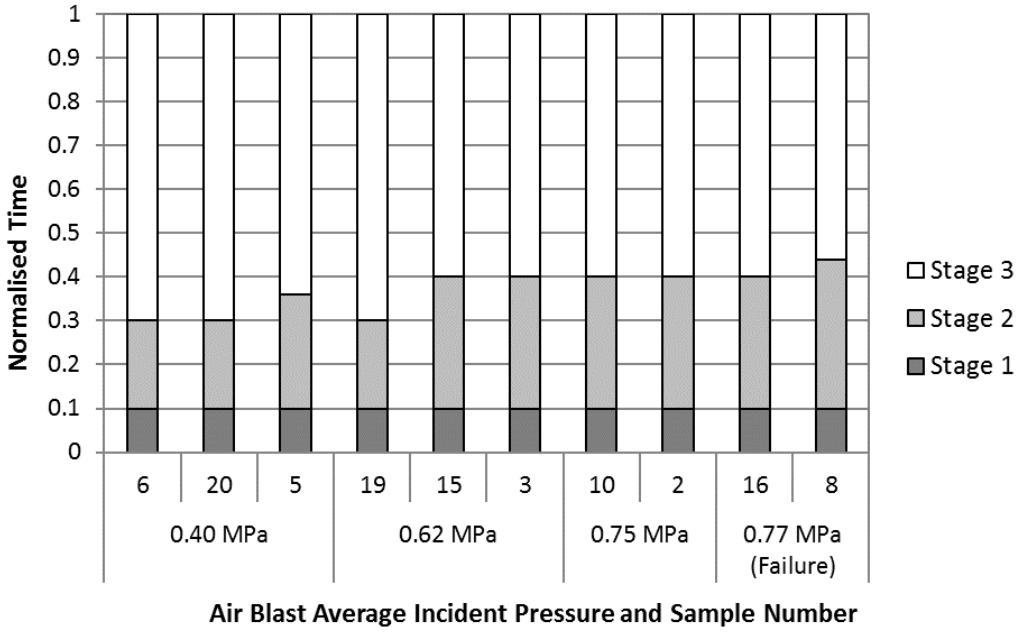

Figure 5.25: Comparison of air-blast loading against the normalised stages of deformation

As can be seen from Figure 5.25 it was clear that the majority of the deformation during the period till maximum localised displacement was in the form of global flexural bending (stage 3), with initial indentation (stage 1) being mitigated due to the distributed loading (loading area ratio = 0.5 as calculated in the previous chapter). The remainder of the generalised deformation was loosely characterised as a transitional stage 2, which for this type of loading (distributed) was not well defined when compared to that of a typical impact loading regime. The resulting specimen behaviour for each of the air-blast pressures produces almost identical normalised deformation behaviour, which again supports the fact that the incident air-blast pressure magnitude has no effect on the specimen's response. Table 5.4 contains the final averaged proportions for each stage with respect to normalised time.

Table 5.6: Air-blast stages of deformation with respect to normalised time

	Air Blast
Stage 1	0.10
Stage 2	0.27
Stage 3	0.63

From this table we conclude that the indentation (stage 1) for the air-blast loading was consistent across all pressures, with the length of the transition (stage 2) showing a possible increasing trend before moving onto global flexural bending which forms the majority of the behaviour.

5.3.3 Comparison of Loading Conditions

Drawing direct comparisons from between the two different loading conditions was difficult due to two key factors, the first being the different support fixtures and the second being the difference in the loading area. For the ballistic impact experiments the loading area was stated to have a ratio of 0.143 between the projectile diameter and the minimum special dimension, whereas for the air-blast experiment the loading area ratio was 0.5 (loading area of $1963.5mm^2$ versus $18145.8mm^2$). Because of the major difference in this ratio, it would be difficult to distinguish how each type of loading condition effects the initial onset of localised deformation before transiting through to global flexural bending. Though the supports were obviously different (cantilever and 3-point bend), taking the localised horizontal slice deformation can look to remove fixture effects. By doing so the results from the 2 different case studies may be compared, and if resultant visible damage was the connecting factor between loading conditions rather than energy then some generalised comparisons may be made. Table 5.7 compares the stages of deformation for all the loading conditions with respect to normalised time, which displays some major differences.

Table 5.7: Comparison of the stages of deformation with respect to normalised time

	Steel	Ice	Air Blast
Stage 1	0.39	0.51	0.10
Stage 2	0.47	0.49	0.27
Stage 3	0.14	0	0.63

It would appear that both of the ballistic impact loading conditions lead to almost exclusive indentation behaviour leading up to maximum out-of-plane displacement, whereas the air-blast conditions demonstrate mainly global flexural bending. Given the difference in the loading areas as mentioned previously, no conclusion can be drawn given this major difference, but it does motivate a potential predictive numerical modelling study for the future.

5.4 Chapter Summary

During the experimental case studies, identical CFRP specimens where subjected to three different loading regimes each at three predetermined intensities. High-speed photography was used alongside 3D DIC in order to obtain information surrounding each specimen's response, as well as out-of-plane displacement data of the rear surfaces. After analysing the experimental data gathered, the following conclusions can be finally drawn:

- Overview

    1. The initial differences between the loading conditions can be generally defined as a localised process zone in the case of the rigid steel projectile, through to a transition from a local to a global process zone for the ice projectile during fragmentation, and finally a global process zone for the case of the air-blast loading.
    2. The loading conditions were different in terms of energy and surface area, but the resultant damage observed from the loading conditions produces visually similar levels of global damage as discussed in the previous chapter (experiment methodology).

- Ballistic Loading

    1. For projectiles of the same size a rigid (steel) impact demonstrates more defined indentation of the specimens before the transition into global flexural bending, whereas fragmenting (ice) projectiles produce initial indentation but upon fragmentation any local indentation was more gradually transitioned to distributed loading leading to global flexural bending.

2. Comparing each of the specimens normalised responses in time and out-of-plane displacement shows that impacts with the same projectile materials show similar responses, but the comparison between the two different projectile materials shows the indentation stage to be more localised for that of the rigid (steel) even at significantly lower impact energies, and proves that fragmentation leads to more widely distributed loading even at high energy levels.
3. During the transition to the global flexural bending resulting from each impact, due to the damage appearing at the rear surface the rigid (steel) projectiles cause a gradual concave to convex curvature deformation profile throughout the transitional stage. Whereas the fragmenting (ice) projectiles causes a more prominent concave deformation profile towards the centre, before a more sudden and aggressive change to a convex curvature upon reaching global flexural bending.
4. Damage at the rear surface of the specimens occurs much sooner when the projectile was rigid (steel) than that of the fragmenting (ice) projectile, this was likely due to the almost instantaneous fragmentation of the ice projectile on impact causing more widely distributed loading and therefore a longer impact duration even at the clearly higher impact energies.
5. The indentation stage of behaviour for the fragmenting (ice) impacts was marginally longer than that of the rigid (steel) impacts, which was a result of the higher impact energy of the ice projectiles. Then the global flexural bending behaviour (stage 3) was clearly present when approaching normalised time = 1.0 for rigid (steel) impacts, but for the fragmenting (ice) impacts there was no clearly distinguishable stage 3 for most cases until t = 1.0.

- Blast Loading

1. The rear surfaces of the specimens mostly remained intact at the centre and so the centre point displacement can be analysed. The changes in the oscillation period before and after the appearance of delamination prove that the reduced stiffness resulting from the damage does affect the specimen's response by approximately a 25% increase in the oscillation period where it can be measured before and after.

2. The deformation resulting from the different air-blast incident pressures appears to be very similar, and initial observations support the typical deformation seen for this type of specimen fixture demonstrates a spherically distributed loading area that propagates into an elliptical shape as the free edges deform away from the shock tube muzzle.
3. Resultant responses for the different incident pressures suggest no obvious differences in behaviour accept from increasing out-of-plane displacement as excepted, but it was clear that each specimen was subjected to distributed loading leading to early global flexural bending and concave curvature of the specimens during loading therefore avoiding any obvious localised indentation.
4. Comparing each of the specimens normalised responses in time and out-of-plane displacement shows that the incident air-blast pressure magnitude has no effect on the specimen's response up until maximum displacement for similar boundary conditions, some level of indentation can be witnessed at very early stages before all specimens enter full global flexural bending for the majority of the loading event.
5. The major and failure damage cases demonstrate greater deformation at the free edges, which can be explained by the clearly seen tensile failure and delamination of the first few plies at the centre of the free edges located at the rear of the specimen. The progression of deformation at the free edge can be seen at each damage level.
6. Indentation of the specimens (stage 1) for air-blast loading was very consistent across all pressures and almost insignificant, the length of the transition stage (stage 2) does show the possibility of an increasing trend but was not conclusive, and finally the global flexural bending of the specimens forms the majority of the behaviour.

- Comparison of the Loading Conditions

1. For the ballistic loaded specimens there were definitive differences between the specimens responses, even at varying loading magnitudes. Whereas for the air-blast loaded specimens no real differences can be seen, apart from the obvious change in out-of-plane displacement.

2. It was clear that at the two extremes, the more localised loading of the rigid (steel) impacts results in localised indentation and greater localised damage, while the air-blast loading clearly results in wider distributed loading resulting in almost instantaneous global flexural bending. The fragmenting (ice) impacts almost form a middle ground between the two, and start out as localised indentation but upon fragmentation transitions to wider distributed loading.
3. Drawing comparisons between the two different loading conditions was difficult due to the different support fixtures and the difference in the loading area, for the impact experiments the loading area ratio was 0.143 and for the air-blast the loading area ratio was 0.5 (loading area diameter of 25mm versus 76mm). This makes distinguishing between indentation and global bending difficult.
4. This analysis could be revisited in the form of a case study at a later stage during numerical modelling as further validation for the development of the models, and as a case study to test the predictive capabilities of the model for either changing the support fixture boundary conditions or the ballistic / blast loading area.

Following the deformation analysis outlined in this chapter, the next chapter shall discuss and analyse the visible and hidden internal damage observed in the specimen post experiment, while making reference to the dynamic responses of each specimen during loading.

Chapter 6

Damage Analysis with X-Ray Tomography

With the deformation behaviour resulting from ballistic and air-blast loading conditions described in Chapter 5 having now been discussed and presented in Chapter 6, this chapter presents and discusses the analysis of the visual and hidden damage in the dynamically loaded specimens using non-invasive X-ray tomography.

6.1 Comparison of Visual Damage

Following the experimental case studies, some preliminary observations of the immediate visual external damage can be made for each of the loading conditions. This should also confirm whether the correct loading magnitudes were chosen to achieve three similar levels for each loading condition as described in Chapter 5. The three varying levels should cover minor damage defined as minimal front and/or rear surface damage, through to major damage, defined as significant damage to the front and/or rear surfaces with, in some cases, full penetration/perforation of the specimen.

6.1.1 Ballistic Impact Damage

Inspecting the specimens following the impacts with both the rigid (steel) and fragmenting (ice) projectiles, two very distinct types of visual damage become apparent. Firstly very localised and therefore more penetrating damage for the rigid projectile, and the second was more wide spread damage to the front surface of the specimen with some signs of possible penetration for the fragmenting projectile.

Figures 6.1 through to 6.3 show the minor, medium and major damage cases for the rigid (steel) projectiles, and Figures 6.4 through to 6.6 show the respective images for the fragmenting (ice) projectiles. In all the figures, (a) shows the front surface and (b) the rear surface of each reference specimen.

First, for the rigid projectile, there are increasing indications of localised indentation to the front surfaces as the impact energy increases, accompanied by the appearance and progression of tensile damage at the centre of the rear surface as the projectiles penetrated further into the specimens as the impact energy increases. Assessing the extent of any delamination as this stage was difficult due to the centralised natural of the damage zone, but obvious changes in the specimen was thickness (as shown in Figure 6.3b) suggests that delamination was present in the localised area following the loading event.

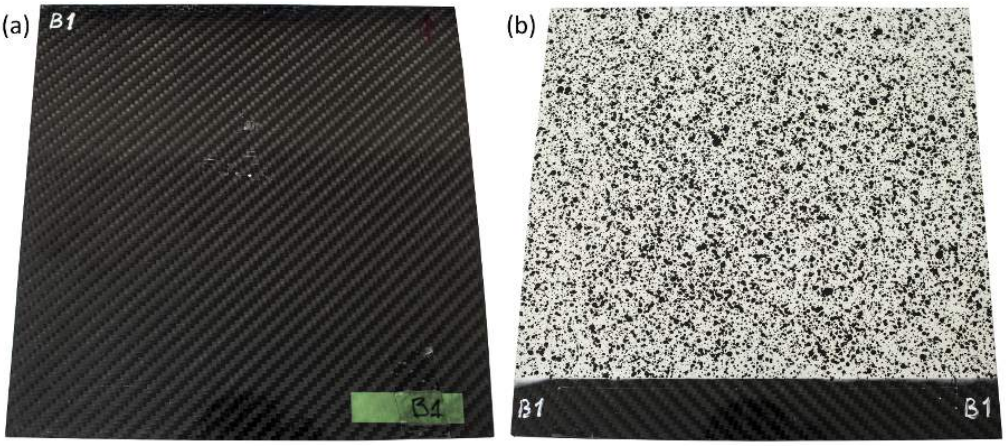

Figure 6.1: Visual external damage - steel impact at 59.5 m/s (minor damage): (a) front surface; (b) rear surface, sample size 195 mm × 195 mm (sample B2)

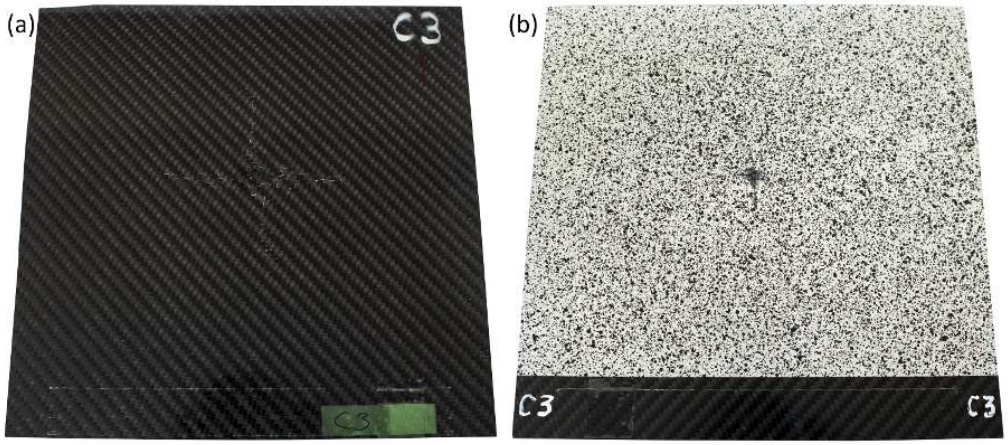

Figure 6.2: Visual external damage - steel impact at 78.5 m/s (medium damage): (a) front surface; (b) rear surface, sample size 195 mm × 195 mm (sample C3)

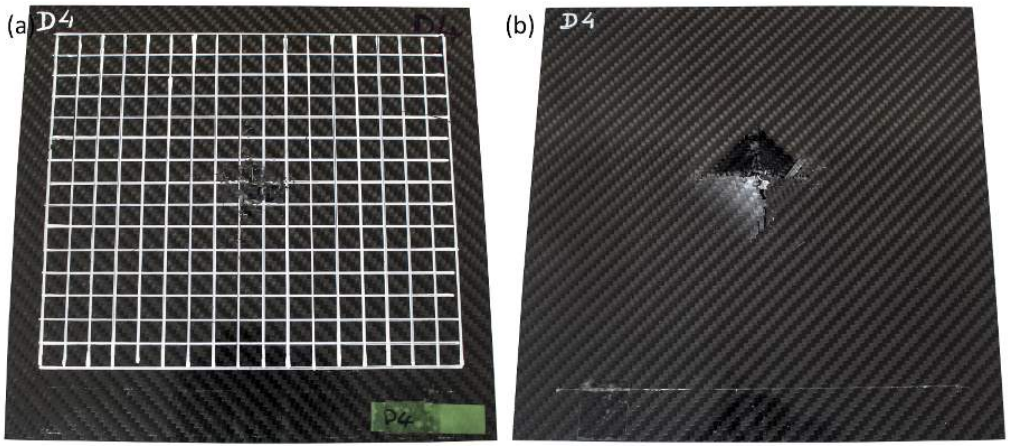

Figure 6.3: Visual external damage - steel impact at 91.5 m/s (major damage): (a) front surface; (b) rear surface, sample size 195 mm × 195 mm (sample D4)

For the fragmenting projectiles, the resultant damage shows some similarities to that of the rigid projectiles but the fragmentation causes a distinctive difference. The fragmenting projectiles still show partial indentation into the specimens causing damage to the front surface, but upon fragmentation below the surface (depth depends on the impact energy), the fragments of the projectile cause catastrophic delamination of the first few front plies. Even at the considerably higher impact energies compared to those of the rigid projectiles, signification damage at the rear surface was only found to be present for the major damage case making full penetration of the specimen unlikely at the impact energies stated.

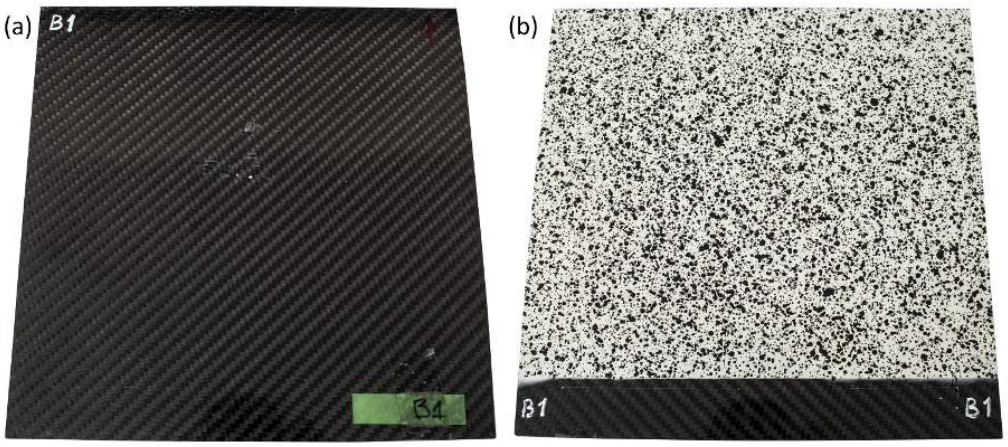

Figure 6.4: Visual external damage - ice impact at 304.0 m/s (minor damage): (a) front surface; (b) rear surface, sample size 195 mm × 195 mm (sample B1)

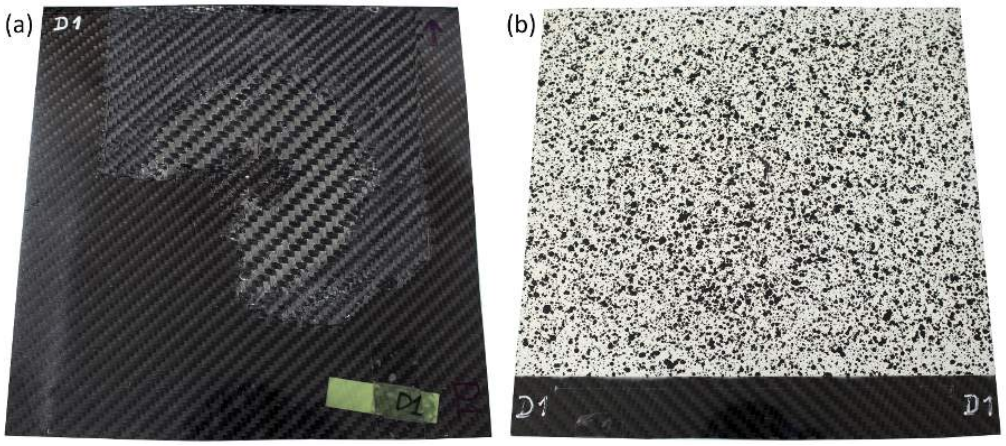

Figure 6.5: Visual external damage - ice impact at 403.0 m/s (medium damage): (a) front surface; (b) rear surface, sample size 195 mm × 195 mm (sample D1)

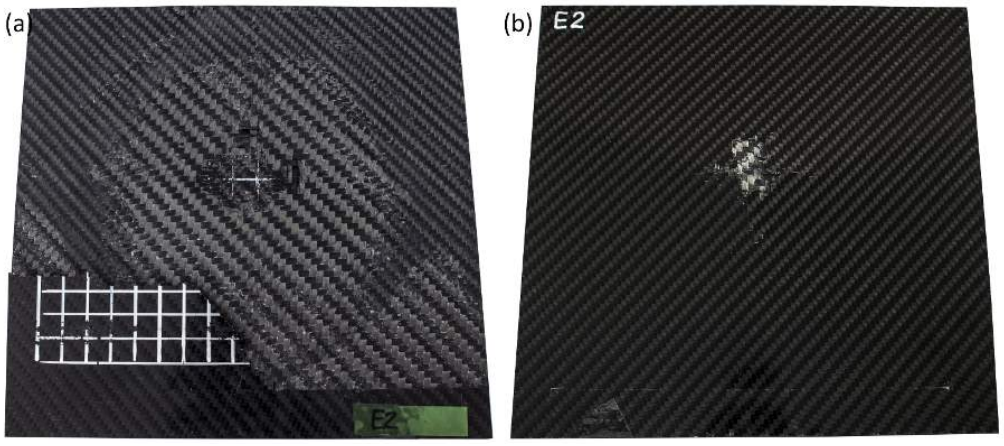

Figure 6.6: Visual external damage - ice impact at 480.0 m/s (major damage): (a) front surface; (b) rear surface, sample size 195 mm × 195 mm (sample E2)

When considering both projectile types, the amount of visual damage was seen to increase as the impact energy also increases as expected, resulting in significant levels of damage for both major damage cases.

6.1.2 Air-blast Damage

For the specimens subjected to the air-blast loading condition, the resultant visual external damage was very different to that of the ballistic impact cases. Instead, they can be compared to that of damage commonly seen in 3-point bending. The first signs of damage appear on the rear surface, as tensile failure of the plies leads to delamination at the point of maximum bending stress. Figures 6.7 through to 6.10 show the minor, medium and major/failure damage cases respectively. The observed visual amount of damage increases as the loading magnitude increases. Each figure presents the front surface (a), the rear surface (b) and the damage at one of the free unsupported edges of the sample (c), with the dashed line indicates the centre of the specimen.

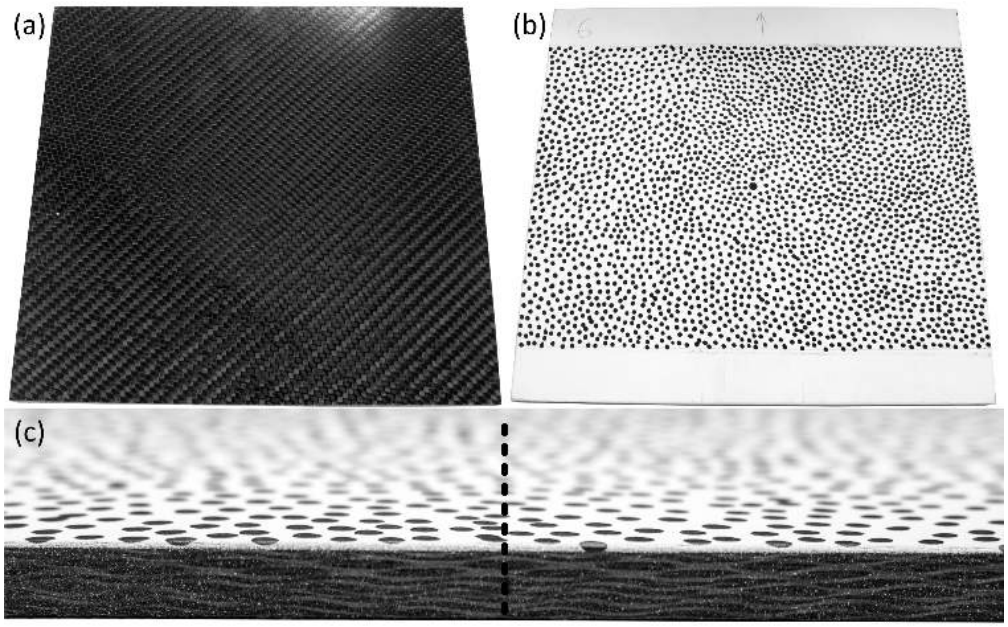

Figure 6.7: Visual external damage - air-blast at 0.40 MPa (minor damage): (a) front surface; (b) rear surface; (c) free edge, sample size 200 mm × 200 mm (Sample 6)

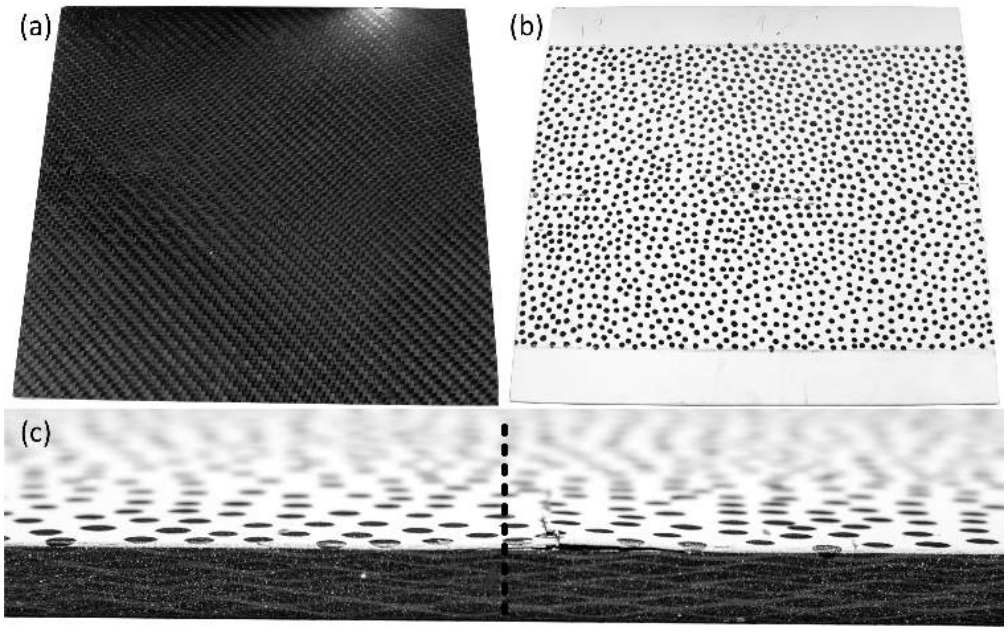

Figure 6.8: Visual external damage - air-blast at 0.62 MPa (medium damage): (a) front surface; (b) rear surface; (c) free edge, sample size 200 mm × 200 mm (sample 19)

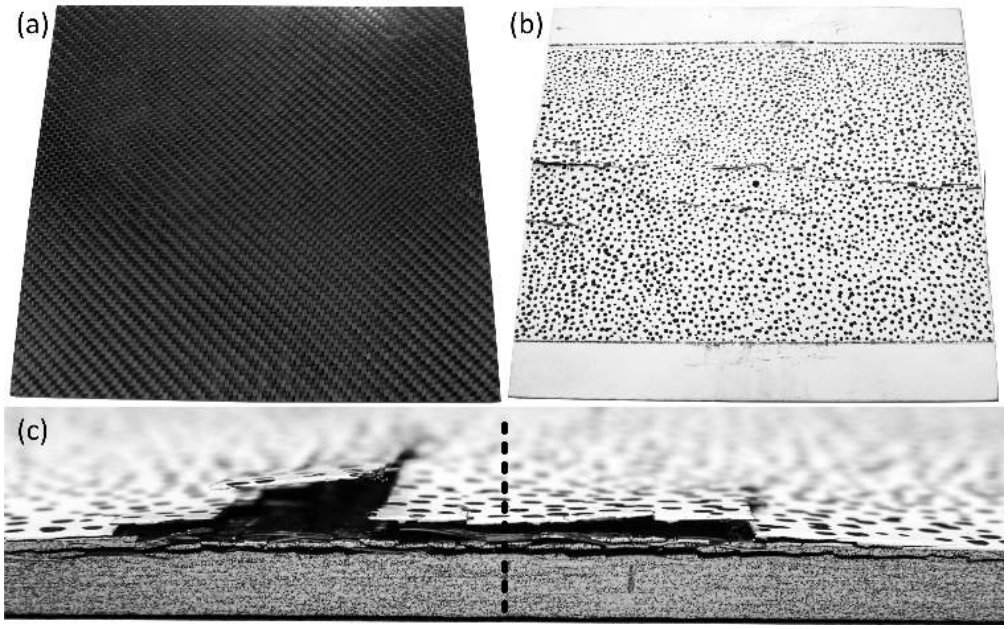

Figure 6.9: Visual external damage - air-blast at 0.80 MPa (major damage): (a) front surface; (b) rear surface; (c) free edge, sample size 200 mm × 200 mm (sample 10)

For all the damage conditions, there was no observable damage seen on the front surface of the specimens. However, the progression of the tensile failure at the rear surface in the centre of the specimen, which can be thought of as the central line of symmetry between the supporting locations, was found to increase with the increase in the incident

wave pressure of the air-blast. This suggests that the tensile failure propagates from the rear surface through to the front surface until complete failure, with delamination of the plies also increasing as the damage progresses through the thickness. Closer investigation showed greater delamination at the free edges of the specimen, which was seen to show large amounts of deformation as described in the previous chapter.

Observing the failed specimen (Figure 6.10) that underwent complete failure through its thickness during the loading event, the resulting damage was catastrophic but still had the central line of horizontal symmetry. Each of the other specimens subjected to the various loading conditions remained against the support fixture during the loading event; however, the specimens that completely failed became free to move inside the restricted enclosure of the experiment setup. Thus, it was unclear whether the damage seen in the failed specimens was caused by the actual loading event, or by the subsequent interaction with the enclosure. Therefore, from this point on, the failed specimens were disregarded from the damage analysis for the air-blast loading condition, leaving the minor through to major damage case specimens to form suitable damage levels for the case study.

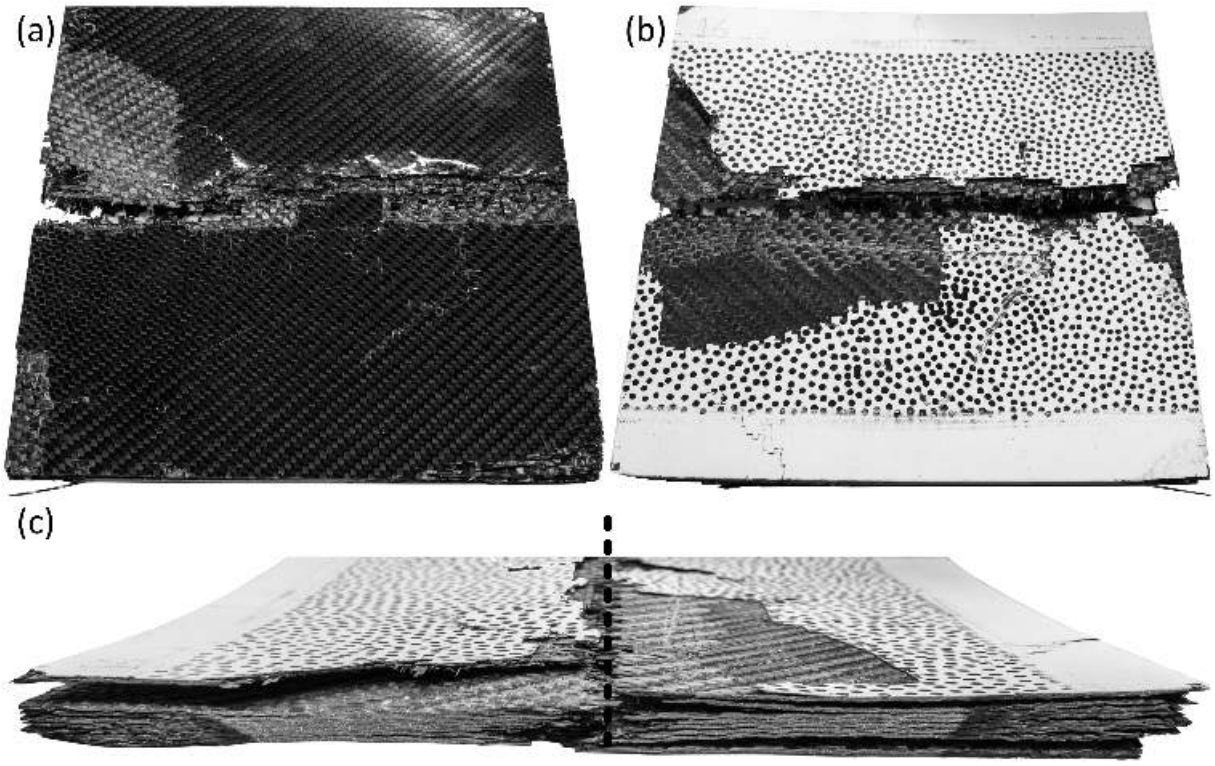

Figure 6.10: Visual external damage - air-blast at 0.78 MPa (failure damage): (a) front surface; (b) rear surface; (c) free edge (sample 16)

6.2 Analysis Methodology

With a clear understanding of the resultant visual external damage caused by each of the different loading conditions, an appropriate methodology can be defined for the in-depth analysis of the damage in each specimen. This methodology was broken down into a number of stages: description of the X-ray tomography, scan configuration and, finally, the post processing of the scans and analysis of the obtained results.

6.2.1 Description of X-Ray Tomography Configuration

The process of X-ray computed tomography (CT) utilises a combination of multiple X-ray images of a specimen taken at different angles in a reconstructed three-dimensional volume, in which cross-sectional (tomographic) internal slices can be viewed. The two-dimensional planar X-ray images are combined using a technique called a radon transform, which is commonly known as the filtered-back projection algorithm, to over-lay and superimpose the images in order to build up the reconstructed 3D volume based upon the original equipment configuration.

A simplified schematic diagram of the X-ray computed tomography process is shown in Figure 6.11, and shows the projection relationship between the X-ray point source and the 2D detector; this can help to understand the potential limitation of this analysis technique. Put simply, the closer the specimen is to the source, the finer the resolutions but the smaller the viewable area, and, oppositely, the further from the source, the larger the viewable area but courser the resolution. Therefore, when considering the best configuration for the specimens discussed above, there were some limitations because of their physical size.

All of the specimens were inspected after each experiment using a Metris 160 H-XT XCT system to investigate the extent of the internal (hidden) damage and its spatial distribution. Each scan was conducted at 140 kV and 130 μA using a tungsten target, with 2650 radiography projections (X-ray images) taken over a 360 ° rotation of each specimen at an exposure of 500 ms. In order to increase the quality of each scan, effort was made to initially increase the sharpness of the originally acquired 2D X-ray projections and to minimise any loss in image quality upon reconstruction. This was achieved by taking 8 images (or frames) per projection before averaging them out in order to reduce granular noise; hence each image was digitally sharpened before being passed to reconstruction.

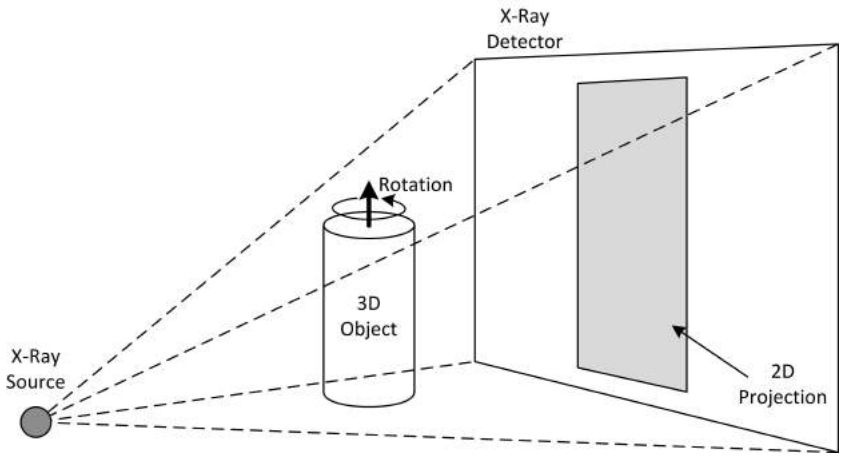

Figure 6.11: Simplified schematic diagram of X-ray computed tomography

An example of a sharpened projection in shown in Figure 6.12. Given the size of the sample and the limitations of the scanner, the total volume scanned for each specimen was 180 mm x 140 mm x 20 mm at a resolution of 97 μm. Because of the large aspect ratio of the specimens, beam hardening had to be utilised at the reconstruction stage in order to balance the grey scale contrast across the cross section.

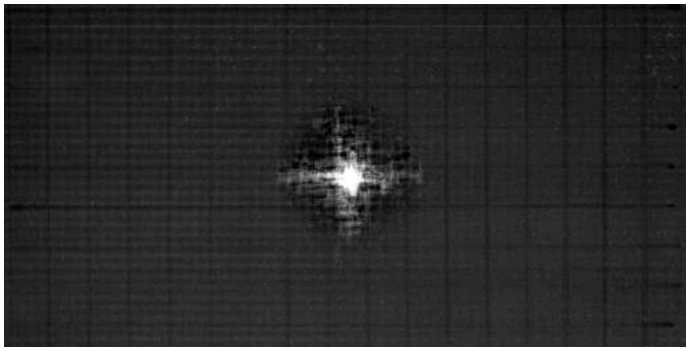

Figure 6.12: Example of a sharpened X-ray tomography projection

6.2.2 Post-processing of X-Ray Tomography Scans

The reconstructed volumes were analysed using the commercial VGStudio Max software, and utilised multiple render settings in order to create optimal ways to visualise the resultant damage. Figure 6.13 shows a typical histogram from one of the specimen CT scans, these histograms represent the intensities of the grey scale voxels (3D pixels) within the reconstructed volumes. By setting upper and lower limits, certain regions of the volume can be removed (based upon their grey scale values), e.g. air, leaving the damaged

specimen in view. The lower end of the selected region, where the dip in the histogram can be seen, represents the transition from air to the specimen material, which can be thought of as "external edges". By reducing the limits to only 25% of the lower end, the external edges are then highlighted as the damaged areas within each specimen as a "cloud".

Figure 6.13: X-ray tomography reconstruction histograms: (a) general 3D view; (b) internal damage view

Figures 6.14 and 6.15 utilise these rendering settings, in order to visualise both the solid body and highlighted damaged in both 3D and 2D respectively. Figure 6.14(a) shows the original rendered specimen volume, while Figure 6.14(b) shows the damaged external edges with the rendered volume transparency set to 10%. This transparent view allowed the "damaged" voxels to be stacked or superimposed through the volume, therefore increasing the intensity (grey scale value) as the amount of external edges or damage increased in the area. The original rendered specimens cross-section is shown in Figures 6.15(a), with Figure 6.15(b) then showing the damaged external edges with the internal area set to a solid grey colour, again highlighting the damage.

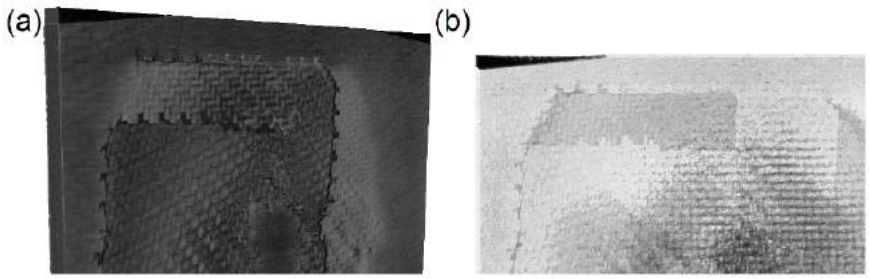

Figure 6.14: X-ray tomography example rendered 3D reconstructions: (a) general 3D view; (b) internal damage view

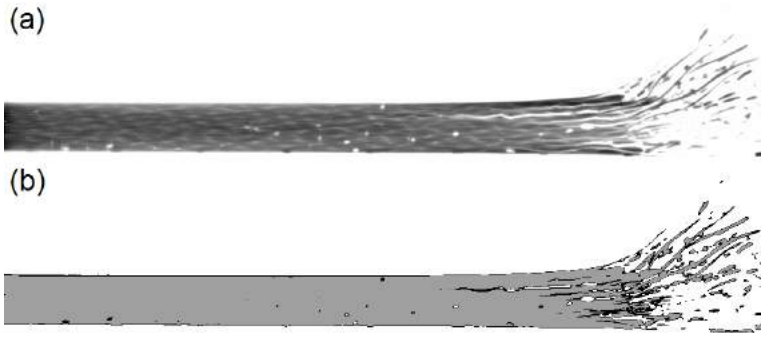

Figure 6.15: X-ray tomography example rendered 2D reconstructions: (a) general 2D section view; (b) damage section view

Following the post-processing of each specimen's X-ray CT scans as described above, it was possible to quantitatively analyse and compare all of the scan results. This allowed a deeper understanding of the effect of the various loading conditions on the amount and spatial distribution of the internal damage, while linking back to the deformation analysis presented in the previous chapter.

6.3 Comparison between Visible Damage and Hidden Damage

By using the rendering settings as described above, each specimen's scan can be analysed side by side. It is worth noting that each scan had a reconstructed volume of 180 mm x 140 mm x 20 mm volume due to limits of the scanner, and a resultant pixel/voxel resolution of 97 μm. This resolution should not be confused with detectable feature size; in order to see a feature in the reconstructed volume, it must be multiple pixels/voxels across. Therefore, tracking damage and delamination through the specimens maybe difficult with these full specimen scans.

6.3.1 Ballistic Ice and Steel Projectile Impacts

Starting with the rigid (steel) projectiles, Figure 6.16 shows the comparison of damage between the different impact velocities. In the figure, a sectional view of each specimen is shown along with a close up view of the impact zone; this demonstrates the increasing surface and internal damage with the increasing impact energy as was discussed earlier in

the chapter. The transparent damage clouds are also shown for each velocity, again clearly demonstrating the increasing cloud area and intensity of the damage towards the centre of the cloud. Additional figures for the repeated specimens can be found in Appendix B.

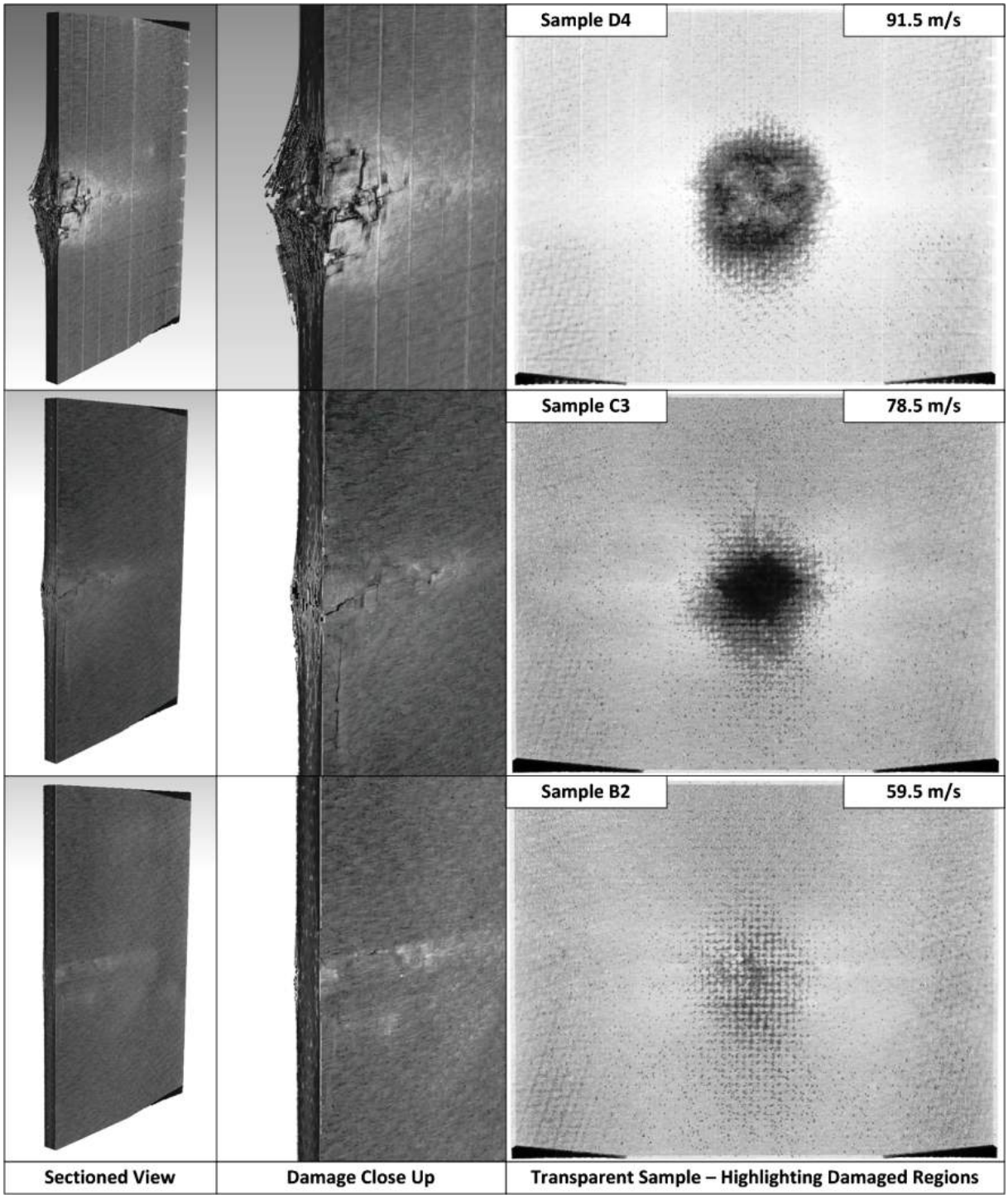

Figure 6.16: Solid (steel) impact 3D renders: effect of velocity

From this analysis it can be seen that for the rigid projectiles the area of the damage cloud was similar across the three impact energy levels, suggesting that the resulting damage area (which includes de-lamination) remained highly localised with increasing impact velocity for the same projectile size. Instead, the increasing energy led to greater penetration of the sample, as shown by the increased compressive damage at the point of impact and resulting rear surface tensile failure.

This was confirmed by the 2D sectional views shown in Figures 6.17 and 6.18, with the spread of the damage cloud remaining similar but specimen penetration was clearly shown at higher impact energies. The vertical YZ sections (Figure 6.18) also shows the effect of the cantilever clamping method, as the damage extends down towards the fixture as expected for dynamic loading such as this.

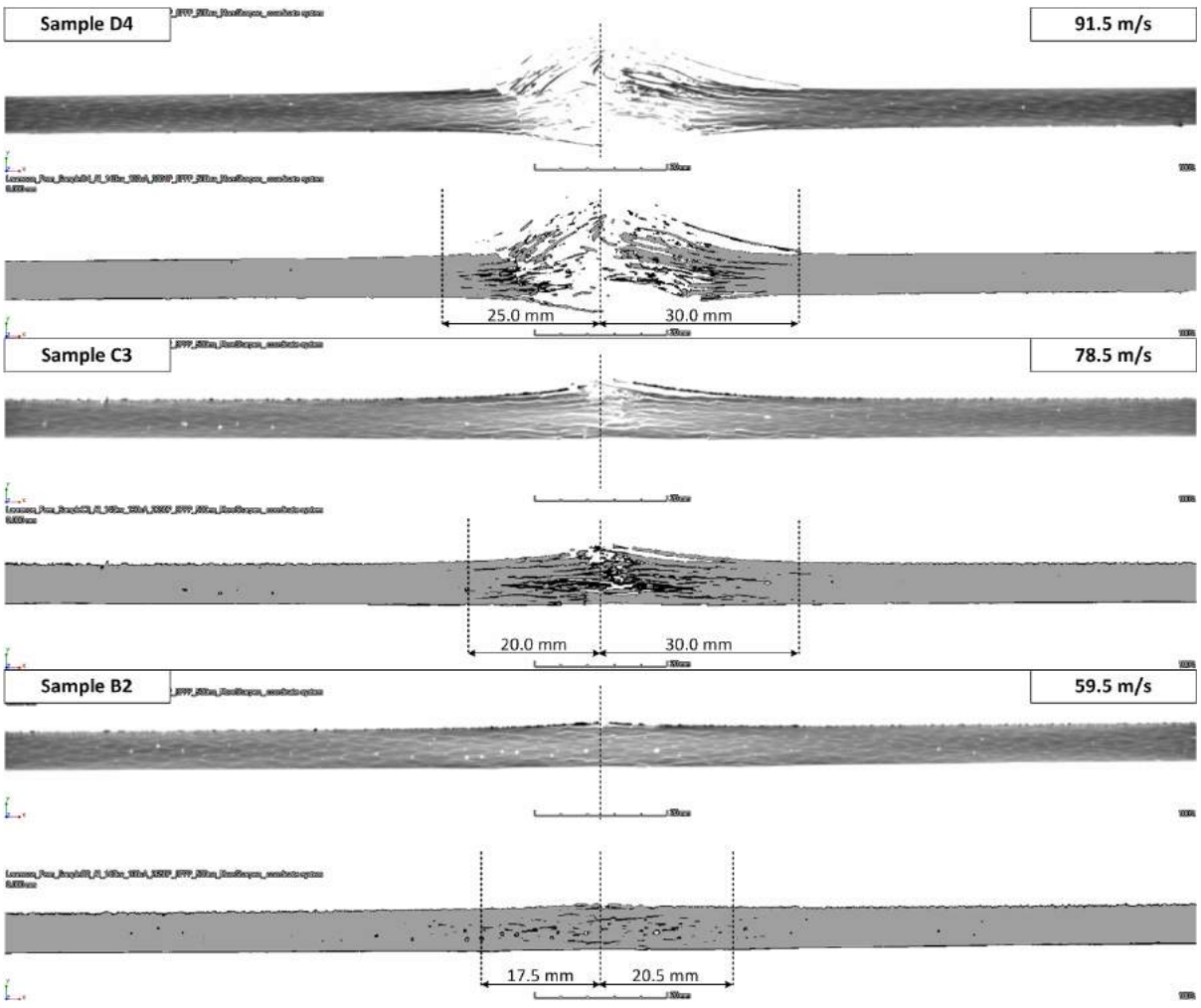

Figure 6.17: Solid (steel) impact 2D horizontal XY section: effect of velocity

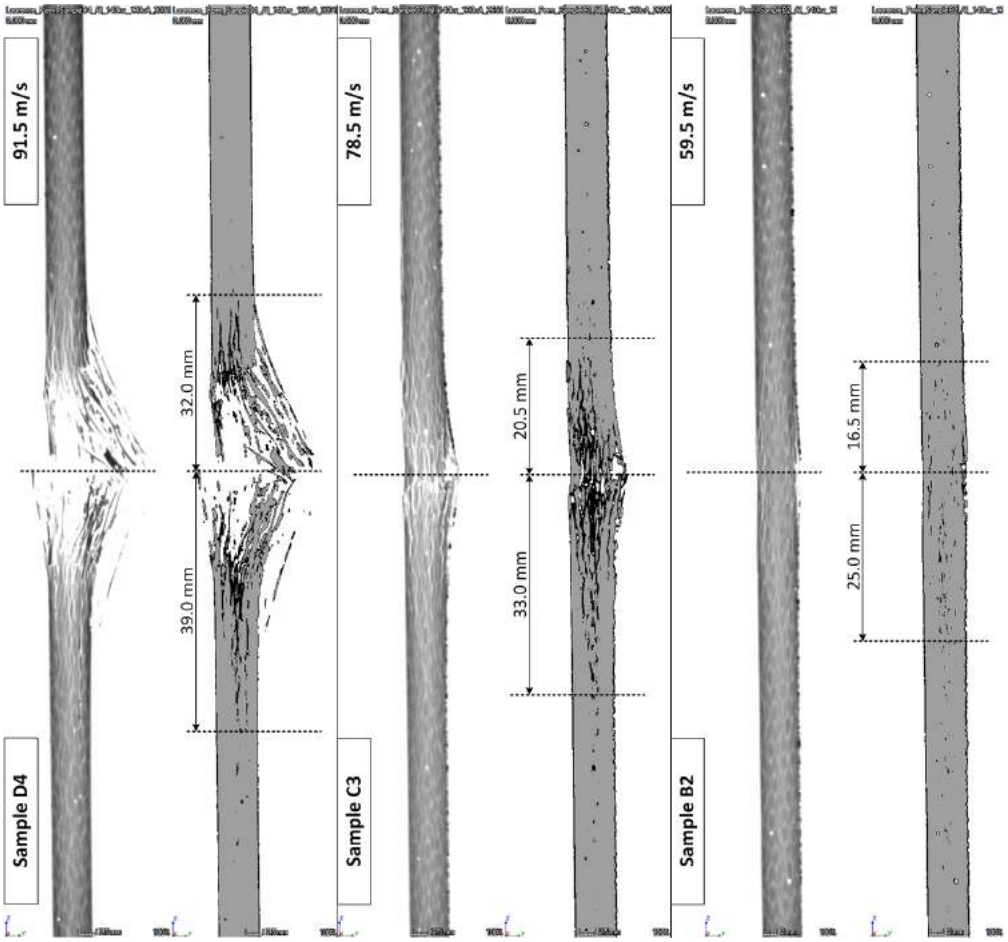

Figure 6.18: Solid (steel) impact 2D vertical YZ section: effect of velocity

When assessing the results of the impacts with the fragmenting (ice) projectiles, Figure 6.19 shows the comparison of damage for the different impact velocities. A sectional view of each of the specimens was shown within the figure, along with a close up view of the impact zone, this demonstrates the increasing surface and internal damage with increasing impact energy. The transparent damage clouds are shown for each, again clearly showing the increasing cloud area and intensity of the damage towards the centre of the cloud. In comparison to the rigid projectiles, the fragmenting projectiles cause catastrophic internal damage as well as external damage as seen above. Additional figures for the repeated specimens can be found in Appendix B.

For the fragmenting projectiles, it can be seen that the area of the damage cloud displays a definite increase across the three impact energy levels, suggesting that the resulting damage area which includes major de-lamination in these specimens drastically increases with increasing impact velocity for the same projectile size. Compared to that

of the rigid projectiles, there was no signs of significant penetration; instead, partial indentation and then de-lamination of the first few plies of the specimen from the front surface was observed.

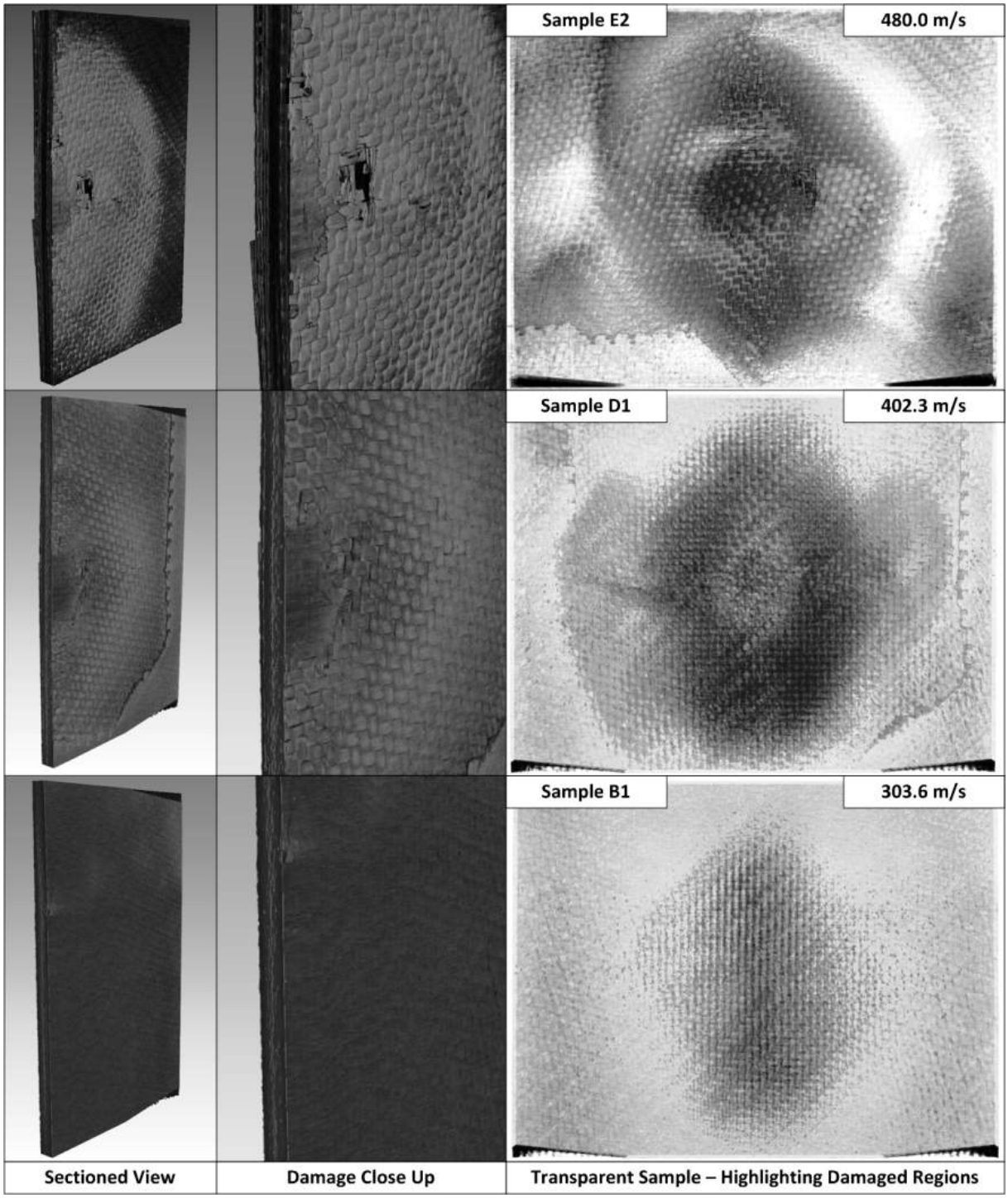

Figure 6.19: Fragmenting (ice) impact 3D renders: effect of velocity

This was also confirmed when looking at the 2D sectional views shown in Figures 6.20 and 6.21, with the spread of the damage cloud increasing with increasing impact energy but shows no signs of localised penetration. The vertical YZ sections shown in Figure 6.21 also show the effect of the cantilever clamping method, even though its less clear due to significantly more wide spread damage. Additional figures for the repeated specimens can be found in Appendix B.

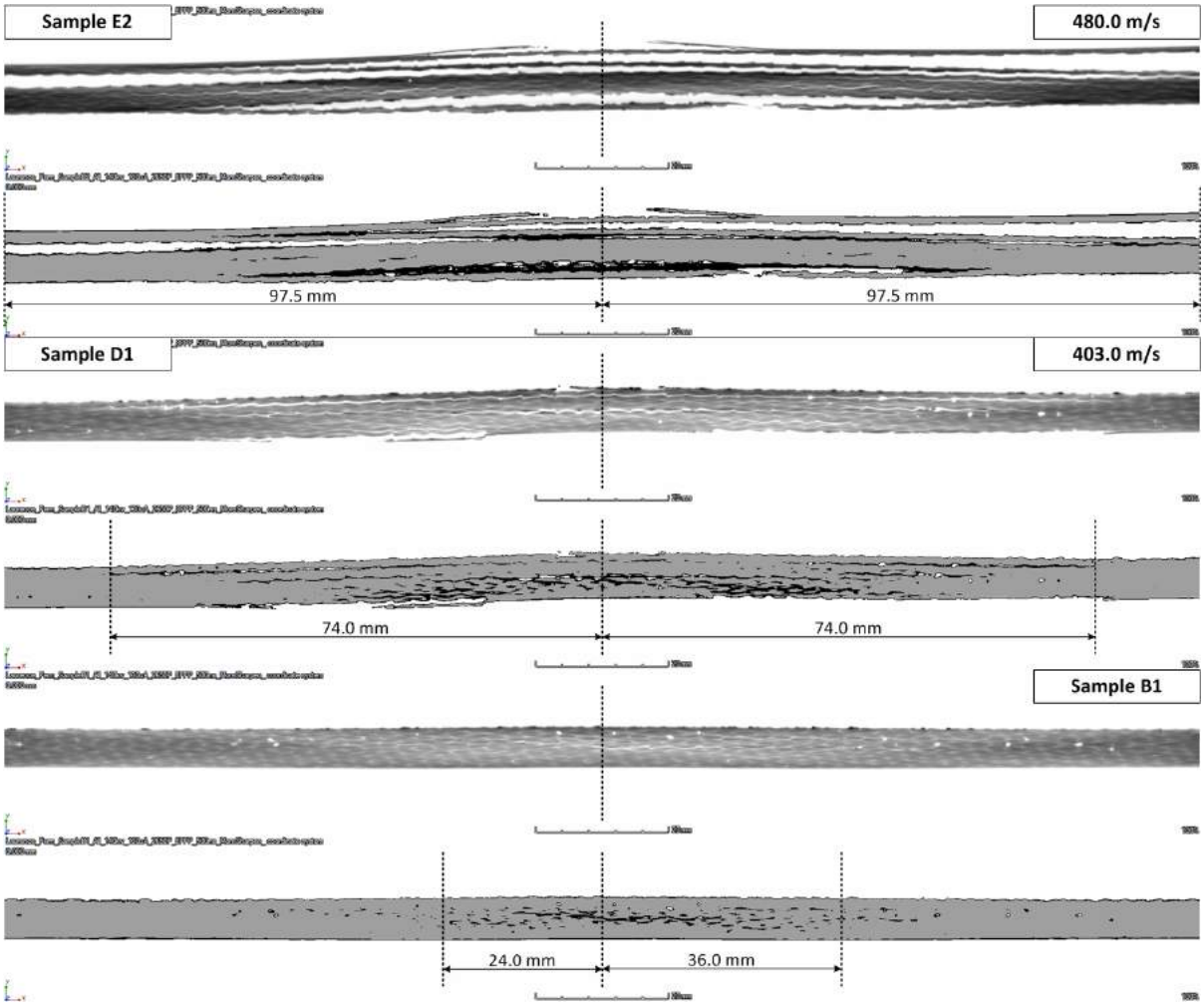

Figure 6.20: Fragmenting (ice) impact 2D horizontal XY section: effect of velocity

Table 6.1 contains a summary of the horizontal and vertical spread of the observable damage and the estimated total area for both the rigid and fragmenting projectiles based on a standard shape approximation; that, although initially unclear, once averaged does show an increasing trend in the damage cloud area with increasing energy for both projectile types. As expected, after observing the visual damage as discussed in Section 6.1, this increasing trend was more pronominal for impacts with the fragmenting (ice) projectile

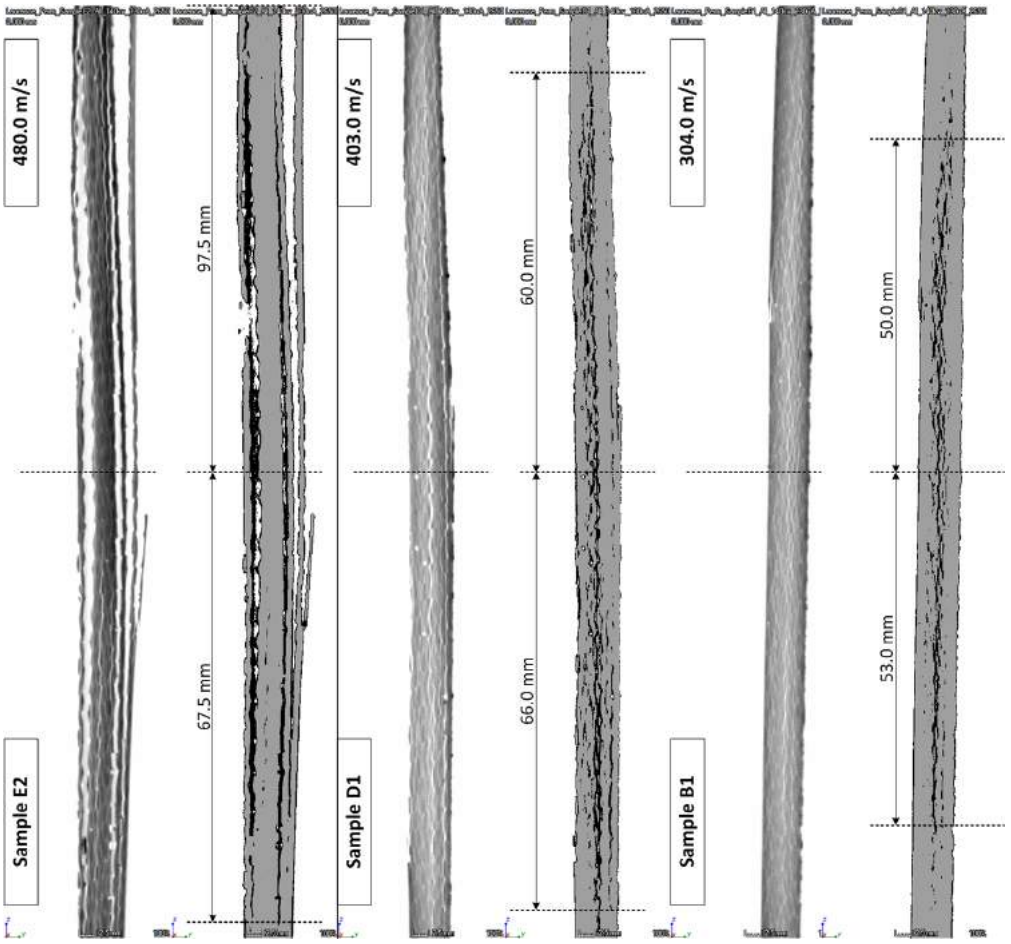

Figure 6.21: Fragmenting (ice) impact 2D vertical YZ section: effect of velocity

compared to that of the rigid steel projectile with increasing impact energy. It should be noted that specimen D2 (results can be found in Appendix B) displayed significant delamination between two plies for the medium damage case, this delamination was removed from the results presented leaving only the expected damage cloud.

When comparing the similarities between the rigid (steel) and fragmenting (ice) projectiles, it was clear that the damage observed at this level seems to be repeatable for each loading condition and symmetric about the vertical mid plane. Then, as expected, the chosen loading magnitudes produced varying levels of damage from minor damage.

Table 6.1: Ballistic steel and ice impact: maximum out-of-plane displacement and damage cloud

	Damage Level	Sample	Projectile Velocity (m/s)	Impact Energy (J)	Max Out-of-plane disp. (mm)	Damage Cloud Horizontal (mm)	Damage Cloud Vertical (mm)	Damage Shape Approx.	Damage Cloud Area (mm^2)
Steel	Minor	B2	59.40	96.50	7.23	38.00	41.50	Oval	1238.57
		B4	60.00	98.46	7.36	35.00	43.00	Oval	1182.02
		B5	59.00	95.21	7.27	33.00	74.50	Oval	1930.90
		Average	59.47	96.72	7.29	-	-	Oval	1450.50
	Medium	C3	78.40	168.11	8.00	50.00	53.50	Oval	2100.94
		D2	78.60	168.97	8.88	62.50	63.00	Oval	3092.51
		D5	78.40	168.11	7.59	46.40	52.00	Oval	1895.01
		Average	78.47	168.39	8.16	-	-	Oval	2362.82
	Major	D4	91.40	228.48	-	55.00	71.00	Oval	3066.98
		E3	91.20	227.48	-	62.00	66.50	Oval	3238.20
		E5	91.80	230.49	-	66.00	71.00	Oval	3680.38
		Average	91.47	228.82	-	-	-	Oval	3328.52
Ice	Minor	A4	304.00	346.56	5.35	56.00	76.00	Oval	3342.65
		B1	304.00	346.56	5.95	60.00	103.00	Oval	4853.76
		B3	303.00	344.28	5.88	41.00	71.00	Oval	2286.29
		Average	303.67	345.80	5.73	-	-	Oval	3494.24
	Medium	C2	402.00	606.02	6.63	135.00	107.00	Oval	11345.08
		D1	403.00	609.03	6.60	148.00	126.00	Oval	14646.10
		D3	402.00	606.02	6.42	139.00	124.50	Oval	13591.71
		Average	402.33	607.02	6.55	-	-	Oval	13194.30
	Major	E1	481.00	867.60	-	195.00 (max)	165.00	Rectangle	32175.00
		E2	480.00	864.00	-	195.00 (max)	165.00	Rectangle	32175.00
		E4	479.00	860.40	-	195.00 (max)	163.00	Rectangle	31785.00
		Average	480.00	864.00	-	-	-	Rectangle	32045.00

The averaged data from Table 6.1 is then presented in Figure 6.22, and confirms that the both projectile types led to an increasing damage cloud area with increasing impact energy. For the rigid projectile this trend was less prominent than that of the fragmenting ice. It was thought that with higher impact energies the damage cloud area could reach a maximum due to the localised damage as the result of projectiles perforation into the specimen. As for the fragmenting projectile, it was clear that with increasing impact energy a larger damage cloud area should result in the maximum area reached. This was due to the observed transition from a localised indentation to the global distributed loading as the projectile fragments.

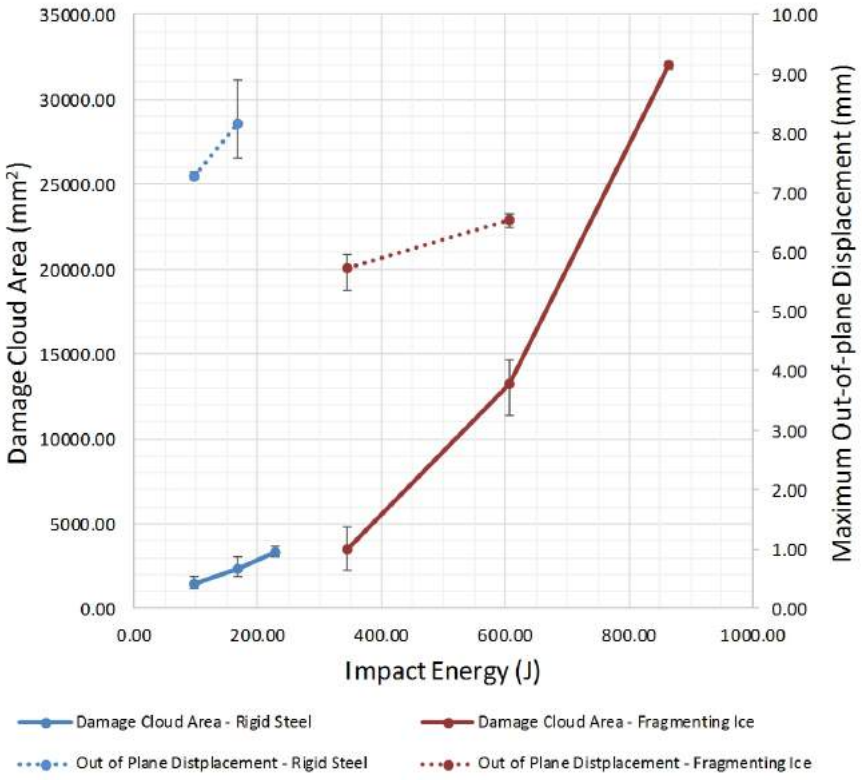

Figure 6.22: Effect of impact energy on the through thickness damage clouds and out-of-plane displacements for rigid and fragmenting projects

6.3.2 Air Blast

For the air-blast loading, Figure 6.23 shows the comparison of damage between the different levels of incident pressure. The figure shows a sectional rear view of each of the specimens along with a close up view of the damaged zone. This demonstrates the increasing rear surface damage with the increasing incident pressure of the air-blast shock-wave

as shown earlier in the Chapter. The figure also shows the transparent damage clouds for each, again clearly showing the increasing cloud area and intensity of the damage towards the centre of the cloud. Additional figures for the repeated specimens can be found in Appendix B.

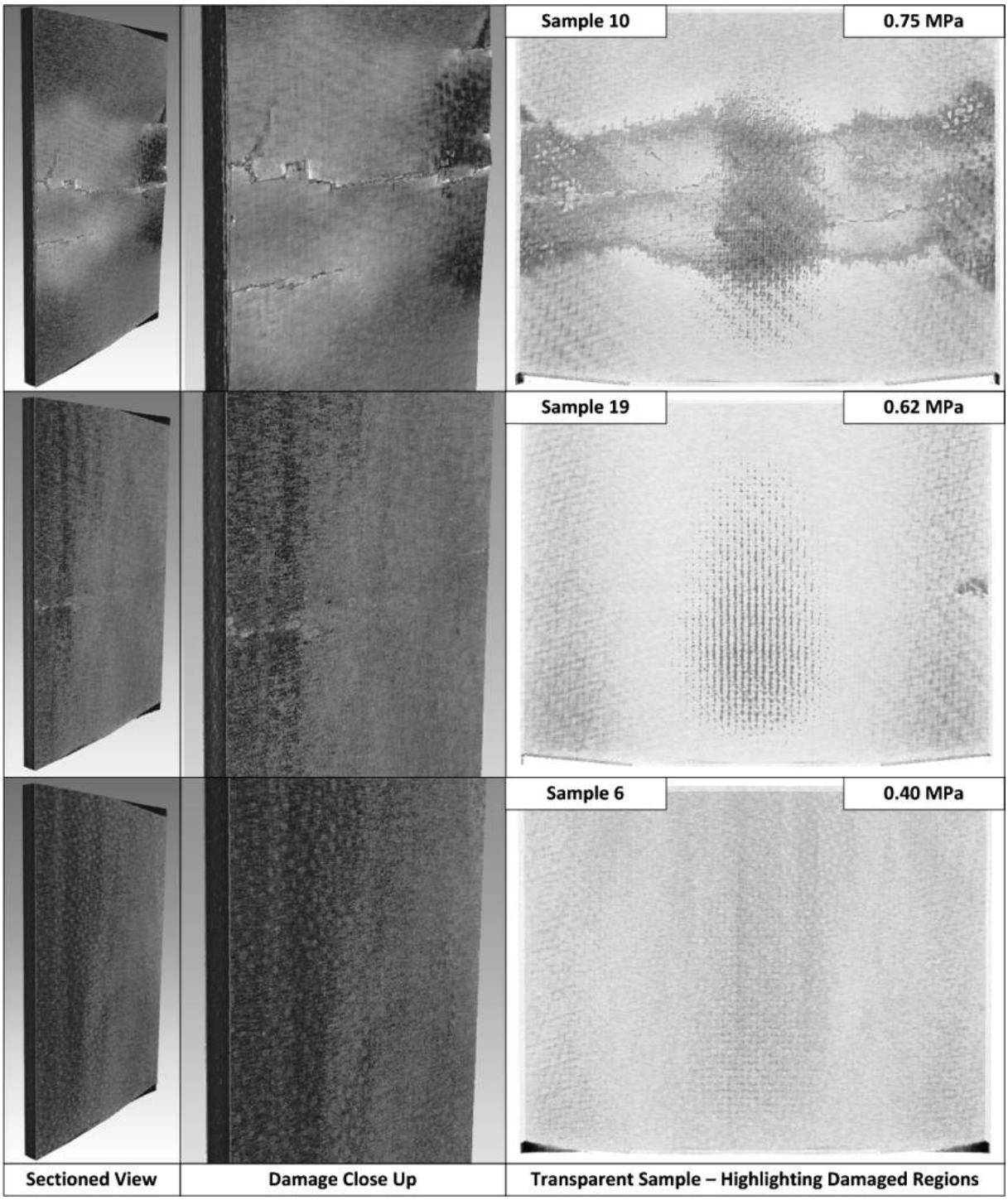

Figure 6.23: Air-blast 3D volume renders: effect of incident pressure

The damage seen across the specimens can be loosely compared to that for standard static 3-point bending. For this type of composite, the first signs of damage appear along a central line between the supports where the bending stresses were greatest. This central line of symmetry can be clearly seen in the damage cloud between the supporting locations, showing tensile fracture of the individual plies towards the centre, followed by delamination of the damaged plies towards the supports. The increasing levels of tensile failure and delamination at the free edges of the specimen can also be observed, transforming the elliptical loading area and initial damage into a central horizontal rectangular band of damage as the magnitude of the incident pressure increases.

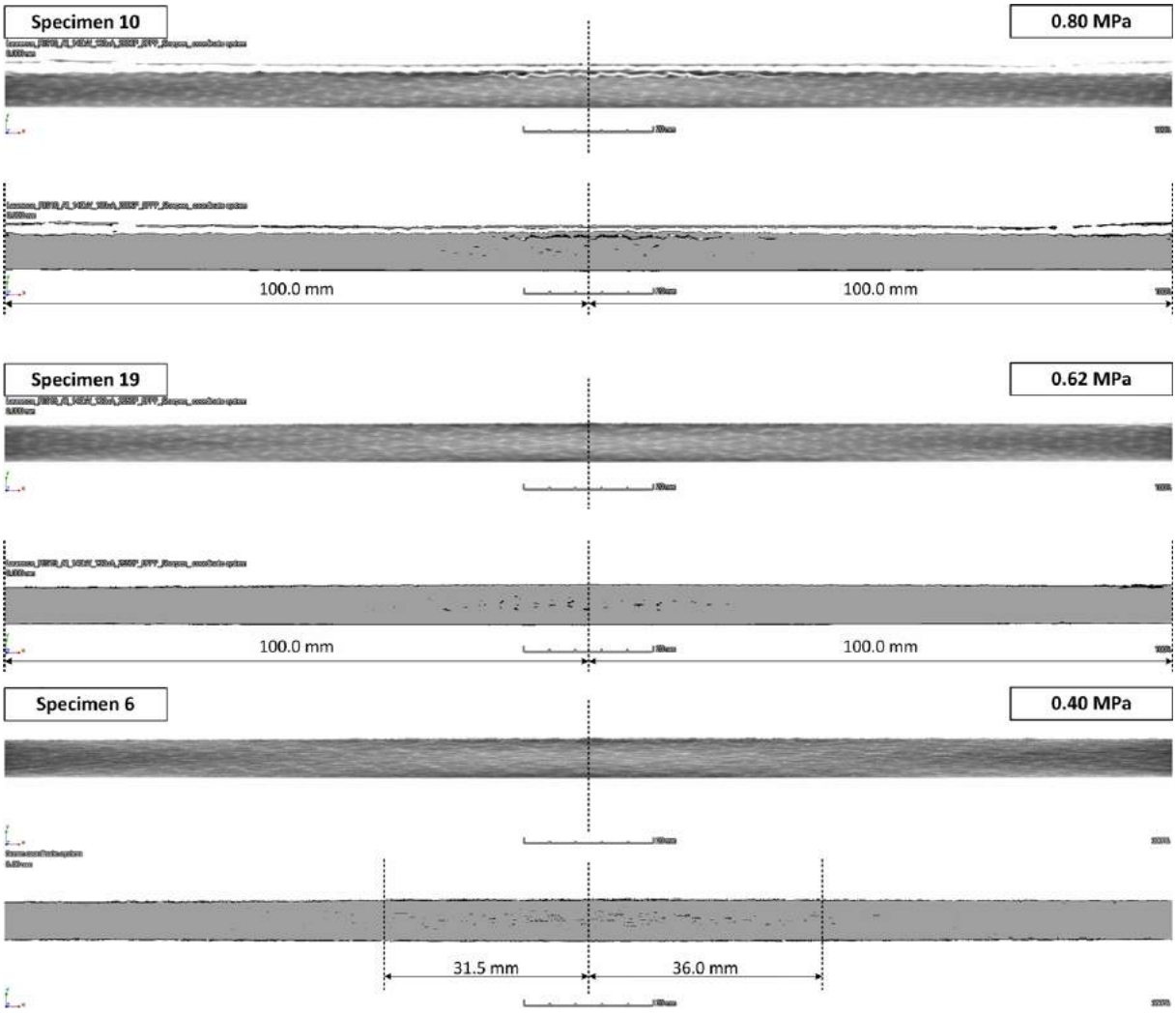

Figure 6.24: Air-blast 2D horizontal XY section: effect of incident pressure

These observations were confirmed by looking at the 2D sectional views as shown in Figures 6.24 and 6.25; the spread of the damage cloud increased with increasing incident

pressure but showed no signs of localisation either internally or at the specimen's front surface. All of the specimens exhibited symmetric damage in both the horizontal and vertical planes, which was expected given the symmetry of the specimen fixture and loading conditions. Additional figures for the repeated specimens can be found in Appendix B.

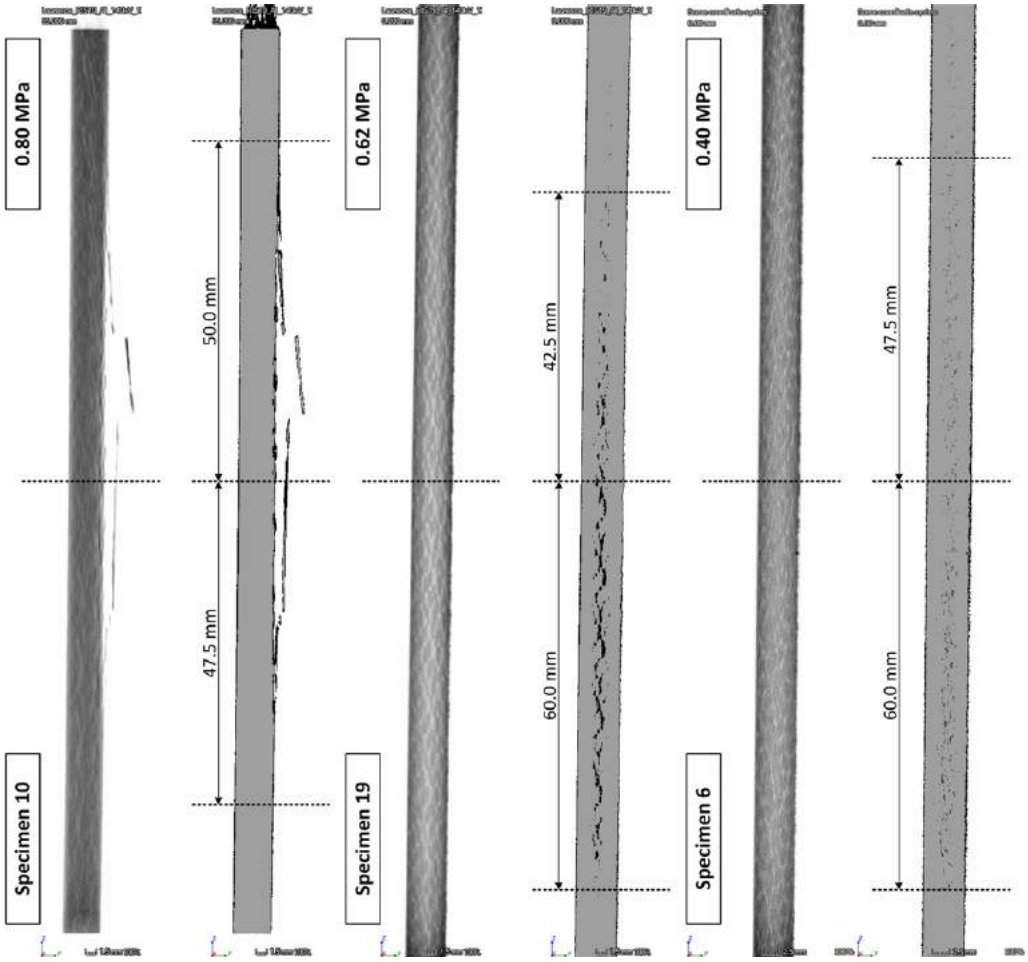

Figure 6.25: Air-blast 2D vertical YZ section: effect of incident pressure

Table 6.2 contains a summary of the horizontal and vertical spread of the observable damage and the estimated total area based upon a standard shape approximation. Although it was not obvious at lower incident pressure, the trend became more prominent with increasing pressure. As expected, after analysis of the visual damage discussed in Section 6.1, this increasing trend was shown to plateau as the major damage case was reached before then showing a sudden rise to complete damage across the whole specimen. This demonstrates that the incident pressure chosen for the major damage case (0.8 MPa) was in fact close to the critical level before complete failure, once the pressure was sufficient enough.

Table 6.2: Air-blast maximum out-of-plane displacement and damage cloud

	Damage Level	Sample	Incident Pressure (MPa)	Shockwave Velocity (m/s)	Max Out-of-plane Disp. (mm)	Damage Cloud Horizontal (mm)	Damage Cloud Vertical (mm)	Damage Shape Approx.	Damage Cloud Area (mm^2)
Air Blast	Minor	5	0.397	597.37	4.59	62.5	105	Oval	5154.18
		6	0.397	597.81	4.78	67.5	107.5	Oval	5699.05
		20	0.404	606.30	4.89	61.5	106	Oval	5120.01
		Average	0.399	600.49	4.75	-	-	Oval	5324.41
	Medium	3	0.620	744.64	7.49	200 (max)	107.5	Oval	16886.06
		15	0.626	752.32	7.70	200 (max)	102.5	Oval	16100.66
		19	0.607	778.38	7.40	200 (max)	102.5	Oval	16100.66
		Average	0.618	758.45	7.53	-	-	Oval	16362.46
	Major	2	0.696	795.14	8.83	200 (max)	103.5	Rectangle	20700.00
		10	0.801	836.42	9.61	200 (max)	97.5	Rectangle	19500.00
		Average	0.748	815.78	9.22	-	-	Rectangle	20750.00
	Failure	8	0.770	835.32	9.24	200 (max)	200 (max)	Rectangle	40000.00 (All)
		16	0.777	806.45	10.06	200 (max)	200 (max)	Rectangle	40000.00 (All)
		Average	0.773	820.89	9.65	-	-	Rectangle	40000.00 (All)

Although this 2D sectional method of analysis did allow the estimation of the damage cloud dimensions, the complexity of the actual cloud shape for the air-blast loading cases resulted in the calculated area being defined as the total spread of damage within either an elliptical shape for the minor case or a rectangle shape for the other cases.

As in the case of ballistic loading, the averaged data from Table 6.2 is presented in Figure 6.26, and confirms that there was a trend in which the damage cloud area increases and plateaus with increasing incident pressure before the pressure was sufficient enough to cause complete and catastrophic failure across the whole specimen. The maximum out-of-plane deformation also confirms the hypothesis that the major case was close to the critical point just before failure, since the complete failure occurred with only a slight increase in the incident pressure and, therefore, displacement.

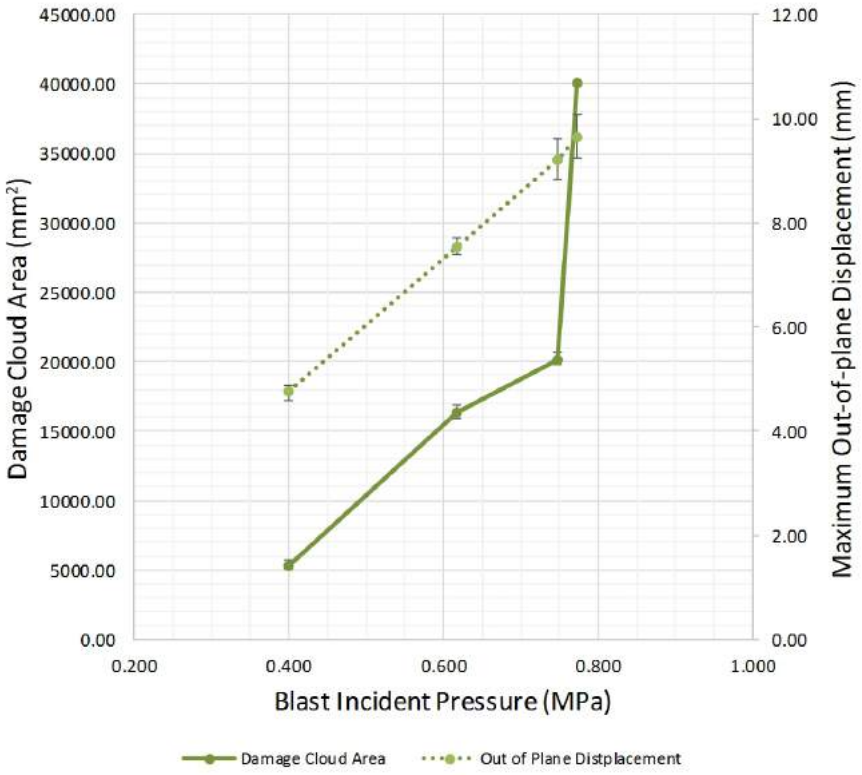

Figure 6.26: Effect of air-blast incident pressure on the through thickness damage clouds and out-of-plane displacements for rigid and fragmenting projects

6.4 Comparison between loading conditions

As mentioned in the previous chapter, drawing direct comparisons between the two different loading conditions was difficult due to different types of support fixtures and the difference in the loading areas. For the ballistic impact experiments the loading area had a ratio 0.143 between the projectile diameter and the minimum specimen dimension, whereas for the air-blast experiment the loading area ratio was 0.5 (a loading area difference of 25 mm versus 76 mm). Because of the major difference in this ratio, it would be difficult to distinguish the effect of each type of loading condition on the resultant damage. Because of this, no meaningful quantitative comparisons of the damage observed can be made between the ballastic and air-blast conditions. Still, the damage observed supports the deformation discussion from the previous chapter. The rigid projectile led to more localised indentation and therefore localised damage, then in contrast, the air-blast showed no signs of indentation and instead resulted in only damage associated with global bending. Finally, the fragmenting ice projectile then demonstrated an intermediate case, with initial indentation before transitioning to distributed global loading following the fragmentation of the projectile.

6.5 Chapter Summary

During the experimental case studies, identical CFRP specimens where subjected to three different loading regimes, each at three predetermined magnitudes of intensity. Following the full deformation analysis, X-ray tomography was used in order to obtain detailed information about the internal damage cloud in each specimen caused by each dynamic loading event. After analysing the experimental data collated, the following conclusions can be finally drawn:

- Overview

    1. Initial observations regarding the visual external damage were made for each loading condition, confirming their suitability for the chosen damage levels required for the case study.
    2. A suitable X-ray tomography scanning regime was established and used to acquire reconstructions of 180 mm x 140 mm x 20mm in volume (due to limits

of the scanner) of each specimen's internal damage, at a resultant pixel/voxel resolution of 97 μm enabling quantitative damage analysis.

- Ballistic Loading

  1. Both projectile materials and resulting impact regimes displayed two distinct types of visual damage, where for both cases the damage cloud area and its through thickness extent was shown to increase as the impact energy increased.
  2. The rigid (steel) projectiles caused localised indentation to the front surfaces, leading also to the appearance of tensile failure of the plies at the rear surface as the projectile penetrated further into the specimens. Given the localised nature of the impact, the damage cloud was limited to a slight increase in its area, keeping to a localised region as the impact energy increased.
  3. The fragmenting nature of the ice projectiles resulted in partial indentation into the specimen but, upon fragmentation below the surface (with the depth depending on the impact energy), the remains of the projectile caused catastrophic delamination of the first few front surface plies with no clear signs of any further penetration. Given the wide spread nature of the resulting visual damage, the damage cloud was found to clearly increase in area as the impact energy increased.
  4. Because of the fragmentation of the ice projectile, higher impact energies were required to observe any damage at the rear surface when compared to that of the rigid projectile, making penetration unlikely at the impact energies under study.

- Blast Loading

  1. The damage observed can be compared to that of 3-point bending, with the first signs of damage appearing along a central line between the supports at the rear surface as tensile failure of the plies leading to delamination where the bending stresses were greatest.
  2. The extent of the tensile failure at the rear surface increased with increasing air-blast pressure magnitude, suggesting that damage propagated from the rear

surface through to the front surface where no observable damage was observed until complete failure.

3. Damage was more prominent at the centre and free edges of the specimen, where the out-of-plane deformation reached the local maximum. As a result, the elliptical loading area was transformed into a central horizontal band of damage as the air-blast magnitude increased.

- Comparison of Loading Conditions

1. No direct quantitative comparison between the ballistic and air-blast loading conditions can be drawn given the difference in the support configurations and loading areas.
2. The observed damage supported the conclusions drawn with the framework of the deformation analysis for the comparison of the loading conditions.

The next chapter presents the development of a phenomenological based continuum damage modelling approach for the CFRP composite, followed by validation against the experiment results presented previously and in Chapter 5.

Chapter 7

Development of Numerical Modelling

Following the literature survey outlined in previous chapters, this chapter shall present and discuss the creation and development of a meso-scale modelling strategy for carbon fibre-reinforce polymers (CFRPs) via a phenomenological continuum damage mechanics (CDM) approach. The material model was therefore be based upon significant physically linked parameters that can be obtained via experimental and extrapolation techniques described in the next chapter.

A constitutive phenomenological material model presented in this chapter is developed with the following aims to include:

1. Physically relevant input parameters.
2. Damage evolution, including historical degradation.
3. Strain-rate sensitivity of mechanical properties.

The main objective of the constitutive phenomenological intra-ply based approach is to model a laminated CFRP composites response to high velocity ballistic impacts of both rigid vs. fragmenting projectiles, as well as air-blast shock-wave loading with reasonable accuracy while also providing full volumetric tracking of the evolution of damage and structural degradation. Full details of the modelling approach are discussed next.

7.1 Orthotropic Elasticity Relationship

For woven composite plies, the elastic stress-strain relationship is defined assuming an approximated orthotropic response where there are two planes of physical symmetry where material parameters are independent in each direction. For this behaviour, 9 parameters are required to fully describe the elastic response using a generalised Hooke's law as below:

$$\{\sigma_{ij}\} = C^0_{ijkl}\,\{\varepsilon_{kl}\}\ , \tag{7.1}$$

where σ_{ij} is the second order stress tensor, ε_{kl} is the second order strain tensor and C^0_{ijkl} is the fourth order stiffness tensor. Fully expanded, equation 7.1 can be define as follows in matrix form:

$$\begin{bmatrix}\sigma_{11}\\ \sigma_{22}\\ \sigma_{33}\\ \sigma_{12}\\ \sigma_{23}\\ \sigma_{13}\end{bmatrix} = \begin{bmatrix} C^0_{11} & C^0_{12} & C^0_{13} & 0 & 0 & 0\\ C^0_{21} & C^0_{22} & C^0_{23} & 0 & 0 & 0\\ C^0_{31} & C^0_{32} & C^0_{33} & 0 & 0 & 0\\ 0 & 0 & 0 & C^0_{44} & 0 & 0\\ 0 & 0 & 0 & 0 & C^0_{55} & 0\\ 0 & 0 & 0 & 0 & 0 & C^0_{66}\end{bmatrix} \begin{bmatrix}\varepsilon_{11}\\ \varepsilon_{22}\\ \varepsilon_{33}\\ \varepsilon_{12}\\ \varepsilon_{23}\\ \varepsilon_{13}\end{bmatrix}\ , \tag{7.2}$$

where each term is then defined as follows:

$$\begin{aligned} C^0_{11} &= \frac{1-\nu_{23}\nu_{32}}{E_2E_3\alpha}\,,\\ C^0_{22} &= \frac{1-\nu_{13}\nu_{31}}{E_1E_3\alpha}\,,\\ C^0_{33} &= \frac{1-\nu_{12}\nu_{21}}{E_1E_2\alpha}\,,\\ C^0_{12} = C^0_{21} &= \frac{\nu_{21}+\nu_{31}\nu_{23}}{E_2E_3\alpha}\,,\\ C^0_{23} = C^0_{32} &= \frac{\nu_{32}+\nu_{31}\nu_{12}}{E_1E_3\alpha}\,,\\ C^0_{13} = C^0_{31} &= \frac{\nu_{31}+\nu_{21}\nu_{32}}{E_2E_3\alpha}\,,\\ C^0_{44} &= 2G_{12}\,,\\ C^0_{55} &= 2G_{23}\,,\\ C^0_{66} &= 2G_{13}\,, \end{aligned} \tag{7.3}$$

$$\alpha = \frac{1 - \nu_{12}\nu_{21} - \nu_{23}\nu_{32} - \nu_{13}\nu_{31} - 2\nu_{12}\nu_{23}\nu_{31}}{E_1 E_2 E_3} \,. \tag{7.4}$$

7.1.1 Stiffness Degradation Following Damage Evolution

To track historical structural degradation of the composite plies during possible unloading, a damage tensor $\mathbf{d}$ is used to calculate the effective stress as a result of stiffness degradation via the continuum damage mechanics (CDM) approaches discussed in previous chapters. As a result the original generalisation for Hooke's law (Equation 7.1) can be modified as follows, to include this damage tensor which will degrade the original stiffness matrix as damage evolution progresses with time:

$$\{\sigma_{ij}\} = C^0_{ijkl}(\mathbf{d}) \{\varepsilon_{kl}\} \,. \tag{7.5}$$

This damage tensor $\mathbf{d}$ introduces a number of new damage evolution parameters; de_{f11t}, de_{f11c}, de_{f22t}, de_{f22c}, de_{m33t} and de_{m33c} which are defined as damage evolution for each of the tensile and compressive failure modes in the 3 local coordinate directions and are discussed further in Section 7.5. From these individual components, global damage evolution values can then be expressed as follows:

$$\begin{aligned} de_{f11} &= (1 - de_{f11t})(1 - de_{f11c}) \,, \\ de_{f22} &= (1 - de_{f22t})(1 - de_{f22c}) \,, \\ de_{m33} &= (1 - de_{m33t})(1 - de_{m33c}) \,. \end{aligned} \tag{7.6}$$

These global damage evolution values for fibre and matrix degradation, are considered alongside similar values for shear damage de_{s12}, de_{s23} and de_{s13} to then form the damage tensor $\mathbf{d}$ which then degrades the undamaged fourth order stiffness tensor C^0_{ijkl} via Equation 7.2. A simplified version of Equation 7.5 with damage tensor $\mathbf{d}$ is shown in Equation 7.7 following the work of Lópes et al. (2009) and Muñoz et al. (Muñoz et al.) and modified appropriately for a 2×2 twill woven composite:

$$
\begin{aligned}
C_{11} &= (1 - de_{f11})C^0_{11}\,, \\
C_{22} &= (1 - de_{f22})C^0_{22}\,, \\
C_{33} &= (1 - de_{f11})(1 - de_{f22})(1 - de_{m33})C^0_{33}\,, \\
C_{12} = C_{21} &= (1 - de_{f11})(1 - de_{f22})C^0_{12}\,, \\
C_{23} = C_{32} &= (1 - de_{f22})(1 - de_{m33})C^0_{23}\,, \\
C_{13} = C_{31} &= (1 - de_{f11})(1 - de_{m33})C^0_{13}\,, \\
C_{44} &= (1 - de_{s12})C^0_{44}\,, \\
C_{55} &= (1 - de_{s23})C^0_{55}\,, \\
C_{66} &= (1 - de_{s13})C^0_{66}\,.
\end{aligned}
\tag{7.7}
$$

All global damage parameters de_{f11}, de_{f22}, de_{m33}, de_{s12}, de_{s23} and de_{s13} are linked to damage evolution and therefore have a range of between 0 to 1, as shown in Figure 7.1 up until the point that damage initiation is reached ($O \rightarrow A$) these values will remain at 0 and will then become 1 when the material is considered to be fully damaged in the given mode ($A \rightarrow C$). Any unloading when the global damage parameters are between 0 and 1 results in reduced stiffness ($C_{ijkl} = (\mathbf{d})C^0_{ijkl}$) along the path marked from $B \rightarrow O \rightarrow B$ before further increasing the damage evolution until completely damaged. The method of calculating damage evolution is discussed in detail in Section 7.5 of this chapter.

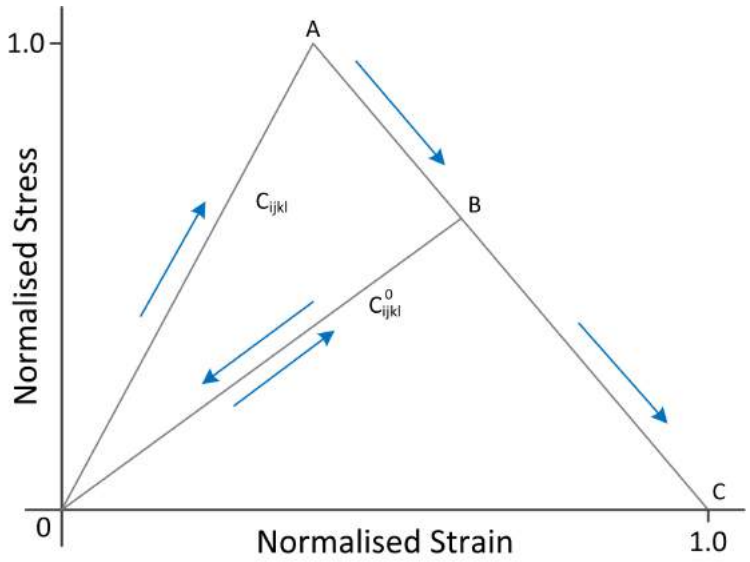

Figure 7.1: Generalised loading and unloading path with damage evolution

7.1.2 Tensile Compressive Asymmetry

In order to include asymmetrical elastic tensile and compressive difference observed during the loading of CFRPs, the strain calculated in both 11 and 22 local directions (in which the greatest asymmetry is observed) is used to determine whether the element should be considered under tensile or compression. Given the minimal difference in the out of plane 33 elastic parameters, it was determined that this approach was suitable going forward and was therefore defined as follows:

$$\begin{aligned} &\varepsilon_{11}, \varepsilon_{22}, \varepsilon_{33} \geq 0 \rightarrow Tensile\,, \\ &\varepsilon_{11}, \varepsilon_{22}, \varepsilon_{33} < 0 \rightarrow Compressive\,. \end{aligned} \tag{7.8}$$

7.2 Strain-rate Sensitivity

Many studies discussed in previous chapters discuss how the applied loading rate has shown, both an increase in stiffness and strength of laminated CFRP composites as strain-rate increases (Koerber et al. 2010, Daniel et al. 2011a). It is worth noting at this stage that there is no clear evidence to suggest that the applied strain rate has any affect on fracture energy (ultimate failure strain), therefore this element of sensitivity is not included in the presented model (Hsiao et al. 1999).

7.2.1 Effect on Elasticity

To describe the effect on the elastic parameters, the relations varies linearly with the logarithm of strain rate as defined below:

$$E\left(\dot{\varepsilon}\right) = E\left(\dot{\varepsilon_0}\right)\left[m_e \log\left(\frac{\dot{\varepsilon}}{\dot{\varepsilon_0}}\right) + 1\right], \tag{7.9}$$

where $E\left(\dot{\varepsilon}\right)$ is the updated elastic modulus at the given strain rate, $E\left(\dot{\varepsilon_0}\right)$ is the elastic modulus at the reference strain rate and m_e is a material parameter found via curve fitting to experimentally obtained data.

7.2.2 Effect on Strength

To model the strength of the laminated CFRP plies, a linear relationship with the logarithm of strain rate is defined for both normal and shear directions as defined below:

$$X\left(\dot{\varepsilon}\right) = X\left(\dot{\varepsilon_0}\right)\left[m_x \log\left(\frac{\dot{\varepsilon}}{\dot{\varepsilon_0}}\right) + 1\right], \tag{7.10}$$

where $X\left(\dot{\varepsilon}\right)$ is the updated strength at the current strain rate, $X\left(\dot{\varepsilon_0}\right)$ is the original strength at the quasi-static strain rate, $\dot{\varepsilon}$ is the current strain rate and m_x is a scaling parameter found via curve fitting to experimentally obtained data.

7.3 Damage Initiation

The laminated composite plies are modelled as a homogeneous and orthotropic material, with all the chosen failure criteria expressed in terms of stress components based on the ply-level stresses σ_{11}, σ_{22}, σ_{33}, σ_{12}, σ_{23} and σ_{13}. It should be noted that the indices 11, 22, 33, 12, 13, 23 denote the local in-plane wrap and fill fibre directions, the out of plane through thickness direction and finally the shear planes respectively for a woven composite ply. By considering the full 3D stress states, rather than 2D which is typical of the shell element approach, the model can provide an accurate representation of the stress field through the thickness of the individual plies.

7.3.1 Fibre Failure Modes

In order to evaluate fibre failure modes within the plies, a modified version of Hashin's failure criteria was adapted for the woven composite plies (Hashin 1980):

Tensile Fibre Failure - Fill 11 Direction

$$\left(\frac{\sigma_{11}}{X_{11t}^{dyn}}\right)^2 + \left(\frac{\sigma_{12}}{S_{12}}\right)^2 + \left(\frac{\sigma_{13}}{S_{13}}\right)^2 \geq 1, \quad di_{f11t} = 1\,, \tag{7.11}$$

Tensile Fibre Failure - Wrap 22 Direction

$$\left(\frac{\sigma_{22}}{X_{22t}^{dyn}}\right)^2 + \left(\frac{\sigma_{12}}{S_{12}}\right)^2 + \left(\frac{\sigma_{23}}{S_{23}}\right)^2 \geq 1, \quad di_{f22t} = 1\,, \tag{7.12}$$

Compressive Fibre Failure - Fill 11 Direction

$$\left(\frac{\sigma_{11}}{X_{11c}^{dyn}}\right) + \left(\frac{\sigma_{12}}{S_{12}}\right) + \left(\frac{\sigma_{13}}{S_{13}}\right) \geq 1, \quad di_{f11c} = 1\,, \tag{7.13}$$

Compressive Fibre Failure - Wrap 22 Direction

$$\left(\frac{\sigma_{22}}{X_{22c}^{dyn}}\right) + \left(\frac{\sigma_{12}}{S_{12}}\right) + \left(\frac{\sigma_{23}}{S_{23}}\right) \geq 1, \quad di_{f22c} = 1\,. \tag{7.14}$$

7.3.2 Matrix Failure Modes

To evaluate matrix failure modes within the plies, a modified version of Puck and Schürmann failure criteria was adapted for the woven composite plies and matrix failure relating to any of the directions within the 3D continuum elements (Puck and Schürmann 1998):

Matrix Failure

$$\begin{aligned}\left(\frac{\sigma_{11}^2}{2X_{11}^{dyn}}\right) + \left(\frac{\sigma_{22}^2}{2X_{22}^{dyn}}\right) + \left(\frac{\sigma_{12}}{S_{12}}\right)^2 + \left(\frac{\sigma_{13}}{S_{13}}\right)^2 + \left(\frac{\sigma_{23}}{S_{23}}\right)^2 \\ + \left(\frac{\sigma_{33}^2}{X_{33t}^{dyn} X_{33c}^{dyn}}\right) + \sigma_{33}\left(\frac{1}{X_{33t}^{dyn}} + \frac{1}{X_{33c}^{dyn}}\right) \geq 1\,, \\ Tensile \rightarrow \sigma_{33} > 0, \quad di_{m33t} = 1\,, \\ Compressive \rightarrow \sigma_{33} < 0, \quad di_{m33c} = 1\,.\end{aligned} \tag{7.15}$$

7.4 Shear response

The shear response of a FRC is often dominated by the non-linear behaviour of the matrix while undergoing stiffness degradation, which has been found to be a result of combined micro cracking and plasticity. Therefore the non-linear semi-empirical shear model originally proposed by Berbinau et al. (1999; 1999) as shown in Equation 7.16 has been included within the presented model to capture this behaviour in each of the shear directions:

$$\tau_{ij} = S_{ij}\left[1 - exp\left(-\frac{G_{ij}^0 \gamma_{ij}}{S_{ij}}\right)\right], \tag{7.16}$$

where S_{ij} is the ultimate shear strength, G_{ij}^0 is the shear modulus and γ_{ij} is the instantaneous shear strain. Then damage initiation in each of the shear directions is then calculated as follows:

$$di_{ij} = \frac{\sigma_{ij}}{S_{ij}}\,, \tag{7.17}$$

where σ_{ij} is the shear stress and S_{ij} is the ultimate shear strength.

7.5 Damage Evolution

For a linear elastic brittle material like a CFRP, both damage initiation and evolution will accumulate along a bilinear path like the one shown in Figure 7.2 for each of tensile and compressive failure modes in the 3 local coordinate directions. The initial positive slope ($O \rightarrow A$) corresponds to the linear elastic behaviour up until damage is fully initiated (Equations 7.11 - 7.15 in Section 7.3), after which the negative slope ($A \rightarrow C$) is defined as stiffness degrading damage evolution.

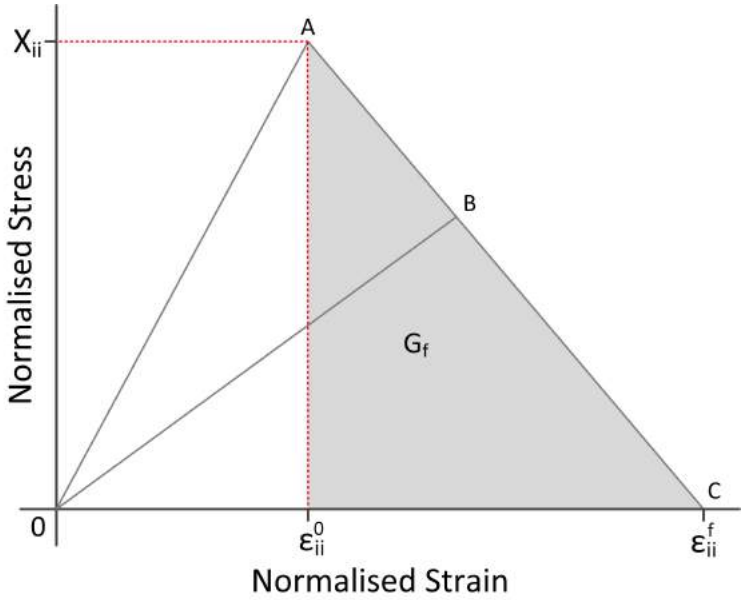

Figure 7.2: Generalised loading and unloading path with damage evolution

This approach to continuum stiffness degradation has been developed in order to be suitable for the presented 2 x 2 twill woven CFRP, and is calculated as follows for each of the six damage modes:

$$de_{ii} = \frac{\varepsilon_{ii}^{f}\left(\varepsilon_{ii} - \varepsilon_{ii}^{0}\right)}{\varepsilon_{ii}\left(\varepsilon_{ii}^{f} - \varepsilon_{ii}^{0}\right)}, \tag{7.18}$$

where ε_{ii} is the current equivalent strain, ε_{ii}^{0} is the equivalent strain at which damage initiation $di_{ii} = 1$ and is obtained during calculation of di_{ii} and cannot be overridden once stored, ε_{ii}^{f} is the strain at which damage evolution is complete $de_{ii} = 1$ (fully damaged) and ε_{ii} is the current strain component. A form of Equation 7.18 is then used to calculate the damage evolution for each of the tensile and compressive failure modes in the 3 local coordinate directions, and so de_{ii} is defined as de_{f11t}, de_{f11c}, de_{f22t}, de_{f22c}, de_{m33t} and

de_{m33c}. Once calculated, these individual values are combined into the 3 local coordinate directions using Equation 7.6, to then show the global damage evolution value (de_{f11}, de_{f22}, de_{m33}) which are then used for stiffness degradation once the CFPR plies become damaged using Equation 7.7 all defined back in Section 7.1.

For the shear directions in which non-linear behaviour is included, the non-linear strain model needs to be split into its elastic component γ_{ij}^{e} and in-elastic component γ_{ij}^{in} as below (Shi et al. 2012):

$$\gamma_{ij}^{in} = \gamma_{ij} - \gamma_{ij}^{e} = \gamma_{ij} - \frac{\tau_{ij}}{G_{ij}^{0}}\,, \tag{7.19}$$

where τ_{ij} is the non-linear shear stress in each direction, and G_{ij}^{0} is the shear modulus in each shear direction. Then in order to calculate the damage evolution of each of the shear directions follow damage initiation, Equation 7.18 must be updated to account for the non-linear shear behaviour and the offset of the damage initiation strain. The modified version of this equation is shown below:

$$de_{ij} = \frac{\gamma_{ij}^{f}\left[2\left(\gamma_{ij} - \gamma_{ij,0}^{in}\right) - \gamma_{ij}^{f}\right]}{\left(\gamma_{ij}^{f} + \gamma_{ij,0}^{in} - \gamma_{ij}\right)\left(\gamma_{ij} - \gamma_{ij,0}^{in}\right)}\,, \tag{7.20}$$

where γ_{ij} is the instantaneous shear strains, $\gamma_{ij,0}^{in}$ is the inelastic shear strain at damage initiation, and γ_{ij}^{f} is the shear failure strain.

When considering the loading and unloading case mentioned earlier like path $B \rightarrow O \rightarrow B$ in Figure 7.2, it is important to consider the correct time at which damage begins to evolve irreversibly. Therefore the following have be added to ensure damage propagates correctly in time:

$$\varepsilon_{ii} = max(\varepsilon_{ii}, \varepsilon_{ii}^{0})\,, \tag{7.21}$$

$$\begin{aligned} de_{ii} > de_{ii-1} \quad &\rightarrow \quad de_{ii} = de_{ii}\,, \\ de_{ii} < de_{ii-1} \quad &\rightarrow \quad de_{ii} = de_{ii-1}\,. \end{aligned} \tag{7.22}$$

The failure strain ε_{ii}^{f} is then calculated from the defined failure energies; G_{ft}, G_{fc}, G_{mt}, G_{mc} and G_{sh} (J/m^2), and is derived as follows, shear failure strains γ_{ij}^{f} are calculated in the same way:

$$G_f = \int_0^{\delta_f} \sigma(u).du \quad \rightarrow \quad G_f = \frac{1}{2} X_{ii} \delta_{ii}^f \,, \tag{7.23}$$

$$\delta_{ii}^f = \frac{2G_f}{X_{ii}} \,. \tag{7.24}$$

The mesh dependency of this calculation was then resolved by converting the displacement to strain in the given direction using the characteristic length of the element (L_e) as proposed by Lapczyk and Hurtado (2007), such that $\delta_{ii}^f = L_e \varepsilon_{ii}^f$ making the final form as follows:

$$\varepsilon_{ii}^f = \frac{2G_f}{X_{ii} L_e} \,. \tag{7.25}$$

7.6 Element Deletion Criteria

Element deletion was employed to remove elements once failure criteria had been met, and the damage has fully evolved as calculated in Equation 7.18 using d_{f11t}, d_{f11c}, d_{f22t}, d_{f22c}, d_{m33t} and d_{m33c}. Due to the woven nature of laminated CFRP composites, elements will only be removed once the damage values associated with fibre failure d_{f11} and d_{f22} reach maximum damage = 1 at the internal integration point of the element. When one of these conditions are met in either the 11 or 22 direction, the element is removed from the mesh and offers no subsequent support during deformation. In order to avoid numerical difficulties, each damage variable was limited to 0.999 so that the elements retain some residual stiffness.

7.7 User-Defined Subroutine

A vectorised user-defined material subroutine (VUMAT) was written in Fortran 77, and was implemented into the ABAQUS Explicit (6.14-4) solver given the inclusion of; time dependence for loading, inertia effects, ability to handle complex contact interactions and element deletion to account for material failure. In its general form, the implementation process for the VUMAT subroutine follows the steps outlined below in order to model the intra-ply composite behaviour:

1. Call the VUMAT subroutine with the iterative strain and time increments, then read in all relavent material parameters and existing state dependant variables (SDVs).
2. Initiate the first stress state when time = 0, and set initial state dependant variable (SDV) values.
3. Update total strain and strain rate components from the previous increments, update all elastic components with reference to the current strain rates and then determine if the integration point (element) is in tension or compression.
4. Construct the stiffness matrix and calculate and update the current components of stress.
5. Update all failure (strength) values with reference to the current strain rates and then determine the damage initiation value using the Hashin's and Puck's failure criteria (0-1).
6. Once damage initiation is = 1, calculation damage evolution and determine the degradation of the material and therefore stiffness matrix.
7. If damage evolution values are > 0 and larger than the previous step, then also recalculate the reducing stress and overwrite the previous value.
8. If damage evolution values are = 1 in either of the fibre directions, flag and element for deletion and return to ABAQUS.

A fully detailed flowchart of this modelling approach is presented in Figures 7.3 - 7.6. Figure 7.3 presents the main structure of VUMAT subroutine, then Figures 7.4 - 7.6 outlined the damage algorithm that includes; the damage initiation based on the Hashin's and Puck's theories as discussed in Section 7.3, the damage evolution based on the criteria discussed in Section 7.5, and finally the element-deletion strategy as discussed in Section 7.6. A full breakdown of the material parameters and state dependant variables used in this VUMAT are then listed in Tables 7.1 - 7.3.

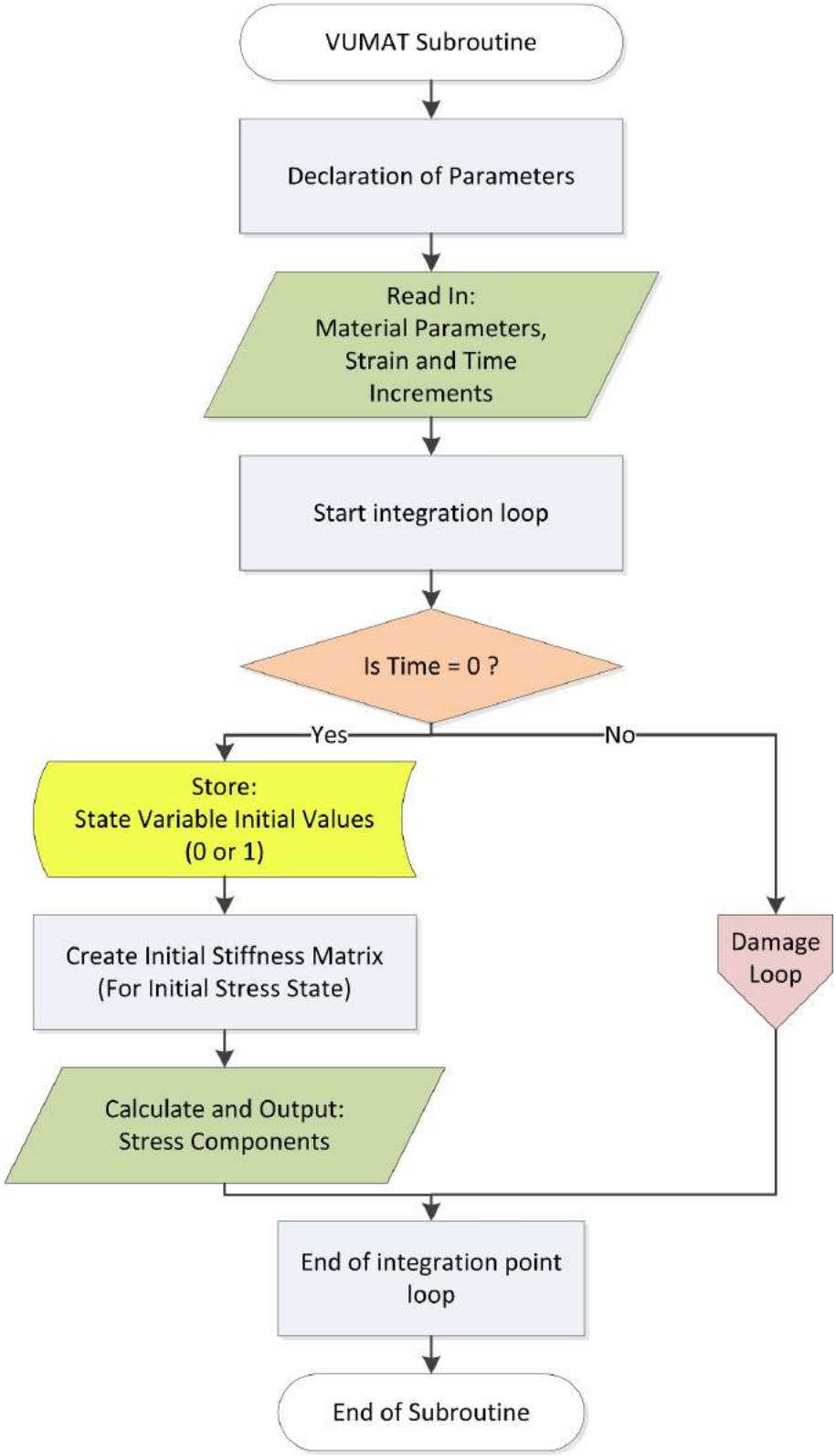

Figure 7.3: Main structure of the VUMAT phenomenological intra-ply based modelling approach

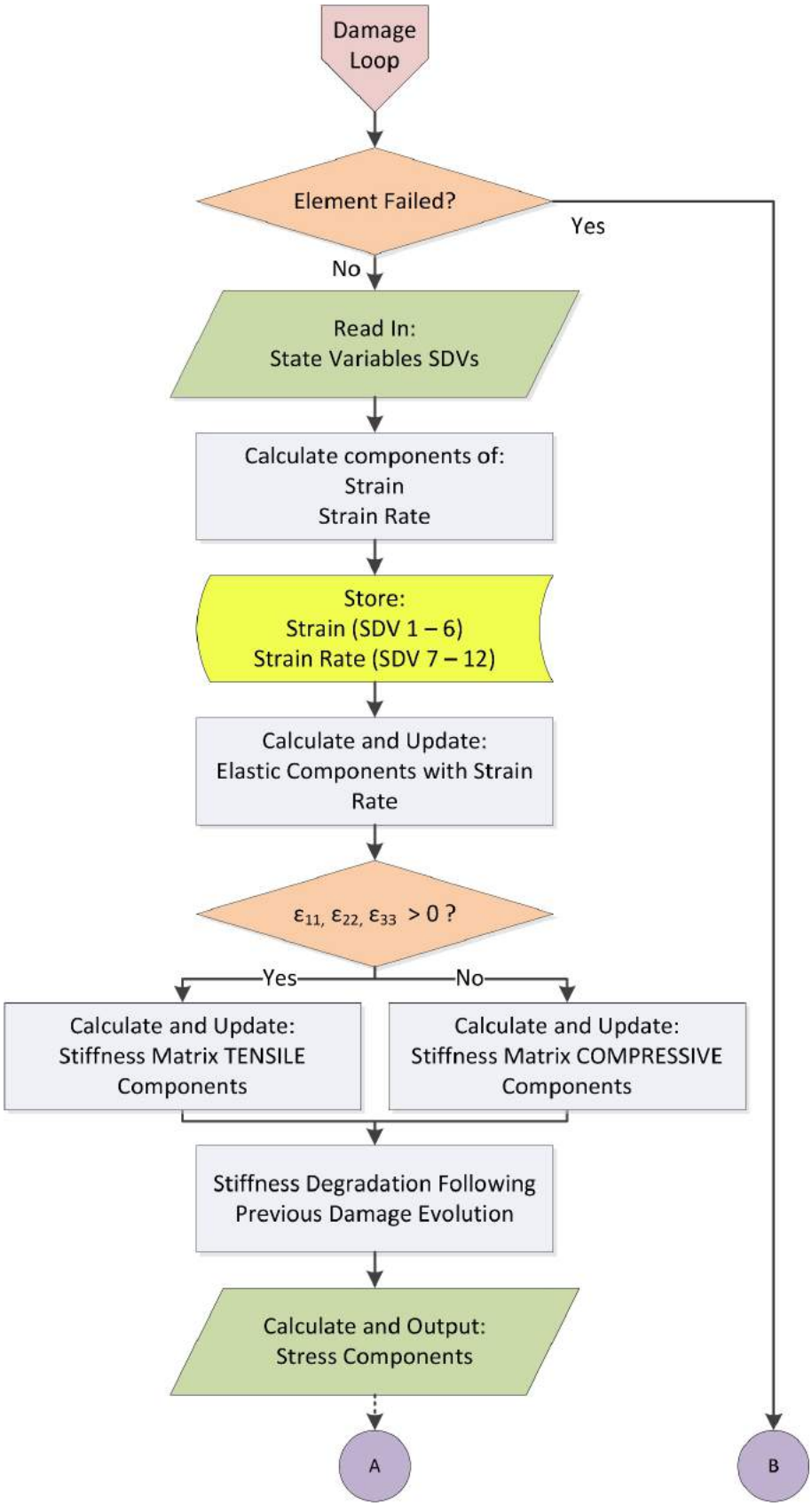

Figure 7.4: Damage loop of the VUMAT phenomenological intra-ply based modelling approach (Part 1 of 3)

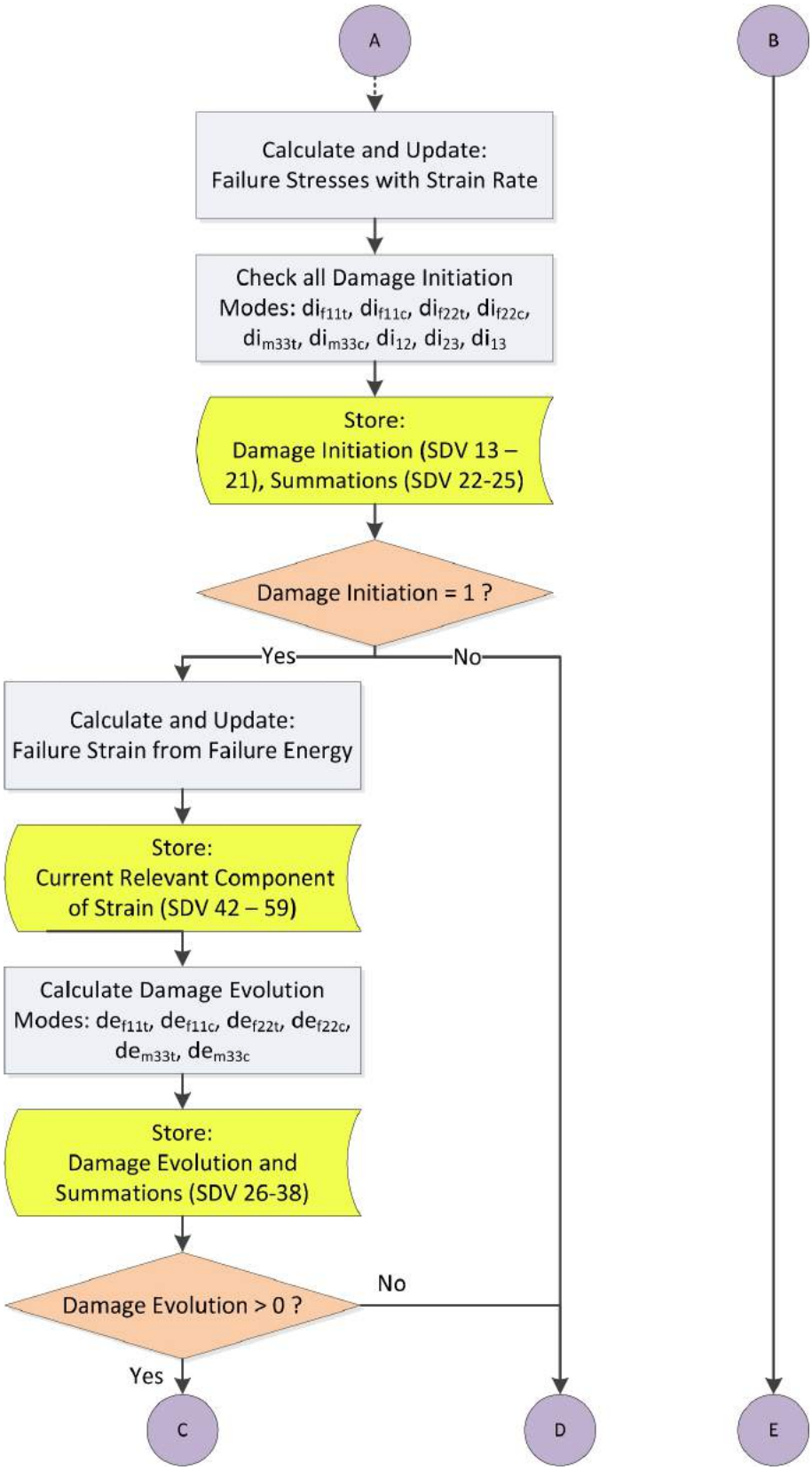

Figure 7.5: Damage loop of the VUMAT phenomenological intra-ply based modelling approach (Part 2 of 3)

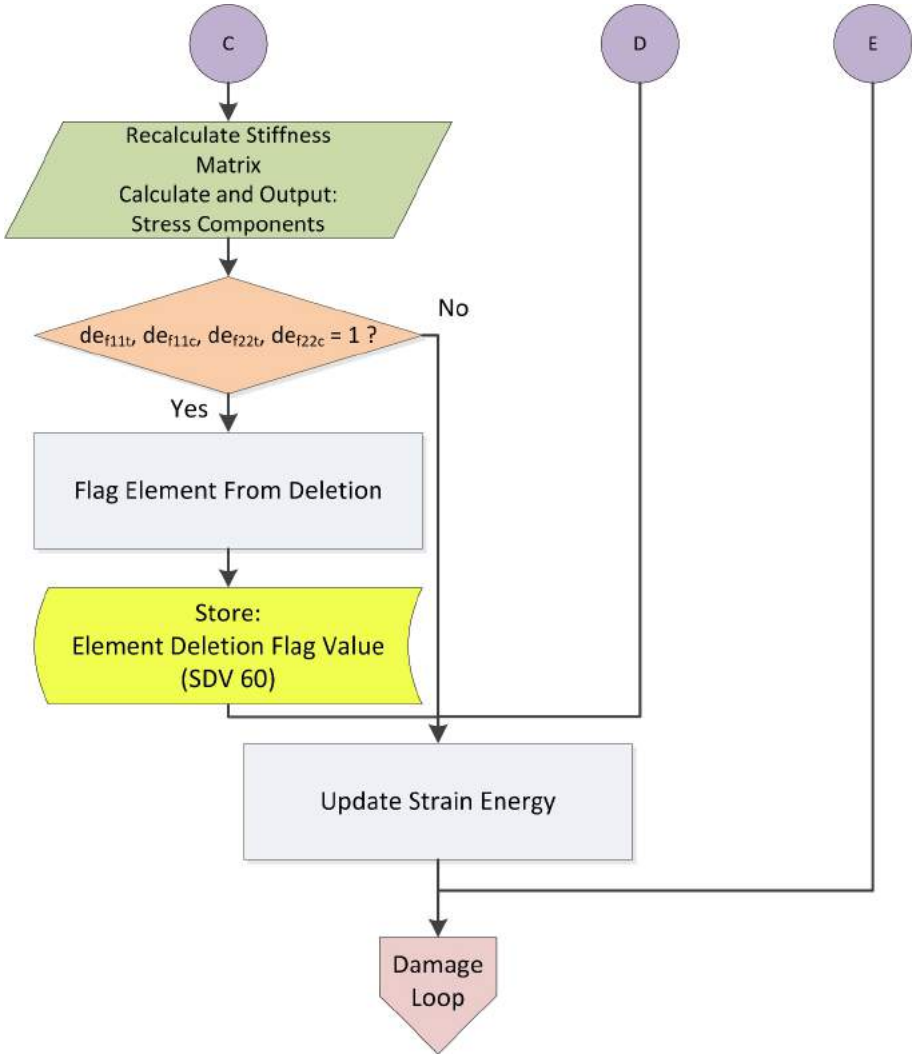

Figure 7.6: Damage loop of the VUMAT phenomenological intra-ply based modelling approach (Part 3 of 3)

Table 7.1: Material elastic parameters used with the defined VUMAT model

Parameter	Unit	Description
E_{11t}	(GPa)	Tensile elastic modulus in fibre 11 direction
E_{22t}	(GPa)	Tensile elastic modulus in fibre 22 direction
E_{33t}	(GPa)	Tensile elastic modulus in through ply direction
E_{11c}	(GPa)	Compressive elastic modulus in fibre 11 direction
E_{22c}	(GPa)	Compressive elastic modulus in fibre 22 direction
E_{33c}	(GPa)	Compressive elastic modulus in through ply direction
ν_{12}	-	Poisson's ratio in 12 plane
ν_{23}	-	Poisson's ratio in 23 plane
ν_{13}	-	Poisson's ratio in 13 plane
G_{12}	(GPa)	Shear modulus in 12 plane
G_{23}	(GPa)	Shear modulus in 23 plane
G_{13}	(GPa)	Shear modulus in 13 plane

Table 7.2: Material damage parameters used with the defined VUMAT model

Parameter	Unit	Description
X_{11t}	(MPa)	Tensile failure strength in fibre 11 direction
X_{22t}	(MPa)	Tensile failure strength in fibre 22 direction
X_{11c}	(MPa)	Compressive failure strength in fibre 11 direction
X_{22c}	(MPa)	Compressive failure strength in fibre 22 direction
X_{33t}	(MPa)	Tensile failure strength in through ply 33 direction
X_{33c}	(MPa)	Compressive failure strength in through ply 33 direction
S_{12}	(MPa)	Shear failure strength in 12 plane
S_{23}	(MPa)	Shear failure strength in 23 plane
S_{13}	(MPa)	Shear failure strength in 13 plane
G_{ft}	(J/m^2)	Tensile damage evolution energy - fibre (11 & 22)
G_{fc}	(J/m^2)	Compressive damage evolution energy - fibre (11 & 22)
G_{mt}	(J/m^2)	Tensile damage evolution energy - through ply (33)
G_{mc}	(J/m^2)	Compressive damage evolution energy - through ply (33)
G_{sh}	(J/m^2)	Shear damage evolution energy

Table 7.3: Output SDVs used with the defined VUMAT model

SDV	Symbol	Description	
SDV 1 - 6	$\varepsilon_{11}, \varepsilon_{22}, \varepsilon_{33}, \varepsilon_{12}, \varepsilon_{23}, \varepsilon_{13}$	Components of strain	
SDV 7 - 12	$\dot{\varepsilon}_{11}, \dot{\varepsilon}_{22}, \dot{\varepsilon}_{33}, \dot{\varepsilon}_{12}, \dot{\varepsilon}_{23}, \dot{\varepsilon}_{13}$	Components of strain rate	
13	di_{f11t}	DI	Tensile in fibre 11 direction
14	di_{f22t}		Tensile in fibre 22 direction
15	di_{f11c}		Compressive in fibre 11 direction
16	di_{f22c}		Compressive in fibre 22 direction
17	di_{m33t}		Tensile in through ply 33 direction
18	di_{m33c}		Compressive in through ply 33 direction
19 - 21	di_{12}, di_{23},di_{13}		Shear in 12, 23, 13 plane
22 - 24	di_{f11}, di_{f22}, di_{m33}	DI	Summation in normal directions
25	di_{sh}		Summation in shear directions
26	de_{f11t}	DE	Tensile in fibre 11 direction
27	de_{f22t}		Tensile in fibre 22 direction
28	de_{f11c}		Compressive in fibre 11 direction
29	de_{f22c}		Compressive in fibre 22 direction
30	de_{m33t}		Tensile in through ply 33 direction
31	de_{m33c}		Compressive in through ply 33 direction
32 - 34	de_{f11}, de_{f22}, de_{m33}	DE	Summation in normal directions
35	de_{12}	DE	Shear 12 direction
36	de_{23}		Shear 23 direction
37	de_{13}		Shear 13 direction
38	de_{sh}	DE	Summation in shear directions
39 - 41	ε_{p12}, ε_{p23}, ε_{p13}	Components of plastic strain	
42 - 59	ε_{ii}^{0}, ε_{ii}^{f}	Initiation and failure strains	
60	$lDelFlag$	Element deletion flag	

7.8 Validation of User-Defined Model: Charpy Impact

Validation of the constitutive phenomenological intra-ply based VUMAT model was conducted via direct comparison to Charpy impact hammer tests on the same CFRP composite described throughout the presented research, this method was chosen following successful single element testing as the damage mechanisms would differ between an in-plane and out-of-plane impact resulting in a more comprehensive validation. For these Charpy hammer impact experiments, samples of the 5.6 mm thick 2 x 2 Twill woven CFRP were cut to 55 x 10 mm and positioned for either an in-plane or out-of-plane impact as shown in Figure 7.7. The idea is to minimise the presents of delamination in the in-plane impact and focus on the ply behaviour and VUMAT performance, and then include it in the out-of-plane impact to add in the cohesive zone surface behaviour. While this method will not confirmed the validity of the developed model completely given the complex nature of the behaviour, it does give the opportunity to validate against the type of characteristic behaviour seen and check the various outputs are within the correct orders of magnitude to set a good foundation going forward. The model presented was created using the commercial software ABAQUS 6.14, with an integrated User Defined Subroutine (VUMAT) for the CFRP model. Four physical samples were subjected to each of the Charpy hammer impact test orientations, the results are presented in Table 7.4 below.

Table 7.4: Charpy impact hammer experimental test results (J)

Sample	No. 1	No. 2	No. 3	No. 4	Average
In-Plane	7.66	8.96	7.73	8.41	8.19
Out-Plane	6.87	7.49	6.80	7.35	7.13

Both the supports and hammer were assumed to be rigid bodies, with the CFRP specimen containing 132160 eight-node, isoparametric, hexahedral elements (C3D8R) after mesh convergence with 2 elements through the thickness of the surfaces plies and 3 element through the thickness of the bulk plies. The striker was given a predefined velocity of 3.1235 m/s to match that of the experiment, and the density was scaled in order to achieve the required striker kinetic energy of 10 J.

The material parameters used within the VUMAT described previously can be found in Tables 7.5 & 7.6, these parameters were derived from experimental testing of the CFRP

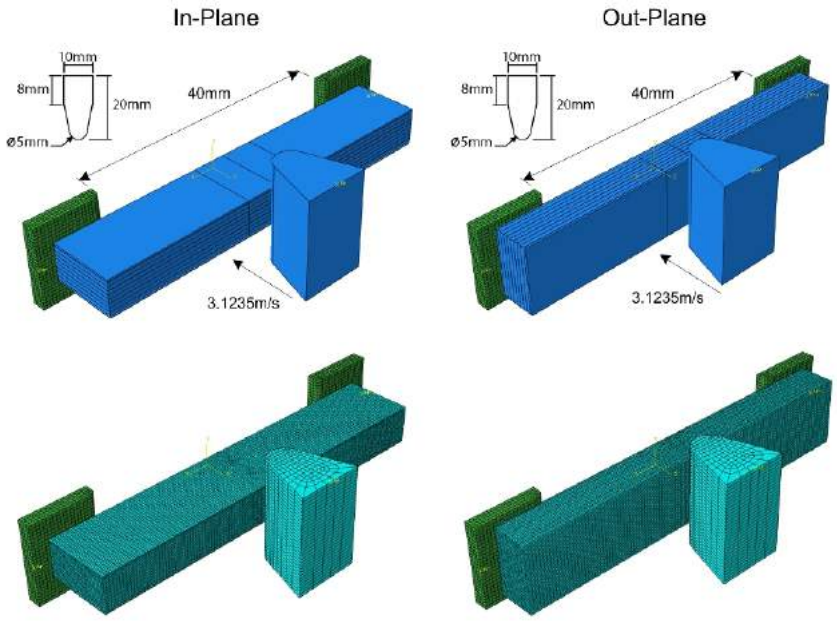

Figure 7.7: Charpy impact hammer validation model setup

described previously as well as additional extrapolation of some parameters against referenced experimental papers. A full explanation of how the parameters were extrapolated and obtained can be found in Chapter 8 next.

Table 7.5: VUMAT elastic material parameters for woven CFRP

(a) Material elastic parameters (quasi-static)

Parameter	Value	Unit
E_{11t}^{Quasi}	51.0	(GPa)
E_{22t}^{Quasi}	51.0	(GPa)
E_{33t}^{Quasi}	8.0	(GPa)
E_{11c}^{Quasi}	45.4	(GPa)
E_{22c}^{Quasi}	45.4	(GPa)
E_{33c}^{Quasi}	8.0	(GPa)
ν_{12}^{Quasi}	0.06	-
ν_{23}^{Quasi}	0.3	-
ν_{13}^{Quasi}	0.3	-
G_{12}^{Quasi}	4.0	(GPa)
G_{23}^{Quasi}	3.0	(GPa)
G_{13}^{Quasi}	3.0	(GPa)

(b) Material elastic parameters (dynamic)

Parameter	Value	Unit
E_{11t}^{Dyn}	52.2	(GPa)
E_{22t}^{Dyn}	52.2	(GPa)
E_{33t}^{Dyn}	8.0	(GPa)
E_{11c}^{Dyn}	46.5	(GPa)
E_{22c}^{Dyn}	46.5	(GPa)
E_{33c}^{Dyn}	9.6	(GPa)
ν_{12}^{Dyn}	0.06	-
ν_{23}^{Dyn}	0.3	-
ν_{13}^{Dyn}	0.3	-
G_{12}^{Dyn}	5.2	(GPa)
G_{23}^{Dyn}	3.9	(GPa)
G_{13}^{Dyn}	3.9	(GPa)

Table 7.6: VUMAT damage material parameters for woven CFRP

(a) Material damage parameters (quasi-static)

Parameter	Value	Unit
X_{11t}^{Quasi}	520.0	(MPa)
X_{22t}^{Quasi}	520.0	(MPa)
X_{11c}^{Quasi}	471.4	(MPa)
X_{22c}^{Quasi}	471.4	(MPa)
X_{33t}^{Quasi}	73.0	(MPa)
X_{33c}^{Quasi}	320.1	(MPa)
S_{12}^{Quasi}	100.0	(MPa)
S_{23}^{Quasi}	100.0	(MPa)
S_{13}^{Quasi}	100.0	(MPa)
G_{ft}^{Quasi}	75000	(J/m^2)
G_{fc}^{Quasi}	25000	(J/m^2)
G_{mt}^{Quasi}	2500	(J/m^2)
G_{mc}^{Quasi}	2500	(J/m^2)
G_{sh}^{Quasi}	2250	(J/m^2)

(b) Material damage parameters (dynamic)

Parameter	Value	Unit
X_{11t}^{Dyn}	594.2	(MPa)
X_{22t}^{Dyn}	594.2	(MPa)
X_{11c}^{Dyn}	849.9	(MPa)
X_{22c}^{Dyn}	849.9	(MPa)
X_{33t}^{Dyn}	107.8	(MPa)
X_{33c}^{Dyn}	348.6	(MPa)
S_{12}^{Dyn}	194.9	(MPa)
S_{23}^{Dyn}	194.9	(MPa)
S_{13}^{Dyn}	194.9	(MPa)
G_{ft}^{Dyn}	75000	(J/m^2)
G_{fc}^{Dyn}	25000	(J/m^2)
G_{mt}^{Dyn}	2500	(J/m^2)
G_{mc}^{Dyn}	2500	(J/m^2)
G_{sh}^{Dyn}	2250	(J/m^2)

Delamination of the individual CFRP plies was achieved using a bi-linear traction-separation cohesive zone surface model with a quadratic norminal stress criterion which is again fully explained in Chapter 8 next, however the parameters used are presented in Table 7.7 below following work by Turon et al. (2007).

When examining the samples post impact test (Figure 7.9), it is clear that tensile fibre failure is the dominant damage mode for both orientations with delamination being present for the out-of-plane orientation. In comparison to the model results shown in Figure 7.9, tensile fibre failure along the length of the sample shown as SDV 27 (direction 22) is captured reasonably accurately (apart from the perfect failure in comparison to the more random failure in reality). The same may be said for the observed delamination as shown by CSDMG, where minimal occurs for the in-plane orientation as to be expected and then more substantial separation of the plies occurs for the out-of-plane orientation. Figure 7.8 then compares the energy absorption observed within the two models against the average captured by the experiments, the results from the model show good agreement of the user defined material subroutine for the CFRP to its actual physical behaviour.

Table 7.7: Delamination material parameters for twill woven CFRP (Turon et al. 2007; Mendes and Donadon 2014)

Parameter	Value	Unit
k_n^o	7.45E-5	(GPa)
k_t^o	2.87E-5	(GPa)
k_s^o	2.87E-5	(GPa)
t_n^o	73.0	(MPa)
t_t^o	100.0	(MPa)
t_s^o	100.0	(MPa)
G_n^o	600	(J/m^2)
G_t^o	5500	(J/m^2)
G_s^o	5500	(J/m^2)

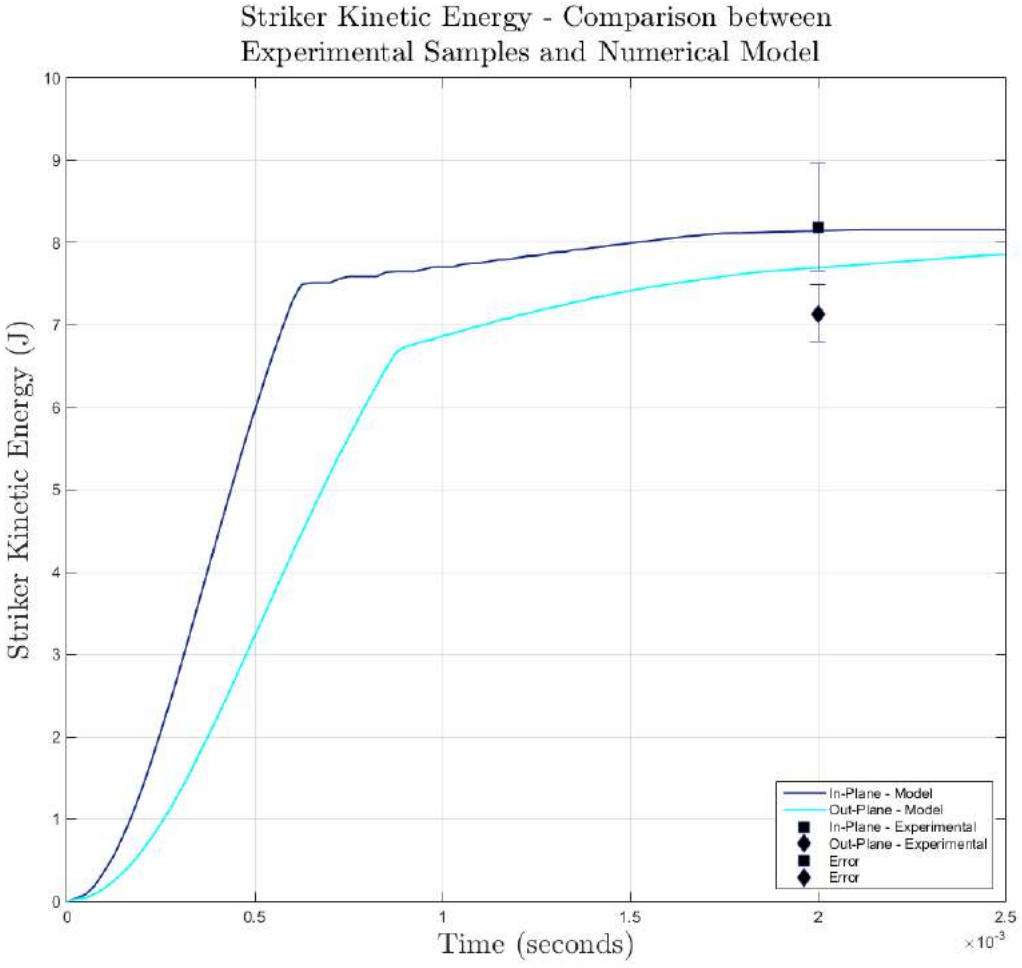

Figure 7.8: Charpy impact hammer validation model setup

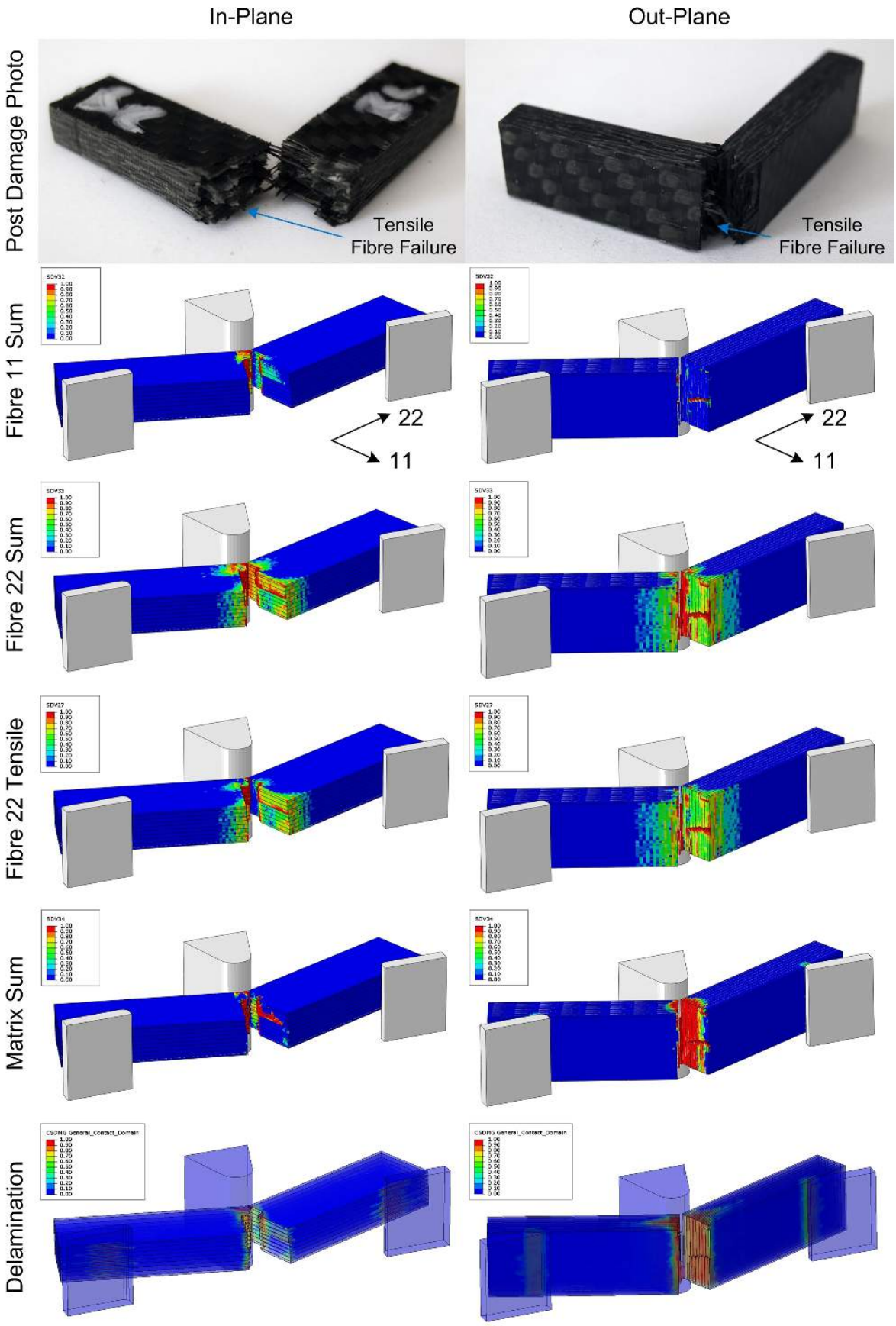

Figure 7.9: Charpy impact hammer model results

7.9 Chapter Summary

In summary, a meso-scale modelling strategy for carbon fibre-reinforce polymers (CFRPs) via a phenomenological continuum damage approach has been proposed, with initial validation efforts showing that the model functions as intended and provides good similarity to experimental data. The VUMAT model delivers accurate through-thickness stress responses, strain-rate sensitive behaviour for both stiffness and strength, and full damage-initiation and evolution tracking with stiffness degradation. The model combines the advantages of previously proposed damage models by Hashin (1980) and by Puck and Schürmann (1998), which were suitably modified in order to model a woven laminate along with the through-thickness stress response. Damage evolution is then modelled using the concept of equivalent displacement until failure, with mesh-sensitivity being mitigated by incorporating the characteristic length of a finite-element in the formulation.

The developed material model was implemented in ABAQUS Explicit FE software, which is used for effectively simulating dynamic events with damage propagation until failure with element deletion. The motivation behind the development of this model is to analyse the response of the laminated woven composite, described in previous chapters, under various dynamic loading conditions. These include ballistic-impact of both rigid and fragmenting projectiles as well as air-blasts, following the additional validation of the VUMAT subroutine mentioned previously.

In the next chapter, the developed phenomenological continuum damage approach is used to model the ballistic impact response of both rigid steel and fragmenting ice projectiles along with air blast response of the previously described woven CFRP. The chapter also contains details of how the chosen material parameters where obtained, as well as describing the approach to delamination modelling via the use of cohesive zone surfaces. For each loading condition there is details of model creation and chosen analysis based upon experiments in Chapter 5, followed by discussion of results linking back to experimental results presented in Chapters 6 and 7. Finally the hypothetical what if scenarios of an air-blast before an impact, or an impact before an air-blast will be presented and discussed via the use of three further numerical models.

Chapter 8

Modelling CFRP: Ballistic and Air-blast Case Studies

In this chapter, the previously described phenomenological continuum damage approach was used to model the ballistic impact response of both rigid steel and fragmenting ice projectiles along with air-blast response of the chosen woven CFRP. The chapter also contain details of how the chosen material parameters where obtained, as well as describing the approach to delamination modelling via the use of cohesive zone surfaces. For each loading condition there are details of model creation and chosen analysis based upon experiments in Chapter 4, followed by discussion of results linking back to experimental results presented in Chapters 5 and 6. Finally the hypothetical what if scenarios of an air-blast before an impact, or an impact before an air-blast are be presented and discussed via two further numerical models.

8.1 CFRP Specimen Details and Chosen Intra-Ply Material Parameters

In this chapter, all numerical models presented for the 2 x 2 twill woven CFRP composite described in Chapter 4 using the same material parameters as previously mentioned and

validated in Chapter 7. For the convenience of the reader, the configuration of the CFRP composite is shown again in Figure 8.1.

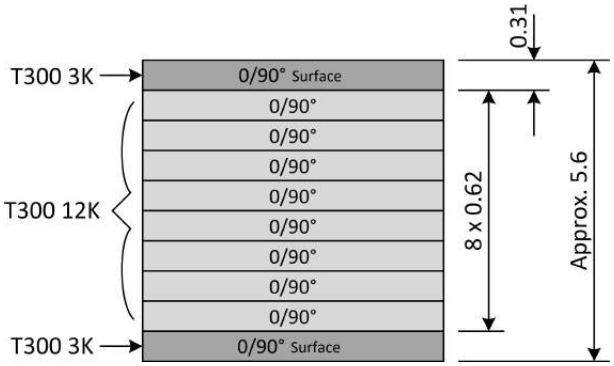

Figure 8.1: Composite panel configuration (all dimensions in mm)

Given the complexity of the parameter set, a new approach to obtaining and expanding a parameter set was developed. The developed approach utilises a literature search of reported experimental results for similarly defined twill woven CFRPs, which are directly compared against each other to obtain an array of common ratios between material parameters. These ratios are then used against quasi-static tensile testing (A damaged sample clearly displaying tensile fibre damage as shown in Figure 8.2), which then enables a full parameter set to be obtained for the CFRP used in this research which has been adjusted to consider the quality of the material. Therefore, the variability of the CFRP material is captured within the parameters as they are all scaled from the tensile testing data. While this methodology does not conclusively enable the accurate definition of the parameter set, it does enable a starting point for modelling. All parameters defined from the literature are found to have similar densities in the region of 1480 kg/m^3, and with a similar volume fraction as defined in Chapter 4. The full parameters and the final parameters used for the numerical modelling are shown in the last row of Tables 8.2 & 8.3, and are used to describe the intra-ply behaviour throughout the remainder of this chapter and correspond with the validated parameters presented in Tables 7.5 & 7.6 in Chapter 7. A recent study by Ravikumar et al. (2013) takes a similar approach by testing multiple materials, and then looks to fit "property change factors" to account for the parameter change with reference to the experimental strain rate proving the suitability of this method for developing this set of modelling parameters.

As mentioned, each ratio obtained via this method was then multiplied by the original CFRP parameters obtained via the tensile testing in order to ensure the behaviour

Figure 8.2: CFRP tensile test specimen - tensile fibre damage

of the CFRP was appropriately scaled. Compressive quasi-static behaviour stems from tensile quasi-static behaviour, then dynamic tensile from quasi-static tensile and dynamic compressive from quasi-static compressive. In the case of the dynamic compressive elastic modulus, because of the lack of data the same ratio of the tensile behaviour has been used for the compressive behaviour. There was also very limited data for the through thickness behaviour of the specific 2 x 2 twill woven CFRP, and so the behaviour of cross-ply uni-direction was used to obtain the necessary ratios which was then used in the same way to get the final material parameters required for the VUMAT model. The strain-rate sensitivity relationship between each set of parameters was modelled using the Equations (7.9 & 7.10) proposed by Daniel et al. (Daniel et al. 2011a) as shown in Chapter 7. As there was limited information for the strain rate sensitivity for each of the shear modulus in the 3 directions, a strain rate coefficient of $m_e = 0.045$ was taken and applied (Daniel et al. 2011a).

Damage evolution energies for each of the defined failure modes are taken from the work of Mendes and Donadon (2014), and are finally presented in Table 8.1.

Table 8.1: CFRP damage evolution energies (Mendes and Donadon 2014)

Parameter	Value	Unit
G_{ft}	75000	(J/m^2)
G_{fc}	25000	(J/m^2)
G_{mt}	2500	(J/m^2)
G_{mc}	2500	(J/m^2)
G_{sh}	2250	(J/m^2)

Table 8.2: Extrapolated CFRP model parameters - elastic

Reference	$E_{11t\&22t}^{Quasi}$ (GPa)	E_{33t}^{Quasi} (GPa)	$E_{11c\&22c}^{Quasi}$ (GPa)	$\frac{E_{11c\&22c}^{Quasi}}{E_{11t\&22t}^{Quasi}}$	E_{33c}^{Quasi} (GPa)	$\frac{E_{33c}^{Quasi}}{E_{33t}^{Quasi}}$	$E_{11t\&22t}^{Dyn}$ (GPa)	$\frac{E_{11t\&22t}^{Dyn}}{E_{11t\&22t}^{Quasi}}$	E_{33t}^{Dyn} (GPa)	$\frac{E_{33t}^{Dyn}}{E_{33t}^{Quasi}}$	$E_{11c\&22c}^{Dyn}$ (GPa)	$\frac{E_{11c\&22c}^{Dyn}}{E_{11c\&22c}^{Quasi}}$	E_{33c}^{Dyn} (GPa)	$\frac{E_{33c}^{Dyn}}{E_{33c}^{Quasi}}$	G_{12}^{Quasi} (GPa)	$G_{23\&13}^{Quasi}$ (GPa)	ν_{12} -	$\nu_{23\&13}$ -
Studied CFRP	51.0	8.0																
Ullah et al. 2012a	59.0	8.0													3.8	3.0	0.050	0.300
Hadavinia and Ghasemnejad 2009	59.5														3.4		0.100	
Foroutan et al. 2013	60.0														4.9		0.060	
Cruz et al. 1996	51.8		48.2	*0.931*											2.9		0.042	
Zhou et al. 2001	69.1		58.7	*0.849*											4.4		0.050	
Hou and Ruiz 2000	68.3						69.9	*1.024*							4.8		0.055	
Melin and Asp 1999		10.5							10.5	*1.000*								
Hosur et al. 2001					5.1								5.6	*1.098*				
Daniel et al. 2011b					11.2								14.5	*1.295*				
Averages	61.28	9.25	53.45	*0.890*	8.15	*1.00*	69.90	*1.024*	10.50	*1.000*	-	-	10.05	*1.196*	4.03	3.00	0.060	0.300
CFRP Model Parameters	51.0	8.0		45.4		8.0		52.2		8.0		46.5		9.6	4.032	3.000	0.060	0.300

Table 8.3: Extrapolated CFRP model parameters - strength

Reference	$F_{11t\&22t}^{Quasi}$ (MPa)	F_{33t}^{Quasi} (MPa)	$F_{11c\&22c}^{Quasi}$ (MPa)	$\frac{F_{11c\&22c}^{Quasi}}{F_{11t\&22t}^{Quasi}}$	F_{33c}^{Quasi} (MPa)	$\frac{F_{33c}^{Quasi}}{F_{33t}^{Quasi}}$	$F_{11t\&22t}^{Dyn}$ (MPa)	$\frac{F_{11t\&22t}^{Dyn}}{F_{11t\&22t}^{Quasi}}$	F_{33t}^{Dyn} (MPa)	$\frac{F_{33t}^{Dyn}}{F_{33t}^{Quasi}}$	$F_{11c\&22c}^{Dyn}$ (MPa)	$\frac{F_{11c\&22c}^{Dyn}}{F_{11c\&22c}^{Quasi}}$	F_{33c}^{Dyn} (MPa)	$\frac{F_{33c}^{Dyn}}{F_{33c}^{Quasi}}$	S_{12}^{Quasi} (MPa)	$S_{23\&13}^{Quasi}$ (MPa)	S_{12}^{Dyn} (MPa)	$S_{23\&13}^{Dyn}$ (MPa)
Studied CFRP	520.0	73.0																
Ullah et al. 2012a	859.0		673.0	*0.783*											120.0			
Hadavinia and Ghasemnejad 2009	597.0														94.0			
Foroutan et al. 2013	670.0						748.0	*1.116*							87.0		164.0	
Cruz et al. 1996	562.6		602.6	*1.071*											84.1			
Zhou et al. 2001	592.0		497.0	*0.840*											83.0			
Hou and Ruiz 2000	545.0		507.0	*0.930*			637.0	*1.169*			914.0	*1.803*			128.0		225.0	
Melin and Asp 1999		79.0							124.0	*1.570*								
Hosur et al. 2001					778.0								630.0	*0.810*				
Daniel et al. 2011b		65.0			285.0	*4.385*			90.0	*1.385*			390.0	*1.368*				
Averages	637.60	72.00	569.90	0.91	531.50	4.38	692.50	1.14	107.00	1.48	914.00	1.80	510.00	1.09		100.0		194.50
CFRP Model Parameters	520.0	73.0		471.2		320.1		594.2		107.8		849.4		348.6	100.0	100.0	194.50	194.50

8.2 Delamination Modelling

Delamination of the individual CFRP plies was achieved using cohesive zone surfaces (CZS) available in Abaqus Explicit, the use of CZSs avoids having to embed and use thin cohesive zone elements (CZEs) which can adversely affect and reduce the stable time increment leading to longer run times. The use of CZSs for modelling delamination has also been validated previously in Chapter 7, and have proven to exhibit the require response.

Like with CZEs, CZSs offer the ability to capture the initiation and evolution of delamination damage by employing a bi-linear traction-separation model, with the degradation of the inter-ply region propagating under the combined influence of normal and shear stresses via a quadratic nominal stress criterion as follows:

$$\left[\frac{t_n}{t_n^o}\right]^2 + \left[\frac{t_s}{t_s^o}\right]^2 + \left[\frac{t_t}{t_t^o}\right]^2 = 1\,, \tag{8.1}$$

where t_n, t_t and t_s are the instantaneous components of normal and shear traction at the surface, and t_n^o, t_t^o and t_s^o are the maximum values of associated stress in each of the direction. Once this criterion is met the interface begins to delaminate and the stiffness starts to degrade linearly, this degradation then follows a mixed mode power law criterion as follows:

$$\left[\frac{G_n}{G_n^o}\right]^\beta + \left[\frac{G_s}{G_s^o}\right]^\beta + \left[\frac{G_t}{G_t^o}\right]^\beta = 1\,, \tag{8.2}$$

where G_n, G_t and G_s are the instantaneous fracture energies in both the normal and shear directions, and G_n^o, G_t^o and G_s^o are the critical energy values associated with each of the directions. The parameters used and mentioned in the previous chapter for the delamination modelling where obtained in the following way. Firstly for the elastic response, the elastic stiffness was estimated via the empirical formula presented by Turon et al. (2007) below:

$$K = \frac{\alpha E_{33}}{t}\,, \tag{8.3}$$

where K is the interface stiffness, E_{33} if the stiffness of the CFRP ply in the through thickness direction, t is the thickness of the adjacent CFRP ply, and α is an adjustment parameter which was set to $\alpha = 55$ (Turon et al. 2007).

Following this approach for delamination modelling, the parameters presented in Table 8.4 where used to describe the inter-ply behaviour throughout the remainder of this chapter and correspond with the validated parameters presented in Tables 7.5 & 7.6 in Chapter 7. The Interlaminar strengths are stated to be similar to that of the through thickness strength and the associated shear strengths (Lópes et al. 2009), as so the appropriate material parameters from Table 8.3 where the damage evolution energies are taken from the work of Mendes and Donadon (2014).

Table 8.4: Delamination material parameters for woven CFRP (Turon et al. 2007; Mendes and Donadon 2014)

Parameter	Value	Unit
k_n^o	7.45E-5	(GPa)
k_t^o	2.87E-5	(GPa)
k_s^o	2.87E-5	(GPa)
t_n^o	73.0	(MPa)
t_t^o	100.0	(MPa)
t_s^o	100.0	(MPa)
G_n^o	600	(J/m^2)
G_t^o	5500	(J/m^2)
G_s^o	5500	(J/m^2)

Following delamination of the individual plies a general contact rule was applied between the separated surfaces, this rule was defined as a hard contact with a defined frictional value of 0.65 after delamination (Schön 2004).

8.3 Finite Elements and Mesh Sensitivity

For all numerical models in this chapter, each individual ply was represented by eight-node, isoparametric, hexahedral elements C3D8R elements with a single integration point and enhanced hour-glassing control, and meshing approaches were keep similar to one another in order to avoid any difficulties in analysing results once convergence was achieved.

All models remained as fully 3D without utilising any symmetric boundary conditions, as to avoid any complications associated with element deletion at the boundaries.

When considering the inevitable large deformations and the complexity of the developed phenomenological continuum damage model, mesh sensitivity was very important and efforts should always be made to find an optimum mesh size while balancing computation efficiency. Given the nature of the C3D8R element with a single integration point, there should always be multiple elements through the thickness of each CFRP ply within the model. Given the physical thickness of the plies, 2 elements were placed through the thickness of the surfaces plies and 3 element through the thickness of the bulk plies, this helped achieve a good balance between accuracy and the resulting stable time increment calculated within the explicit solver and therefore the computation efficiency achieved.

The convergence study was based upon the localised impact of the rigid steel ballistic projectile model, where the behaviour and failure of the CFRP plies and delamination localised heavily on the localised mesh. With cohesive zone surfaces (CZSs) being utilised to model delamination in the numerical studies in this chapter, as long as the adjacent surface element sizes and associated nodal positions are similar between plies this approach should be equivalent and deemed sufficiently accurate of the results presented. The work presented by Turon et al. (2007) identifies a method of obtaining an approximate size of cohesive zone for delamination, based upon the inter-ply parameters the maximum global seed size of the mesh can be determined to ensure that delamination as accurately represented across the whole model as shown below:

$$l_{cz} = ME\frac{G_c}{(\tau^0)^2}, \tag{8.4}$$

where M is a parameter dependant on the cohesive zone model, E is the elastic modulus of the material, G_c is the energy release rate in the given direction, and τ^0 in the ultimate interface strength in the given direction. Using this length of the cohesive zone and applying 5 elements across the distance, an approximate element size for accurately capturing delamination can be obtained (Turon et al. 2007). For the models and materials proposed, the maximum adjacent element size falls at approx. 2mm.

To determine mesh convergence, an increment of a full rigid steel impact model (to be described in more detail later in the chapter) was analysed for various mesh sizes, a

full path across the back of the specimen was then plotted for each result. This resulted a minimum element size of 0.5 mm for the centre of the specimens where damage was expected, then at the edges the mesh can be relaxed out to 2mm where minimal damage will be present. Full meshes are be shown in later figures for each model.

8.4 Ballistic Modelling: Steel vs. Ice

8.4.1 Approaching Ballistic Modelling

With the CFRPs inter-ply and intra-ply material parameters defined, both approaches for the rigid and fragmented projectiles need to be chosen in order to correctly apply the observed complex loading conditions as seen in Chapter 5. For the rigid projectile the steel shall be simply modelled as a linear elastic solid as no damage or plasticity was observed, then for the fragmenting projectiles a smooth particle hydrodynamics (SPH) failure approach has been chosen following the literature review in Chapter 3 to model the fragmenting ice projectile to then distribute the load across the specimens surface. The CFRP specimen's behaviour was modelled using the constitutive phenomenological intra-ply based VUMAT model with the parameters defined earlier in this chapter, and the specimen and boundary condition dimensions are shown in Figure 8.3 where the only difference between the two ballistic models was the approach to the projectiles behaviour. The model presented was created using the commercial software ABAQUS 6.14-4.

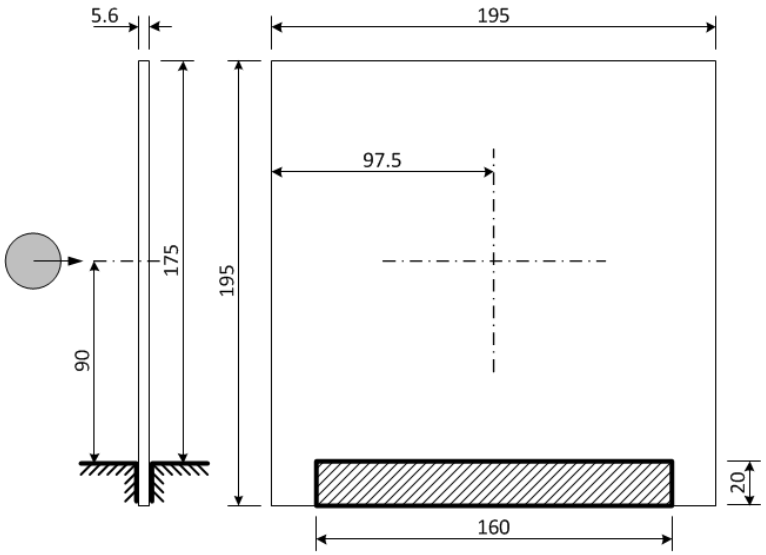

Figure 8.3: Ballistic experimental fixture schematic diagram (all dimensions in mm)

The steel projectile was modelled as a linear elastic solid, using the parameters defined in Table 8.5. The ice projectile was then modelled via a strain rate dependant compressive strength based model with a tensile pressure cut-off failure criteria as proposed by Tippmann et al. (2013), the parameters for this model are shown in Table 8.6.

Table 8.5: Steel material parameters

Parameter	Value	Unit
Elastic Modulus: E	210.0	(GPa)
Poisson's Ratio: ν	0.3	-
Density: ρ	7600	(kg/m^3)

Table 8.6: Ice material parameters Tippmann et al. 2013

(a) Ice material parameters

Parameter	Value	Unit
Elastic Modulus: E	9.38	(GPa)
Poisson's Ratio: ν	0.33	-
Density: ρ	900	(kg/m^3)
Tensile Failure Pressure	0.517	(MPa)
Compressive yield strength	5.2	(MPa)

(b) Ice strain-rate parameters

Strain Rate (s^{-1})	Yield Ratio
0	1
0.1	1.01
0.5	1.50
1	1.71
5	2.20
10	2.42
50	2.91
100	3.13
500	3.62
1000	3.84
5000	4.33
10000	4.55
50000	5.04
100000	5.25
500000	5.75
1000000	5.96

For both of the ballistic model, the CFRP specimen contains 441392 eight-node, isoparametric, hexahedral elements (C3D8R) after mesh convergence with 2 elements through the thickness of the surfaces plies and 3 element through the thickness of the bulk plies. The mesh was refined within a circular region double the size of the projectile at the impact location, in order to increase accuracy as discussed previously. The projectiles were given the predefined velocities shown in Table 8.7, to match that of the experiments. The final model setup and mesh is shown in Figure 8.4.

Table 8.7: Ballistic steel and ice projectile initial velocities

Projectile	Damage Level	Initial Velocity (m/s)	Projectile Diameter (mm)	Incident Energy (J)
Steel	Major	91.5	23.8	229.0
	Medium	78.5		168.5
	Minor	59.5		96.8
Ice	Major	480.0	25.0	864.0
	Medium	403.0		609.0
	Minor	304.0		346.6

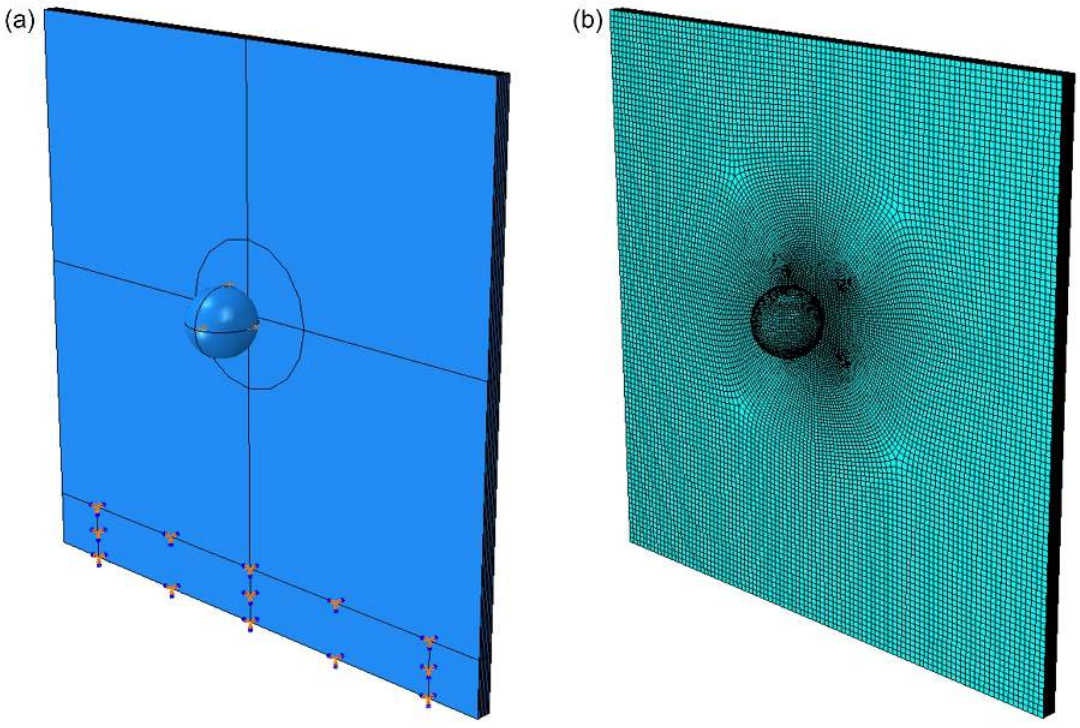

Figure 8.4: Ballistic impact model setup: (a) assembly; (b) mesh

8.4.2 Deformation Validation

The finite-element models of the ballistic impact case studies were first validated using experimental results for the deformation analysis, by analysing the behaviour of the model vs. the experiment the characteristics of the rigid vs. fragmenting impacts can be confirmed. Figure 8.5 below demonstrates the impact of the two regimes, and shows the characteristic indentation of the rigid steel projectile against the fragmenting ice project at 0.1 ms after impact. Damage analysis and validation shall be discussed later in the chapter, but Figure 8.5 does give an insight into the fibre failure model (SDV62).

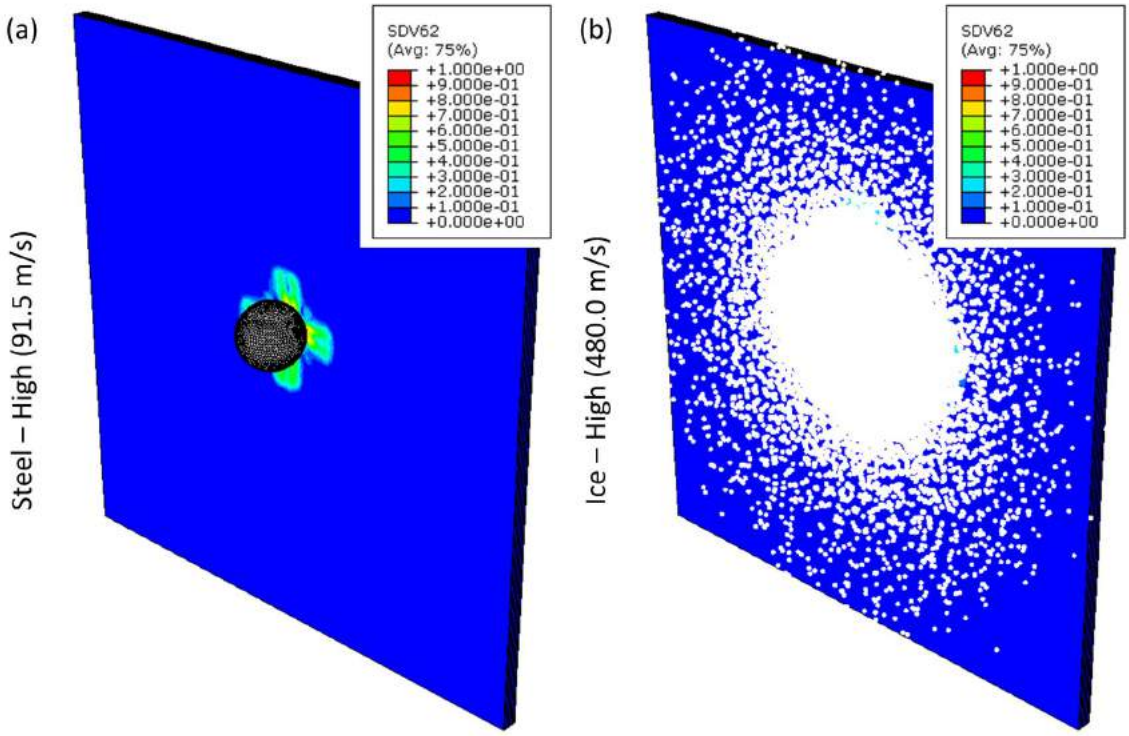

Figure 8.5: Ballistic impact model results: (a) steel projectile at 91.5 m/s; (b) ice projectile at 480.0 m/s (0.1 ms), fibre failure model (SDV62)

Delving deeper in the analysis of the specimens deformation during each of the impacts, the VUMAT model created for the CFRP specimens can be assessed for its suitability for the loading conditions investigated. Figures 8.6 - 8.8 show the behaviour of each of the modelled specimens vs. the experiment for the first 0.5 ms of the rigid steel impacts cases. As can be seen from the low and mid project velocities (59.5 and 78.5 m/s) where the DIC was present in the experiments, the model result shows clear similarities for both out of plane displacement and the specimens curvature during loading.

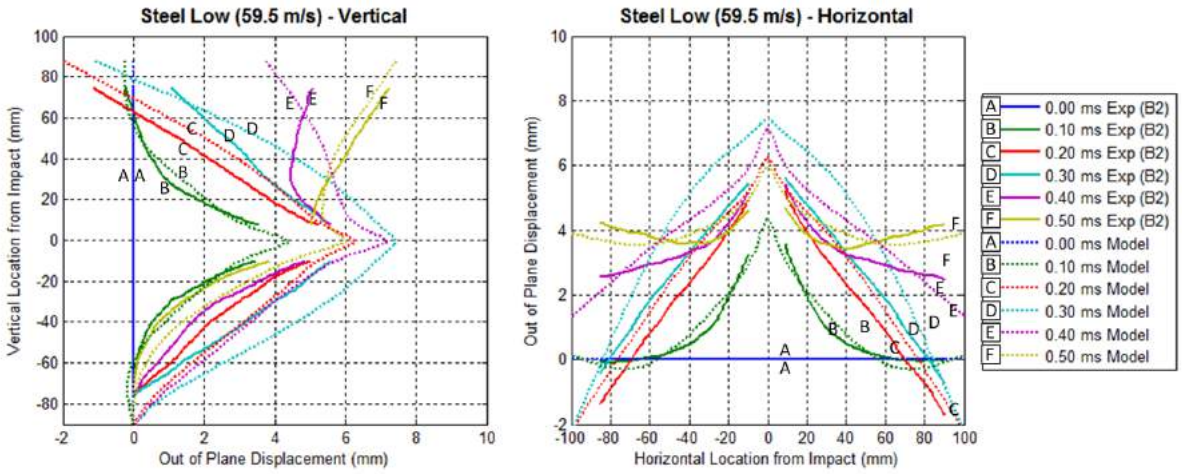

Figure 8.6: Out-of-plane displacement: experiment vs. model - steel impact 59.5 m/s

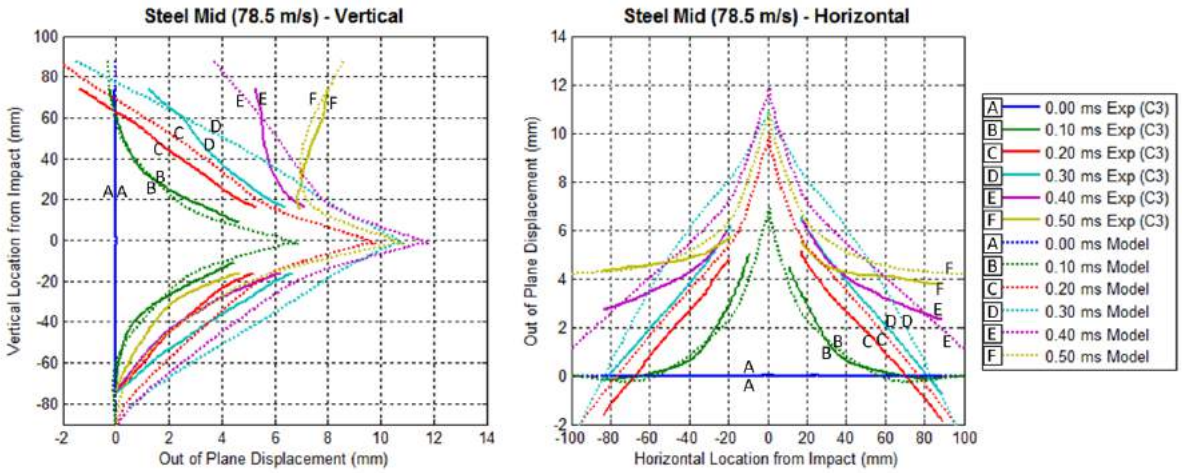

Figure 8.7: Out-of-plane displacement: experiment vs. model - steel impact 78.5 m/s

There was clear agreement of the out-of-plane displacement throughout the first stages of the impact, with both results showing accurate transitions from the localised indentation to global bending as discussed in Chapter 5. The slight variations that can be seen were likely due to the time shift between the experimental high-speed footage and the defined time step outputs from the model result, although time shift alignment was carried out on all results presented there was likely to be some misalignment due to the limitations on the shutter speed of the high speed cameras and resultant set increments of the DIC data. From this the model only version of the steel projectile at 91.5 m/s shown in Figure 8.8, can be taken as an appropriate result following the success of the other two load cases.

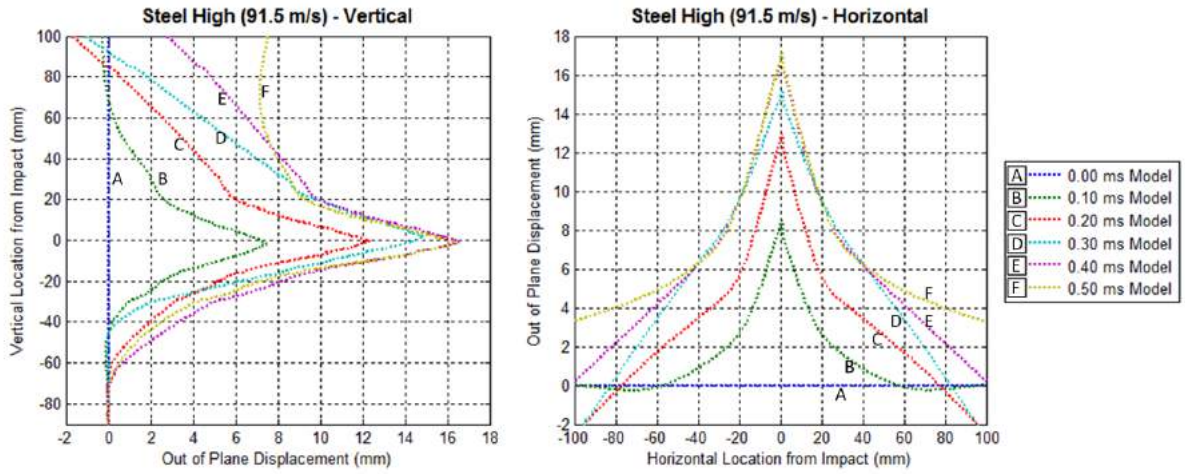

Figure 8.8: Out-of-plane displacement: experiment vs. model - steel impact 91.5 m/s

Moving onto the fragmenting ice projectiles as shown in Figures 8.9 - 8.11, the analysis of the result was not so clear. The first stages of the slowest impact (304.0 ms in Figure 8.9) the experiment shows greater initial indentation but overall the magnitude and curvature of the specimens was seen to be similar. Comparing this to the mid velocity ice impact (403.0 ms in Figure 8.10), the result show good correlation through the whole impact.

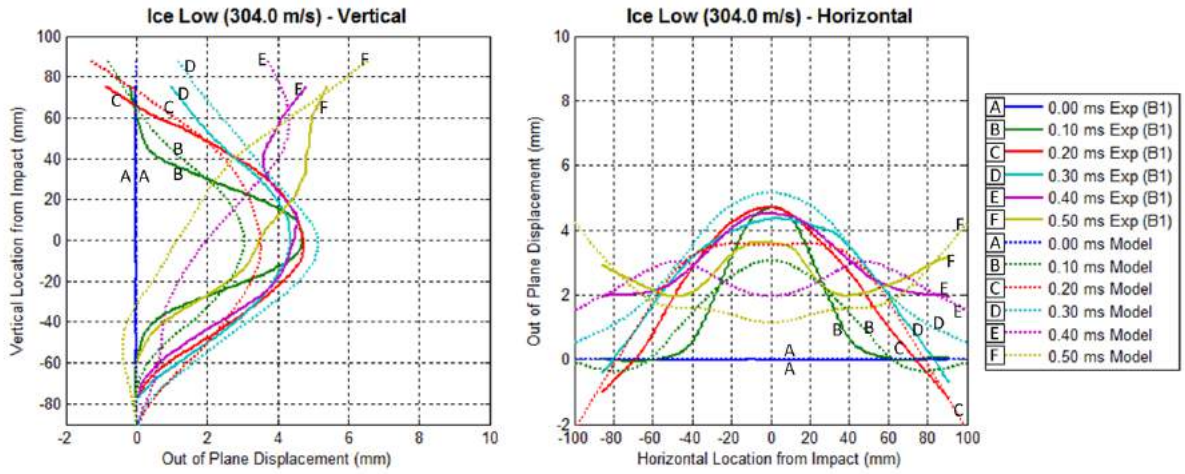

Figure 8.9: Out-of-plane displacement: experiment vs. model - ice impact 304.0 m/s

Given the success of the rigid steel validation shown earlier and for the mid velocity ice projectile, its thought that the general discrepancy between computational results and experimental data was due to the complex nature of the fragmenting ice projectile. This resultant loading condition imposed on the composite, led to reduced indentation when compared to predictions from the numerical models. As well as this, the time shift be-

tween the experiment and model could have also been a factor specially when the impact duration was so short when compared to the frame rate of the high speed camera. The maximum out-of-plane displacement does show a reasonable correlation between numerical predictions and experimental results with correct transition of specimen curvature during loading. The effect of this on the damage analysis is discussed later in the chapter.

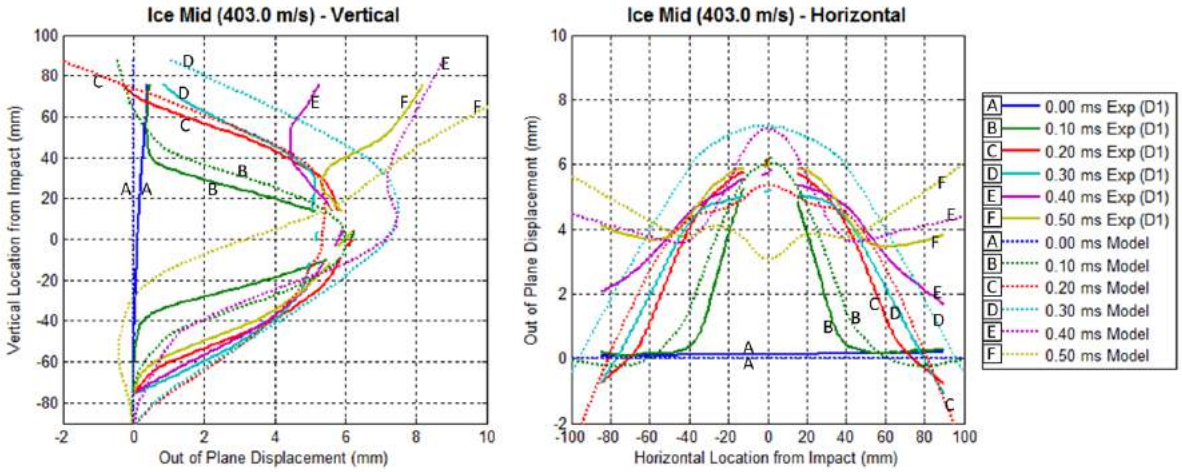

Figure 8.10: Out-of-plane displacement: experiment vs. model - ice impact 403.0 m/s

As for the highest velocity result, the results are as expected and show similar behaviour which was thought to be approximately correct. But with the possibility of the reduced indentation at the early stages, it was unlikely that the same damage will be seen when compared to that of the specimens as shown in Chapter 6 where the front plies were completely removed when the projectile fragments inside the specimen.

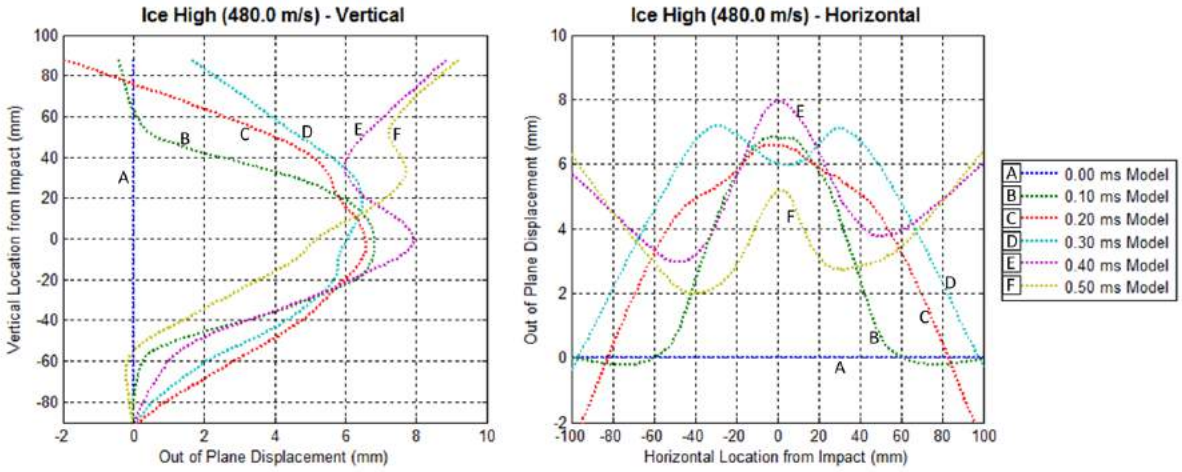

Figure 8.11: Out-of-plane displacement: experiment vs. model - ice impact 480.0 m/s

With this in mind, the validation of this model was difficult to conclusively confirm. The model results do show accurate maximum out of plane displacement with correct transitions of specimen curvature during loading, but the reduced initial indentation for the lowest velocity projectile does show a slight difference. Therefore although the whole model was not validated in it entirety, the VUMAT for the CFRP does show the correct specimen behaviour even if the ice projectile may have effect the final result.

8.4.3 Damage Validation

The validation from the deformation analysis continues through to the damage analysis for the rigid steel projectiles. Firstly looking at the summaries of the various CFRP failure modes as shown in Figure 8.12, the major damage mode was confirmed to be tensile fibre failure (a) with very limited matrix damage localised to the point of impact (b). Careful analysis of the through thickness direction revealed a distributed cone formation of damage from the front to back surface, which is typical for this type of impact regime. As to be expected for the rigid projectile, the damaged area remains highly localised through all of the loading conditions, with the both the matrix (b) and shear (c) damage being almost identical and the fibre failure area only increase slightly as also witnessed during the experimental damage analysis in Chapter 6. Overall visually the damage within the model matches the damage seen as a result of the experiments.

The same was seen when reviewing the through thickness damage within the CFRP specimen as a result of the rigid projectile impact (as shown in Figure 8.13), although the damage area does increase with increasing projectile velocity and impact energy the area remains localised. As to be expected the model reveals delamination damage at the boundary condition which again is typical of these types of experimental and model setup conditions, this was not something that was shown during the X-ray tomography given the size limitation of the scan area as discussed in Chapter 6 and was something that cannot be avoided with the given proximity to the impact location. Again visual analysis of the impact zones does shown good agreement between the model and experimental results. A numerical comparison of the damage areas seen in the model vs. the experiments is presented in Figure 8.16 following the discussion of the ice projectile impacts next, but the results presented demonstrate good characteristic behaviour and therefore the developed CFRP VUMAT model is shown to be suitable to predict CFRP behaviour.

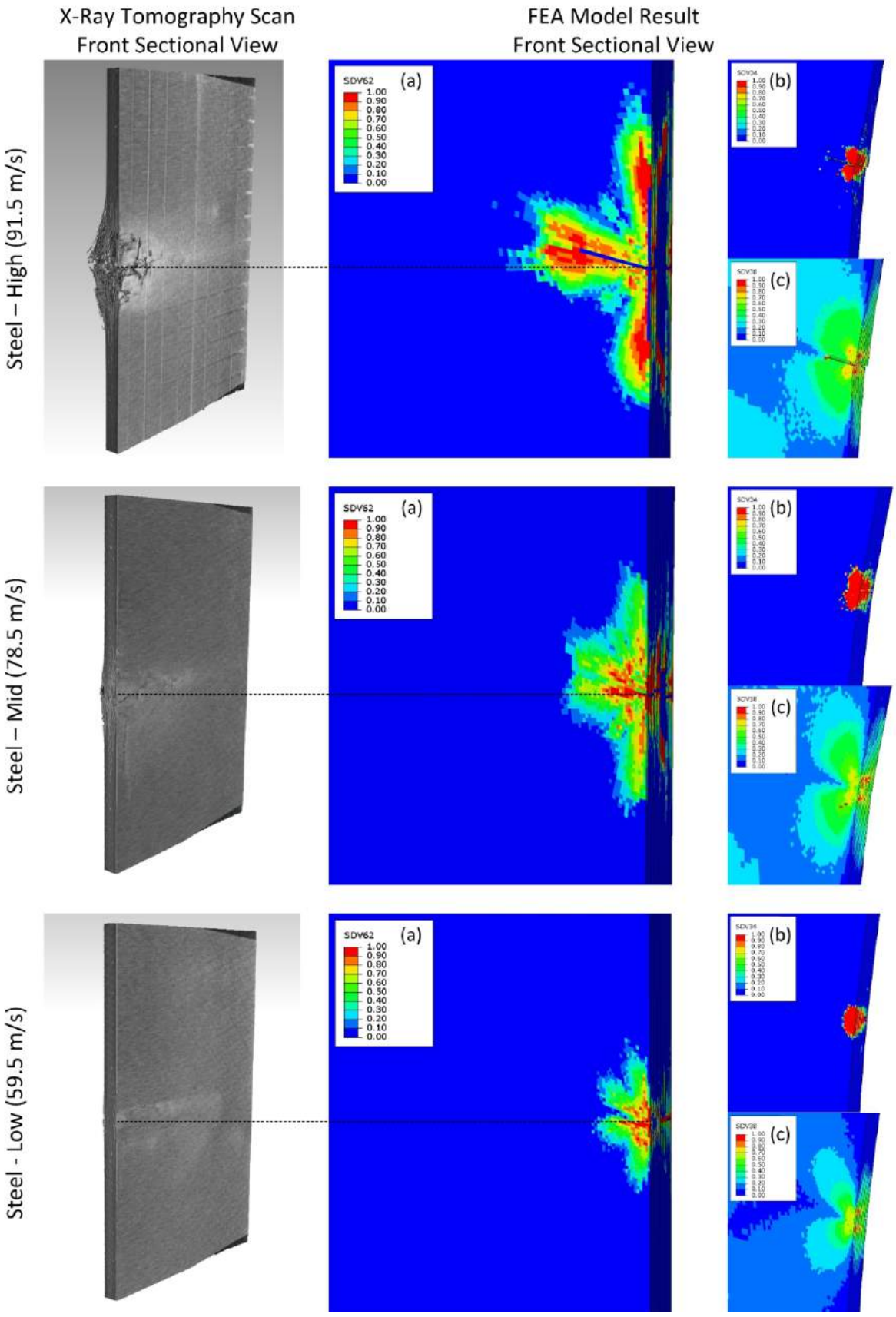

Figure 8.12: Ballistic steel impact model damage results: (a) fibre damage; (b) matrix damage; (c) shear damage

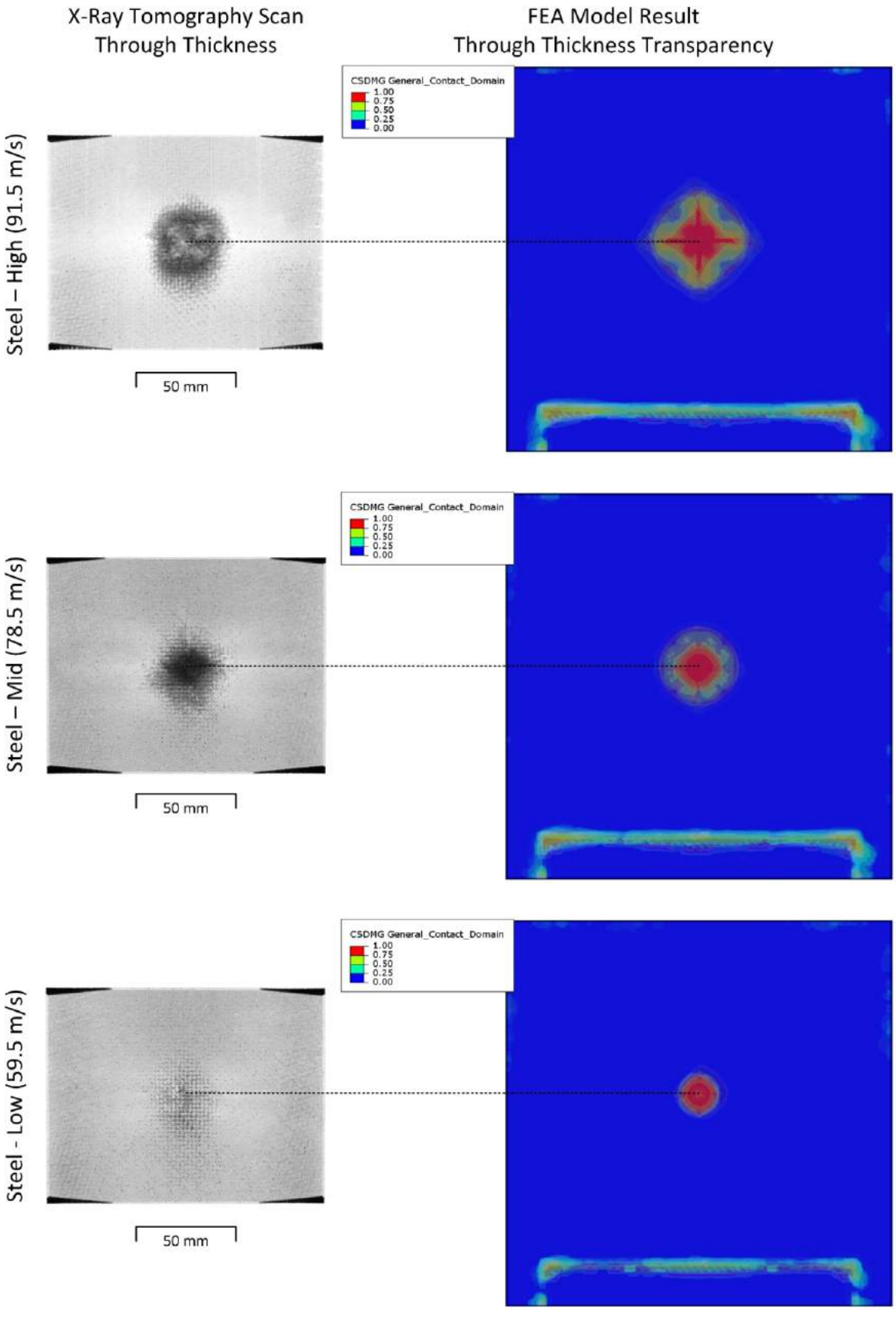

Figure 8.13: Ballistic steel impact model damage results - through thickness damage cloud

Following validation of the deformation behaviour resulting from the fragmenting ice projectile, the comparisons of the damage reveals more about why the model result may not have been entirely comparable as discussed previously. Starting with the summaries of the failure modes as shown in Figure 8.14, its clear that the damage seen for the lowest velocity impact (304.0 m/s) showed no significant fibre damage (a) as expected and only limited matrix (c) and shear damage (c). Reviewing the damage of the mid (403.0 m/s) and high (480 m/s) velocity impacts the reasoning for the observed difference becomes clearer, previously the deformation analysis observed a lack of initial indentation which again can be seen in the failure modes. Both higher velocity impacts showed reduced fibre failure on the front surfaces of the CFRP specimens when compared to the experiments as a result of reduced localised indentation, this then changes the impact process significantly as the ice does not fragment inside the specimen as witnessed in the experiments and shown in Chapter 6. Therefore although the model result demonstrates the correct characteristics of the impact damage for the given projectile type, the model presented does lack the ability to produce the observed indentation to correctly define the ice behaviour.

The through thickness damage of the CFRP specimen confirms this further (as shown in Figure 8.15), as although the damage area did increase with increasing projectile velocity and impact energy, the issue surrounding the ice behaviour model propagates through. The lowest impact velocity (304.0 m/s) showed the damage area remains localised but not as wide spread as show in the experiment, this was likely due to the reduce indentation which then effects the transition of the specimen curvature and the resultant delamination. The same can be said for the mid (403.0 m/s) and high (480 m/s) velocity impacts where the reduced indentation then effects the delamination as well, but also the lack of front ply tensile fibre failure which then allowed the ice projectile to fragment inside the specimen and therefore would increase the delamination even further. The artefacts seen in figure 8.15 are a feature of increasing mesh size away from the area of impact, although not ideal these artefacts were deemed to have significantly not effected the results given the challenges mentioned when obtaining the correct ice behaviour. The validation of this model was difficult to confirm, the results have shown accurate trends in the damage seen but the effect of the reduced initial indentation does result in a slight difference from the experimental results observed. Therefore the previous conclusion of stating the whole model was not validated in it entirety still stands.

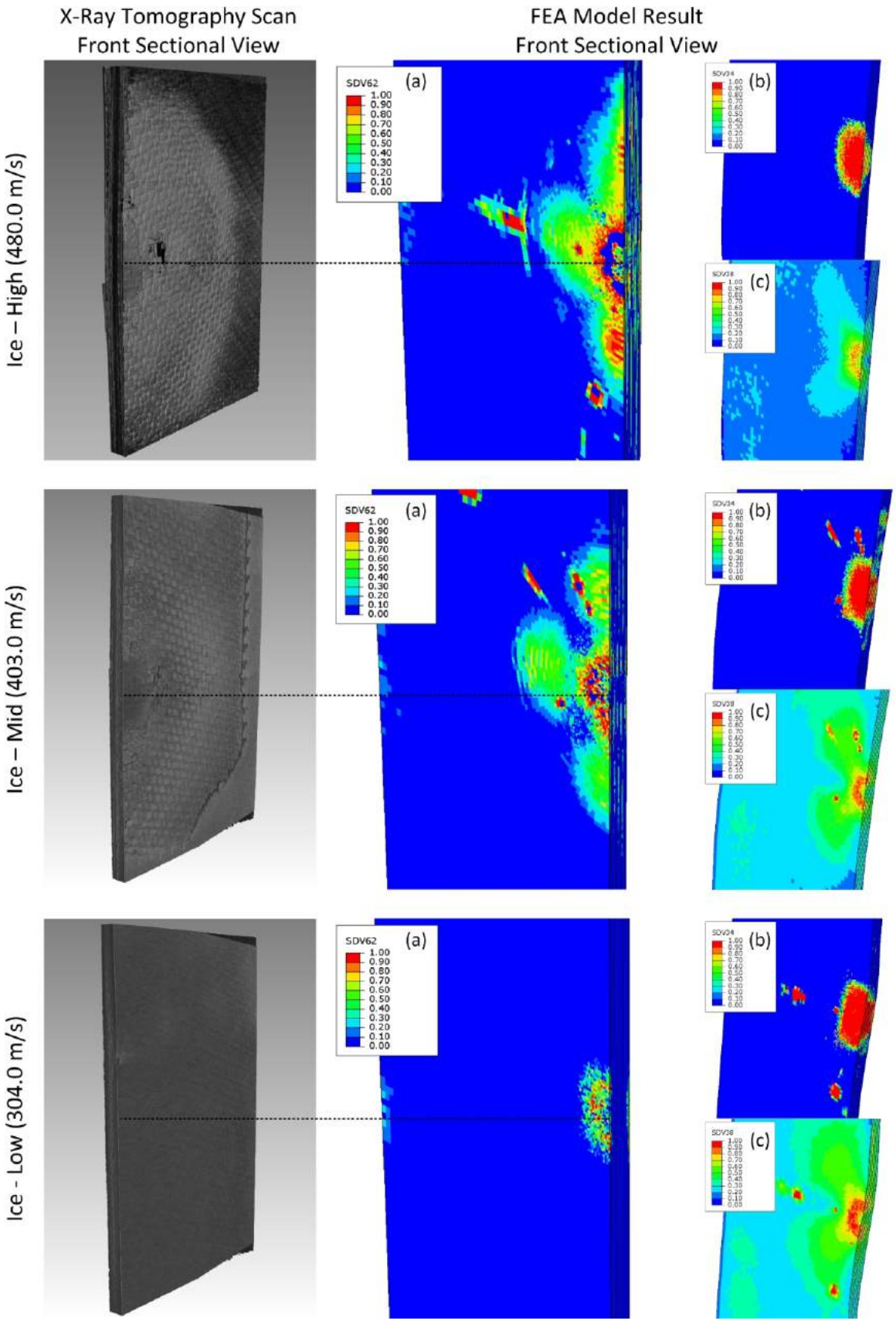

Figure 8.14: Ballistic ice impact model damage results: (a) fibre damage; (b) matrix damage; (c) shear damage

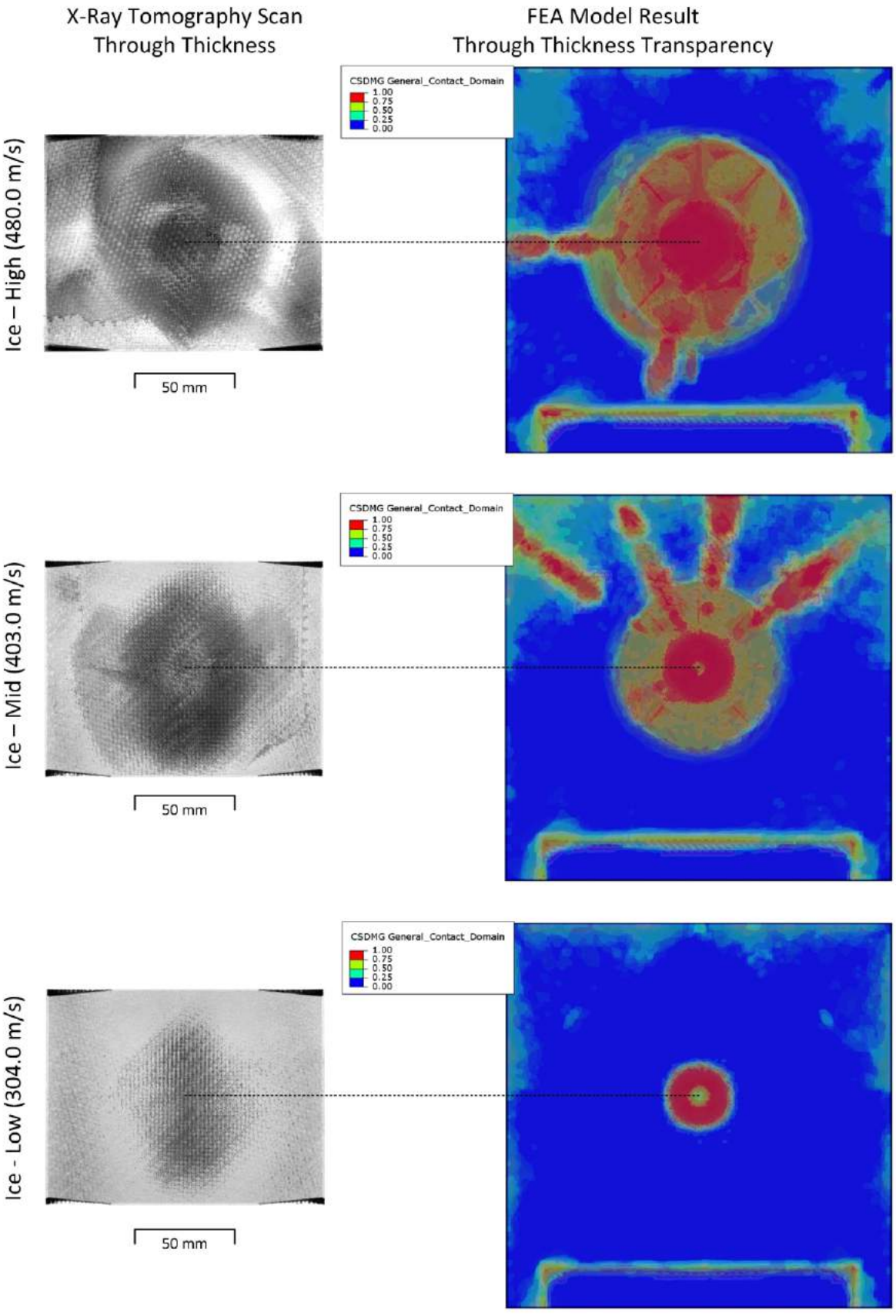

Figure 8.15: Ballistic ice impact model damage results - through thickness damage cloud

A numerical comparison of the resulting damage areas is shown in Figure 8.16, where the previous statements are validated further. For the rigid steel impacts the damage areas show good agreement for each loading condition as well as a good match to the observed trend, but for the fragmenting ice impacts the points discussed previously are confirmed. At the lowest ice projectile velocity (impact energy) the resulting damage area was shown to be closest to the experimental results, but as the velocity (impact energy) increases, this trend diverges away due to the lack of catastrophic damage. It can be seen here that the localised indentation does lead to a considerable increase in the observed damaged area, without this mechanism the model results are affected significantly and the validation of the whole model becomes challenging because of the fragmenting projectile type.

However, from the results presented the VUMAT developed for the CFRP composite was still deemed to be suitably accurate to model the various ballistic loading conditions. Even with the deviation of the damage result shown for the fragmenting ice projectile, the model still shows the ability to match and predict the deformation behaviour of the CFRP specimens for both loading conditions within the present region.

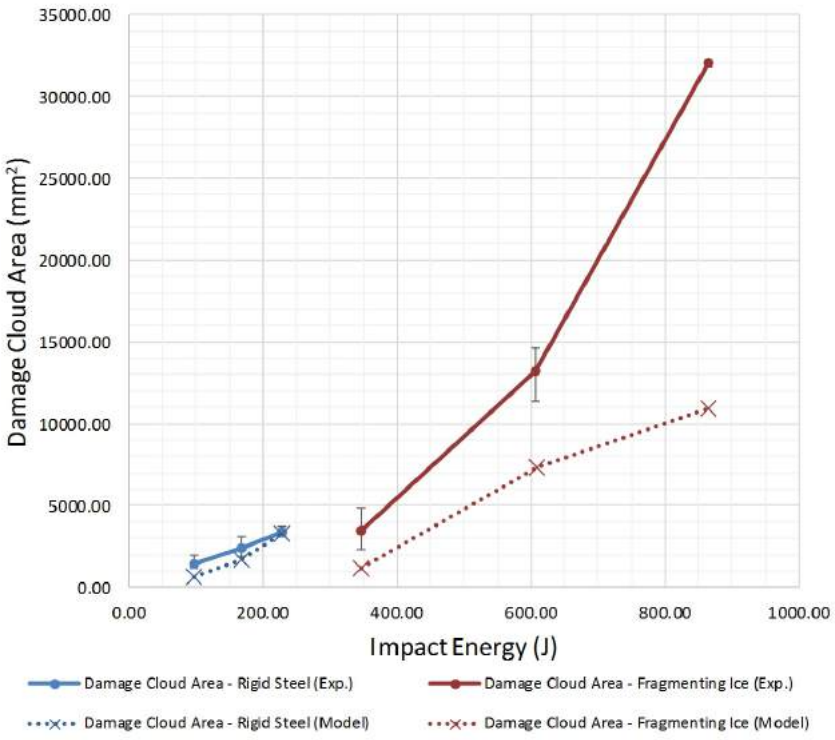

Figure 8.16: Experiments vs model results; a comparison of the through thickness damage clouds for both the rigid steel and fragmenting ice projects vs. impact energy

8.5 Dynamic Air Blast Modelling

8.5.1 Approaching Air Blast Modelling

For the air-blast modelling the CFRP specimen's behaviour was modelled using the constitutive phenomenological intra-ply based VUMAT model with the same parameters used previously, then a Coupled Eulerian Lagrangian (CEL) approach was chosen to model the fluid structure interaction between the air-blast and the CFRP specimen. This method was chosen as the complex interaction can still propagation as the lagrangian meshed domain breaks down like for example in the event of element deletion due to the CFRP fibre failure mode, this would be the limitation with the Fluid Structure Interaction (FSI) approach, hence why it was not chosen. The specimen, shock tube and knife edge boundary condition dimensions are shown in Figure 8.17 and match the experimental setup discussed in Chapter 4, then as mentioned previously the model presented was created using the commercial software ABAQUS 6.14-4.

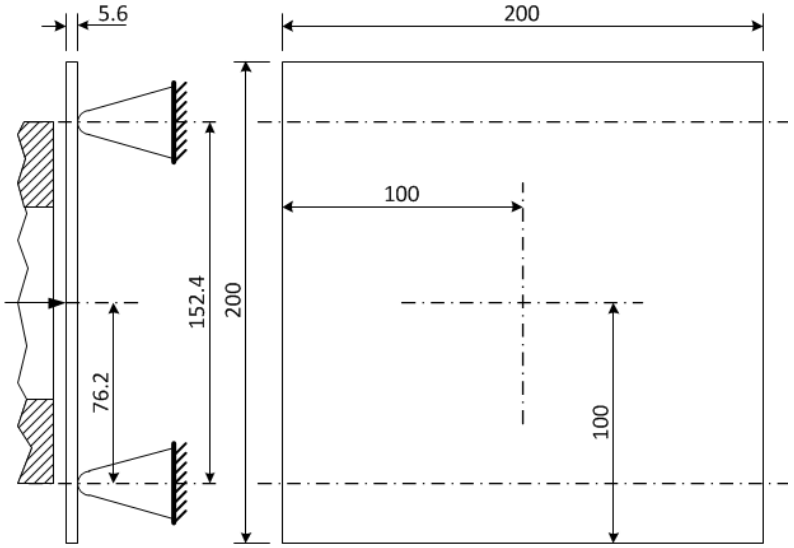

Figure 8.17: Air-blast experimental fixture schematic diagram (all dimensions in mm)

The Eulerian domain within the model comprised of air which was defined to be at ambient temperature and pressure and modelled using the ideal-gas equation of state with typical values assigned for specific heat and dynamic viscosity which will account for changes in density given the fundamental behaviour of the air-blast shockwave, the parameters used are shown in Table 8.8.

Table 8.8: Air Parameters

Parameter	Value	Unit
Density: ρ	1.293	(kg/m^3)
Gas Constant: R	287.058	-
Ambient Pressure	101325	(Pa)
Specific Heat: C_p	717.6	(J/K)
Dynamic Viscosity: μ	6.924E-6	$(Pa.s)$

For the air-blast model, the CFRP specimen contains 833280 eight-node, isoparametric, hexahedral elements (C3D8R) after mesh convergence with 2 elements through the thickness of the surfaces plies and 3 element through the thickness of the bulk plies matching that of the ballistic models. Then the Eulerian domain contains 274440 eight-node, single integration point hexahedral elements EC3D8R. The air-blast pressure profiles were then defined as shown in the profile in Figure 8.18, and given magnitudes of 0.4, 0.6 and 0.8 MPa to match that of the experiments. The difference away from the typical profile of the incident wave seen in Figure 8.18, and forms a more triangular waveform, and was deemed negligible, the profile shown in the figure is an exaggeration and only a representation. The negative phase of the profile was not included, given the duration of the model was relatively short in comparison. The final model setup and mesh used is shown in Figure 8.19, the figure shows a sectioned view revealing the CFRP specimen inside the Eulerian domain, as well as the CFRP specimen and the supporting knife edge matching the experimental setup.

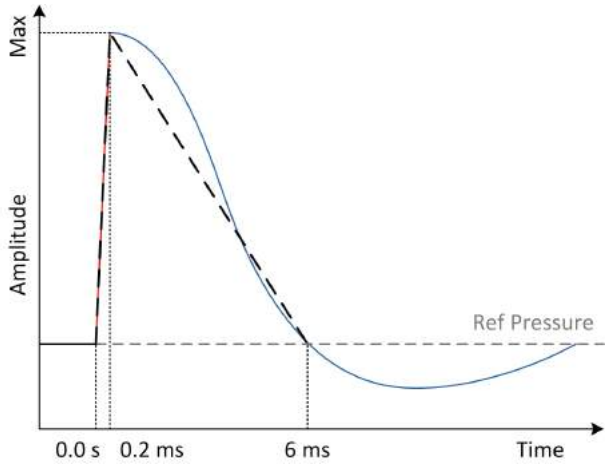

Figure 8.18: Air blast input pressure profile (- - - dashed line)

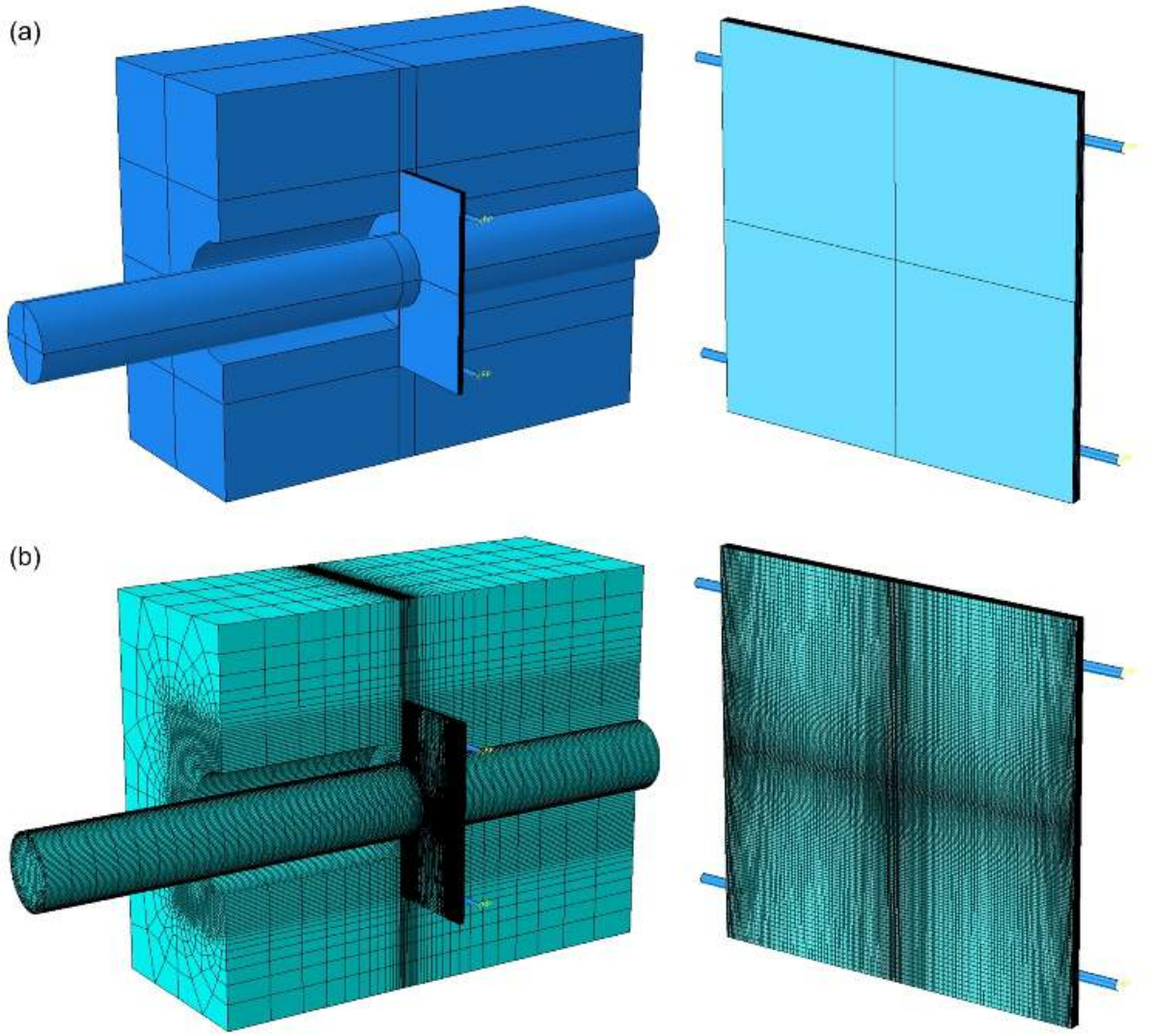

Figure 8.19: Air-blast model setup: (a) assembly; (b) mesh

8.5.2 Deformation Validation

The finite-element models of the air-blast case studies were first validated using experimental results from the deformation analysis, matching the process used for the ballistic impact models presented previously. By analysing the behaviour of the model vs. the experiment the characteristics of the air-blasts can be compared, therefore validating the suitability of the CFRP VUMAT model for this type of loading condition. Unlike the ballistic impact modelling, the larger and more complex air blast models took considerably longer to solve and as a result there was a limited run time for these models, so the first 0.35ms of the deformation shall be analysed matching that of the fine out of plane

displacement plot shown in Chapter 5, and then the remaining model was allowed to run out for a total of 3 ms which was more than enough time for the damage to propagate fully as shown in Chapter 5 & 6. Figure 8.20 below demonstrates both (a) the propagating incident pressure within the eulerian domain and (b) the CFRP specimen response after the wave has interacted with the surface, this shows the characteristic global bending of the specimen at 0.35 ms after first interaction with the shock-wave front. Damage analysis and validation shall be discussed later in the chapter.

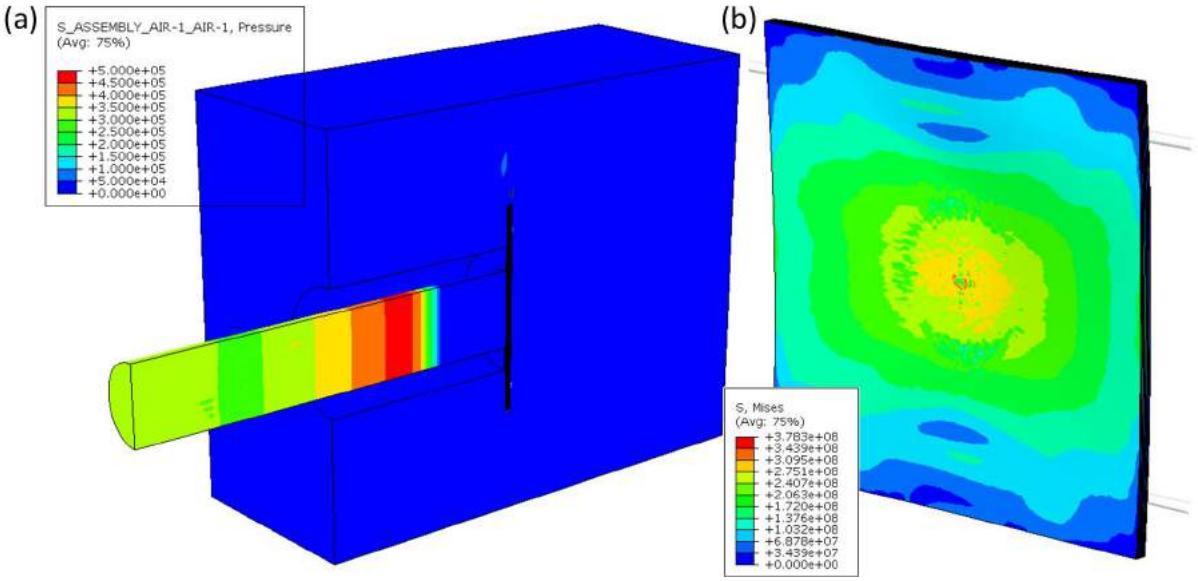

Figure 8.20: Air-blast model results: (a) propagating incident pressure wave; (b) CFRP specimen behaviour at 0.35 ms

When reviewing the deformation analysis an indirect assessment of the behaviour can be seen in the incident and reflected pressure waves as discussed in Chapter 5, the reflected wave demonstrates how the elastic behaviour and damage effects the incoming incident wave to then form a unique reflected which in this case travels back down the shock tube. The reflected waves for the three air-blast loading conditions is shown in Figure 8.21 at the same location of the measured pressure in the experiments discussed in Chapter 4, and as shown the reflected waves show good accuracy when compared to that of the experimental results. As expected the incoming incident waves match correctly confirming an accurate input, and then the reflected waves then shown good agreement for both peak magnitude and downward decay of the expansion of the wave which proves that the stiffness of the CFRP within the model was an accurate representation of the real specimens.

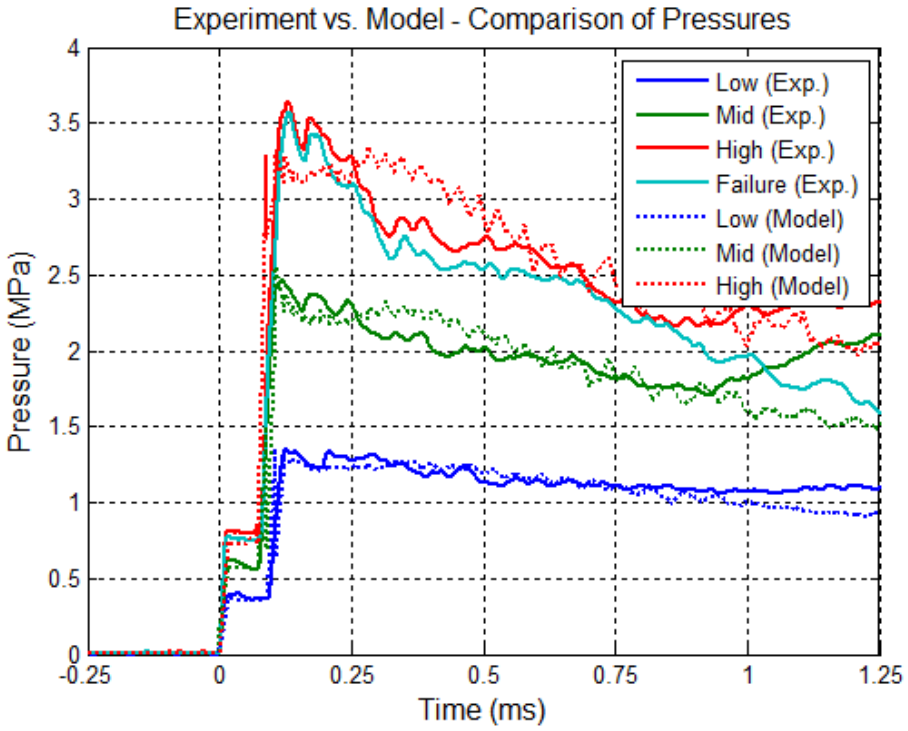

Figure 8.21: Comparison of the incident and reflected shock wave pressures - experiment vs. model

The analysis of the CFRP specimens deformation during each of the air-blasts was assessed in the same way as the impact cases, this begins to confirm whether the VUMAT model was then suitability for the shock wave loading conditions. From Chapter 5, it has been shown that the curvature and magnitude of the out of plane deformation does scale with an increase of incident pressure. With this in mind the results from the model should support this, and show similar trends across each of the model outputs matching in turn each of the experiments.

Figure 8.22 - 8.24 show the model deformation results for the low (0.4 MPa), mid (0.6 MPa) and high (0.8 MPa) incident pressure waves, and demonstrates that the magnitudes also scale as discussed previously while also showing an accurate match for both curvature and approximate out-of-plane displacement to that of the experimental results. Although the model results do strongly match that of the experiments, there was a slight different towards the higher incident pressure waves where the results seem to diverge slightly, this was likely to do with the time shift between the experimental data capture and camera frame rate as seen in the previous ballistic impact comparisons. Overall the deformation behaviour seen in the model was a very good match to that of the experiments.

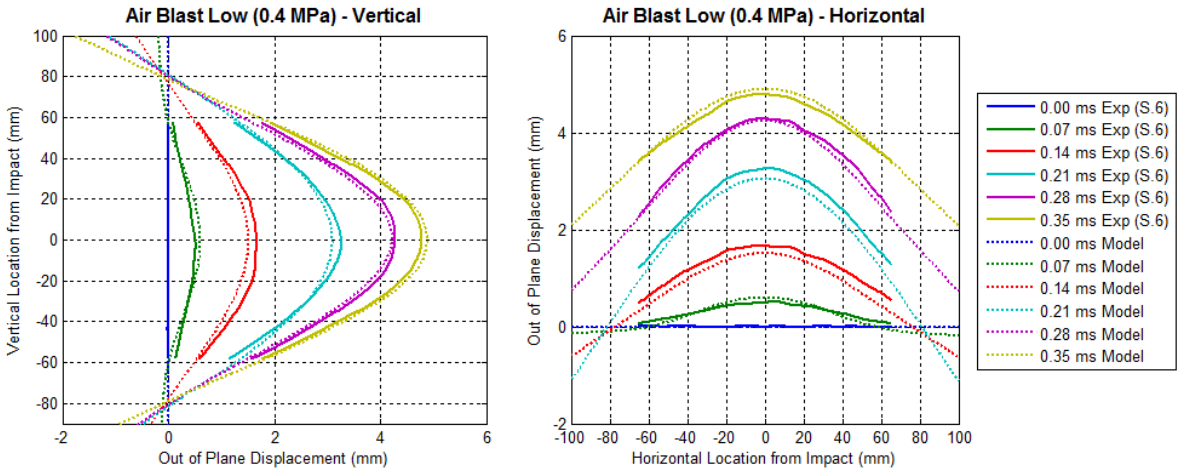

Figure 8.22: Out-of-plane displacement: experiment vs. model - air-blast 0.4 MPa

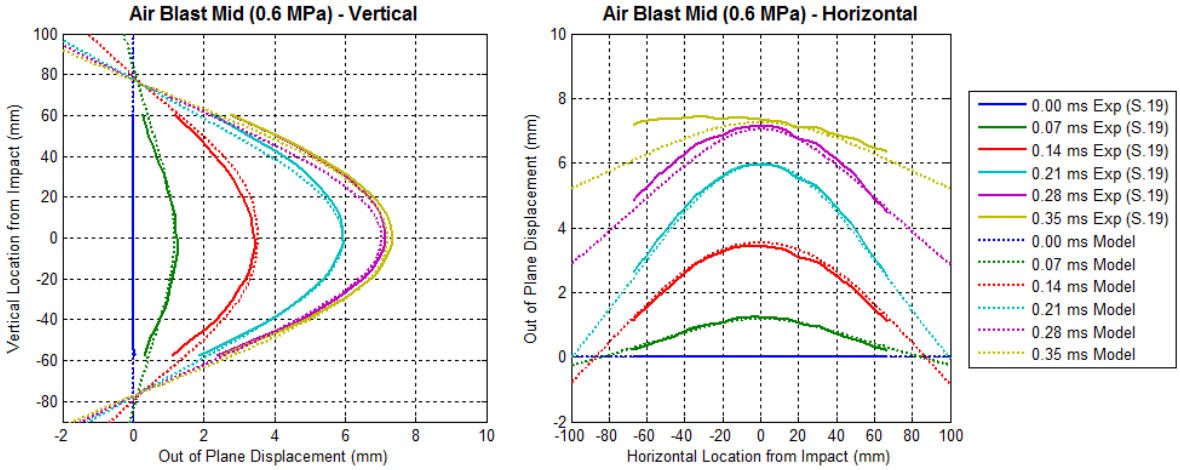

Figure 8.23: Out-of-plane displacement: experiment vs. model - air-blast 0.6 MPa

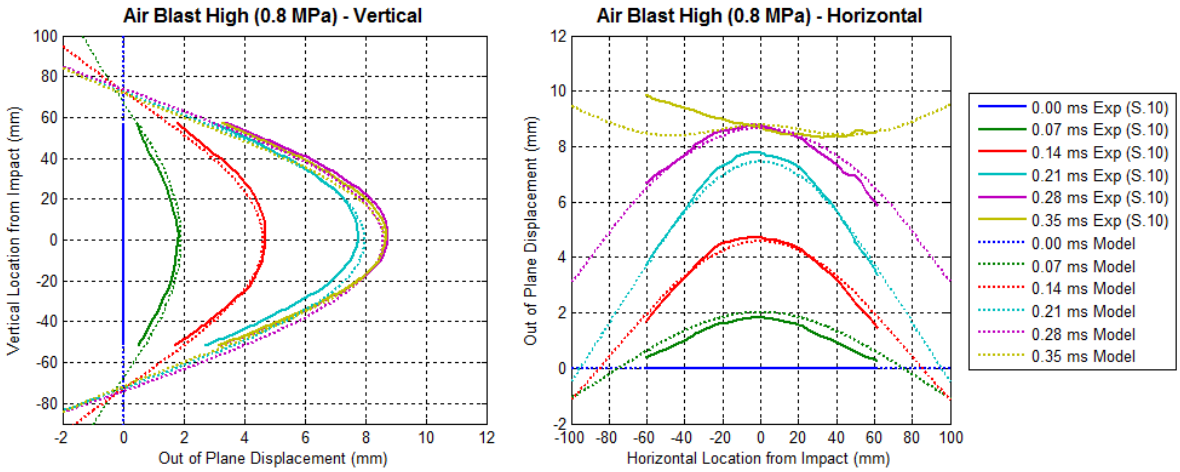

Figure 8.24: Out-of-plane displacement: experiment vs. model - air-blast 0.8 MPa

8.5.3 Damage Validation

The successful validation from the deformation analysis also continues through to the damage analysis for the air blast loading conditions. First, looking at the summaries of the various CFRP failure modes as shown in Figure 8.25, the major damage mode was confirmed to be tensile fibre failure (a) at the rear surface of the specimens similar to that seen in the experiments discussed in Chapter 6. Aside from fibre failure there was very limited damage witnessed for each of the other modes even at the higher incident pressures, again confirming the non-localised behaviour of the global air-blast loading condition being similar to that of the 3-point bending damage. Careful analysis of the tensile fibre damage seen at the rear of the specimen again also confirms further agreement with the experimental results, showing initial signs of fibre damage at the free edges which then propagates to the centre once the incident wave in sufficient high enough. Overall visually the damage observed within the model matches the damage seen as a result of the experiments.

This close correlation carries over to the through thickness damage of the CFRP specimen (as shown in Figure 8.26), although the damage area does increase with increasing incident pressure the damage area remains similar until a critical pressure was reached before then resulting in more significant damage as observed in the experiments. As seen from the experimental damage analysis in Chapter 6 the higher 0.8 MPa incident pressure was seen to be the approximate limit of the composites strength, with two of four specimens showing complete failure down the central damages region. This was confirmed by the model which shows significant tensile fibre failure propagating through the specimen from the rear surface at the high (0.8 MPa) incident pressure, but does not result in a complete failure of the specimen into two separate pieces. Following this analysis, the visual damage observed within the model does shown good agreement with that shown in the experimental results therefore validating the suitability of the developed VUMAT for the air-blast loading condition.

Similar to the ballistic impact analysis, a numerical comparison of the damage areas is shown in Figure 8.27. For the air-blast models the damaged areas show good agreement for each incident pressures, as well as, a good match to the observed upward trend therefore further confirming the validation of the developed CFRP VUMAT model for loading conditions within the presented loading region.

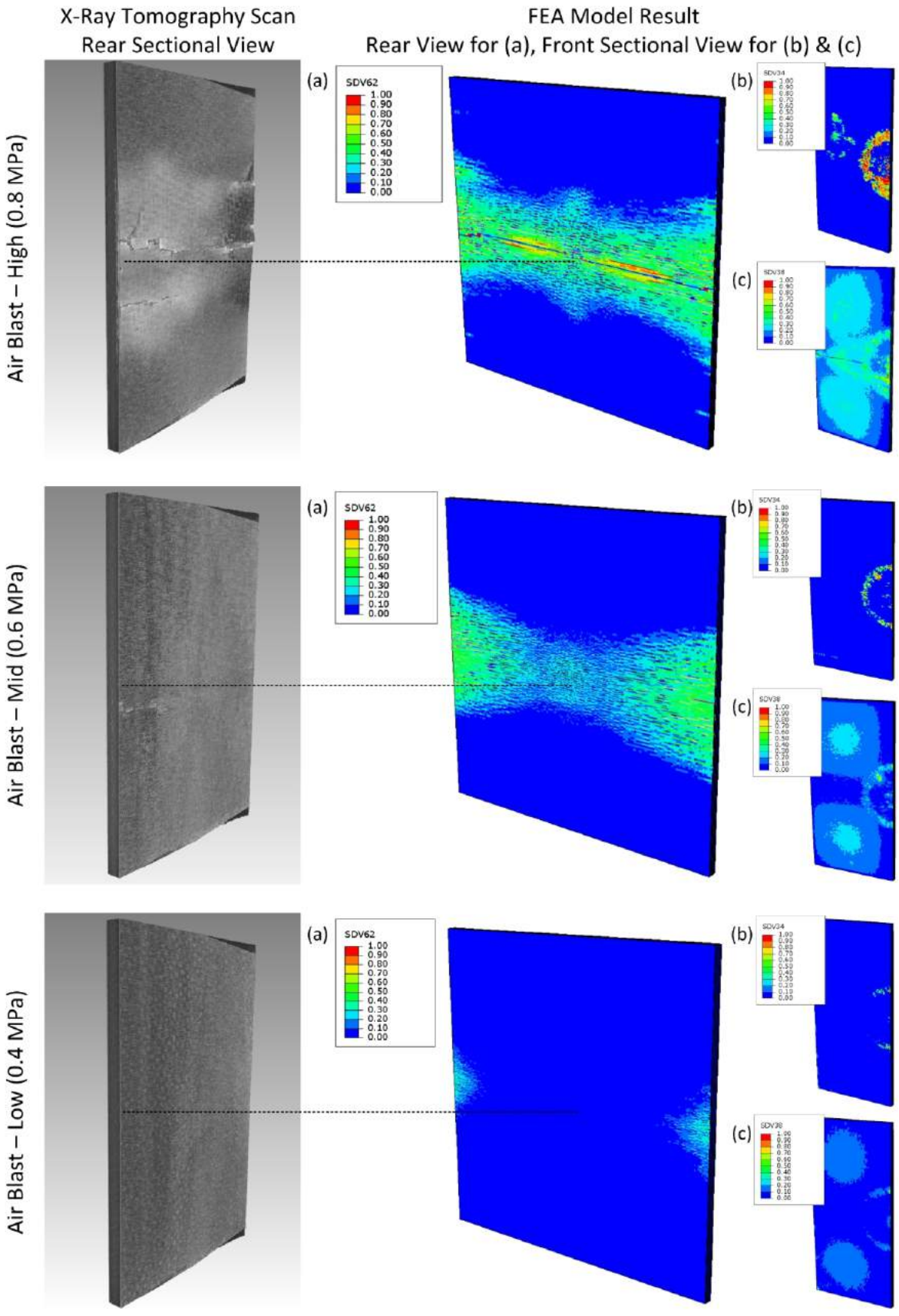

Figure 8.25: Air-blast model damage results: (a) fibre damage; (b) matrix damage; (c) shear damage

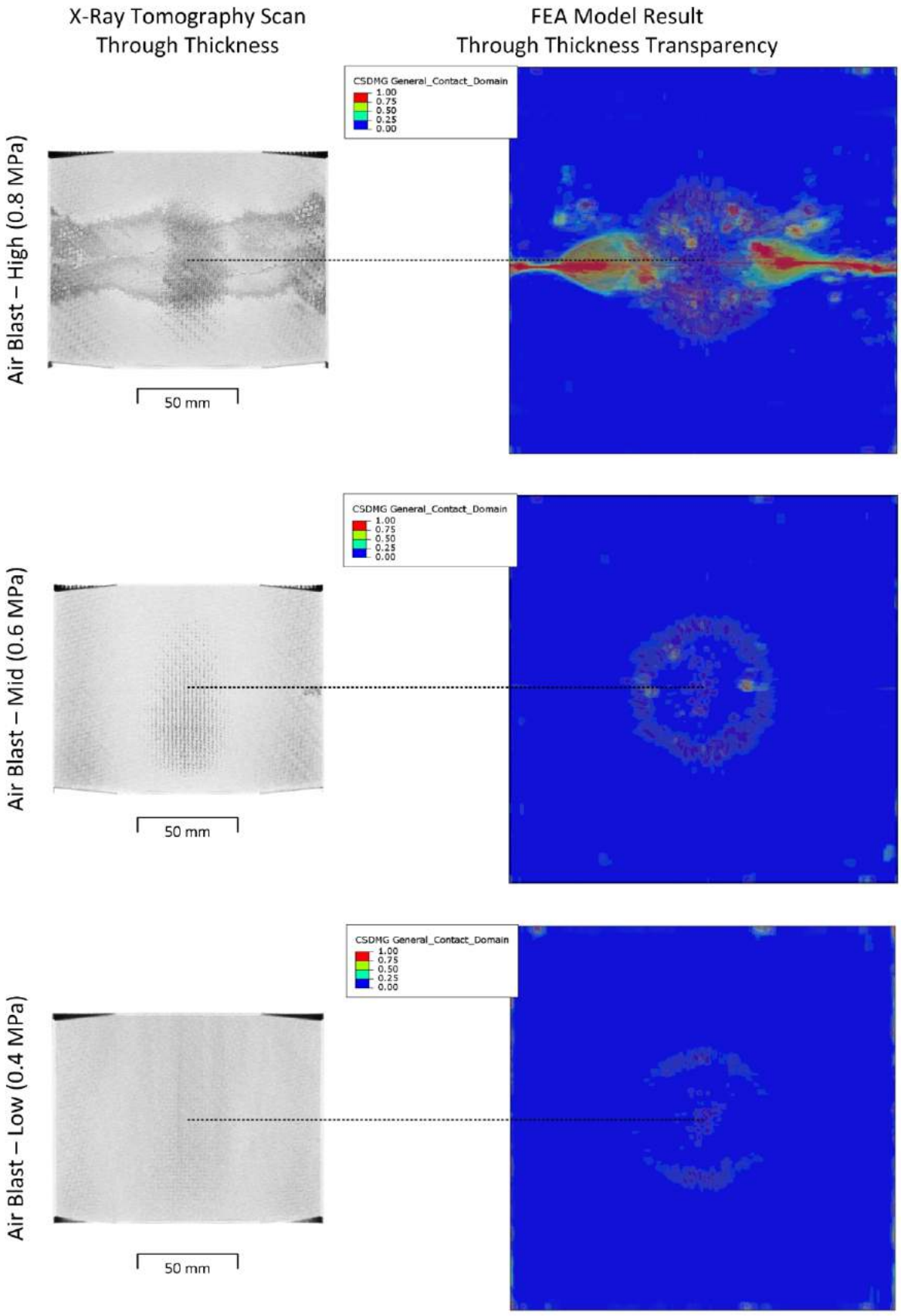

Figure 8.26: Air-blast impact model - through thickness damage cloud

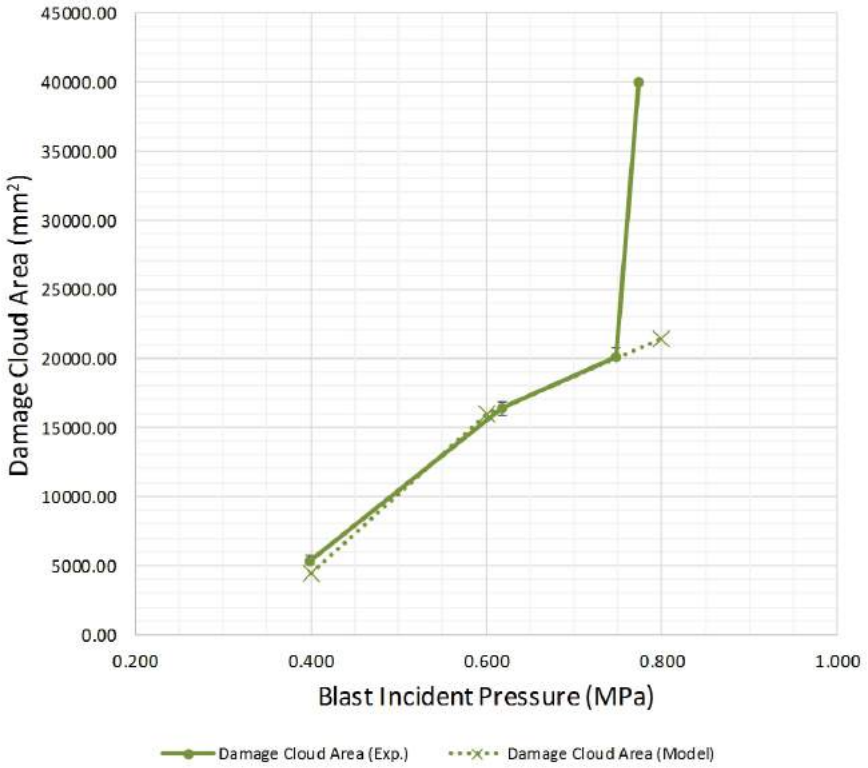

Figure 8.27: Experiments vs model results; a comparison of the through thickness damage clouds for the air-blast loading conditions vs. the blast incident pressure

8.6 Combination Loading of Dynamic Interactions

Following the analysis of the various loading conditions and the model vs. their corresponding experiments, the models presented next represents a hypothetical set of loading conditions. These hypothetical what if? scenarios shall represent an air-blast before an impact and an impact before an air-blast, which was presented and discussed via the use of two further numerical models. All models shall have the exact same set up parameters as the models presented previously, the projectiles were placed in the eulerian domain and allowed to interact with both the air-blast wave (eulerian volume) and the CFRP specimen. It should be noted that any possible changes away from the previously seen models resulting from the projectiles interaction with the eulerian region (air) means that these final results will not be compared back to the previous results, instead the analysis was be limited to these two hypothetical combined loading results and the comparisons between them. The final model setup and mesh in then shown in Figure 8.28.

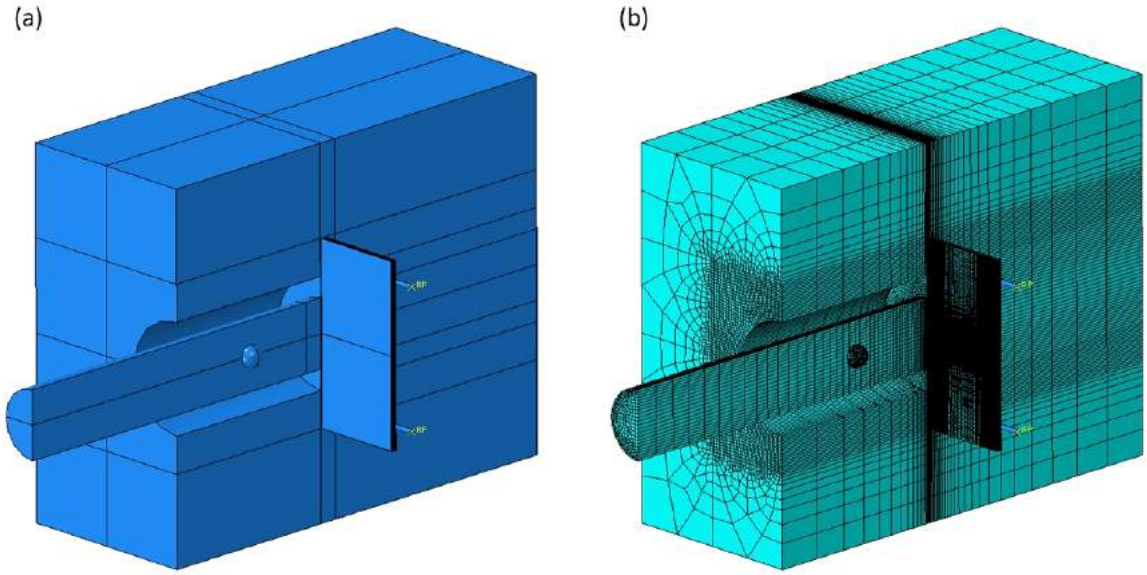

Figure 8.28: Combined air-blast and ballistic impact model setup: (a) assembly; (b) mesh

The two combined loading conditions have been chosen in order to assess the hypothetical scenarios proposed, each of which had the exact same loading parameters consisting of a 0.6 MPa air-blast incident shock wave and a 78.5 m/s rigid steel projectile impact. The only difference was the point in time at which the combined loading conditions meet the CFRP specimens surface, for the purposed study the impact was offset by -0.2 ms and +0.2 ms from the time at which the air-blast interacts with the specimen which has been shown to be within the critical frame of deformation for both loading conditions in Chapter 5. These loading condition scenarios are demonstrated in Figure 8.29 below before then presenting the results.

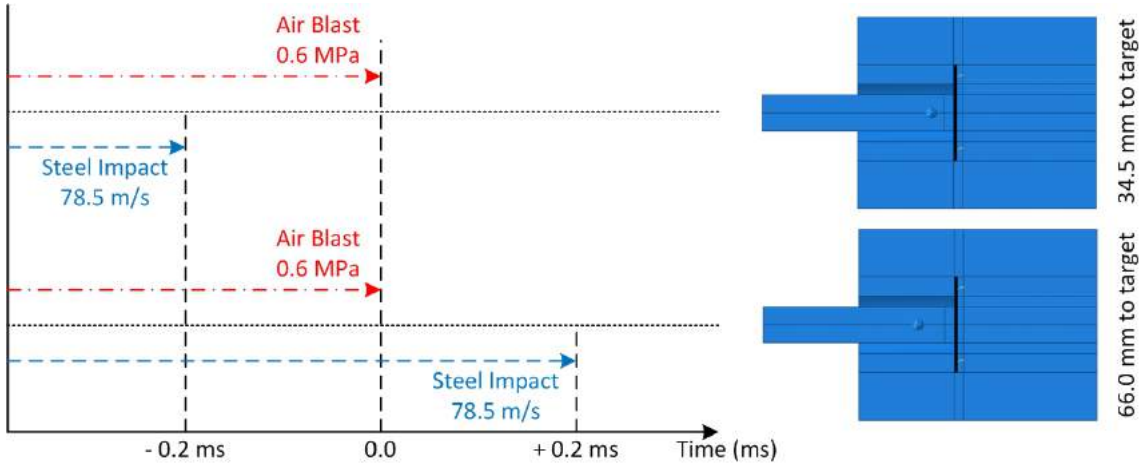

Figure 8.29: Combined air-blast and ballistic impact dynamic loading case offsets

8.6.1 Deformation Analysis

The finite-element models of the combined air-blast and ballistic impact loading condition has led to an insight into how dynamic loading conditions can influence each other during the event. Figure 8.30 below demonstrates how the propagating incident pressure within the eulerian domain can interact with the project as the shock wave passes, as expected, the interaction of the two loading conditions had an effect on each other with the rigid projectile gaining energy and going from 78.5 m/s to 79.4 m/s.

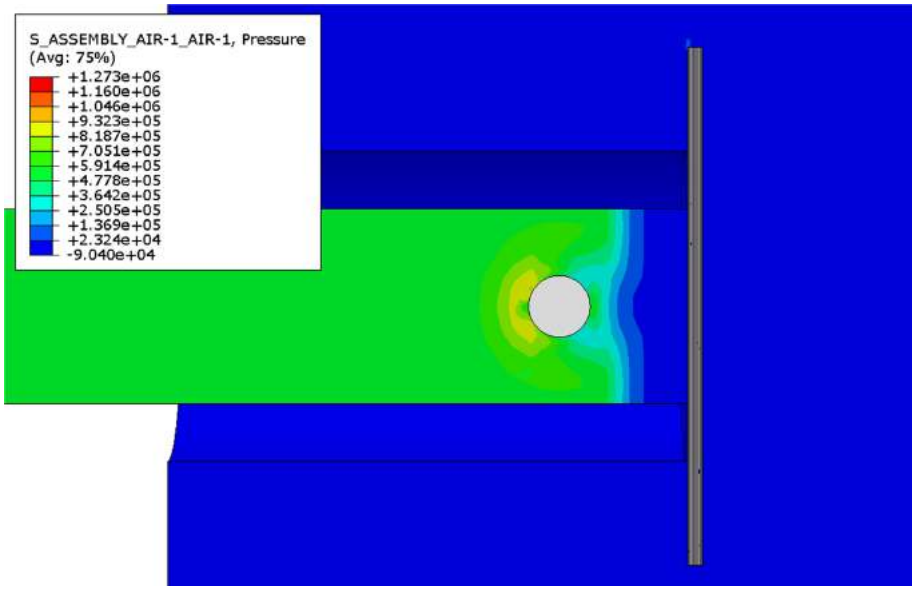

Figure 8.30: Combined air-blast and ballistic projectile loading condition interaction

The analysis of the deformation during the combined loading was assessed the same way as all model results presented previously, but the results of the two combined loading cases are presented together to draw direct comparisons. With the individual mid level loading conditions selected for these models, there was no signification damage expected, only some delamination as seen previously for both types of conditions and perhaps some rear surface tensile failure seen more during the ballistic loading.

The comparative deformation of both combined loading models is presented in Figure 8.31, the results from the models have been time shifted to bring the first interaction of either the impact or the air-blast forward to time = 0 s to see the extent of the damage in a fixed amount of time. From this figure it can be seen that initially both specimens respond in a very similar manor to that of the first loading condition presented previously, but as soon as the time was greater than 0.2 ms the second loading condition interacts

with the specimen and the results become more interesting. For this study only the first 0.6 ms are analysed up until maximum out-of-plane displacement was reached, and was an additional 0.4 ms after the second interaction, which was shown to be sufficient with reference to Chapter 5.

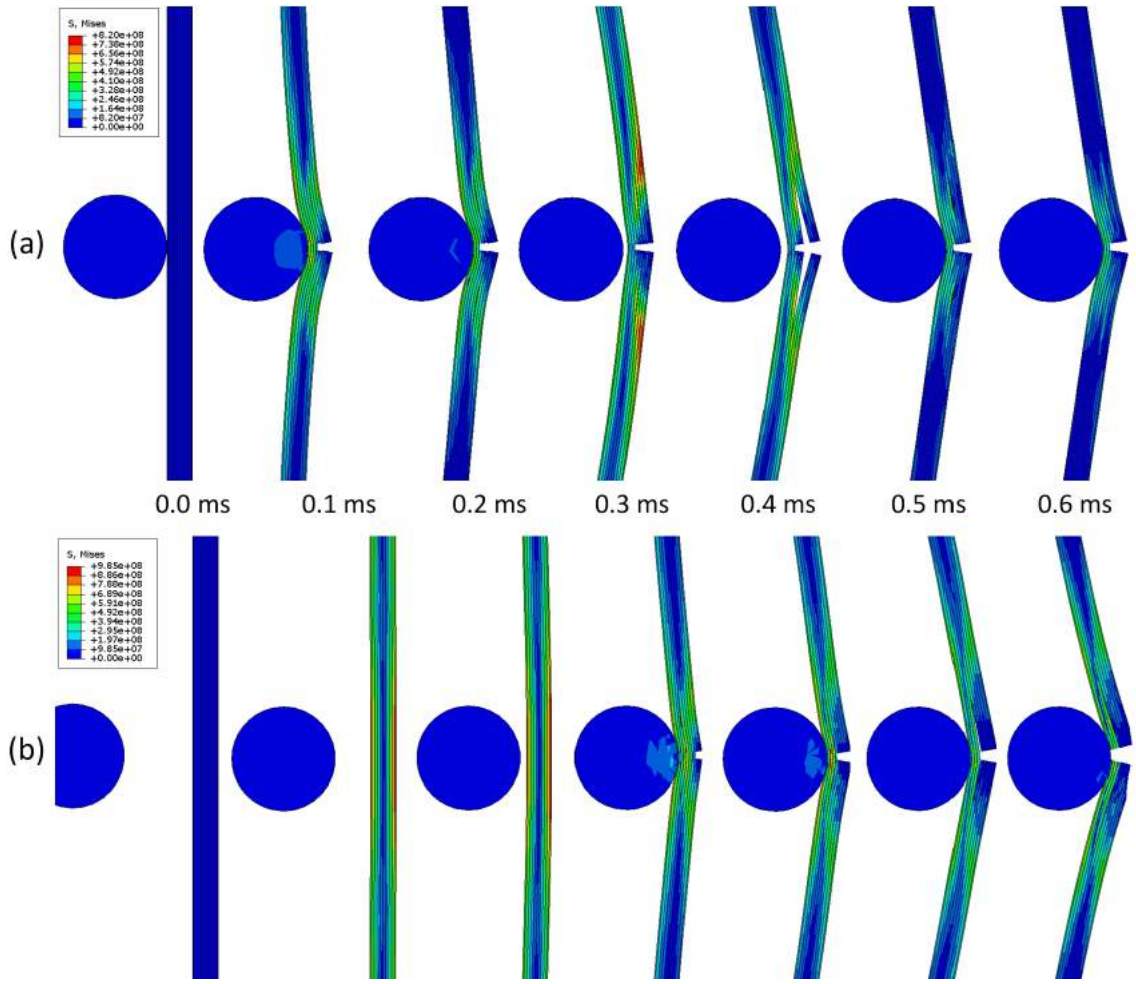

Figure 8.31: Out-of-plane displacement: (a) ballistic impact then air-blast; (b) air-blast then ballistic impact

In the figure above, the following is clearly observable. For the case where the impact was before air-blast, from 0.2 ms onwards the air-blast transitions the projectiles indentation towards global bending to the point that the projectile looses contact with the specimen. As a result the air-blast stops the fibre failure occurring at the earlier stage by removing the region of localised indentation with this transition to the global bending. For the case where the air-blast was before the impact, there does not appear to be any localised regions of indentation even, after the projectile has impacted the sample. This

suggested that the air-blast initiates the global bending from the start, therefore accelerating the specimens surface so that the chances of localised indentation was greatly reduced. In-fact, although this global bending has removed any region of high localised indentation at the early stages, this has resulted in aiding the projectile to completely perforate the specimen later in the interaction. This was down to the added maximum bending stresses in the specimen just before the projectile impacts the surface, this is confirmed and discussed in more detail below.

As can be seen from the line plot below (Figure 8.32 matching the same time frames as Figure 8.31), as soon as the second loading condition begins to interact with the specimen, the characteristics of the deformation begin to change for both cases as shown previously. For the case where the impact comes first (solid lines in figure), the out-of-plane displacement was similar to the magnitudes seen previous but when the air-blast shock wave reaches the specimens the transition to global 3-point bending begins. This global bending and associated acceleration of the specimen begins to mitigate the localised penetration of the impact with a more gradual transition when compared to previous ballistic impact results in Chapter 5, therefore, seemingly reducing the severity of the localised indentation seen within the specimen.

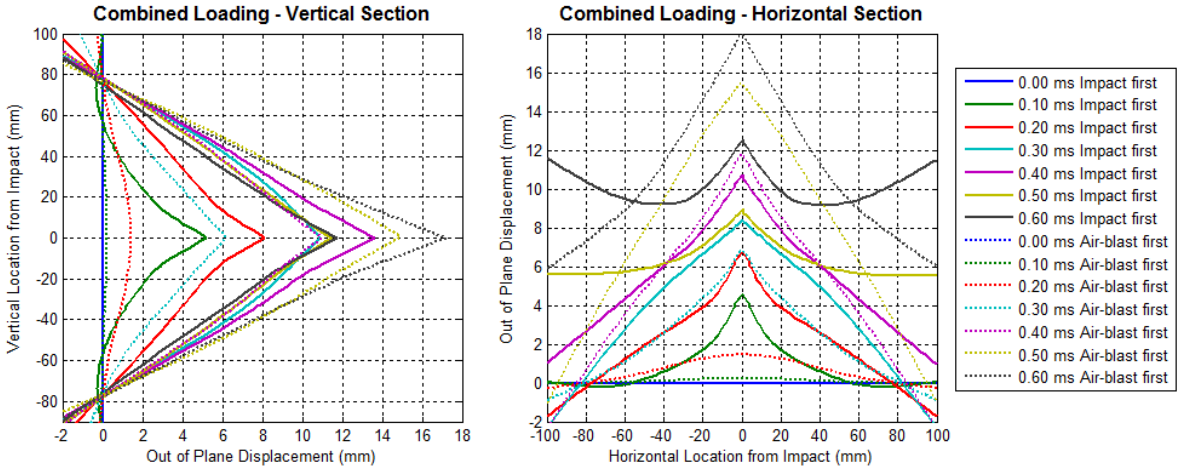

Figure 8.32: Out-of-plane displacement: impact then air-blast vs. air-blast then impact

The results for the air-blast before the impact on the other hand show a different interaction (dashed lines in figure), as mentioned previously it was thought that the global bending of the specimen would accelerate the target surface before the impact and therefore reduces the difference in the impact velocity. While this was partly true, the plot

shows a vast increase in out-of-plane displacement at the later stages, which from looking at the frame by frame analysis shown previously, resulted in an increased perforation of the specimen for this combined condition.

So far the deformation analysis suggests that within the initial stages of the combined loading, an impact before an air-blast pressure wave would be the more desirable case of combined loading, next the damage analysis of both the cases to confirm whether this was true.

8.6.2 Damage Analysis

For the damage analysis at the end of the 0.6 ms of combined loading, the final results show that both combined loading conditions display similar levels of damage. Figure 8.33 below shows the resulted damage observed for: (a) fibre damage; (b) matrix damage; (c) shear damage; (d) delamination. First, for the ballistic impact before the air-blast loading case, tensile failure at the rear surface of the specimen is clearly shown. In contrast to the individual loading cases, the combined case demonstrates both tensile fibre damage centrally as a result of the localised indentation from the projectile, but also the tensile fibre damage at the free edges due to the deformation from the air blast. Fibre damage for the air-blast before ballistic impact was similar, but does show a significant difference. The lack of the fibre damage at the free edges suggest that within the time frame, the free edge do not experience the same deformation as the other condition. This was confirmed by the deformation analysis, and stems from the increase perforation by the projectile later in the interaction which results in greater tensile fibre damage behind the region of impact on the rear surface.

The analysis of the delamination supports the points made previously, both combined loading condition display damage patterns similar to that of both localised ballistic impact in the form of the localised spot and the more global air-blast in the for large ring of damage as discussed previously in Chapter 6. As well as this, both results show the characteristic cross shape of delamination forming from the centre, the air-blast before ballistic impact condition demonstrated a large cross configuration which was a result of the increased tensile failure at the rear surface. For both the combined loading conditions, the extent of the matrix and shear damage remain low and concentrated to the localised indentation regions as expected.

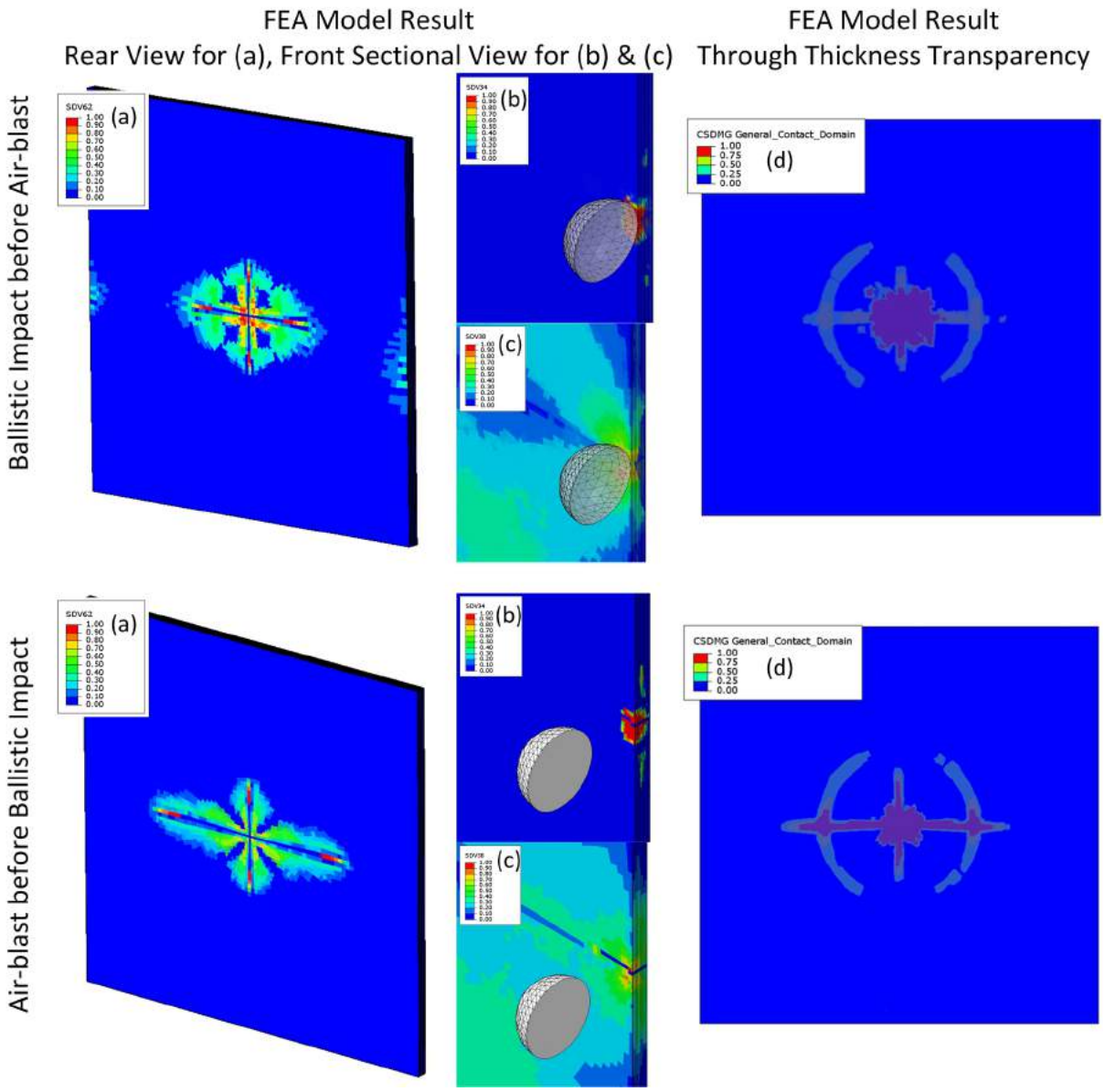

Figure 8.33: Combined loading damage results: (a) fibre damage; (b) matrix damage; (c) shear damage; (d) delamination

8.7 Chapter Summary

In this chapter, the ballistic impact and air-blast response of the chosen 2×2 twill woven CFRP composite was analysed using the phenomenological continuum damage VUMAT model developed in Chapter 7. In order to do this a new approach for obtaining material parameters for the proposed model was developed by extrapolating data from experimental journal papers matching the chosen composite before then appropriately

scaling against tensile testing of the presented CFRP specimens. These parameters were initially validated via the charpy hammer impact model described in the previous chapter, before then progressing onto validating the developed VUMAT model against each of the experiment loading conditions described in Chapter 4.

The developed material model was implemented into the ABAQUS Explicit FE software, were the CFRP specimens were then subjected to each of the ballistic rigid steel, ballistic fragmenting ice, and shock wave air blast loading conditions before then analysing the comparison of the deformation and damage result against the experimental results presented in Chapters 5 and 6. For the ballistic rigid steel projectiles, the developed model showed good agreement for both the deformation profiles of the specimens and then supported the previous conclusion that the damage remains localised and tensile fibre failure was dominant. For the ballistic fragmenting ice projectiles the validation was not so straight forward, while the deformation profiles and damage areas showed some correlation to the experimental data definitive validation could not be given. It was thought that the model approached lacked the ability to produce the required behaviour, which in turn lead to a reduced amount of localised indentation before the ice fragmented. This lack of indentation lead to a significant difference in the transition of the specimens deformation curvature, and to a reduced amount of damage and delamination as the project did not fragment inside the specimen as seen in the experiments. Moving to the air-blast shock wave loading conditions, the deformation profiles from the models showed excellent agreement when compared to the experimental result. The same was seen when examining and comparing the damage observed in the model to that of the results, where damage remained low until a critical pressure was reached and the observed damage increment significantly when tensile fibre failure remained dominant. Following the analysis against each of the dynamic loading conditions and their corresponding experimental results, the development phenomenological continuum damage VUMAT model was deemed to be validated and suitable for modelling and predicting behaviour as a result of loading conditions seen within the presented region.

Finally with the fundamental behaviour of the separate loading conditions analysed and validated, the combination loading of these events which are very rarely mutually exclusive in extreme environments were studied to conclude the research. The exact same modelling approach was employed to predict and analyse the hypothetical scenarios of an impact closely followed by an air-blast and visa-versa, subjecting the CFRP to set

combined loading conditions within the limits of those set out within the scope of the experiment studies. From these final models the following conclusions could be drawn:

- Loading conditions applied in this close proximity, will interact with each other while approaching the target, this can cause a change in magnitudes of the original conditions which needs to be understood if further work is to be completed.
- An air-blast following a projectile can reduce some of the localised indentation observed, therefore reducing some of the tensile fibre damage during early stages of the interaction.
- An air-blast before an impact will globally accelerate the target surface, therefore, reducing the chances of indentation during the early stages due to the reduced projectile impact velocity.
- Later impacts once the air-blast global bending is in progress leads to increased tensile fibre failure and specimen perforation, due to the already high bending stressing at the surfaces of the specimen while at max out-of-plane displacement.
- For either loading case the observed delamination within the specimens will remain localised to the point of any ballistic impact, and will only significantly propagate following tensile fibre failure at the rear surface.

Next and final chapter outlines the conclusions of presented research work and summarises its advantages and outcomes. The research outlook and future work is then also discussed.

Chapter 9

Conclusions and Future Work

9.1 Conclusions

The research presented within this thesis has examined the fundamental behaviour of various dynamic loading conditions on a 2×2 twill woven Carbon Fibre Reinforced Polymer (CFRP) composite, and has included ballistic impact with both rigid steel and fragmenting ice projectiles as well as air-blast shock wave interactions. With CFRPs proven to be a popular choice in many applications given their higher desired and advantageous high strength to weight ratio, their often superior behaviour making them ideal for these extreme loading conditions. In a real environment, these dynamic loading conditions are very rarely mutually exclusive, and so as mentioned originally, it is necessary to analyse the combined loading of both an impact and air-blast shock wave which then creates the following question. Which is the most destructive, a ballistic impact closely followed by an air-blast or visa-versa?

Firstly, the focal point of the research examines the experimental testing of a consistent CFRP specimen material to ballistic rigid steel and fragmenting ice projectiles, as well as air-blast shock wave loading while linking all results to three defined categories of damage. The resulting deformation behaviour was analysed via in-situ digital image correlation from high-speed photography, alongside the post loading damage analysis via X-ray tomography where the through thickness hidden damage can be analysed. This experimental testing series has given a unique opportunity to study the composites be-

haviour when subjected to various loading conditions, which has then in turn enabled comparative analysis via consistent methodologies. From these studies, the fundamental conclusions can be finally drawn with regards to the deformation and damage analysis of the chosen CFRP.

Deformation Analysis

- The initial differences between the loading conditions can be generally defined as a localised process zone in the case of the rigid steel projectile, through to a transition from a local to a global process zone for the ice projectile during fragmentation, and finally a global process zone for the case of the air-blast loading.

- For projectiles of the same size a rigid (steel) impact demonstrates more defined indentation of the specimens before the transition into global flexural bending, whereas fragmenting (ice) projectiles produce initial indentation but upon fragmentation any local indentation is more gradually transitioned to distributed loading leading to global flexural bending.

- Damage at the rear surface of the specimens occurs much sooner when the projectile is rigid (steel) than that of the fragmenting (ice) projectile, this is likely due to the almost instantaneous fragmentation of the ice projectile on impact causing more widely distributed loading and therefore a longer impact duration even at the clearly higher impact energies.

- For the ballistic loaded specimens there are definitive differences between the specimens responses, even at varying loading magnitudes. Whereas for the air-blast loaded specimens no real differences can be seen, apart from the obvious change in out-of-plane displacement.

- It is clear that of the two extremes, the more localised loading of the rigid (steel) impacts results in localised indentation and greater localised damage, while the air-blast loading clearly results in wider distributed loading resulting in almost instantaneous global flexural bending. The fragmenting (ice) impacts almost form a middle ground between the two, and start out as localised indentation but upon fragmentation transitions to wider distributed loading.

Experimental Damage Analysis

- A suitable X-ray tomography scanning regime was found and used to acquire 180 mm x 140 mm x 20mm volume reconstructions (due to limits of the scanner) of each specimen's internal damage, at a resultant pixel/voxel resolution of 97 μm enabling quantitative damage analysis.

- The rigid (steel) projectiles caused localised indentation to the front surfaces, which then leads to the appearance of tensile failure of the plies at the rear surface as the projectile penetrates further into the specimens. Given the localised nature of the impact, the damage cloud is limited to a slight increase in area keeping to a localised region as impact energy increase.

- The fragmenting nature of the ice projectiles results in partial indentation into the specimen but upon fragmentation below the surface, depth depending on the impact energy, the remains of the projectile cause catastrophic delamination with no signs of any further penetration. Given the wide spread nature of resulting visual damage, the damage cloud is seen to clearly increase in area as the impact energy increases.

- For the air-blast cases the damage observed can be compared to that of a three point bending test where the first signs of damage appear along a central line between the supports as tensile failure of the plies leading to delamination where the bending stresses are greatest. The extent of the tensile failure at the rear surface increases with increasing air blast magnitude.

The second part of the research then focused on the development of the meso-scale modelling strategy for carbon fibre-reinforce polymers (CFRPs) via a phenomenological continuum damage approach. The model combines models by Hashin (1980) and by Puck and Schürmann (1998), which were suitably modified in order to model a woven laminate. The modelling approach was incorporated into Abaqus Explicit 6.14-4 as a vectorised user defined subroutine (VUMAT), with inter-ply delamination modelled via cohesive zone surfaces (CZSs). A methodology for material parameters was also developed by extrapolating data from experimental journal papers matching the chosen composite, before then appropriately scaling against tensile testing of the presented CFRP specimens. These parameters were initially validated via a charpy hammer impact model. The developed model was then subjected to each of the ballistic rigid steel, ballistic fragmenting

ice, and shock wave air-blast loading conditions before then analysing the comparison of the deformation and damage against the experimental results. For all loading cases, the developed model showed good agreement for both the deformation profiles of the specimens and the resulting damage observed and was deemed to be suitably validated for modelling and predicting behaviour as a result of loading conditions seen within the presented region.

Finally with the fundamental behaviour of the separate loading conditions analysed and validated, the hypothetical combination loading of these events which are very rarely mutually exclusive were studied to conclude the research. The exact same modelling approach was employed to predict and analyse the hypothetical scenarios of an impact closely followed by an air-blast and visa-versa, subjecting the CFRP to set combined loading conditions within the limits of those set out within the scope of the experiment studies. From these final models the follow fundamental conclusions have been drawn.

- Loading conditions applied is this close proximity will interact with each other while approaching the target, this can cause a change in magnitudes of the original conditions which need to be understood if further work is to be completed.
- An air-blast following a projectile can reduce some of the localised indentation observed, therefore reducing some of the tensile fibre damage during early stages of the interaction.
- An air-blast before an impact will globally accelerate the target surface, therefore, reducing the chances of indentation during the early stages due to the reduced projectile impact velocity.
- Later impacts once the air-blast global bending is in progress leads to increased tensile fibre failure and specimen perforation, due to the already high bending stressing at the surface of the specimen.
- For either loading case the observed delamination within the specimens will remain localised to the point of any ballistic impact, and will only significantly propagate following tensile fibre failure at the rear surface.

Following this, the original question posed at the beginning of this thesis can be answered. In the limits of the modelled loading conditions, an air-blast followed by an impact appears to be most destructive at the earlier stages of a combined interaction.

9.2 Outcomes

Follow these conclusions, the following outcomes from the research are defined below.

Positive Outcomes

- A new experimental contribution to this field of research is in the form of the direct comparison of ice projectiles and their effect on deformation and damage when compared to that of the more typical steel projectile impacts on the same composite, as well as the comparison to air-blast / shock wave loading.
- The developed meso-scale modelling strategy for carbon fibre-reinforced polymer (CFRP) via a phenomenological continuum damage approach provided an accurate assessment of the failure mechanics of the composite under the various dynamic loading conditions without modification which were then validated again the experimental results.
- Successful implementation of a cohesive zone surface approach to inter-ply delamination modelling, which have demonstrated accurate correlation to experimental result while avoiding any adverse effects on computation efficiencies associated with thin cohesive zone elements (reduced stable time increment).
- A new methodology for selecting material parameters was developed by extrapolating data from experimental journal papers matching the chosen composite before then appropriately scaling against tensile testing of the presented composite, all modelling efforts have validated the parameters and therefore the method.
- An study on which combined dynamic loading conditions are the most destructive, an impact closely followed by an air-blast or visa-versa has been answered during early stages of the interaction

Areas Requiring Further Attention

- Although the presented X-ray tomograpy scans and sample photographs where sufficient to determine the damage mechanisms presents as a result of each loading condition, further effort could be made to conduct further scans with improved spacial resolution to enhance the quality of the obtained results in Chapter 6.

- The chosen method for modelling the fragmenting ice projectiles did not result in conclusive validation, while the deformation profiles and damage areas showed some correlation to the experimental data definitive validation could not be given for the whole model. Improving this would conclusively validate the fragmenting ice impact models in Chapter 8.

- The meso-scale modelling strategy for carbon fibre reinforce polymer (CFRP) via the phenomenological continuum damage approach presented in this research is limited to the behaviour of the homogenised plies, and does not account for the behaviour of the individual constituents at a micro-scale and their randomised distribution used to make the composite material and may provide further accuracy when assessing larger structures.

9.3 Recommended Future Work

Following the research presented, the areas discussed below are thought to be those that would provide clear direction to further improve the research area.

1. The presented hypothetical combination of the dynamic loading conditions is only the start of a vast number of modelling scenarios that could be investigated, as well as this, further regimes could be planned in order to experimentally and numerically investigate combined loading conditions as briefly investigated in this research.

2. The model presented in this research assumed uniformly distributed fibres, but in reality this uniformity is never observed. The addition of carefully calibrated parameters to offset the elasticity and strength of the composite across a statistical distribution, would further improve the behaviour of the model and begin to take into consideration the micro-structures random distribution.

3. To explore the added effect of the individual composite constituents and their non-uniform distribution with the plies, and ways of encompassing the micro-scale behaviour to accurate modelling accuracy. Raghavan et al. (2004) proposed an adaptive multi-level computational model that combines a conventional finite-element model with a microstructural Voronoi unit cell FEM (VCFEM), this modelling technique is capable of analysing macro- through to micro-scale behaviour in composite

structures with non-uniform heterogeneous microstructures. A similar approach to this could be used to link the meso-scale model presented in this research, to the micro-scale behaviour by utilising unit cells which could be inserted when neccessary to save on computation resource and excessive run times. Figure 9.1 shows an example of the macro- to micro-scale adaptive geometry and meshing as a result of the adaptive multi-level model which could prove useful when modelling composites.

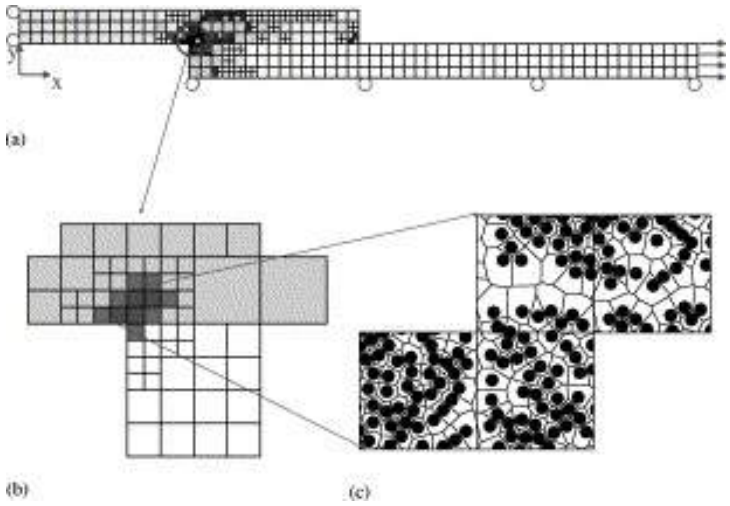

Figure 9.1: (a) Macroscopic model of the multi-level mesh showing boundary conditions, (b) zoomed in region of the macroscopic mesh undergoing level transition, and (c) microscopic analysis in the level-2 regions with VCFEM developed by Raghavan et al. (2004)

Bibliography

ABAQUS (2014). *Abaqus 6.14 Analysis Uner's Manual*. Dassault Systems.

Abisset, E., F. Daghia, and P. Ladevèze (2011). "On the validation of a damage meso-model for laminated composites by means of open-hole tensile tests on quasi-isotropic laminates". In: *Composites Part A: Applied Science and Manufacturing* 42.10, pp. 1515 –1524. ISSN: 1359-835X.

Abrate, Serge (1991). "Impact on Laminated Composites". In: *ASME* 44.4, pp. 155 –190. ISSN: 0003-6900.

— (1994). "Impact on Laminated Composites: Recent Advances". In: *ASME* 47.11, pp. 517 –544. ISSN: 0003-6900.

Agarwal, Bhagwan D., Lawrence J. Broutman, and K. Chandrashekhara (2006). *Analysis and Performance of Fiber Composites*. Third Edition. John Wiley & Sons.

Alif, Nidal, Leif A. Carlsson, and Louis Boogh (1998). "The effect of weave pattern and crack propagation direction on mode I delamination resistance of woven glass and carbon composites". In: *Composites Part B: Engineering* 29.5, pp. 603 –611. ISSN: 1359-8368.

Appleby-Thomas, Gareth J., Paul J. Hazell, and Gussan Dahini (2011). "On the response of two commercially-important CFRP structures to multiple ice impacts". In: *Composite Structures* 93.10, pp. 2619–2627. ISSN: 02638223.

Appleby-Thomas, G.J. et al. (2015). "On the ballistic response of an aerospace-grade composite panel to non-spheroidised fragment simulants". In: *Composite Structures* 119.0, pp. 90 –98. ISSN: 0263-8223.

Asp, Leif and Rickard Juntikka (2009). "High velocity impact on NCF reinforced composites". In: *Composites Science and Technology* 69.9. Special Issue on the 12th European Conference on Composite Materials (ECCM12), organized by the European Society for Composite Materials (ESCM), pp. 1478 –1482. ISSN: 0266-3538.

Backman, Marvin E. and Werner Goldsmith (1978). "The mechanics of penetration of projectiles into targets". In: *International Journal of Engineering Science* 16.1, pp. 1 –99. ISSN: 0020-7225.

Batto, R.A. and E.M. Schulson (1993). "On the ductile-to-brittle transition in ice under compression". In: *Acta Metallurgica et Materialia* 41.7, pp. 2219 –2225. ISSN: 0956-7151.

Berbinau, P., C. Soutis, and I.A. Guz (1999a). "Compressive failure of 0° unidirectional carbon-fibre-reinforced plastic (CFRP) laminates by fibre microbuckling". In: *Composites Science and Technology* 59.9, pp. 1451 –1455. ISSN: 0266-3538.

Berbinau, P. et al. (1999b). "Effect of off-axis ply orientation on 0°-fibre microbuckling". In: *Composites Part A: Applied Science and Manufacturing* 30.10, pp. 1197 –1207. ISSN: 1359-835X.

Boeing (2006). *Boeing 787 From the ground up.* URL: `http://www.boeing.com/commercial/aeromagazine/articles/qtr_4_06/article_04_2.html` (visited on 01/03/2015).

Bogdanovich, Alexander E. et al. (2013). "Quasi-static tensile behavior and damage of carbon/epoxy composite reinforced with 3D non-crimp orthogonal woven fabric". In: *Mechanics of Materials* 62.0, pp. 14 –31. ISSN: 0167-6636.

Bogetti, Travis A. et al. (2004). "Predicting the nonlinear response and failure of composite laminates: correlation with experimental results". In: *Composites Science and Technology* 64.3–4. Failure criteria in fibre reinforced polymer composites Part C: Additional theories conclusions and recommendations, pp. 477 –485. ISSN: 0266-3538.

Bourne, Neil (2013). *Materials in Mechnical Extremes: Fundamentals and Applications.* First Edition. Cambridge University Press.

Bull, D.J. et al. (2013). "A comparison of multi-scale 3D X-ray tomographic inspection techniques for assessing carbon fibre composite impact damage". In: *Composites Science and Technology* 75, pp. 55 –61. ISSN: 0266-3538.

Bunsell, A.R. and J. Renard (2005). *Fundamentals of Fibre Reinforced Composite Materials*. First Edition. Series in Material Science and Engineering. CRC Press.

Callus, P.J. et al. (1999). "Tensile properties and failure mechanisms of 3D woven GRP composites". In: *Composites Part A: Applied Science and Manufacturing* 30.11, pp. 1277 –1287. ISSN: 1359-835X.

Cambridge University, Materials Group (2002). *Material Selection Charts*. URL: `http://www-materials.eng.cam.ac.uk/mpsite/interactive_charts/stiffness-density/NS6Chart.html` (visited on 01/03/2014).

Cantwell, W.J. and J. Morton (1991). "The impact resistance of composite materials — a review". In: *Composites* 22.5, pp. 347–362. ISSN: 0010-4361.

Carraro, P.A. and M. Quaresimin (2014). "Modelling fibre–matrix debonding under biaxial loading". In: *Composites Part A: Applied Science and Manufacturing* 61.0, pp. 33 –42. ISSN: 1359-835X.

Carrere, N, F Laurin, and J F Maire (2012). "Micromechanical-based hybrid mesoscopic 3D approach for non-linear progressive failure analysis of composite structures". In: *Journal of Composite Materials* 46.19-20, pp. 2389–2415.

Carvalho, N.V. De, S.T. Pinho, and P. Robinson (2012a). "Analytical modelling of the compressive and tensile response of woven composites". In: *Composite Structures* 94.9, pp. 2724 –2735. ISSN: 0263-8223.

Combescure, A., Y. Chuzel-Marmot, and J. Fabis (2011). "Experimental study of high-velocity impact and fracture of ice". In: *International Journal of Solids and Structures* 48.20, pp. 2779 –2790. ISSN: 0020-7683.

Cook, Robert D. et al. (2010). *Concepts and Applications of Finite Element Analysis*. Fourth Edition. John Wiley & Sons.

Cruz, Juan Il, C H Shah, and A S Postyn (1996). "Properties of Two Carbon Composite Materials Using LTM25 Epoxy Resin". In:

Cuntze, RG and A Freund (2004). "The predictive capability of failure mode concept-based strength criteria for multidirectional laminates". In: *Composites Science and Technology* 64.3, pp. 343–377.

Dai, S. et al. (2015). "Influence of fibre architecture on the tensile, compressive and flexural behaviour of 3D woven composites". In: *Composites Part A: Applied Science and Manufacturing* 69.0, pp. 195 –207. ISSN: 1359-835X.

Daniel, I.M., B.T. Werner, and J.S. Fenner (2011a). "Strain-rate-dependent failure criteria for composites". In: *Composites Science and Technology* 71.3, pp. 357–364. ISSN: 02663538.

— (2011b). "Strain-rate-dependent failure criteria for composites". In: *Composites Science and Technology* 71.3, pp. 357 –364. ISSN: 0266-3538.

Deka, L.J., S.D. Bartus, and U.K. Vaidya (2009). "Multi-site impact response of S2-glass/epoxy composite laminates". In: *Composites Science and Technology* 69.6. ONR - Dynamic Failure and Durability, pp. 725 –735. ISSN: 0266-3538.

Demiral, Murat et al. (2011). "Finite-Element Simulations of Split Hopkinson Test of Ti-Based Alloy". In: *Advanced Materials Research* 223, pp. 296 –303.

Fagiano, C. et al. (2014). "Computational geometrical and mechanical modeling of woven ceramic composites at the mesoscale". In: *Composite Structures* 112.0, pp. 146 –156. ISSN: 0263-8223.

Foroutan, Rana et al. (2013). "Experimental investigation of high strain-rate behaviour of fabric composites". In: *Composite Structures* 106, pp. 264 –269. ISSN: 0263-8223.

Garcia, I.G., V. Mantic, and E. Graciani (2015). "Debonding at the fibre-matrix interface under remote transverse tension. One debond or two symmetric debonds?" In: *European Journal of Mechanics - A/Solids* -.0, In Press. ISSN: 0997-7538.

Gauch, Erin, James LeBlanc, and Arun Shukla (2012). "Response of preloaded thin composite panels subjected to underwater explosive loading". In: *Computers & Structures* 112–113.0, pp. 342 –353. ISSN: 0045-7949.

Gerlach, Robert, Christian Kettenbeil, and Nik Petrinic (2012). "A new split Hopkinson tensile bar design". In: *International Journal of Impact Engineering* 50.0, pp. 63 –67. ISSN: 0734-743X.

Gorham, D A (1983). "A numerical method for the correction of dispersion in pressure bar signals". In: *Journal of Physics E: Scientific Instruments* 16.6, p. 477.

Greco, Fabrizio, Lorenzo Leonetti, and Paolo Lonetti (2013). "A two-scale failure analysis of composite materials in presence of fiber/matrix crack initiation and propagation". In: *Composite Structures* 95.0, pp. 582 –597. ISSN: 0263-8223.

Gu, Huang (2007). "Tensile behaviours of woven fabrics and laminates". In: *Materials & Design* 28.2, pp. 704 –707. ISSN: 0261-3069.

Hadavinia, H. and H. Ghasemnejad (2009). "Effects of Mode-I and Mode-II interlaminar fracture toughness on the energy absorption of CFRP twill/weave composite box sections". In: *Composite Structures* 89.2, pp. 303 –314. ISSN: 0263-8223.

Hashin, Z. (1980). "Failure Criteria for Unidirectional Fiber Composites". In: *Journal of Applied Mechanics* 47.2, pp. 329 –334.

Herakovich, Carl T. (1998). *Mechanics of Fibrous Composites*. First Edition. John Wiley & Sons.

Hiermaier, Stefan (2008). *Structures Under Crash and Impact: Continuum Mechanics, Discretization and Experimental Characterisation*. First Edition. Springer.

Higuchi, R. et al. (2017). "Progressive failure under high-velocity impact on composite laminates: Experiment and phenomenological mesomodeling". In: *Engineering Fracture Mechanics* 178, pp. 346 –361. ISSN: 0013-7944.

Hopkinson, B. (1914). "A Method of Measuring the Pressure Produced in the Detonation of High Explosives or by the Impact of Bullets". English. In: *Philosophical Transactions of the Royal Society of London. Series A, Containing Papers of a Mathematical or Physical Character* 213, pp. 437 –456. ISSN: 02643952.

Hosur, M.V et al. (2001). "High strain rate compression response of carbon/epoxy laminate composites". In: *Composite Structures* 52.3. Design and Manufacturing of Composite Structures, pp. 405 –417. ISSN: 0263-8223.

Hosur, M.V. et al. (2004a). "Experimental Studies on the High Strain Rate Compression Response of Woven Graphite/Epoxy Composites at Room and Elevated Temperatures". In: *Journal of Reinforced Plastics and Composites* 23.5, pp. 491 –514.

Hosur, M.V. et al. (2004b). "Studies on the off-axis high strain rate compression loading of satin weave carbon/epoxy composites". In: *Composite Structures* 63.1, pp. 75 –85. ISSN: 0263-8223.

Hou, J.P and C Ruiz (2000). "Measurement of the properties of woven CFRP T300/914 at different strain rates". In: *Composites Science and Technology* 60.15, pp. 2829 –2834. ISSN: 0266-3538.

Hsiao, H. M., I. M. Daniel, and R. D. Cordes (1999). "Strain Rate Effects on the Transverse Compressive and Shear Behavior of Unidirectional Composites". In: *Journal of Composite Materials* 33.17, pp. 1620–1642. ISSN: 0021-9983.

Jackson, Matthew and Arun Shukla (2011). "Performance of sandwich composites subjected to sequential impact and air blast loading". In: *Composites Part B: Engineering* 42.2, pp. 155 –166. ISSN: 1359-8368.

Johnson, H.E. et al. (2009). "Modelling impact damage in marine composite panels". In: *International Journal of Impact Engineering* 36.1, pp. 25 –39. ISSN: 0734-743X.

Jones, Stephen J. (1997). "High Strain-Rate Compression Tests on Ice". In: *The Journal of Physical Chemistry B* 101.32, pp. 6099–6101.

Kachanov, L. M. (1958). "On time to rupture in creep conditions (in russian)". In: *Izviestia Akademii Nauk SSSR* 8, pp. 26 –31.

Kaddour, AS and MJ Hinton (2013). "Maturity of 3D failure criteria for fibre-reinforced composites: Comparison between theories and experiments: Part B of WWFE-II". In: *Journal of Composite Materials* 47.6-7, pp. 925 –966. eprint: `http://jcm.sagepub.com/content/47/6-7/925.full.pdf+html`.

Kaddour, AS et al. (2013). "The background to the third world-wide failure exercise". In: *Journal of Composite Materials* 47.20-21, pp. 2417 –2426. eprint: `http://jcm.sagepub.com/content/47/20-21/2417.full.pdf+html`.

Kajberg, Jörgen and K.G. Sundin (2013). "Material characterisation using high-temperature Split Hopkinson pressure bar". In: *Journal of Materials Processing Technology* 213.4, pp. 522 –531. ISSN: 0924-0136.

Karthikeyan, K. et al. (2013). "The effect of shear strength on the ballistic response of laminated composite plates". In: *European Journal of Mechanics - A/Solids* 42.0, pp. 35 –53. ISSN: 0997-7538.

Katayama, M., S. Toda, and S. Kibe (1997). "Numerical simulation of space debris impacts on the Whipple shield". In: *Acta Astronautica* 40.12, pp. 859 –869. ISSN: 0094-5765.

Kim, Hyonny, Douglas A Welch, and Keith T Kedward (2003). "Experimental investigation of high velocity ice impacts on woven carbon/epoxy composite panels". In: *Composites Part A: Applied Science and Manufacturing* 34.1, pp. 25 –41. ISSN: 1359-835X.

Kim, Jang-Kyo and Man-Lung Sham (2000). "Impact and delamination failure of woven-fabric composites". In: *Composites Science and Technology* 60.5, pp. 745 –761. ISSN: 0266-3538.

Koerber, H., J. Xavier, and P.P. Camanho (2010). "High strain rate characterisation of unidirectional carbon-epoxy IM7-8552 in transverse compression and in-plane shear using digital image correlation". In: *Mechanics of Materials* 42.11, pp. 1004–1019. ISSN: 01676636.

Kolsky, H. (1949). "An investigation of the mechanical properties of materials at very high rates of loading". In: *Proceedings of the Physical Society. Section B* 62.11. cited By 1224, pp. 676 –700.

Kotaki, M. and H. Hamada (1997). "Effect of interfacial properties and weave structure on mode I interlaminar fracture behaviour of glass satin woven fabric composites". In: *Composites Part A: Applied Science and Manufacturing* 28.3, pp. 257 –266. ISSN: 1359-835X.

Kumar, Puneet, David S. Stargel, and Arun Shukla (2013). "Effect of plate curvature on blast response of carbon composite panels". In: *Composite Structures* 99, pp. 19 –30. ISSN: 0263-8223.

Langdon, G.S. et al. (2012). "The response of sandwich structures with composite face sheets and polymer foam cores to air-blast loading: Preliminary experiments". In: *Engineering Structures* 36.0, pp. 104 –112. ISSN: 0141-0296.

Langdon, G.S. et al. (2013). "The air-blast response of sandwich panels with composite face sheets and polymer foam cores: Experiments and predictions". In: *International Journal of Impact Engineering* 54.0, pp. 64 –82. ISSN: 0734-743X.

Langdon, G.S. et al. (2014). "The response of polymeric composite structures to air-blast loading: a state-of-the-art". In: *International Materials Reviews* 59.3, pp. 159 –177.

Langdon, G.S., W.C. Lee, and L.A. Louca (2015). "The influence of material type on the response of plates to air-blast loading". In: *International Journal of Impact Engineering* 78.0, pp. 150 –160. ISSN: 0734-743X.

Lapczyk, Ireneusz and Juan A. Hurtado (2007). "Progressive damage modeling in fiber-reinforced materials". In: *Composites Part A: Applied Science and Manufacturing* 38.11. CompTest 2006, pp. 2333 –2341. ISSN: 1359-835X.

Le-tian, Shen, Zhao Shi-da, and Bai Yi-long (1984). "Threshold and some microscopic observations of spallation of phenolic-resin based woven roving glass fiber reinforced composite material". In: *International Journal of Impact Engineering* 2.2, pp. 169 – 178. ISSN: 0734-743X.

LeBlanc, James and Arun Shukla (2011a). "Dynamic response of curved composite panels to underwater explosive loading: Experimental and computational comparisons". In: *Composite Structures* 93.11, pp. 3072 –3081. ISSN: 0263-8223.

— (2011b). "Response of E-glass/vinyl ester composite panels to underwater explosive loading: Effects of laminate modifications". In: *International Journal of Impact Engineering* 38.10, pp. 796 –803. ISSN: 0734-743X.

LeBlanc, James et al. (2007). "Shock loading of three-dimensional woven composite materials". In: *Composite Structures* 79.3, pp. 344 –355. ISSN: 0263-8223.

Lecompte, D et al. (2007). "Study and generation of optimal speckle patterns for DIC". In: *Proceedings of the annual conference and exposition on experimental and applied mechanics*. Vol. 3, pp. 1643 –1649.

Lópes, C.S. et al. (2009). "Low-velocity impact damage on dispersed stacking sequence laminates. Part II: Numerical simulations". In: *Composites Science and Technology* 69.7, pp. 937 –947. ISSN: 0266-3538.

Manshadi, B.D. et al. (2014). "An iterative analytical/experimental study of bridging in delamination of the double cantilever beam specimen". In: *Composites Part A: Applied Science and Manufacturing* 61.0, pp. 43 –50. ISSN: 1359-835X.

Matzenmiller, A., J. Lubliner, and R.L. Taylor (1995). "A constitutive model for anisotropic damage in fiber-composites". In: *Mechanics of Materials* 20.2, pp. 125 –152. ISSN: 0167-6636.

Melin, L. G. and L. E. Asp (1999). "Effects of strain rate on transverse tension properties of a carbon/epoxy composite: studied by moiré photography". In: *Composites Part A: Applied Science and Manufacturing* 30.3, pp. 305 –316. ISSN: 1359-835X.

Mellor, Malcolm and David M. Cole (1982). "Deformation and failure of ice under constant stress or constant strain-rate". In: *Cold Regions Science and Technology* 5.3, pp. 201 –219. ISSN: 0165-232X.

Mendes, P.A.A.E. and M.V. Donadon (2014). "Numerical prediction of compression after impact behavior of woven composite laminates". In: *Composite Structures* 113, pp. 476 –491. ISSN: 0263-8223.

Meyers, Marc A (1994). *Dynamic Behaviour of Materials*. First Edition. John Wiley & Sons.

Mohan, Sasikumar and Sundareswaran Velu (2014). "Ballistic impact behaviour of unidirectional fibre reinforced composites". In: *International Journal of Impact Engineering* 63.0, pp. 164 –176. ISSN: 0734-743X.

Muñoz, R. et al. (2015). "Ballistic performance of hybrid 3D woven composites: Experiments and simulations". English. In: *Composite Structures* 127.Complete, pp. 141–151.

Naghdabadi, R., M.J. Ashrafi, and J. Arghavani (2012). "Experimental and numerical investigation of pulse-shaped split Hopkinson pressure bar test". In: *Materials Science and Engineering: A* 539.0, pp. 285 –293. ISSN: 0921-5093.

Naik, N.K. and Venkateswara Rao Kavala (2008). "High strain rate behavior of woven fabric composites under compressive loading". In: *Materials Science and Engineering: A* 474.1–2, pp. 301 –311. ISSN: 0921-5093.

Naik, N.K. et al. (2010). "High strain rate tensile behavior of woven fabric E –glass/epoxy composite". In: *Polymer Testing* 29.1, pp. 14 –22. ISSN: 0142-9418.

Nunes, L.M., S. Paciornik, and J.R.M. d'Almeida (2004). "Evaluation of the damaged area of glass-fiber-reinforced epoxy-matrix composite materials submitted to ballistic impacts". In: *Composites Science and Technology* 64.7–8, pp. 945 –954. ISSN: 0266-3538.

Nurick, G.N. and J.B. Martin (1989a). "Deformation of thin plates subjected to impulsive loading - A review Part II: Experimental studies". In: *International Journal of Impact Engineering* 8.2, pp. 171 –186. ISSN: 0734-743X.

— (1989b). "Deformation of thin plates subjected to impulsive loading—A review: Part I: Theoretical considerations". In: *International Journal of Impact Engineering* 8.2, pp. 159 –170. ISSN: 0734-743X.

Obert, E. et al. (2014). "Micro and meso modeling of woven composites: Transverse cracking kinetics and homogenization". In: *Composite Structures* 117.0, pp. 212 –221. ISSN: 0263-8223.

Ohtani, K. et al. (2006). "A study of hypervelocity impact on cryogenic materials". In: *International Journal of Impact Engineering* 33.1–12. Hypervelocity Impact Proceedings of the 2005 Symposium, pp. 555 –565. ISSN: 0734-743X.

Okereke, M.I. and A.I. Akpoyomare (2013). "A virtual framework for prediction of full-field elastic response of unidirectional composites". In: *Computational Materials Science* 70.0, pp. 82 –99. ISSN: 0927-0256.

Pandya, Kedar S. et al. (2013a). "Ballistic impact behavior of hybrid composites". In: *Materials & Design* 44.0, pp. 128 –135. ISSN: 0261-3069.

— (2013b). "Ballistic impact behavior of hybrid composites". In: *Materials & Design* 44, pp. 128 –135. ISSN: 0261-3069.

Pankow, M. et al. (2011). "Split Hopkinson pressure bar testing of 3D woven composites". In: *Composites Science and Technology* 71.9, pp. 1196 –1208. ISSN: 0266-3538.

Paris, Federico, and George (2001). "A Study of Failure Criteria of Fibrous Composite Materials". In:

Pernas-Sánchez, J. et al. (2012). "Numerical modeling of ice behavior under high velocity impacts". In: *International Journal of Solids and Structures* 49.14, pp. 1919 –1927. ISSN: 0020-7683.

Pernas-Sánchez, J. et al. (2015). "Analysis of Ice Impact Process at High Velocity". In: *Experimental Mechanics* 55.9, pp. 1669 –1679.

Pernas-Sánchez, J. et al. (2016). "Experimental analysis of ice sphere impacts on unidirectional carbon/epoxy laminates". In: *International Journal of Impact Engineering* 96, pp. 1 –10. ISSN: 0734-743X.

Phadnis, Vaibhav A. et al. (2013). "Drilling in carbon/epoxy composites: Experimental investigations and finite element implementation". In: *Composites Part A: Applied Science and Manufacturing* 47.0, pp. 41 –51. ISSN: 1359-835X.

Phadnis, Vaibhav A. et al. (2014). "Optimising curvature of carbon fibre-reinforced polymer composite panel for improved blast resistance: Finite-element analysis". In: *Materials & Design* 57.0, pp. 719 –727. ISSN: 0261-3069.

Piekutowski, Andrew J. (1987). "Debris clouds generated by hypervelocity impact of cylindrical projectiles with thin aluminum plates". In: *International Journal of Impact Engineering* 5.1–4. Hypervelocity Impact Proceedings of the 1986 Symposium, pp. 509 –518. ISSN: 0734-743X.

Pinho, Silvestre T. et al. (2005). *Failure Models and Criteria for FRP Under In-Plane or Three-Dimensional Stress States Including Shear Non-Linearity*. Technical Report NASA/TM-2005-213530, L-19089. NASA Langley Research Center.

Puck, A. (1992). "Fracture criteria for highly stressed fibre-plastics composites which meet requirements of design practice". In: *Kunststoffe–German Plastics* 82.2, pp. 149 –155.

Puck, A. and H. Schürmann (2002). "Failure analysis of {FRP} laminates by means of physically based phenomenological models". In: *Composites Science and Technology* 62.12–13, pp. 1633 –1662. ISSN: 0266-3538.

Puck, A. and H. Schürmann (1998). "FAILURE ANALYSIS OF FRP LAMINATES BY MEANS OF PHYSICALLY BASED PHENOMENOLOGICAL MODELS". In: *Composites Science and Technology* 58.7, pp. 1045–1067. ISSN: 02663538.

Raghavan, P., S. Li, and S. Ghosh (2004). "Two scale response and damage modeling of composite materials". In: *Finite Elements in Analysis and Design* 40.12. The Fifteenth Annual Robert J. Melosh Competition, pp. 1619 –1640. ISSN: 0168-874X.

Ravikumar, G. et al. (2013). "Analytical and experimental studies on mechanical behavior of composites under high strain rate compressive loading". In: *Materials & Design* 44.0, pp. 246 –255. ISSN: 0261-3069.

Riccio, A. et al. (2014). "Modelling the simulation of impact induced damage onset and evolution in composites". In: *Composites Part B: Engineering* 66.0, pp. 340 –347. ISSN: 1359-8368.

Sasso, M., G. Newaz, and D. Amodio (2008). "Material characterization at high strain rate by Hopkinson bar tests and finite element optimization". In: *Materials Science and Engineering: A* 487.1–2, pp. 289 –300. ISSN: 0921-5093.

Sastry, Y.B. Sudhir et al. (2014). "Studies on ballistic impact of the composite panels". In: *Theoretical and Applied Fracture Mechanics* 72.0. Multiscale Modeling of Material Failure, pp. 2 –12. ISSN: 0167-8442.

Schön, Joakim (2004). "Coefficient of friction and wear of a carbon fiber epoxy matrix composite". In: *Wear* 257.3, pp. 395 –407. ISSN: 0043-1648.

Schneider, E. and F. Schäfer (2001). "Hypervelocity impact research –acceleration technology and applications". In: *Advances in Space Research* 28.9, pp. 1417 –1424. ISSN: 0273-1177.

Schulson, E.M (1990). "The brittle compressive fracture of ice". In: *Acta Metallurgica et Materialia* 38.10, pp. 1963 –1976. ISSN: 0956-7151.

Schulson, Erland M. (1997). "The Brittle Failure of Ice under Compression". In: *The Journal of Physical Chemistry B* 101.32, pp. 6254–6258.

Sevkat, Ercan (2012). "Experimental and numerical approaches for estimating ballistic limit velocities of woven composite beams". In: *International Journal of Impact Engineering* 45.0, pp. 16 –27. ISSN: 0734-743X.

Shaktivesh et al. (2013a). "Ballistic impact performance of composite targets". In: *Materials & Design* 51.0, pp. 833 –846. ISSN: 0261-3069.

— (2013b). "Ballistic impact performance of composite targets". In: *Materials & Design* 51, pp. 833 –846. ISSN: 0261-3069.

Shi, Y., T. Swait, and C. Soutis (2012). "Modelling damage evolution in composite laminates subjected to low velocity impact". In: *Composite Structures* 94.9, pp. 2902 –2913. ISSN: 0263-8223.

Silberschmidt, Vadim V. (2008). "Account for Random Microstructure in Multiscale Models". In: *Multiscale Modelling and Simulation of Composite Materials and Structures*. Springer.

Sket, F. et al. (2012). "Determination of damage micromechanisms and fracture resistance of glass fiber/epoxy cross-ply laminate by means of X-ray computed microtomography". In: *Composites Science and Technology* 72.2, pp. 350 –359. ISSN: 0266-3538.

Sket, F. et al. (2014). "Automatic quantification of matrix cracking and fiber rotation by X-ray computed tomography in shear-deformed carbon fiber-reinforced laminates". In: *Composites Science and Technology* 90, pp. 129 –138. ISSN: 0266-3538.

Soden, P.D., M.J. Hinton, and A.S. Kaddour (1998). "Lamina properties, lay-up configurations and loading conditions for a range of fibre-reinforced composite laminates". In: *Composites Science and Technology* 58.7, pp. 1011 –1022. ISSN: 0266-3538.

Soden, P.D, A.S Kaddour, and M.J Hinton (2004). "Recommendations for designers and researchers resulting from the world-wide failure exercise". In: *Composites Science and Technology* 64.3–4. Failure criteria in fibre reinforced polymer composites Part C: Additional theories conclusions and recommendations, pp. 589 –604. ISSN: 0266-3538.

Talreja (2006). "Multi-scale modeling in damage mechanics of composite materials". In: *Journal of Materials Science* 41.20, pp. 6800–6812. ISSN: 0022-2461.

Talreja and Singh (2008). "Multiscale Modelling for Damage Analysis". In: *Multiscale Modelling and Simulation of Composite Materials and Structures*. Springer.

Talreja, R. (1985). "A continuum mechanics characterization of damage in composite materials". In: *Proceedings of the Royal Society of London A: Mathematical, Physical and Engineering Sciences* 399.1817, pp. 195–216. ISSN: 0080-4630. eprint: `http://rspa.royalsocietypublishing.org/content/399/1817/195.full.pdf`.

Talreja, Ramesh et al. (1992). "Transverse Cracking and Stiffness Reduction in Cross Ply Laminates of Different Matrix Toughness". In: *Journal of Composite Materials* 26.11, pp. 1644–1663.

Tekalur, Srinivasan Arjun, Arun Shukla, and Kunigal Shivakumar (2008a). "Blast resistance of polyurea based layered composite materials". In: *Composite Structures* 84.3, pp. 271 –281. ISSN: 0263-8223.

Tekalur, Srinivasan Arjun, Kunigal Shivakumar, and Arun Shukla (2008b). "Mechanical behavior and damage evolution in E-glass vinyl ester and carbon composites subjected to static and blast loads". In: *Composites Part B: Engineering* 39.1. Marine Composites and Sandwich Structures, pp. 57 –65. ISSN: 1359-8368.

Tekalur, Srinivasan Arjun, Alexander E. Bogdanovich, and Arun Shukla (2009). "Shock loading response of sandwich panels with 3-D woven E-glass composite skins and stitched foam core". In: *Composites Science and Technology* 69.6. ONR - Dynamic Failure and Durability, pp. 736 –753. ISSN: 0266-3538.

Tippmann, Jeffery D., Hyonny Kim, and Jennifer D. Rhymer (2013). "Experimentally validated strain rate dependent material model for spherical ice impact simulation". In: *International Journal of Impact Engineering* 57, pp. 43 –54. ISSN: 0734-743X.

Tsai, Stephen W. and Edward M. Wu (1971). "A General Theory of Strength for Anisotropic Materials". In: *Journal of Composite Materials* 5.1, pp. 58 –80. eprint: `http://jcm.sagepub.com/content/5/1/58.full.pdf+html`.

Turon, A. et al. (2007). "An engineering solution for mesh size effects in the simulation of delamination using cohesive zone models". In: *Engineering Fracture Mechanics* 74.10, pp. 1665 –1682. ISSN: 0013-7944.

Ullah, H. et al. (2012a). "Finite-element modelling of bending of CFRP laminates: Multiple delaminations". In: *Computational Materials Science* 52.1. Proceedings of the 20th International Workshop on Computational Mechanics of Materials - IWCMM 20, pp. 147 –156. ISSN: 0927-0256.

Ullah, Himayat, Andy R. Harland, and Vadim V. Silberschmidt (2012b). "Damage modelling in woven-fabric CFRP laminates under large-deflection bending". In: *Computational Materials Science* 64. Proceedings of the 21st International Workshop on Computational Mechanics of Materials (IWCMM 21), pp. 130 –135. ISSN: 0927-0256.

— (2013). "Damage and fracture in carbon fabric reinforced composites under impact bending". In: *Composite Structures* 101, pp. 144 –156. ISSN: 0263-8223.

Ulven, C, U.K Vaidya, and M.V Hosur (2003). "Effect of projectile shape during ballistic perforation of VARTM carbon/epoxy composite panels". In: *Composite Structures* 61.1–2. Impact on Composites 2002, pp. 143 –150. ISSN: 0263-8223.

Ünal, Ö. and Narottam P. Bansal (2002). "In-plane and interlaminar shear strength of a unidirectional Hi-Nicalon fiber-reinforced celsian matrix composite". In: *Ceramics International* 28.5, pp. 527 –540. ISSN: 0272-8842.

Varas, D. et al. (2013). "Analysis of high velocity impacts of steel cylinders on thin carbon/epoxy woven laminates". In: *Composite Structures* 95.0, pp. 623 –629. ISSN: 0263-8223.

Wallenberger, Frederick T. and Paul A. Bingham (2010). *Fiberglass and glass technology : energy-friendly compositions and applications*. Springer.

Wang, H.W. et al. (2014). "Analysis of effect of fiber orientation on Young's modulus for unidirectional fiber reinforced composites". In: *Composites Part B: Engineering* 56.0, pp. 733 –739. ISSN: 1359-8368.

Wei, Xiaoding et al. (2013a). "A new rate-dependent unidirectional composite model – Application to panels subjected to underwater blast". In: *Journal of the Mechanics and Physics of Solids* 61.6, pp. 1305 –1318. ISSN: 0022-5096.

Wei, Xiaoding et al. (2013b). "Three-dimensional numerical modeling of composite panels subjected to underwater blast". In: *Journal of the Mechanics and Physics of Solids* 61.6, pp. 1319 –1336. ISSN: 0022-5096.

Yahaya, R. et al. (2014a). "Quasi-static penetration and ballistic properties of kenaf–aramid hybrid composites". In: *Materials & Design* 63.0, pp. 775 –782. ISSN: 0261-3069.

— (2014b). "Quasi-static penetration and ballistic properties of kenaf–aramid hybrid composites". In: *Materials & Design* 63, pp. 775 –782. ISSN: 0261-3069.

Yashiro, Shigeki et al. (2013). "Characterization of high-velocity impact damage in CFRP laminates: Part I – Experiment". In: *Composites Part A: Applied Science and Manufacturing* 48, pp. 93 –100. ISSN: 1359-835X.

Yazici, M. (2009). "Loading rate sensitivity of high strength fibers and fiber/matrix interfaces". In: *Journal of Reinforced Plastics and Composites* 28.15, pp. 1869 –1880. ISSN: 0731-6844.

Zhang, Chao, Enock A. Duodu, and Jinan Gu (2017). "Finite element modeling of damage development in cross-ply composite laminates subjected to low velocity impact". In: *Composite Structures* 173, pp. 219 –227. ISSN: 0263-8223.

Zhou, G, J.C Lloyd, and J.J McGuirk (2001). "Experimental evaluation of geometric factors affecting damage mechanisms in carbon/epoxy plates". In: *Composites Part A: Applied Science and Manufacturing* 32.1, pp. 71 –84. ISSN: 1359-835X.

Zidi, Mondher et al. (2000). "Quantitative analysis of the micro-indentation behaviour of fibre-reinforced composites: development and validation of an analytical model". In: *Composites Science and Technology* 60.3, pp. 429 –437. ISSN: 0266-3538.

Zidi, Mondher et al. (2001). "Development of a micro-indentation model simulating different mechanical responses of the fibre/matrix interface". In: *Composites Science and Technology* 61.3, pp. 369 –375. ISSN: 0266-3538.

Zinoviev, Peter A. et al. (1998). "The strength of multilayered composites under a plane-stress state". In: *Composites Science and Technology* 58.7, pp. 1209 –1223. ISSN: 0266-3538.

Zohdi, T.I., P. Wriggers, and C. Huet (2001). "A method of substructuring large-scale computational micromechanical problems". In: *Computer Methods in Applied Mechanics and Engineering* 190.43–44, pp. 5639 –5656. ISSN: 0045-7825.

Zukas, Jonas A. (1976). *Impact Dynamics*. First Edition. John Wiley & Sons.

Appendices

Appendix A

Additional Plots from Digital Image Correlation Deformation Analysis

A.1 Out of Plane Displacement Plots

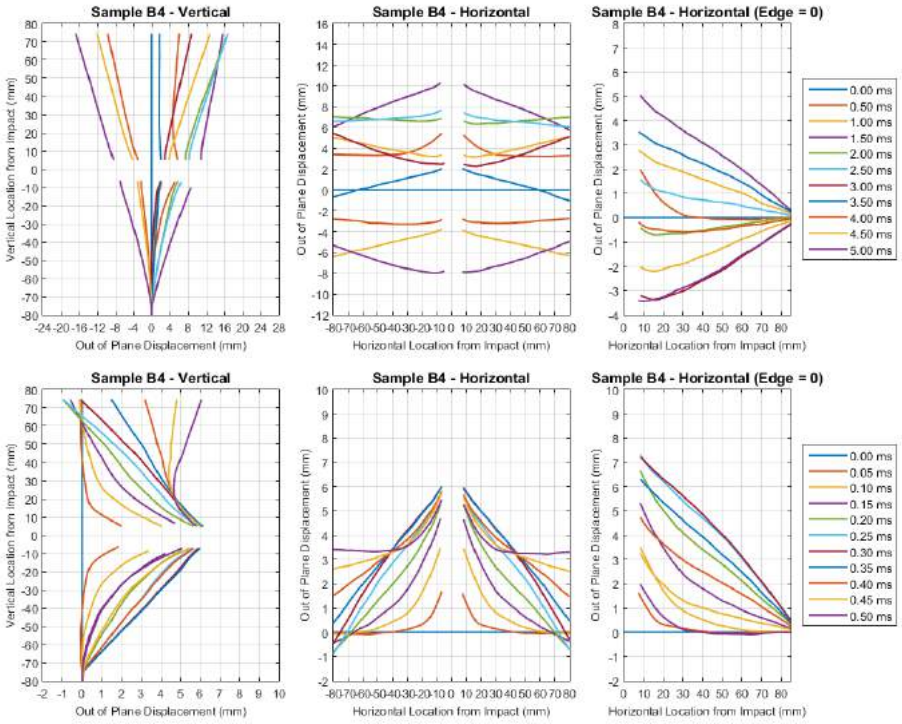

Figure A.1: Steel projectile - low velocity 60.00 m/s (sample B4)

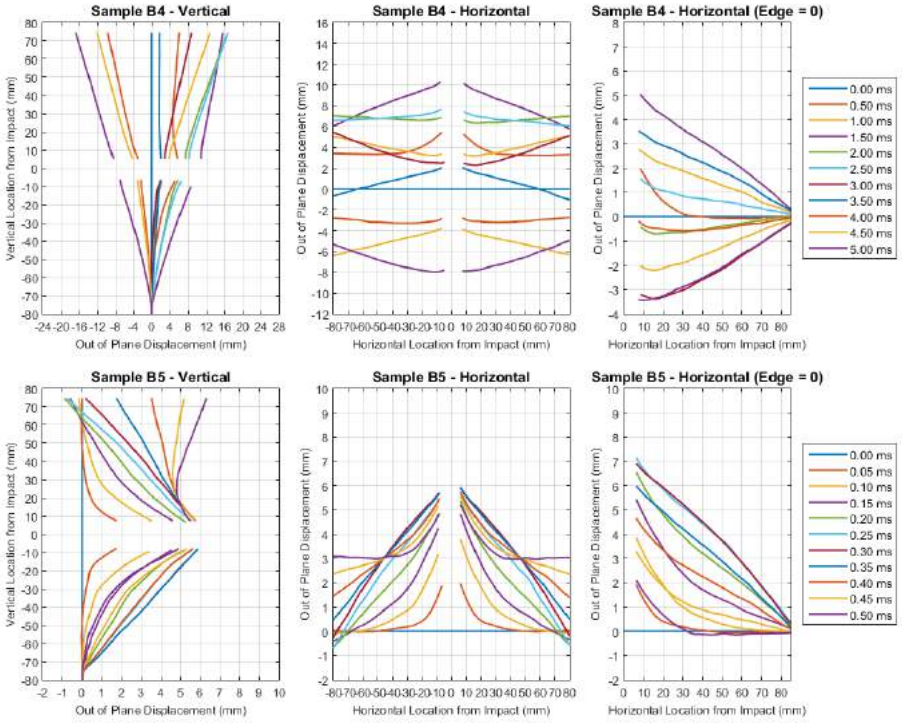

Figure A.2: Steel projectile - low velocity 59.00 m/s (sample B5)

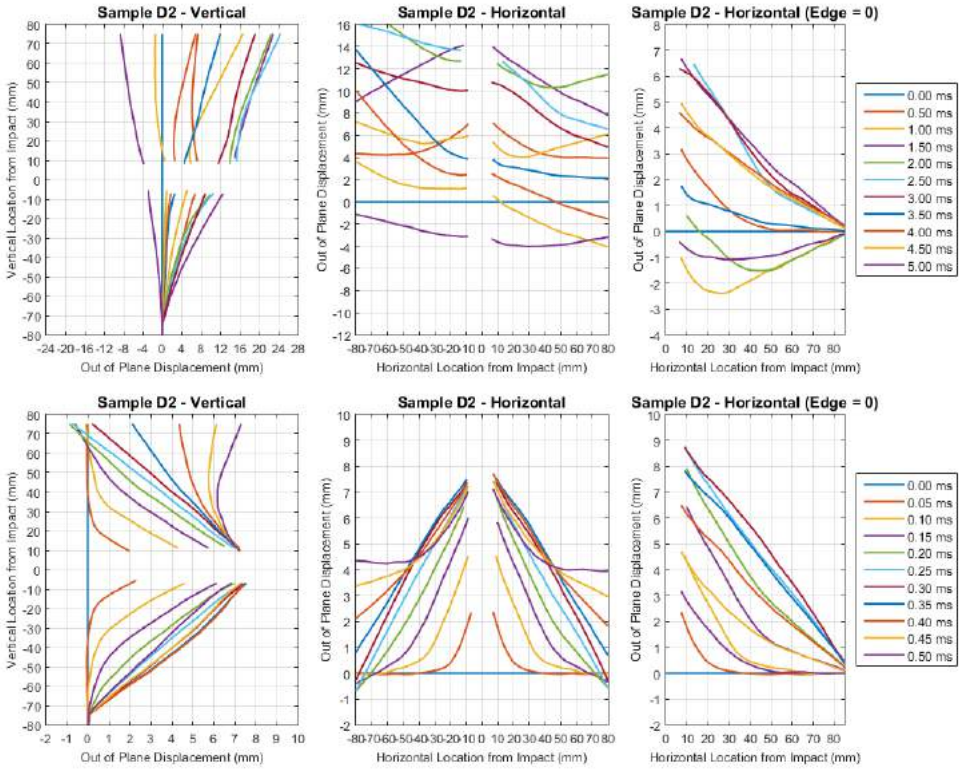

Figure A.3: Steel projectile - mid velocity 78.60 m/s (sample D2)

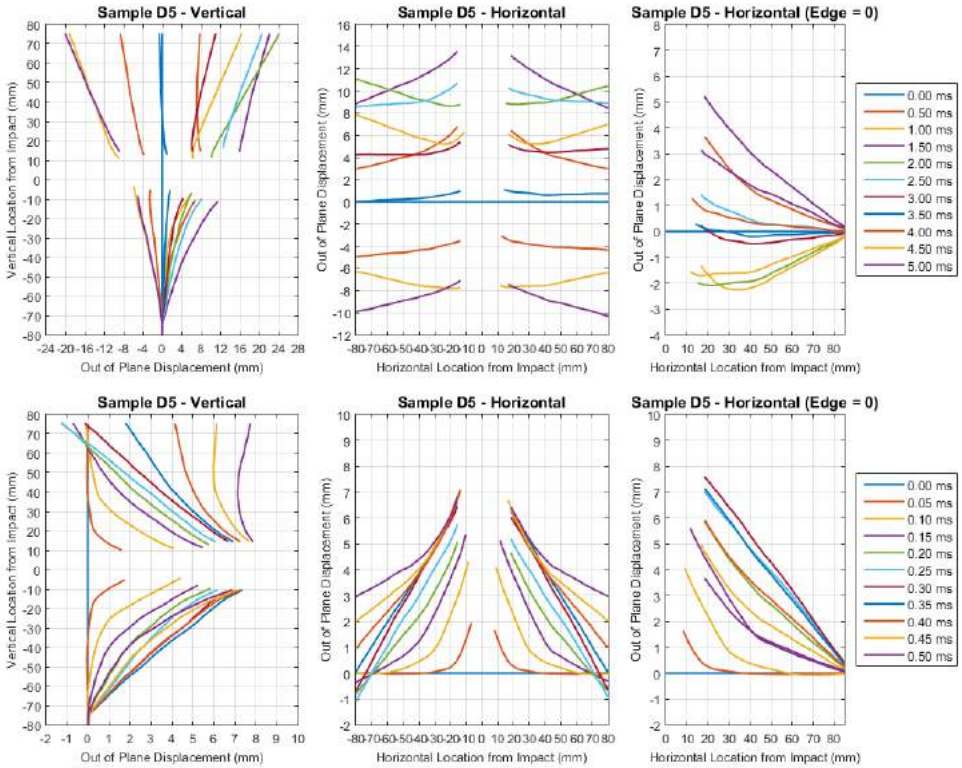

Figure A.4: Steel projectile - mid velocity 78.40 m/s (sample D5)

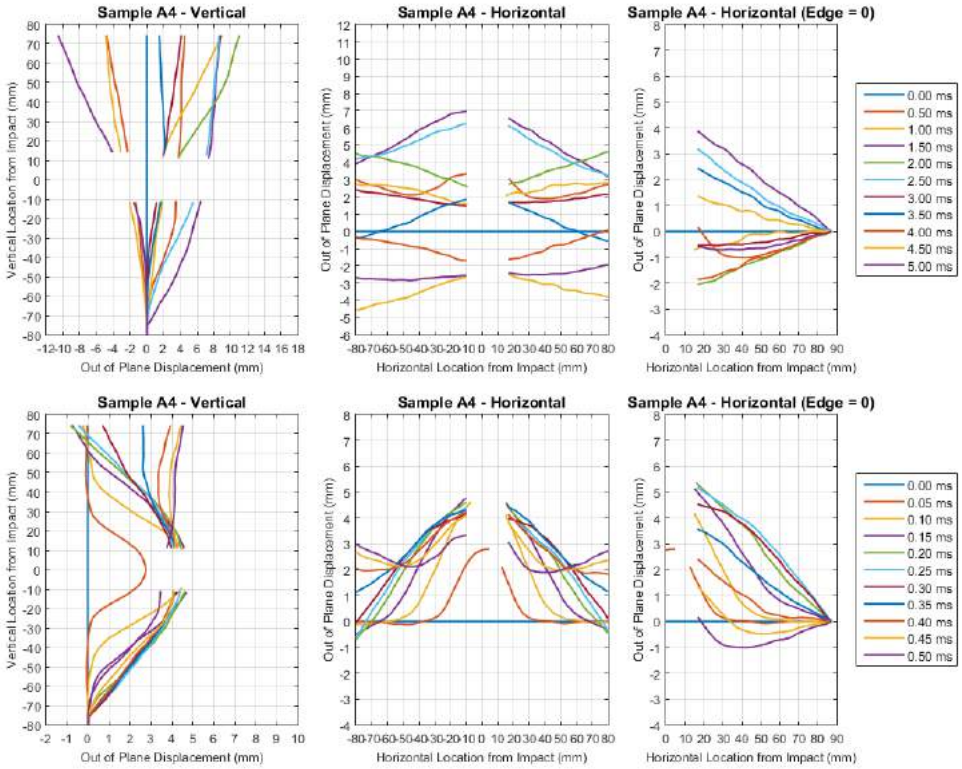

Figure A.5: Ice projectile - low velocity 304.00 m/s (sample A4)

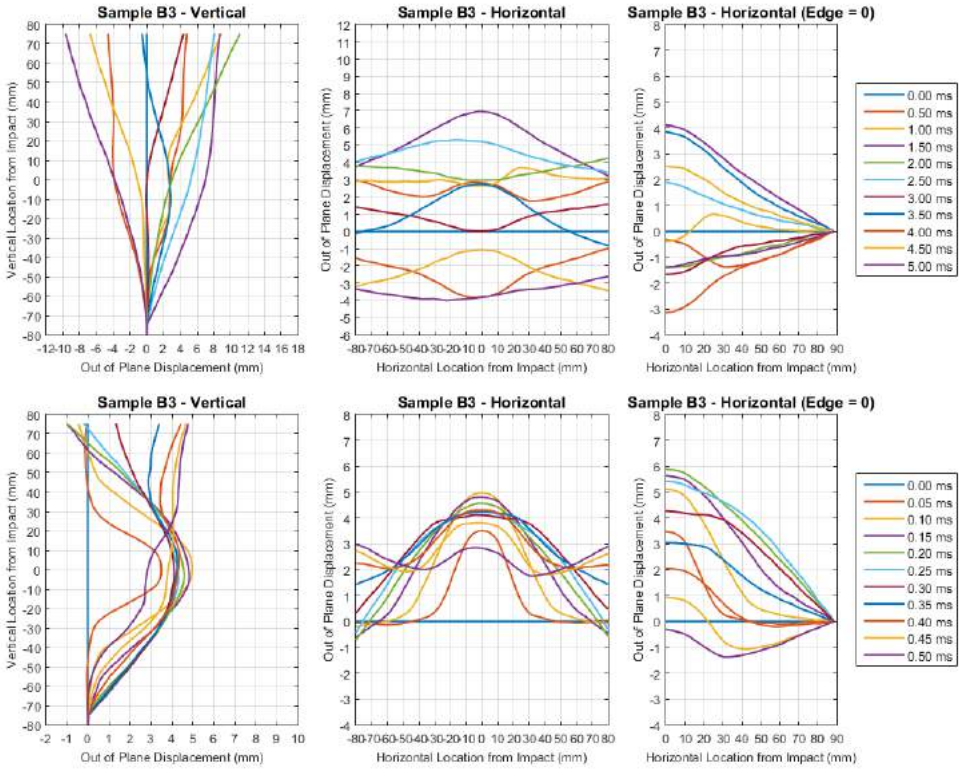

Figure A.6: Ice projectile - low velocity 303.00 m/s (sample B3)

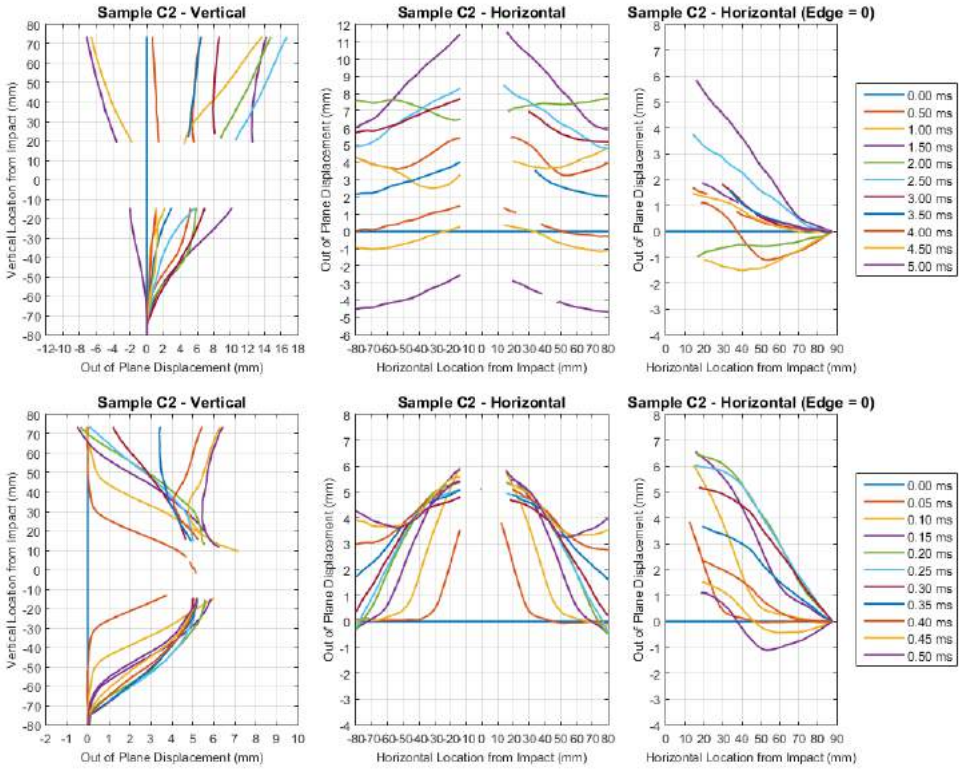

Figure A.7: Ice projectile - mid velocity 402.00 m/s (sample C2)

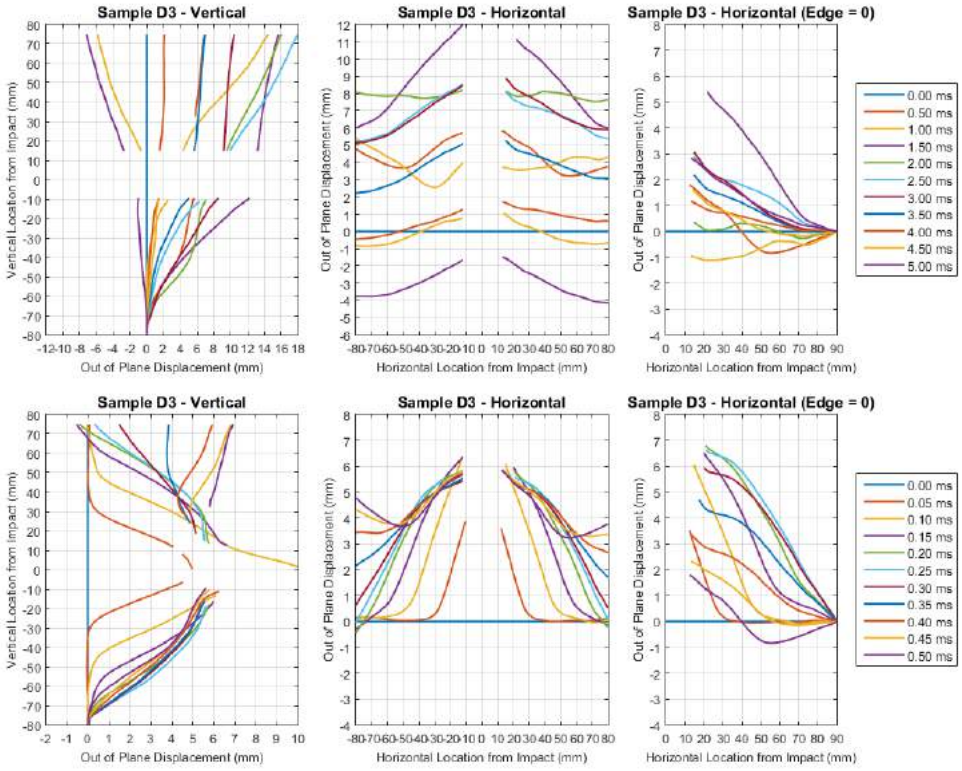

Figure A.8: Ice projectile - mid velocity 402.00 m/s (sample D3)

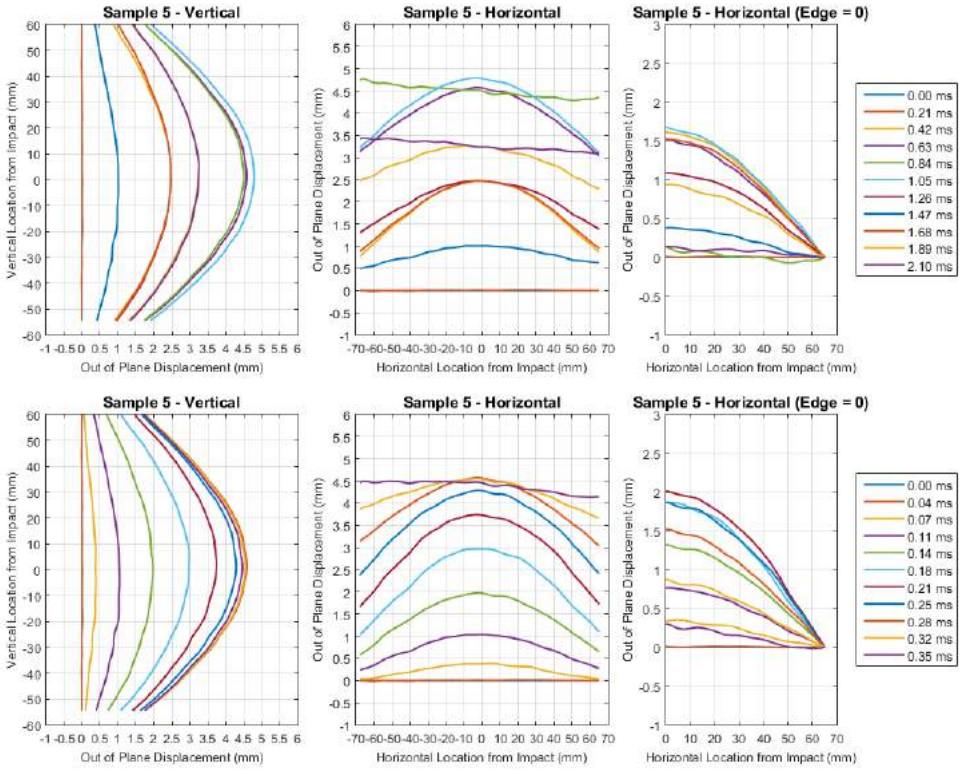

Figure A.9: Air-blast - low incident pressure 0.40 MPa (sample 5)

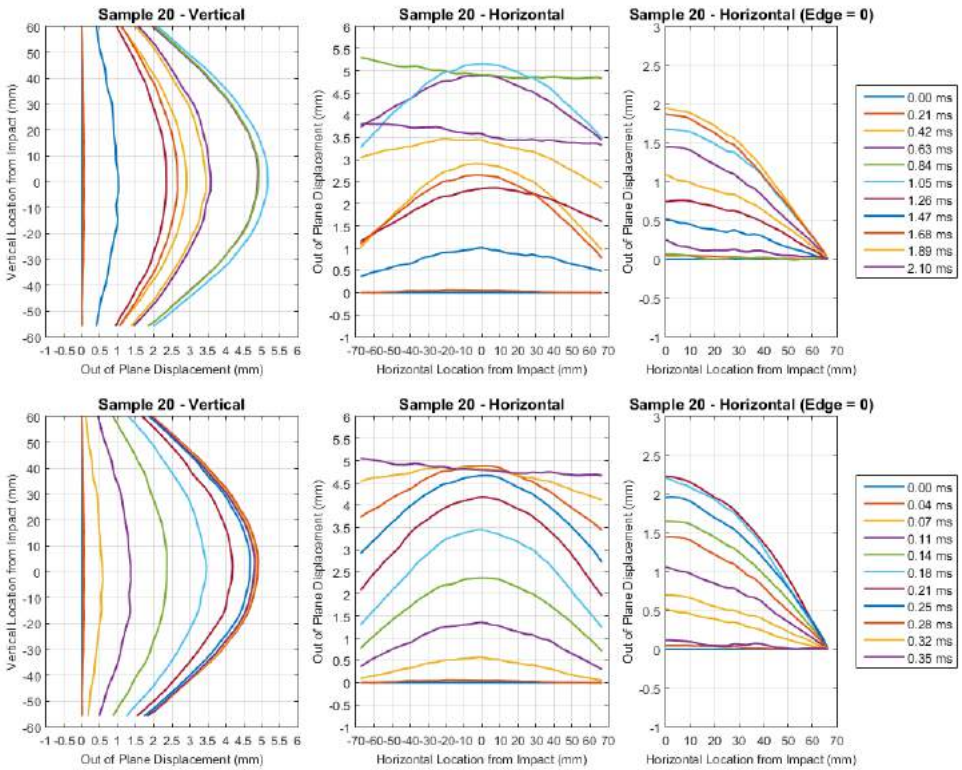

Figure A.10: Air-blast - low incident pressure 0.40 MPa (sample 20)

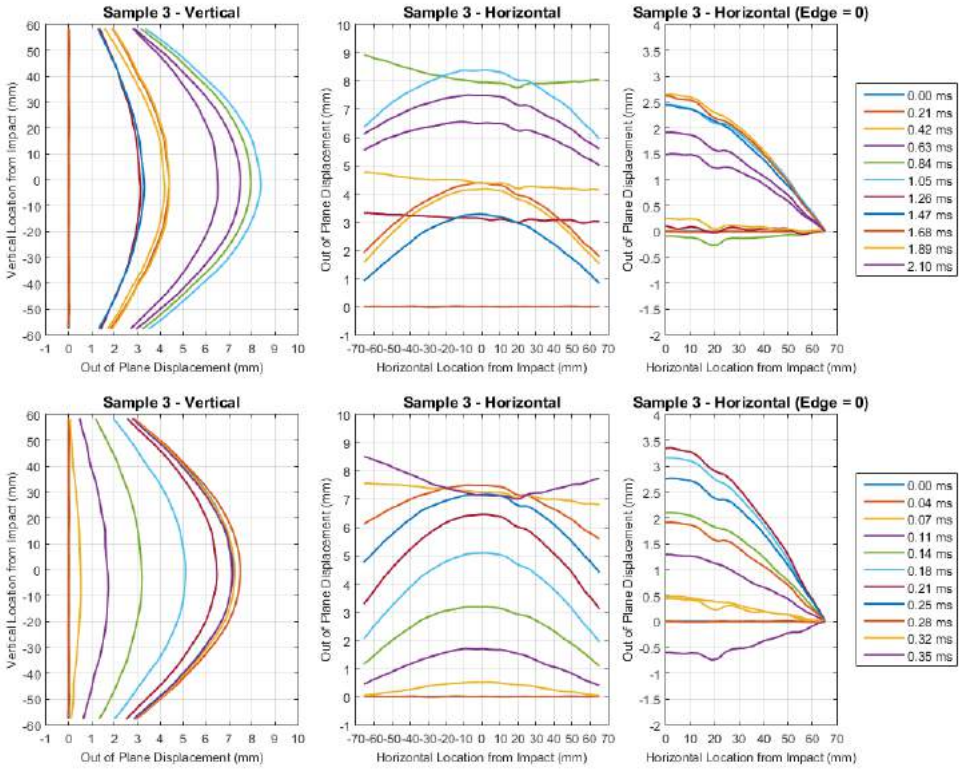

Figure A.11: Air-blast - mid incident pressure 0.62 MPa (sample 3)

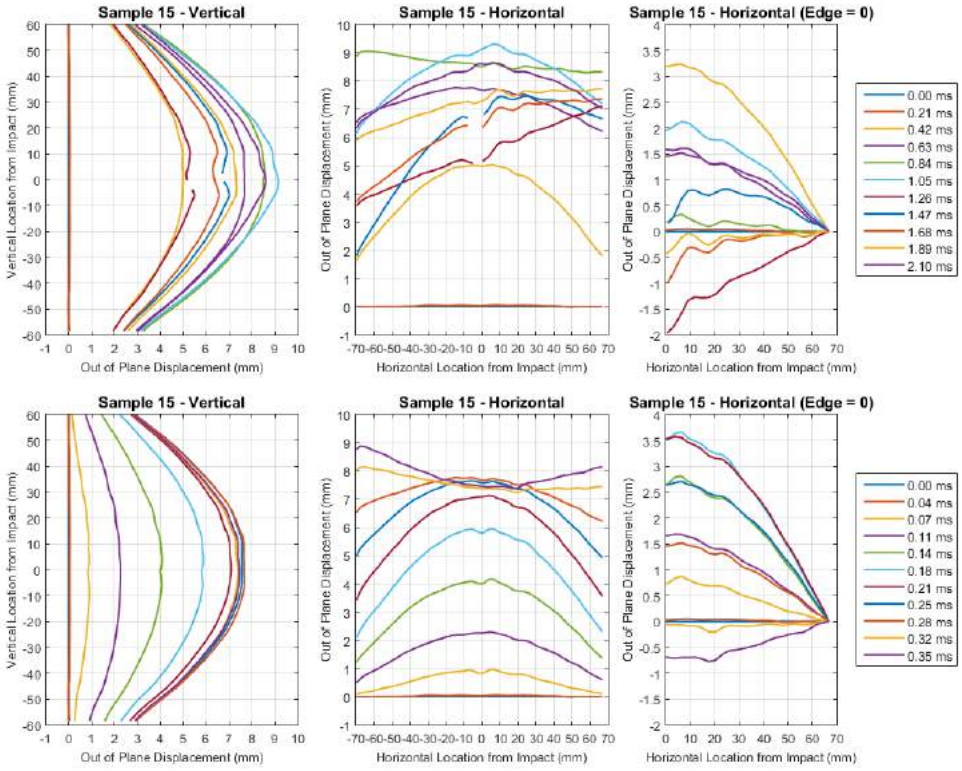

Figure A.12: Air-blast - mid incident pressure 0.62 MPa (sample 15)

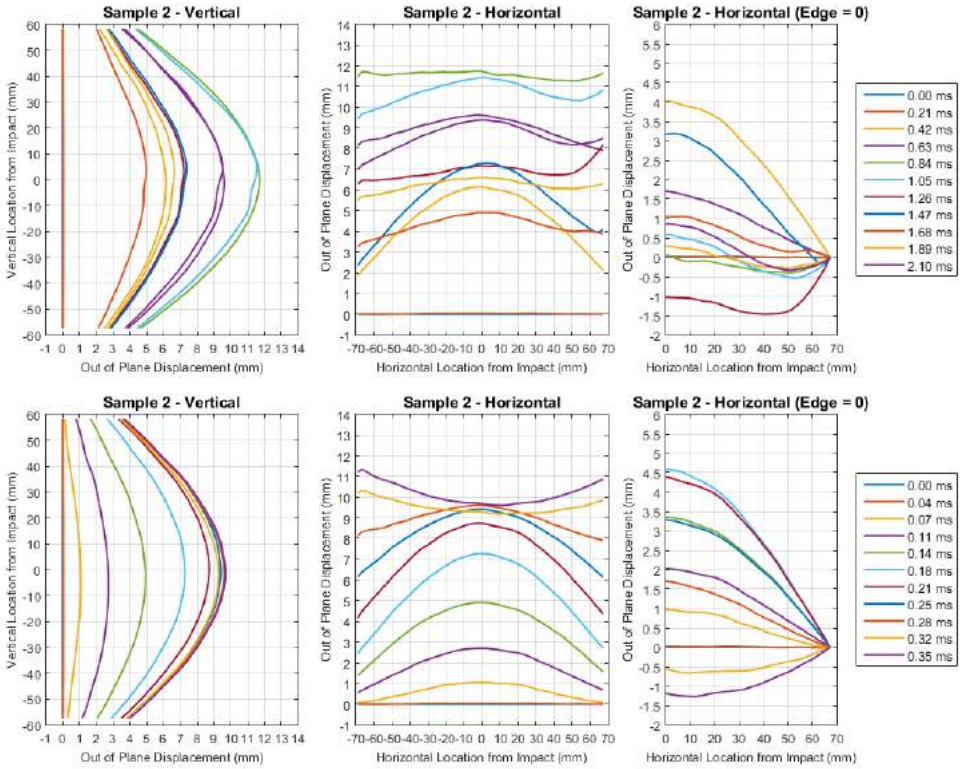

Figure A.13: Air-blast - high incident pressure 0.70 MPa (sample 2)

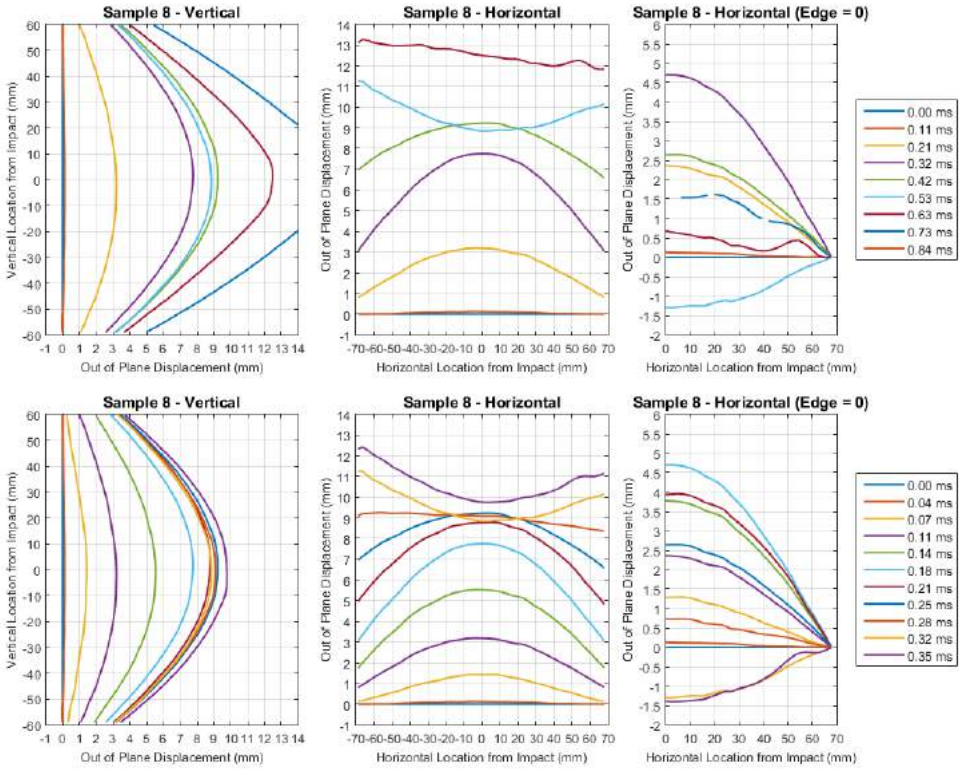

Figure A.14: Air-blast - failure incident pressure 0.80 MPa (sample 8)

A.2 Normalised Out of Plane Displacement Plots

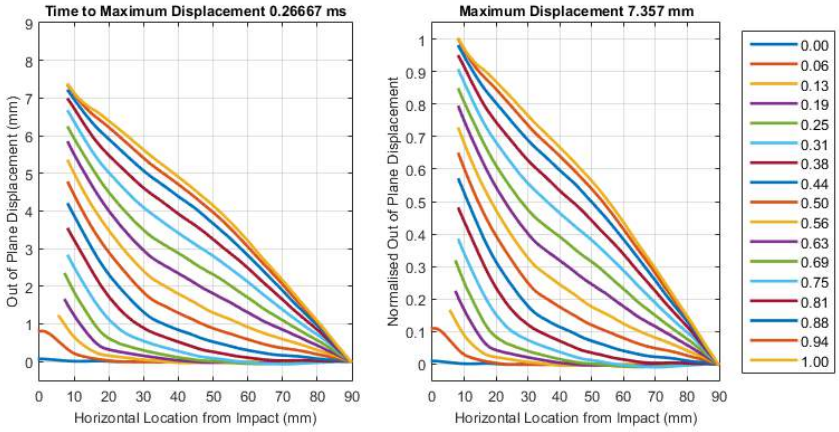

Figure A.15: Steel projectile - low velocity 60.00 m/s - normalised (sample B4)

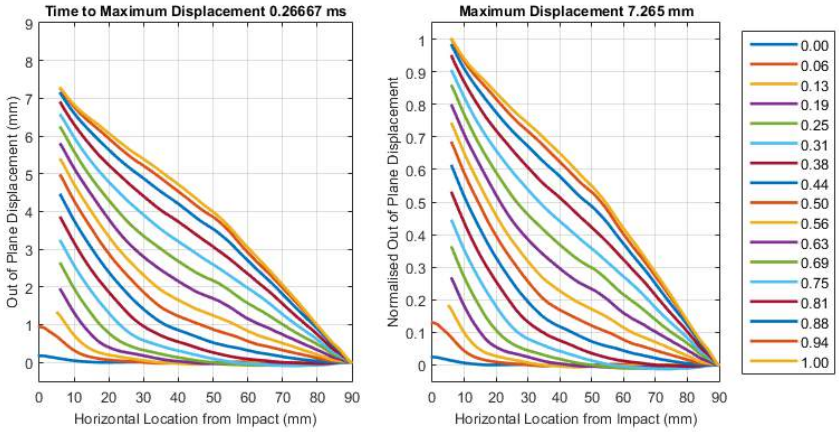

Figure A.16: Steel projectile - low velocity 59.00 m/s - normalised (sample B5)

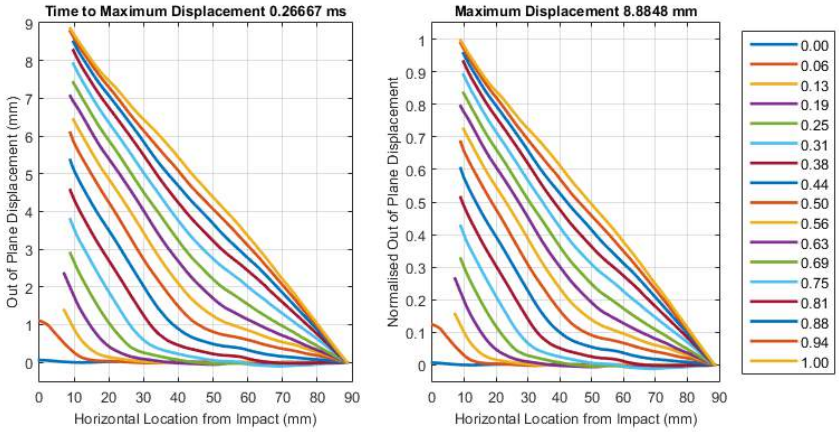

Figure A.17: Steel projectile - mid velocity 78.60 m/s - normalised (sample D2)

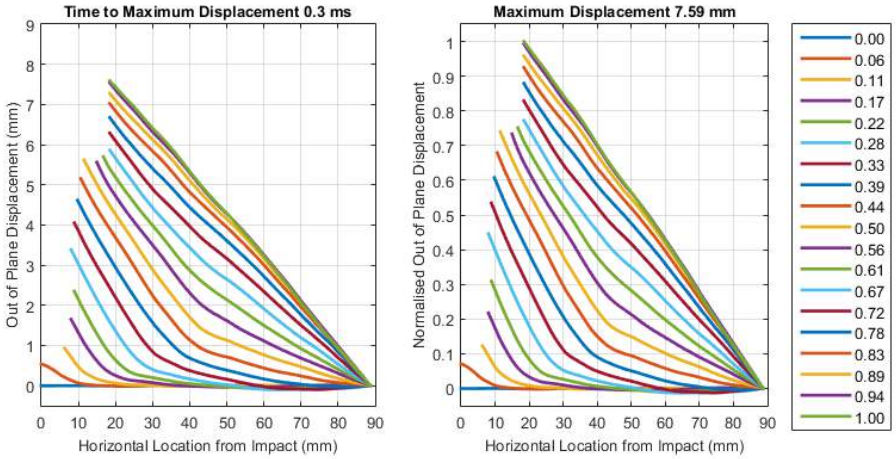

Figure A.18: Steel projectile - mid velocity 78.40 m/s - normalised (sample D4)

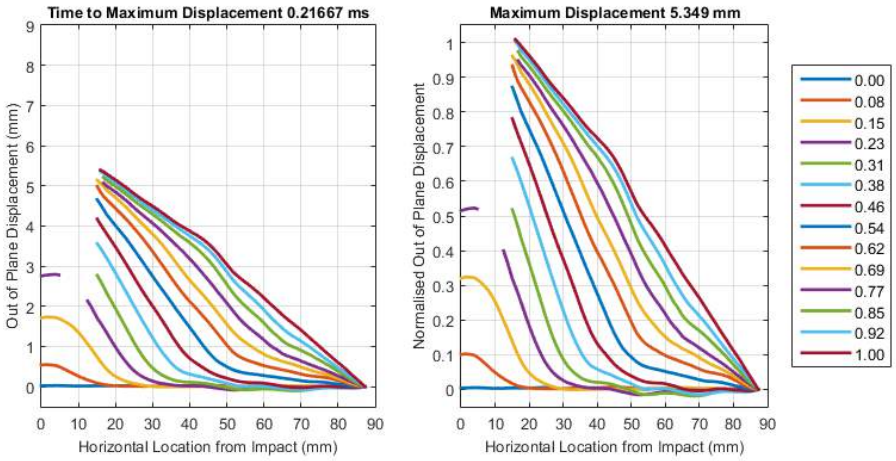

Figure A.19: Ice projectile - low velocity 304.0 m/s - normalised (sample A4)

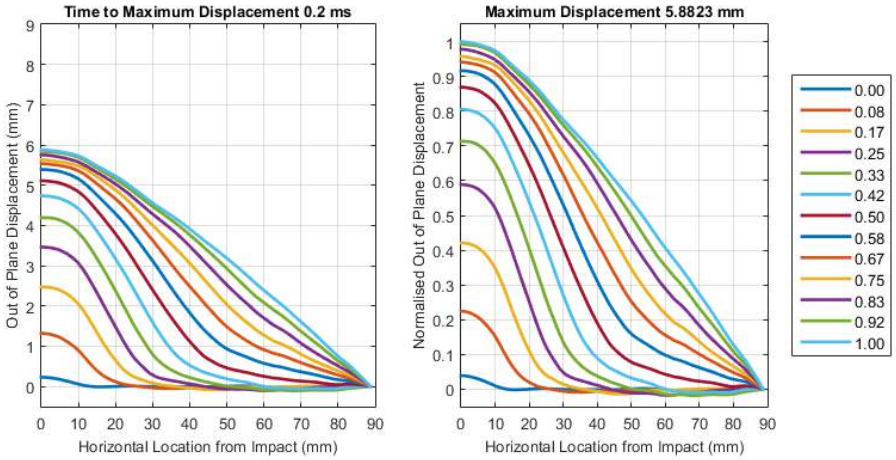

Figure A.20: Ice projectile - low velocity 303.0 m/s - normalised (sample B3)

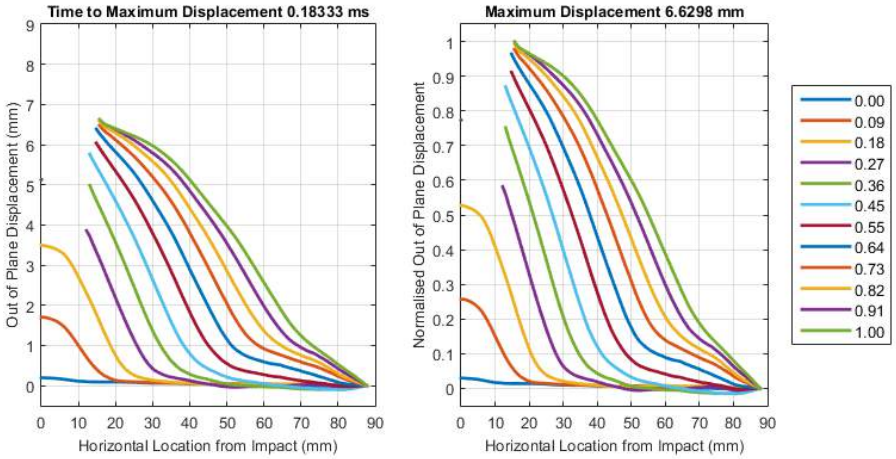

Figure A.21: Ice projectile - mid velocity 402.0 m/s - normalised (sample C2)

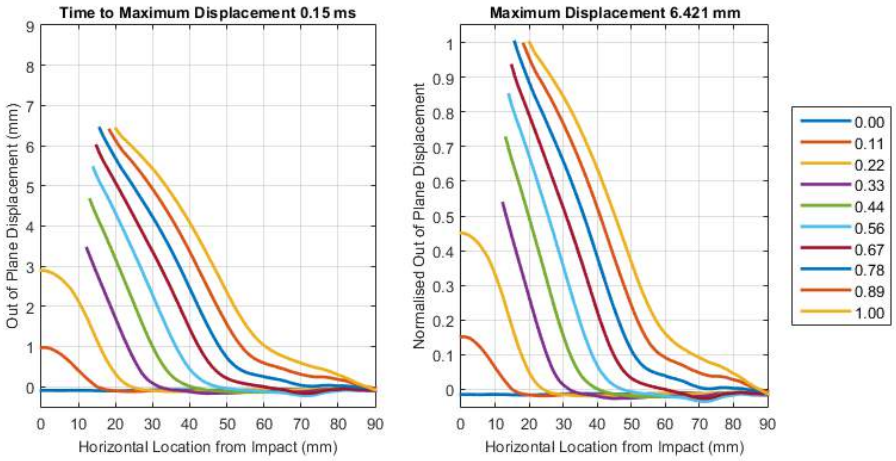

Figure A.22: Ice projectile - mid velocity 402.0 m/s - normalised (sample D3)

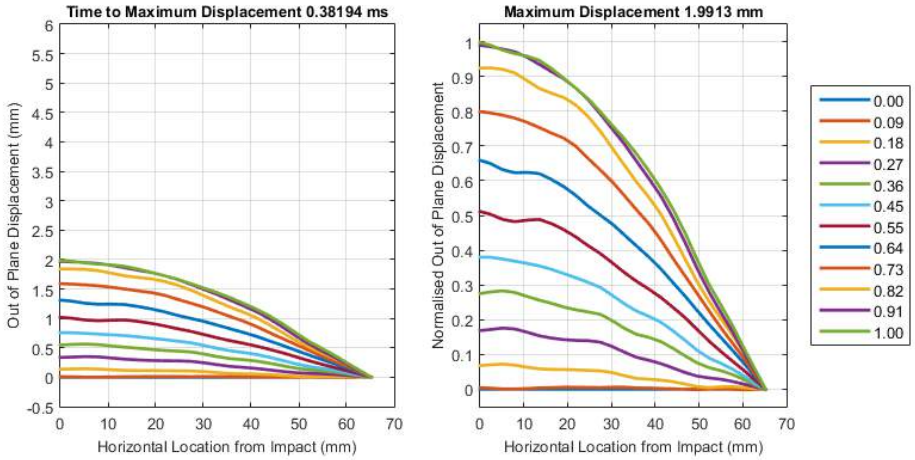

Figure A.23: Air-blast - low incident pressure 0.40 MPa - normalised (sample 5)

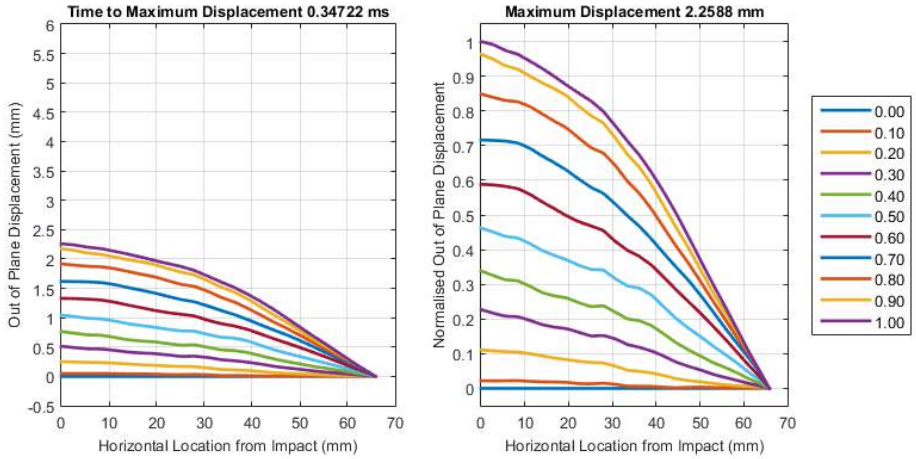

Figure A.24: Air-blast - low incident pressure 0.40 MPa - normalised (sample 20)

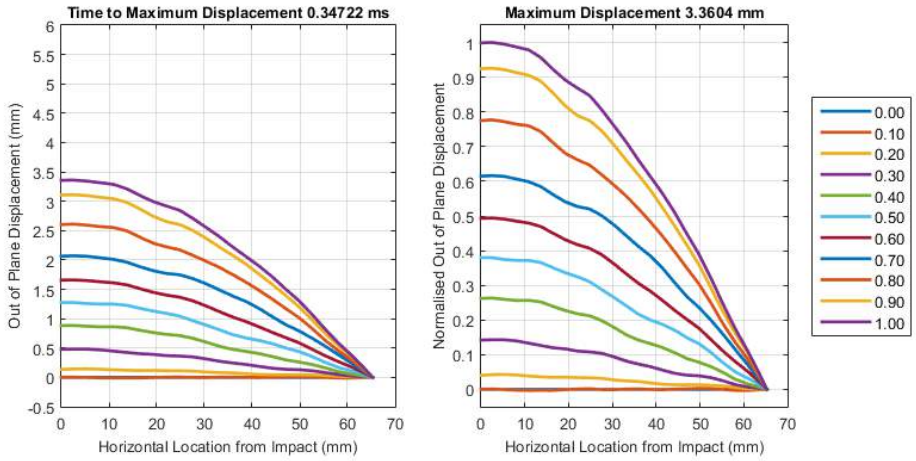

Figure A.25: Air-blast - mid incident pressure 0.62 MPa - normalised (sample 3)

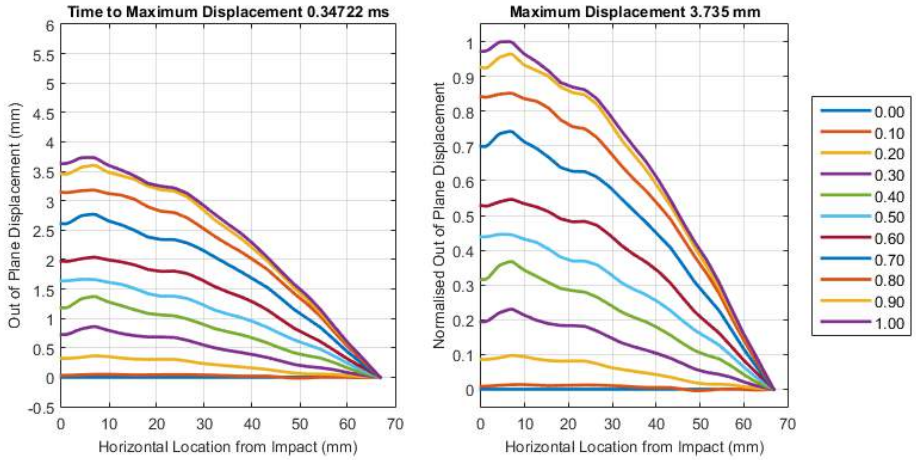

Figure A.26: Air-blast - mid incident pressure 0.62 MPa - normalised (sample 15)

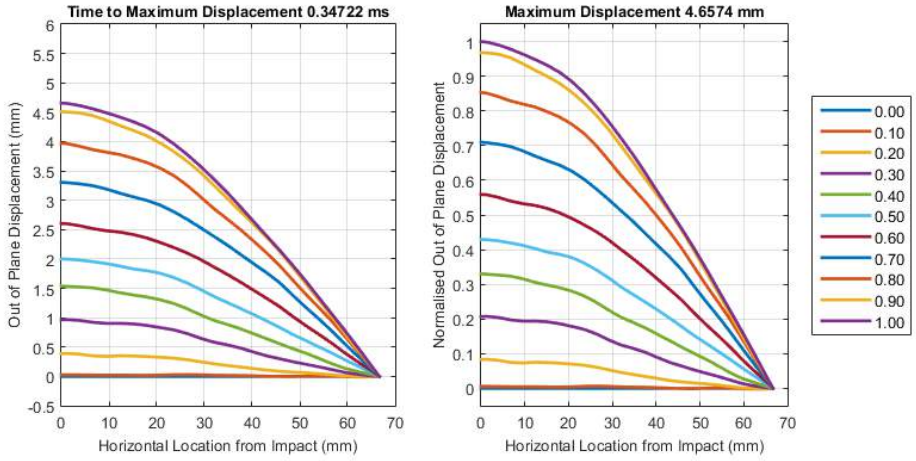

Figure A.27: Air-blast - high incident pressure 0.70 MPa - normalised (sample 7)

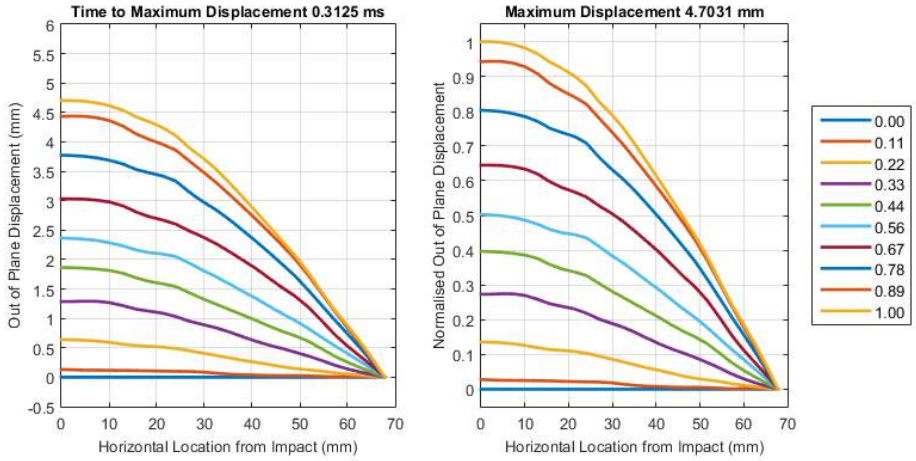

Figure A.28: Air-blast - failure incident pressure 0.80 MPa - normalised (sample 8)

Appendix B

Additional X-Ray Tomography Damage Analysis Images

B.1 3D Volume Renders

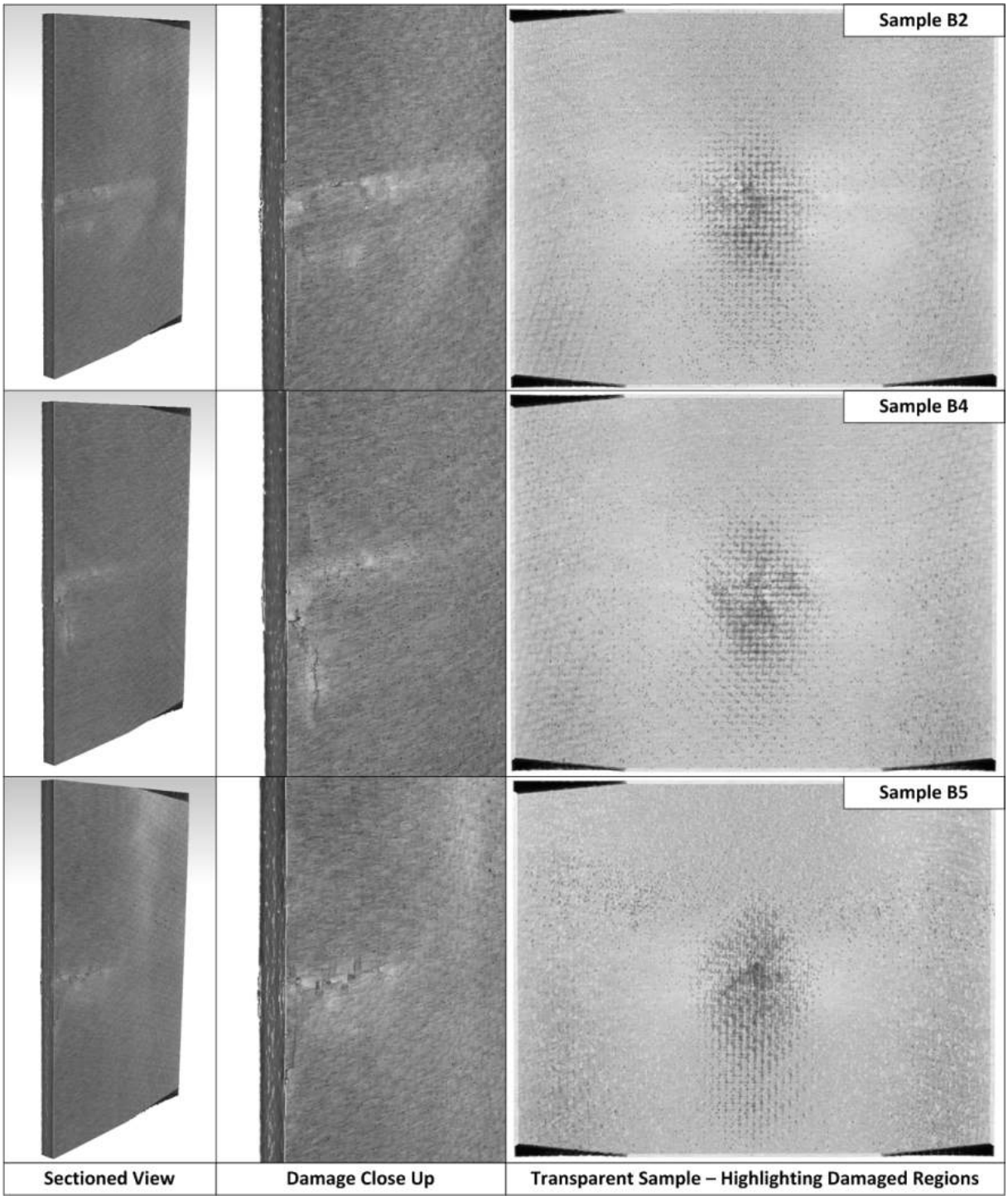

Figure B.1: Steel projectile 3D low velocity comparison (avg. 59.5 m/s)

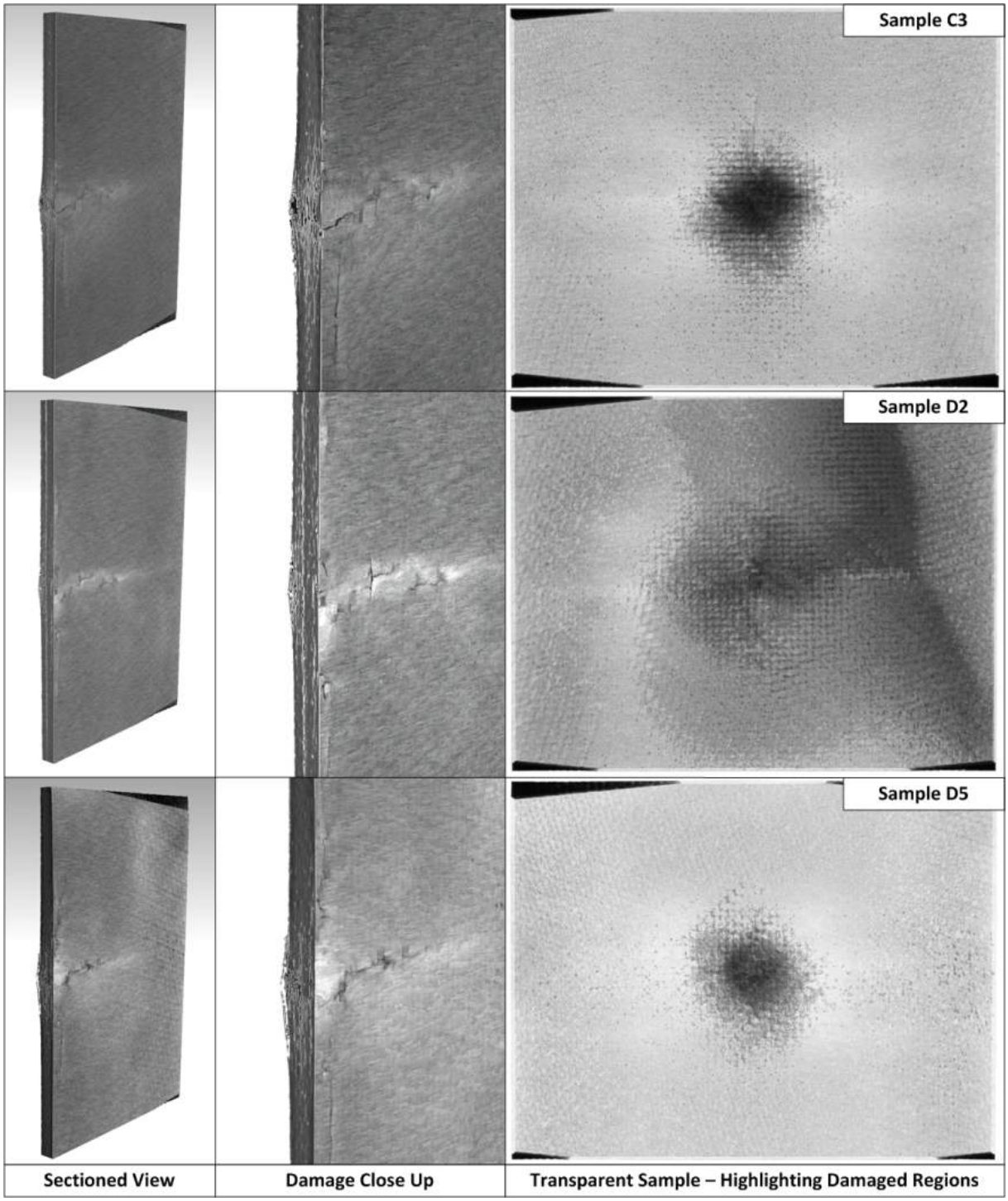

Figure B.2: Steel projectile 3D mid velocity comparison (avg. 78.5 m/s)

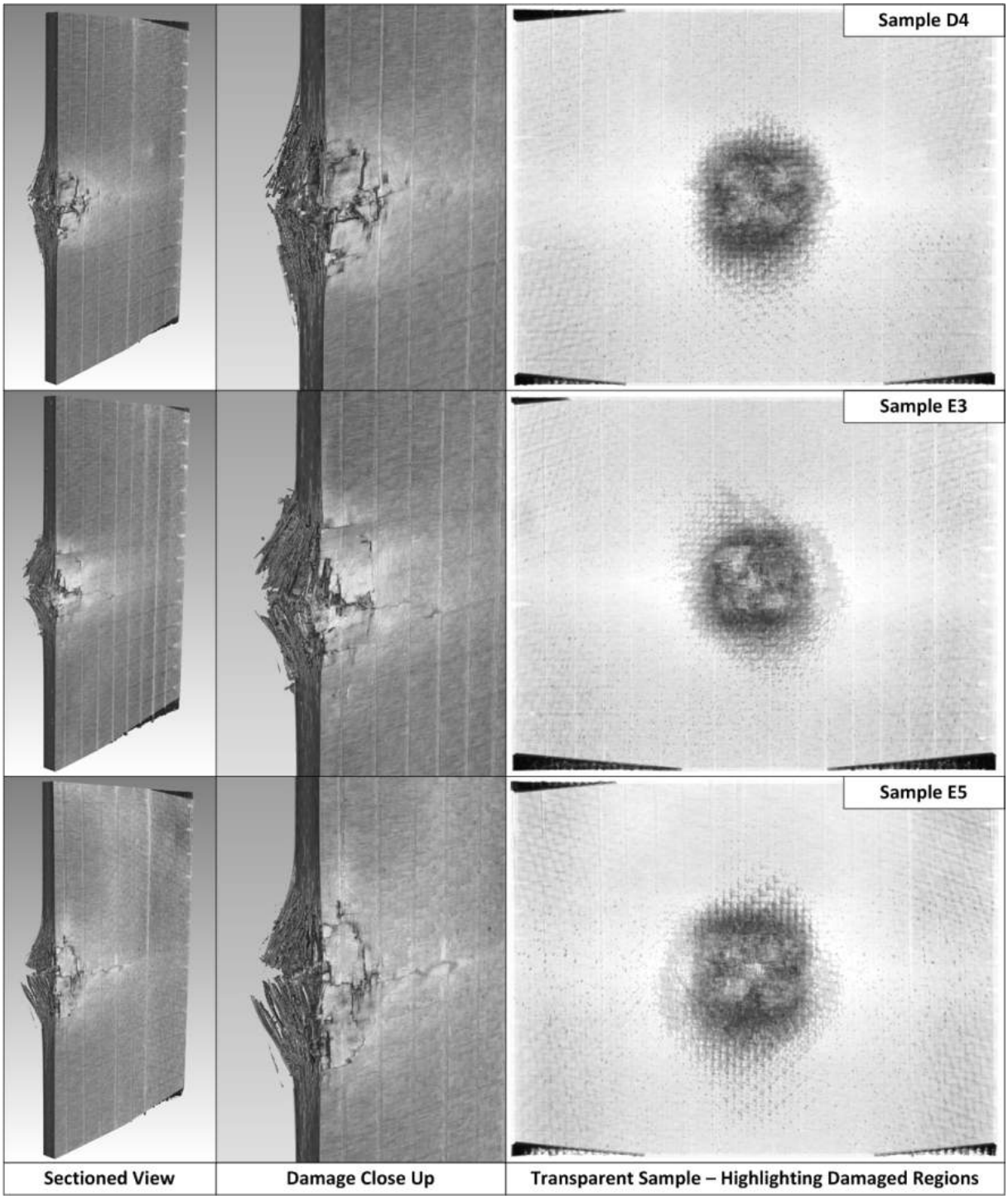

Figure B.3: Steel projectile 3D high velocity comparison (avg. 91.5 m/s)

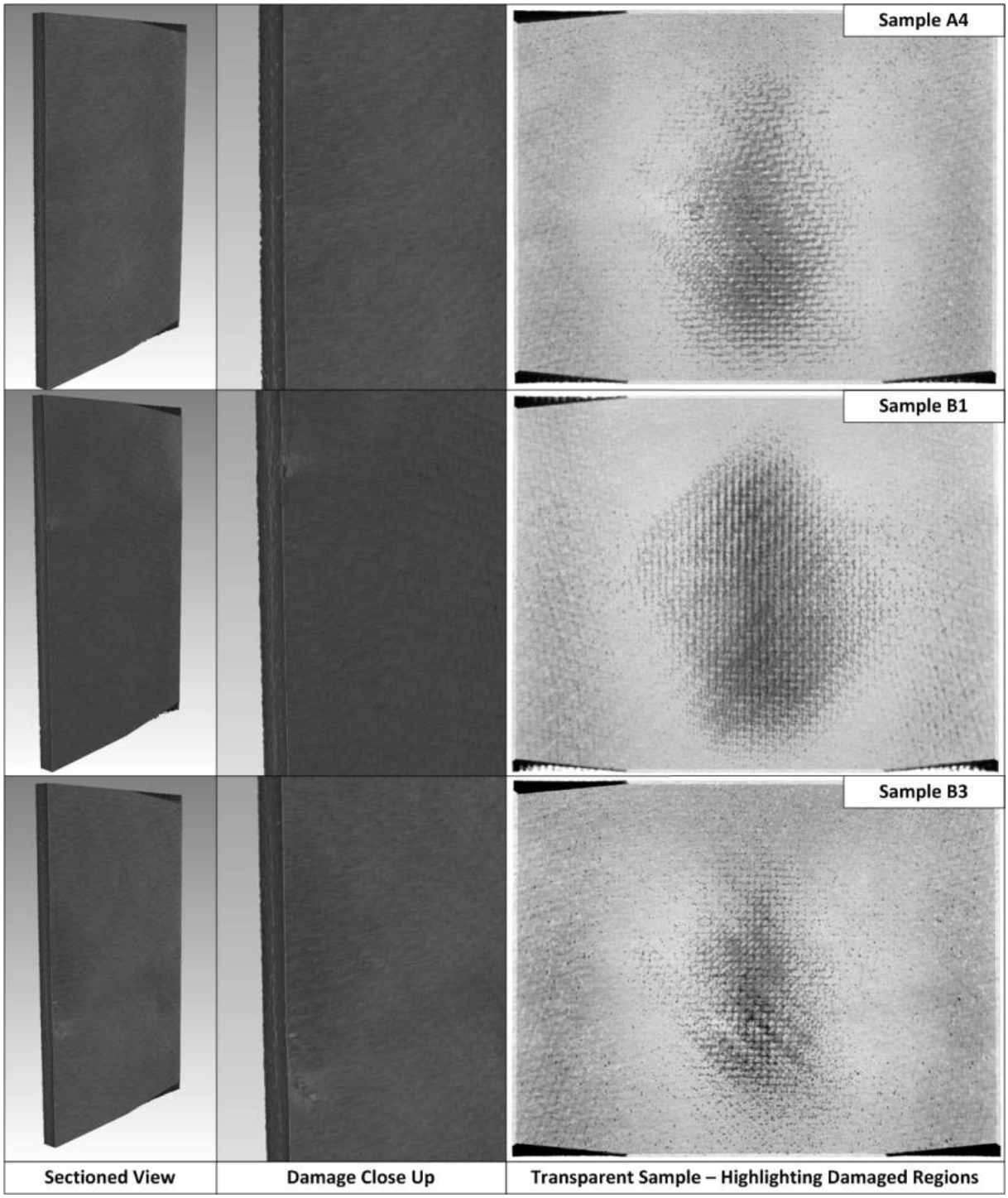

Figure B.4: Ice projectile 3D low velocity comparison (avg. 303.6 m/s)

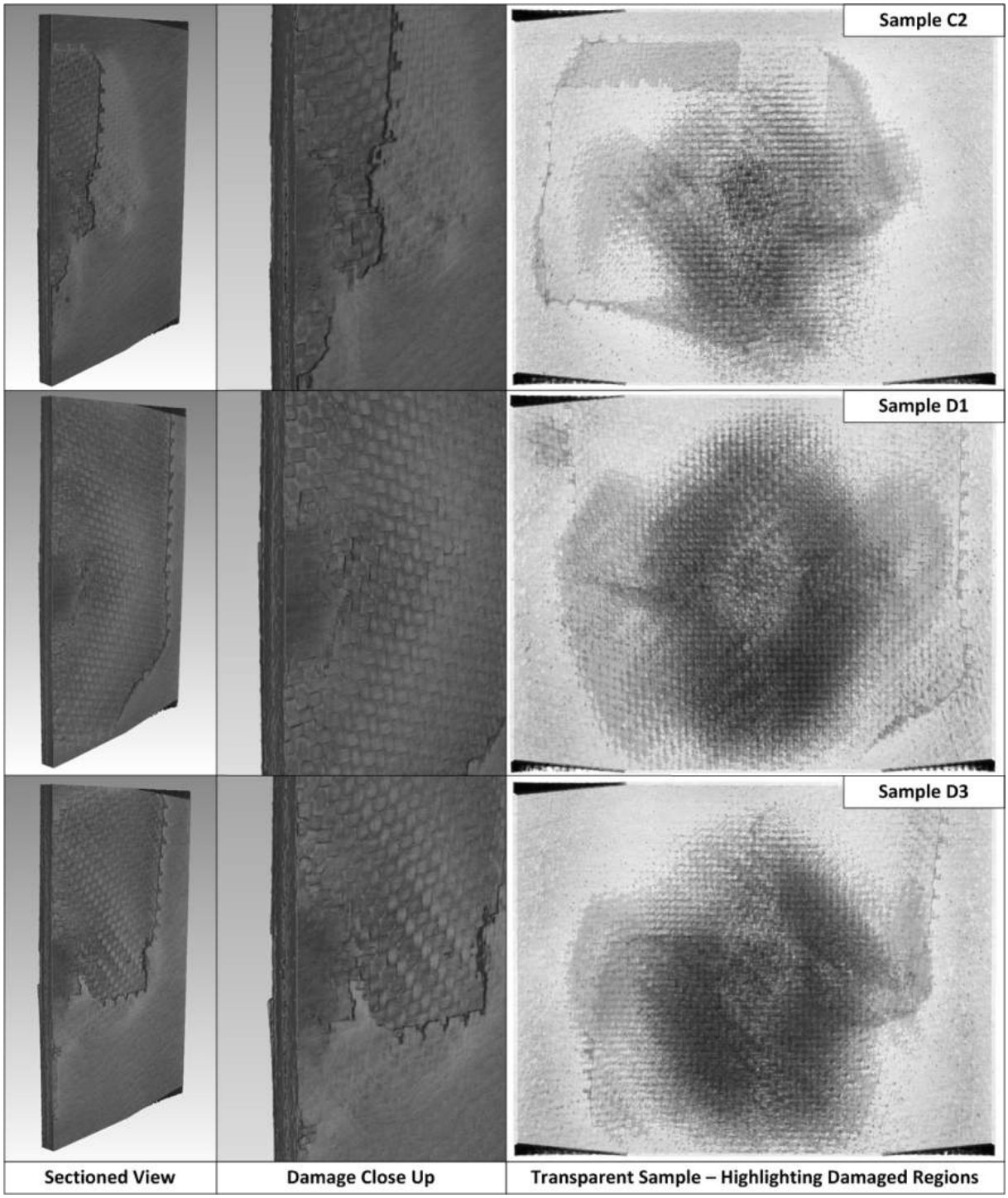

Figure B.5: Ice projectile 3D mid velocity comparison (avg. 402.3 m/s)

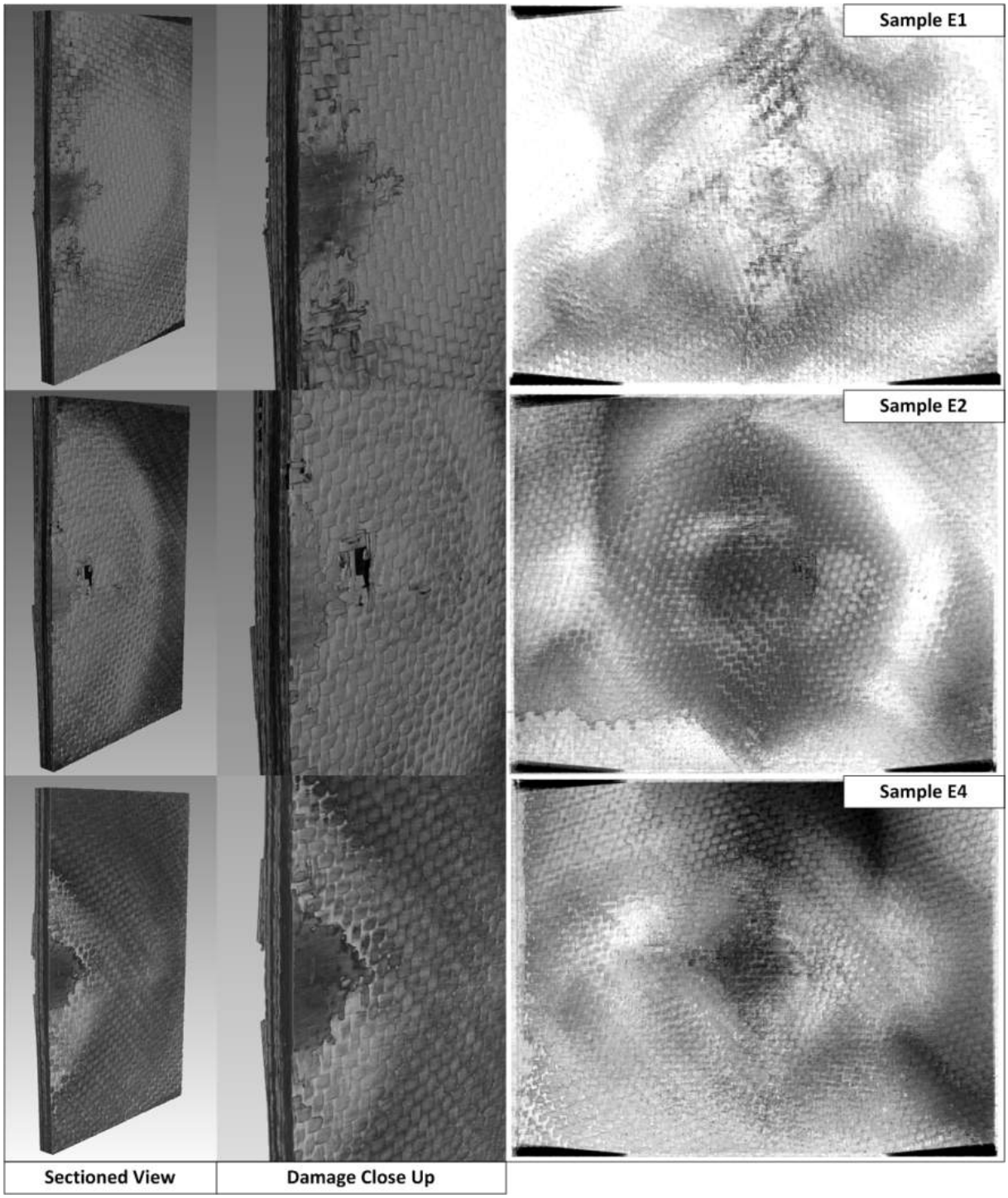

Figure B.6: Ice projectile 3D high velocity comparison (avg. 480.0 m/s)

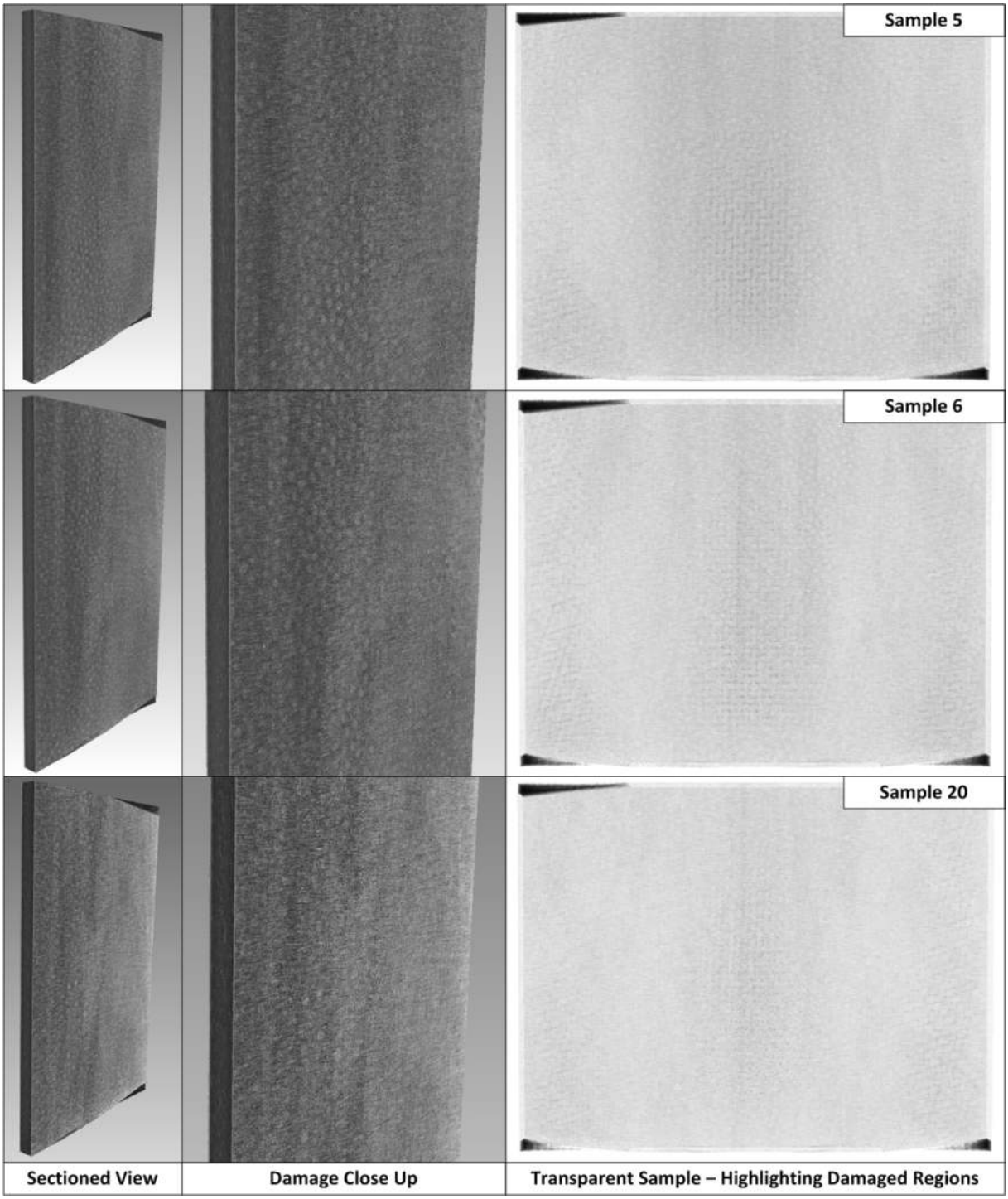

Figure B.7: Air-blast 3D low incident pressure (avg. 0.40 MPa)

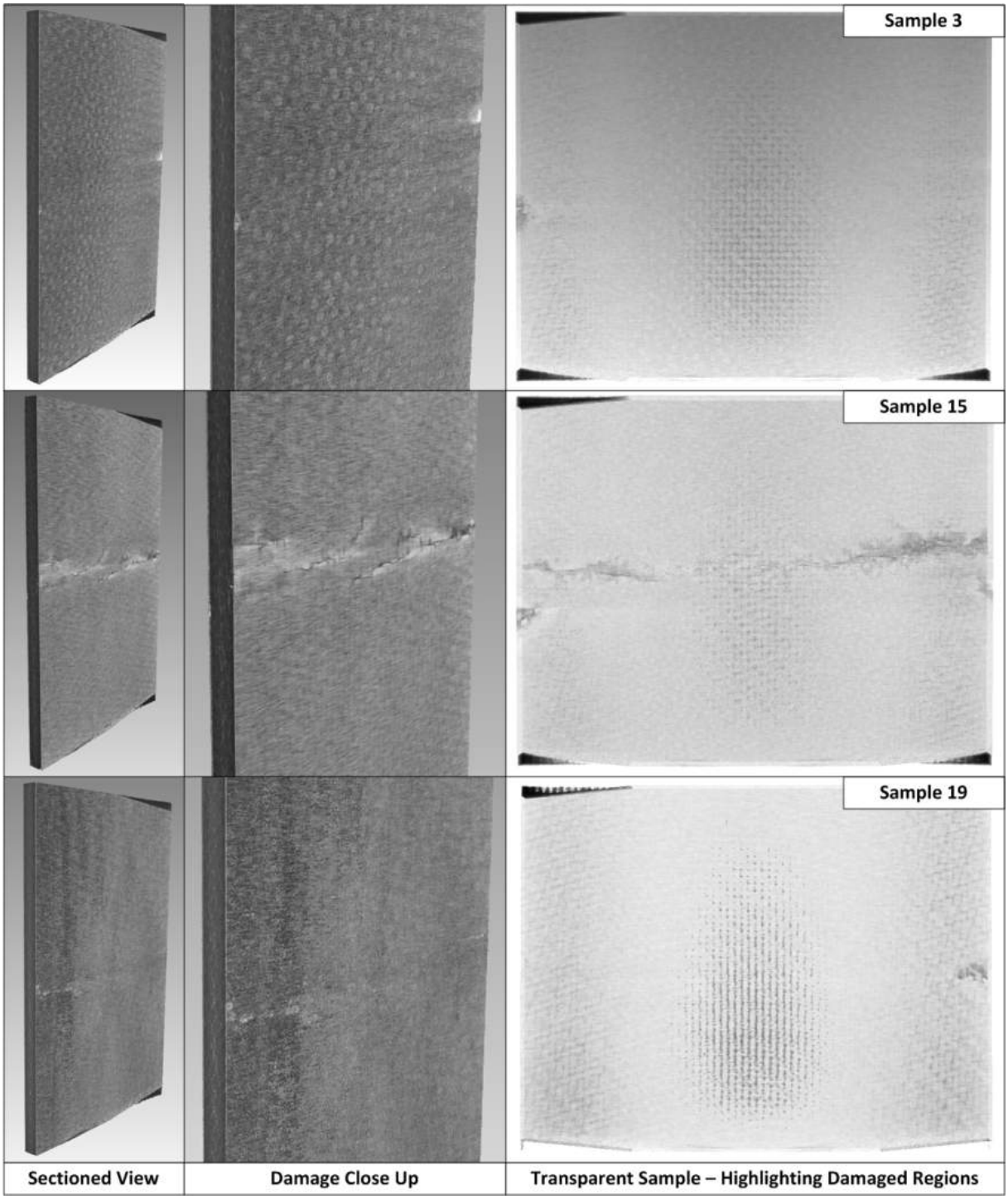

Figure B.8: Air-blast 3D mid incident pressure (avg. 0.62 MPa)

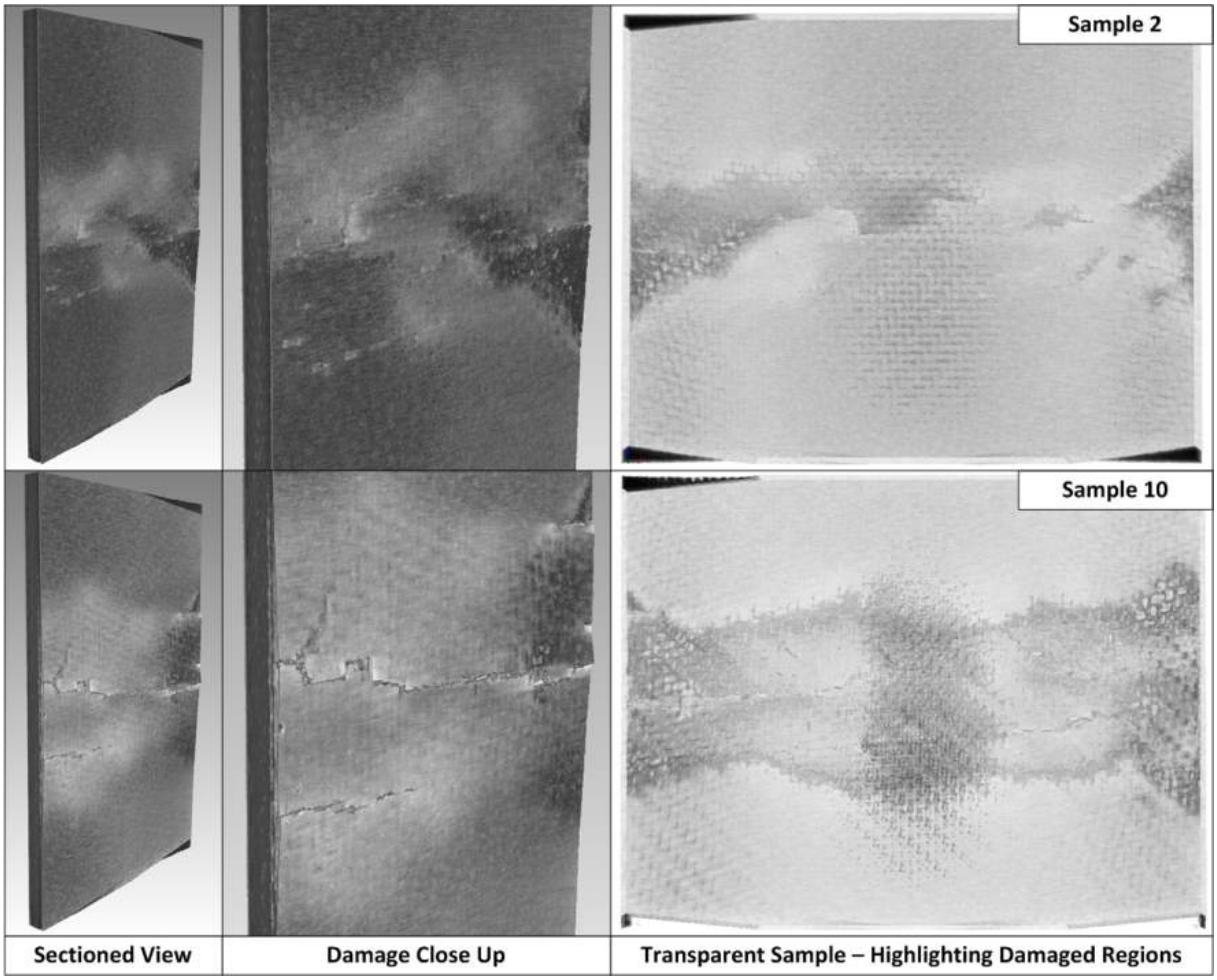

Figure B.9: Air-blast 3D high incident pressure (avg. 0.75 MPa)

B.2 2D Horizontal and Vertical Cross Sections

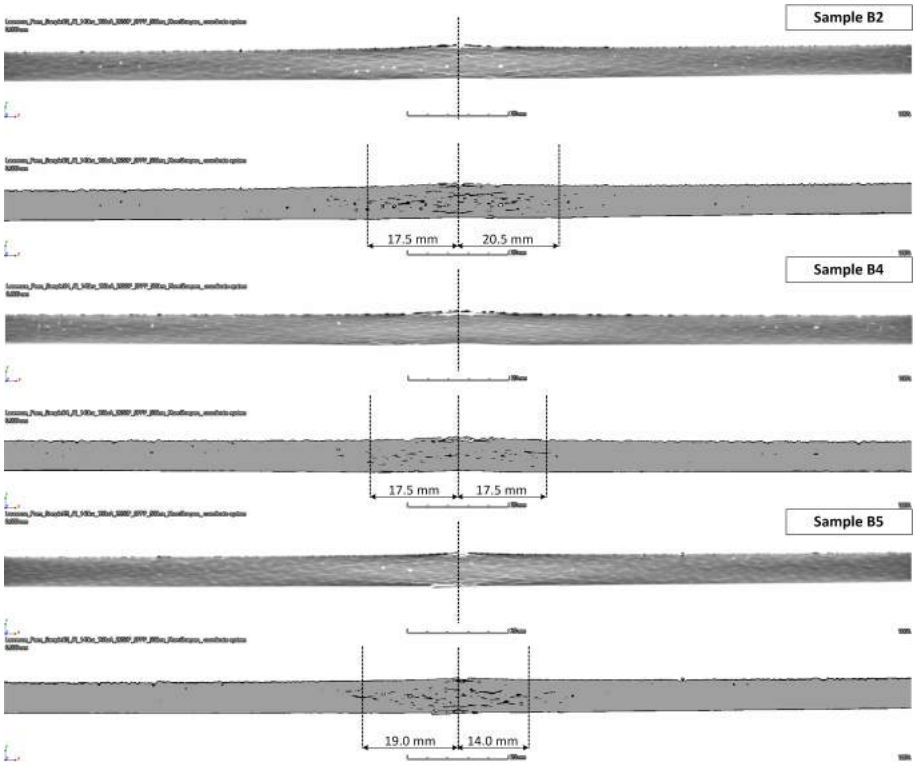

Figure B.10: Steel projectile 2D YZ section low velocity comparison (avg. 59.5 m/s)

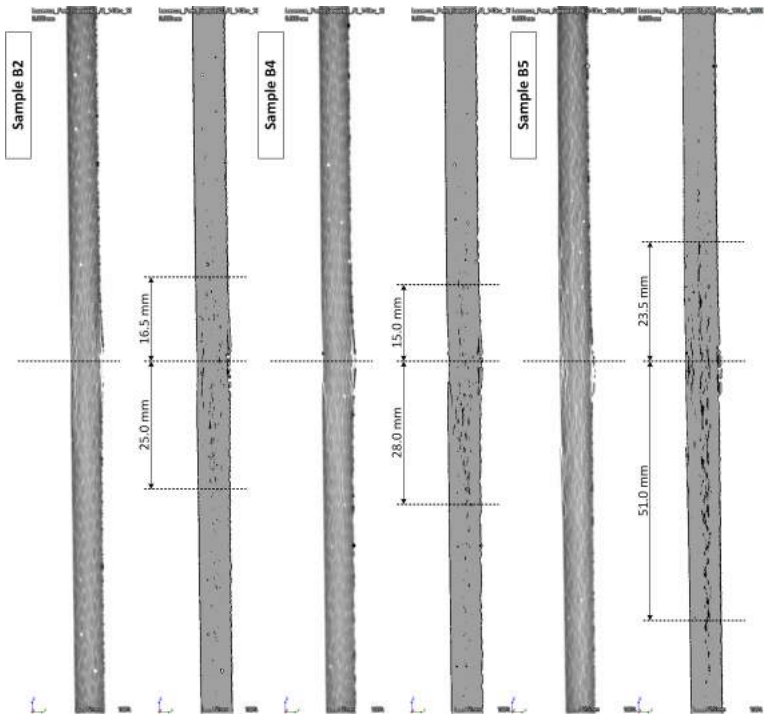

Figure B.11: Steel projectile 2D YZ section low velocity comparison (avg. 59.5 m/s)

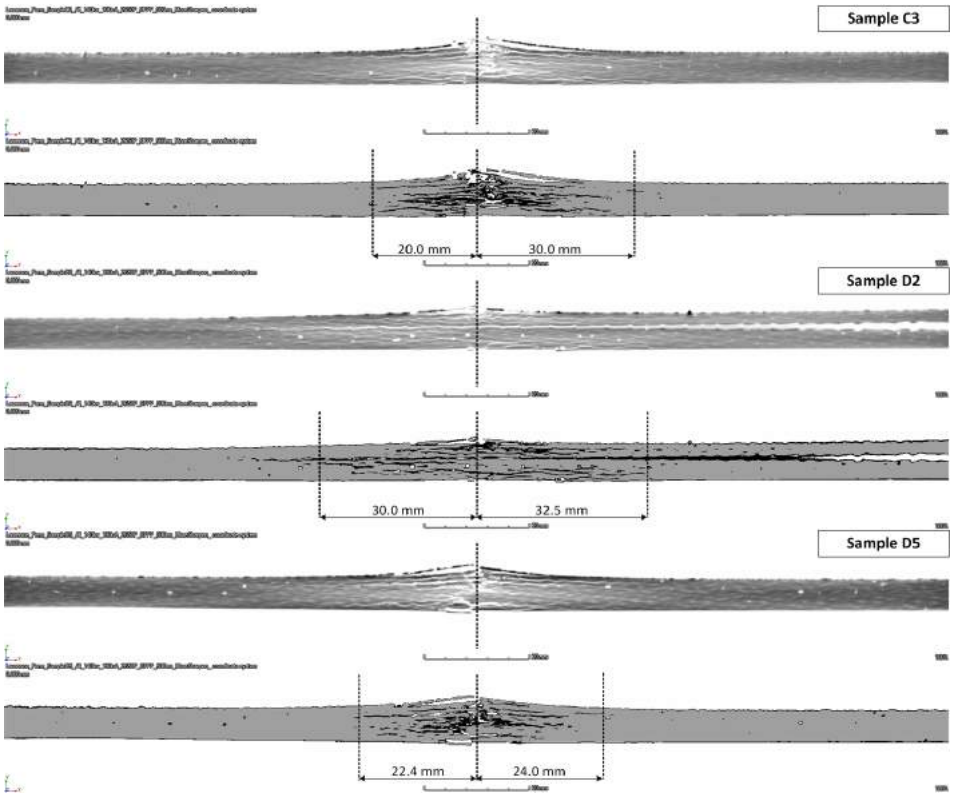

Figure B.12: Steel projectile 2D XY section mid velocity comparison (avg. 78.5 m/s)

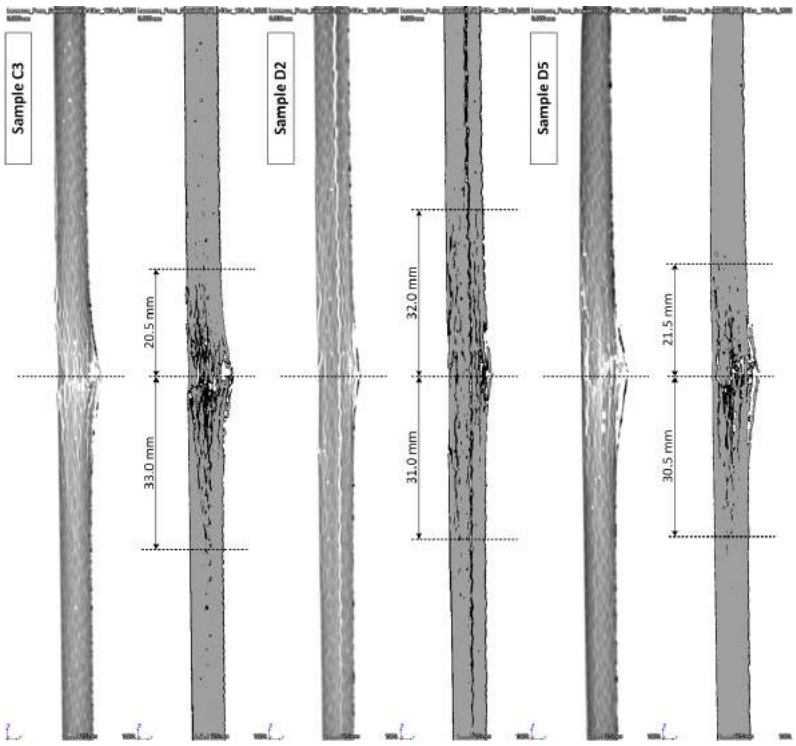

Figure B.13: Steel projectile 2D YZ section mid velocity comparison (avg. 78.5 m/s)

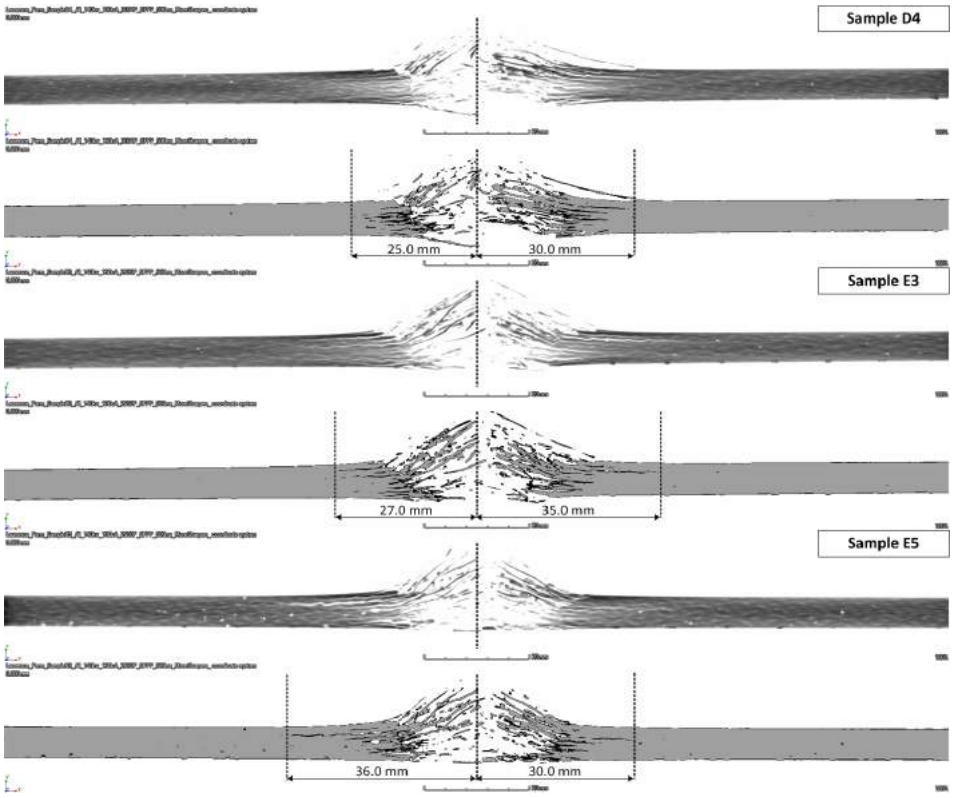

Figure B.14: Steel projectile 2D XY section high velocity comparison (avg. 91.5 m/s)

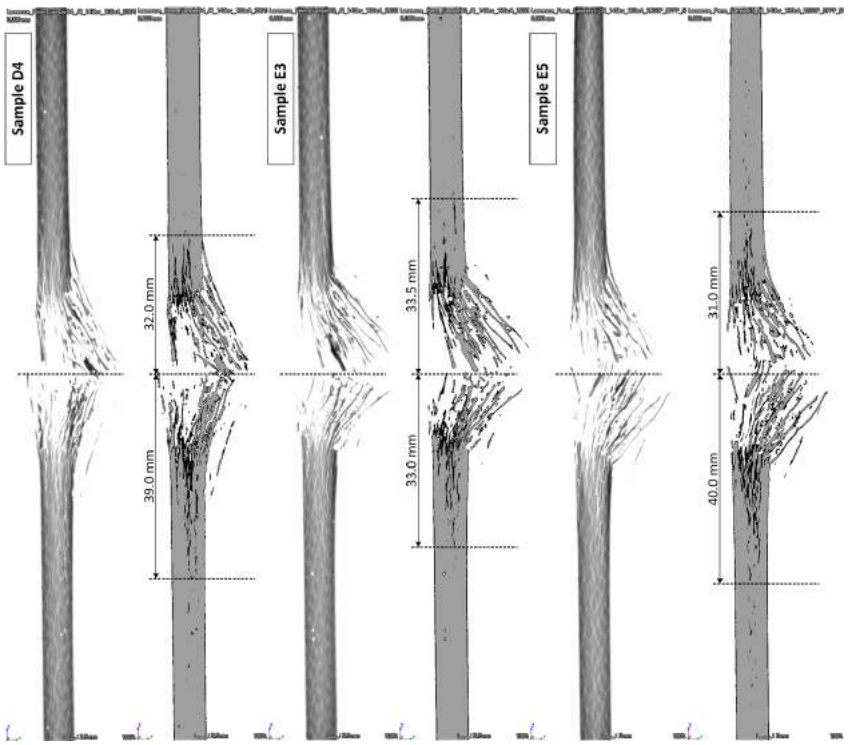

Figure B.15: Steel projectile 2D YZ section high velocity comparison (avg. 91.5 m/s)

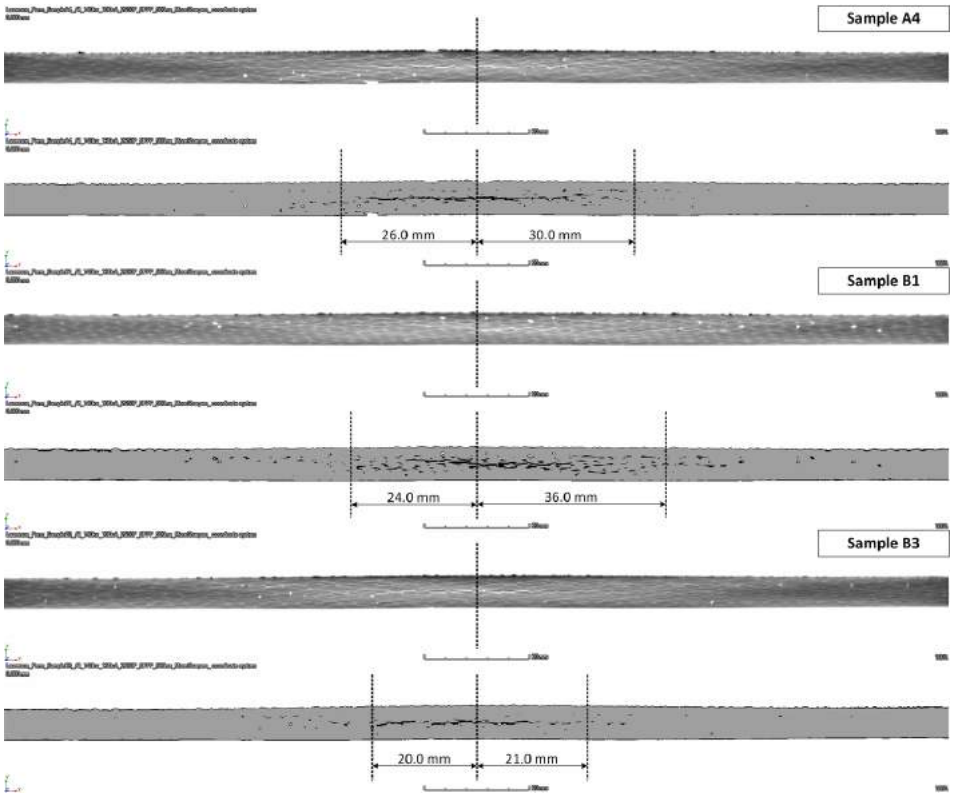

Figure B.16: Ice projectile 2D XY section low velocity comparison (avg. 303.6 m/s)

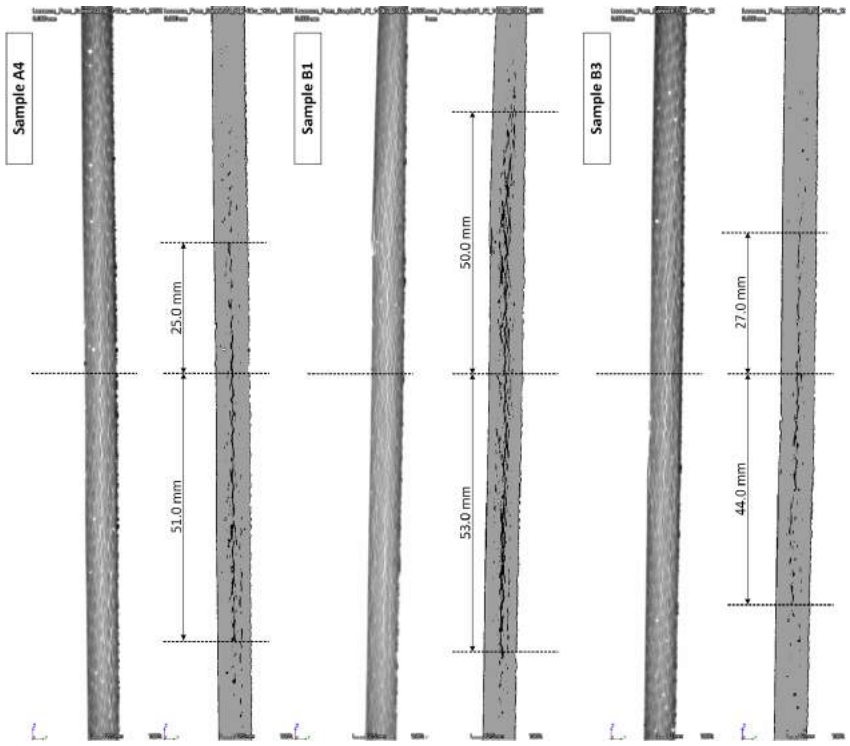

Figure B.17: Ice projectile 2D YZ section low velocity comparison (avg. 303.6 m/s)

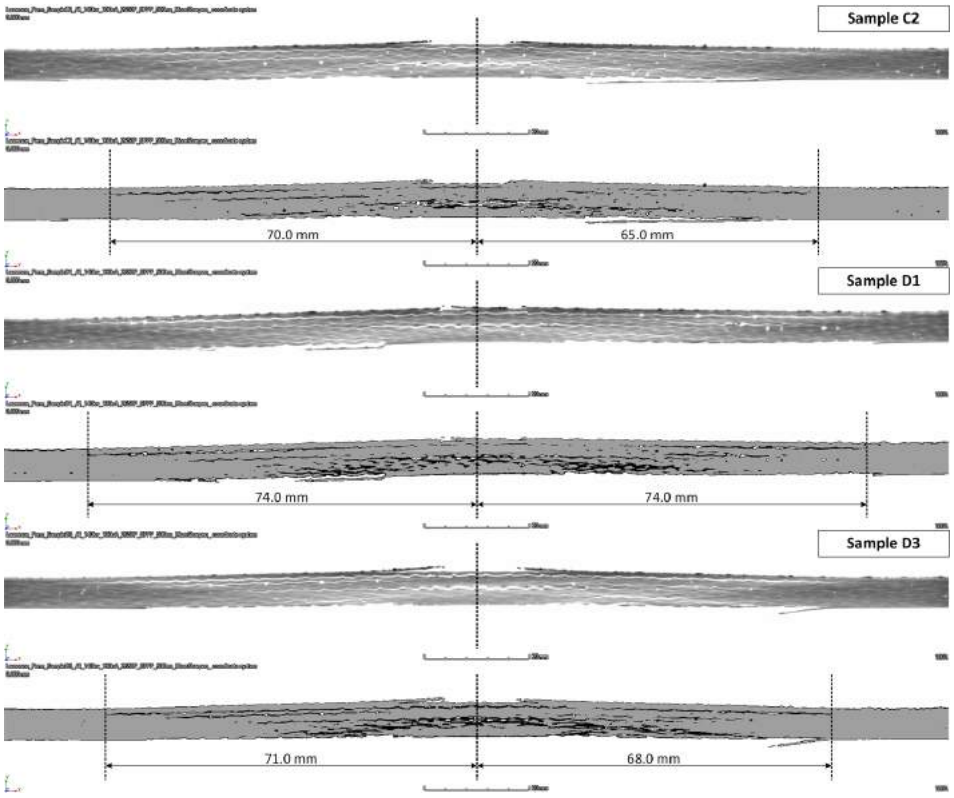

Figure B.18: Ice projectile 2D XY section mid velocity comparison (avg. 402.3 m/s)

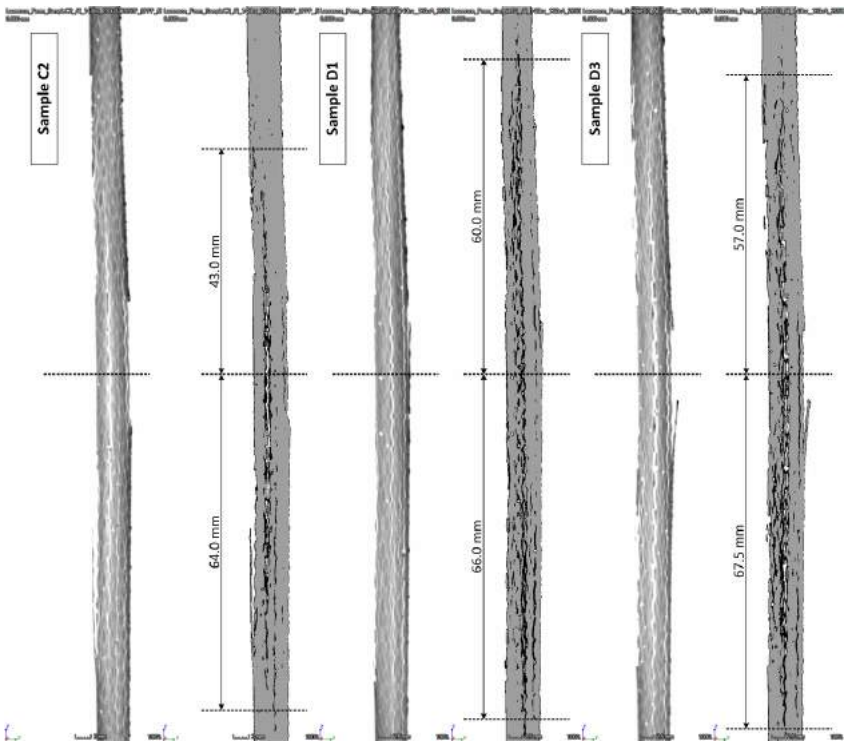

Figure B.19: Ice projectile 2D YZ section mid velocity comparison (avg. 402.3 m/s)

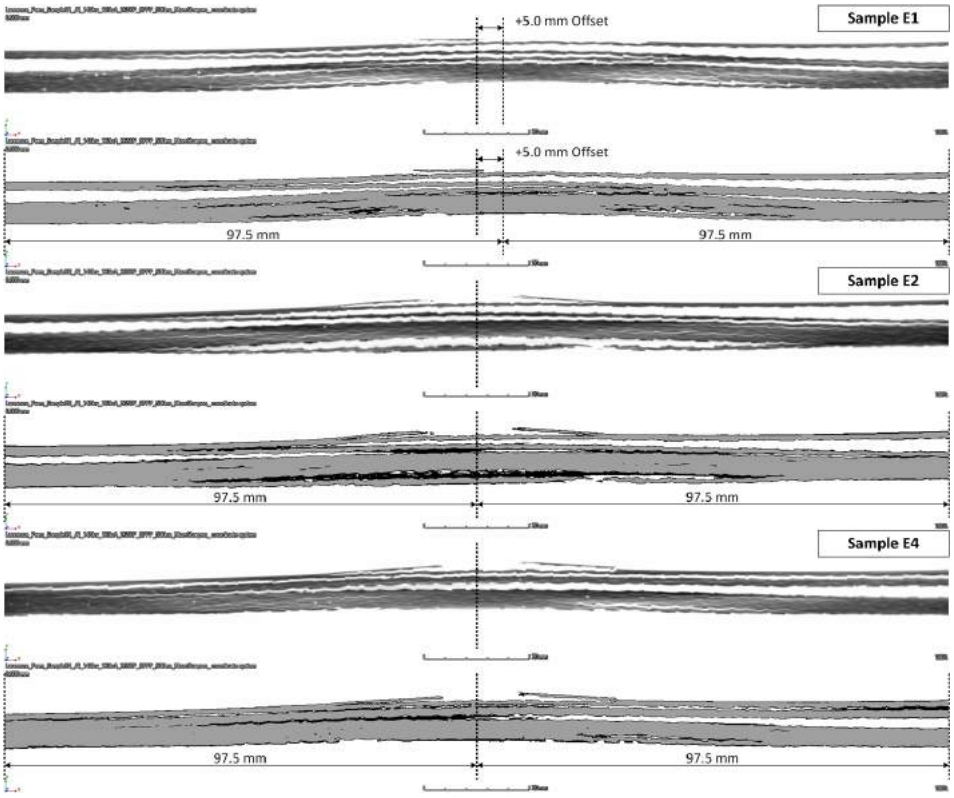

Figure B.20: Ice projectile 2D XY section high velocity comparison (avg. 480.0 m/s)

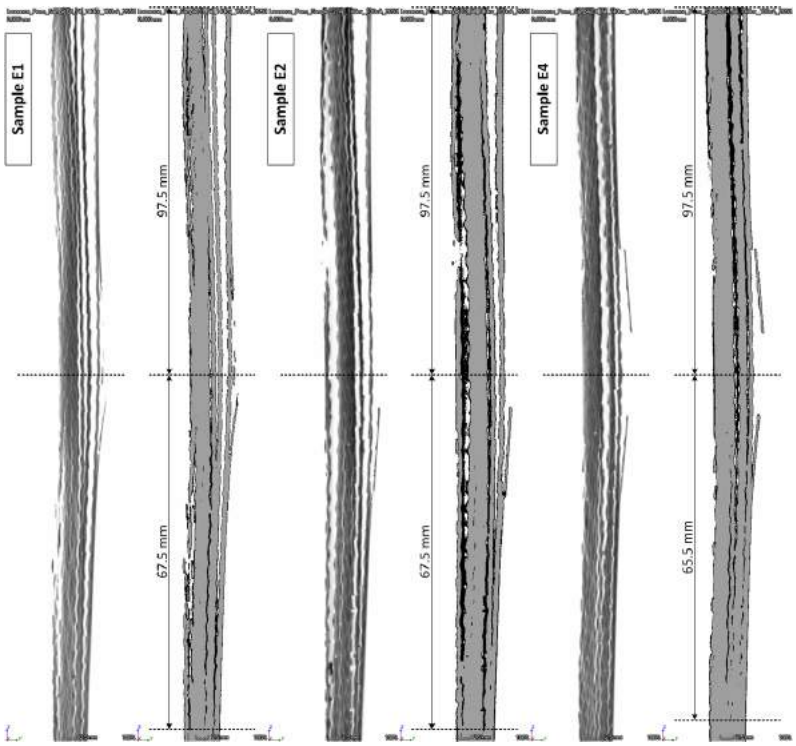

Figure B.21: Ice projectile 2D YZ section high velocity comparison (avg. 480.0 m/s)

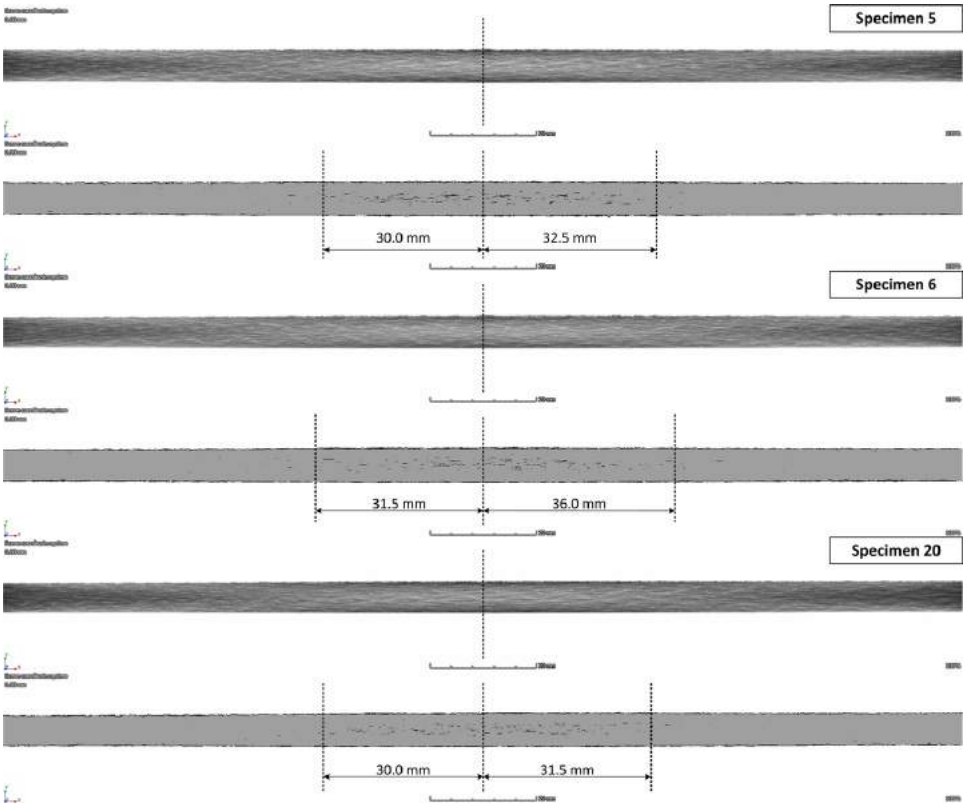

Figure B.22: Blast 2D XY section low incident pressure comparison (avg. 0.40 MPa)

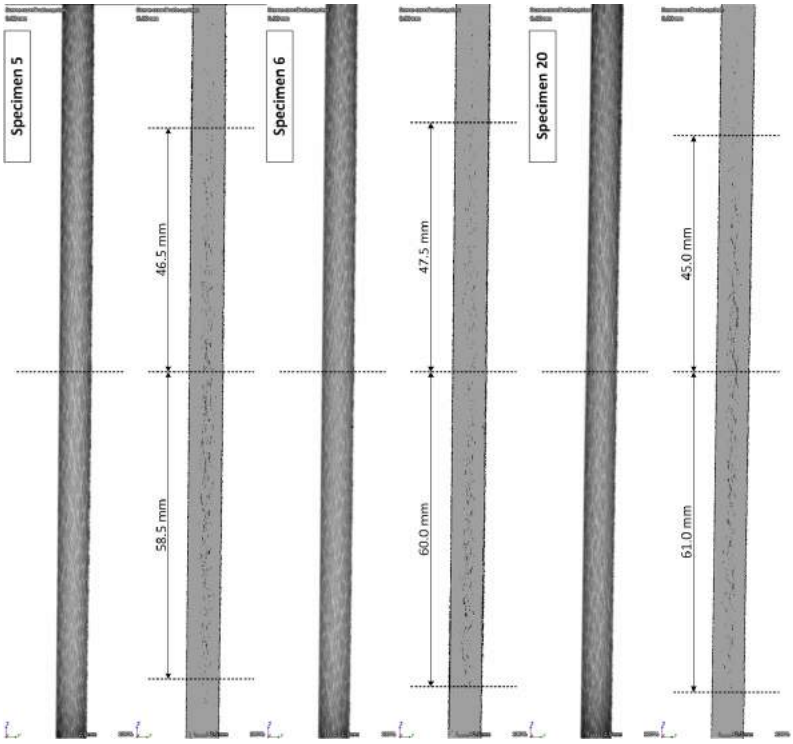

Figure B.23: Blast 2D YZ section low incident pressure comparison (avg. 0.40 MPa)

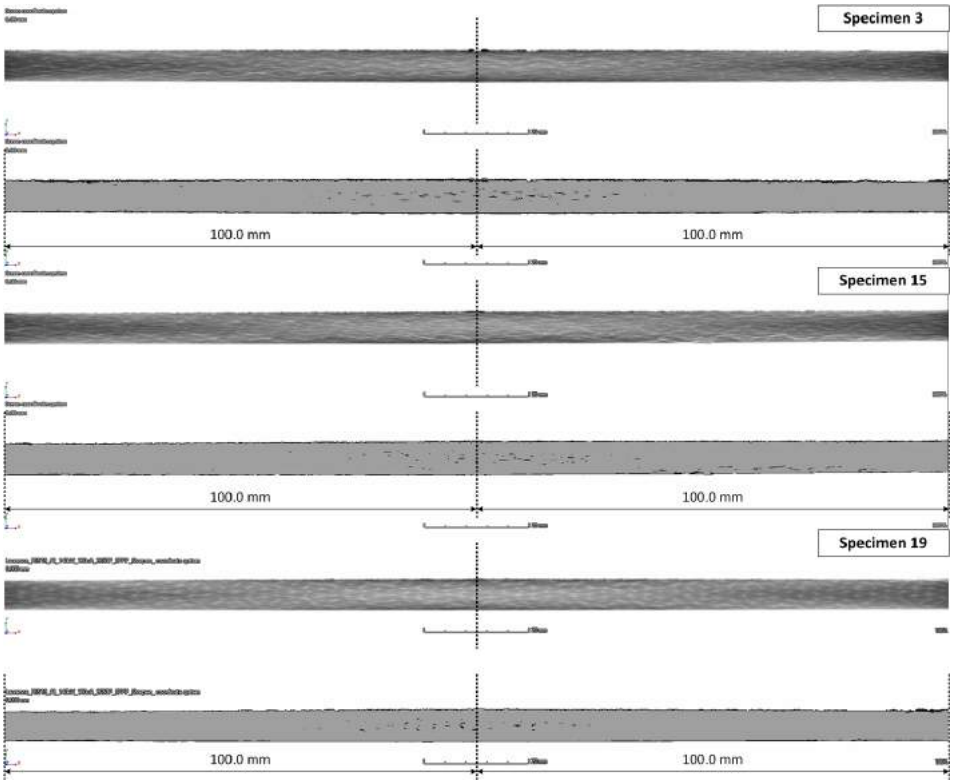

Figure B.24: Blast 2D XY section mid incident pressure comparison (avg. 0.62 MPa)

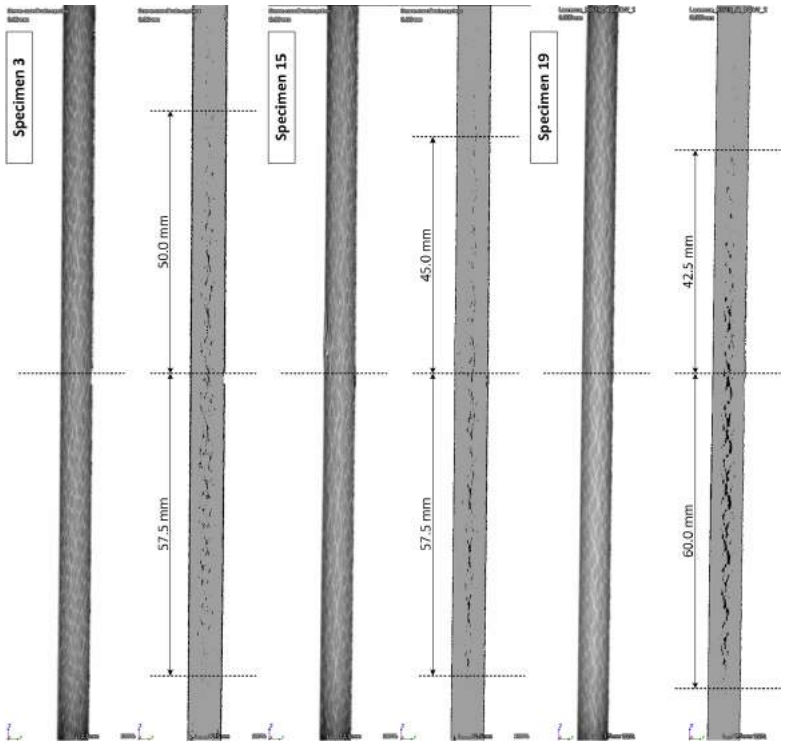

Figure B.25: Blast 2D YZ section mid incident pressure comparison (avg. 0.62 MPa)

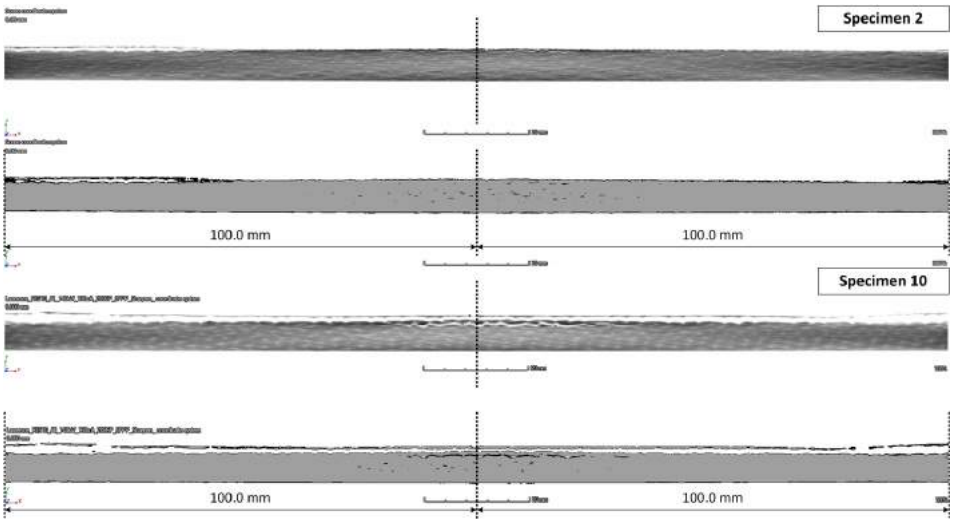

Figure B.26: Blast 2D XY section high incident pressure comparison (avg. 0.75 MPa)

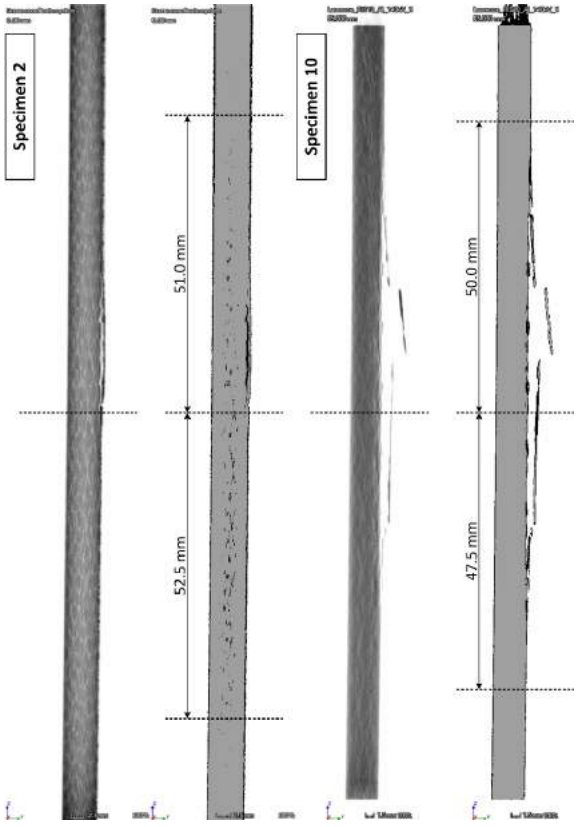

Figure B.27: Blast 2D YZ section high incident pressure comparison (avg. 0.75 MPa)